UNIVERSITY OF OKLAHOMA

GRADUATE COLLEGE

SAFETY AND PERFORMANCE CONSIDERATIONS FOR INTERACTIONS BETWEEN ELECTROMAGNETIC FIELDS AND BIOLOGICAL TISSUE: APPLICATIONS TO HIGH FIELD HUMAN MAGNETIC RESONANCE IMAGING AND TISSUE-IMPLANTED DEVICES

A DISSERTATION

SUBMITTED TO THE GRADUATE FACULTY

in partial fulfillment of the requirements for the

Degree of

DOCTOR OF PHILOSOPHY

By

LIN TANG
Norman, Oklahoma
2010

Downloaded from SHAREOK. Persistent Handle URL: https://hdl.handle.net/11244/319065

SAFETY AND PERFORMANCE CONSIDERATIONS FOR INTERACTIONS BETWEEN ELECTROMAGNETIC FIELDS AND BIOLOGICAL TISSUE: APPLICATIONS TO HIGH FIELD HUMAN MAGNETIC RESONANCE IMAGING AND TISSUE-IMPLANTED DEVICES

A DISSERTATION APPROVED FOR THE
SCHOOL OF ELECTRICAL AND COMPUTER ENGINEERING

BY

Dr. Tamer S. Ibrahim, Co-Chair

Dr. Hong Liu, Co-Chair

Dr. Mark B. Yeary

Dr. Zhisheng Shi

Dr. Michael B. Santos

© Copyright by LIN TANG 2010
All Rights Reserved.

ACKNOWLEDGEMENTS

I would like to express my sincere gratitude to all people who have helped, supported and inspired me during my doctoral study.

I want to show my deepest appreciation to my advisor and co-chair, Prof. Tamer S. Ibrahim, for his guidance during my research and supervision of my dissertation. His advice and invaluable comments greatly directed my research. I truly appreciate his consistent instruction, help and patience especially after his departure from the University of Oklahoma at the end of 2005. His perpetual energy and enthusiasm in work deeply motivated me and will continuously inspire me in my research.

I especially want to thank my co-chair, Prof. Hong Liu, for his consistent help, support and encouragement after Prof Ibrahim's departure. I am very grateful to Prof. Liu for devoting a lot of time, energy and above all, commitment to be my co-chair. I have been deeply influenced by his incomparably profound knowledge.

I would also like to acknowledge my committee members, Prof. Michael B. Santos, Prof. Mark B. Yeary, and Prof. Zhisheng Shi, who generously contributed their time and effort to my study at The University of Oklahoma. I am very grateful for their support and help.

I would like to show my gratitude to Prof. Jinsong Pei, for financially supporting me in my dissertation study.

I would like to thank my colleagues, Dr. Yik-Kiong Hue, Mr. Roney Abraham, and Mr. Doney Abraham for amiable cooperation and data sharing.

The experimental data presented in this dissertation was provided by the ultra high field lab led by Prof. Ibrahim at the University of Pittsburgh.

I would also like to thank the writing center at the University of Oklahoma for revising my dissertation and help in improving my writing skills.

This dissertation would be simply impossible without my family's unflagging love. My parents have been always encouraging me to pursue my interests and dreams. I would not have the opportunity for the education of a doctoral degree without their unlimited love and support. Special thanks go to my dear aunt, Xiaoping, who is always my precious consultant for almost everything. The last and surely the most, I want to acknowledge my darling husband Yadong and my two loving little boys, Andrew and Daniel for their love, support, encouragement and understanding in dealing with the challenges I have faced, for always giving me strength and hope, and for being the motivation of all my work. This dissertation is dedicated to them.

TABLE OF CONTENTS

ABSTRACT xviii
CHAPTER 1 1
INTRODUCTION 1
1.1 Magnetic Resonance Imaging and Brain Machine Interface 1
1.2 Motivations 2
1.2.1 Motive for MRI 2
1.2.2 Motive for BMI 3
1.3 Organization of the Dissertation 4
CHAPTER 2 7
BACKGROUND 7
2.1 Magnetic Resonance Imaging (MRI) 7
2.1.1 Nuclear Magnetic Resonance (NMR) phenomenon 8
2.1.1.1 Spin 8
2.1.1.2 Radio Frequency (RF) Excitation 9
2.1.1.3 T_1 and T_2 Processes 11
2.1.1.4 The Rotation Frame for an RF Field 13
2.1.1.5 Bloch Equations 14
2.1.1.6 RF Pulse Sequences 15
2.1.2 Magnetic Resonance Imaging (MRI) 17
2.1.2.1 Imaging Equation and the Fourier Transform 17
2.1.2.2 Signal Localization and Gradient Rephasing 19
2.1.2.3 Contrast Mechanisms in MRI 20
2.1.2.4 Radiofrequency (RF) Coil 22
2.2 Brain-Machine Interface (BMI) 23
2.2.1 Components of BMI Neuroprosthetic Devices 24
2.2.2 Classification of BMI 25
CHAPTER 3 28
NUMERICAL METHODOLODY – 28
FINITE DIFFERENCE TIME DOMAIN METHOD 28
3.1 Motivation for Using Finite Difference Time Domain Method 28
3.2 FDTD Notations and Equations 30
3.3 Boundary Condition 35
3.2.1 Perfectly Matched Layer (PML) 36
CHAPTER 4 41
B1+ SHIMMING TO OPTIMIZE THE RF COIL'S PERFORMANCE IN MRI WITHIN SAFETY REGULATIONS 41
4.1 Background of Transmit Arrays 42
4.2 Materials and Methods 45
4.2.1 TEM Resonator 45
4.2.2 Human Model 49
4.2.3 Numerical Modeling 53

4.3 Magnetic Field and Power Calculations 57
4.3.1 Inhomogeneous B_1^+ field with increase of B_0 field strength 57
4.3.2 Power Calculations 58
4.3.3 Specific Absorption Rate (SAR) Calculations 60
4.4 Analysis of the RF Power Requirements 60
4.4.1 Coil Excitation 63
4.4.2 Results and Discussion 69
4.4.2.1 Single Element Coil Loaded with Small/Symmetrical Phantom: A Glance into the Quasistatic Predictions 69
4.4.2.2 TEM Resonator Loaded with the Anatomically Detailed Human Head Mesh 73
4.4.3 Summary 90
4.5 UHF MRI Homogenous B_1 Fields with Minimization of RF Power Deposition 93
4.5.1 FDTD Modeling of the Transmit Array 94
4.5.2 Power Calculation and B_1^+ Shimming 94
4.5.3 Experimental Verification 96
4.5.4 Results and Discussion 99
4.5.4.1 Analysis of the B_1^+ Field Distribution 99
4.5.4.2 Power Distribution Analysis 103
4.5.4.3 SAR Analysis 105
4.5.5 Summary 110
4.6 B_1^+ Shimming with Constrained RF Power Deposition and Local SAR Peaks 110
4.6.1 Improved B_1^+ Shimming Scheme 111
4.6.2 Validation of the Optimization Method 113
4.6.3 Results and Discussion 115
4.6.3.1 Analysis of the B_1^+ Field Distribution 115
4.6.3.2 Reduced Power Absorption and Local Peak SAR 117
4.6.4 Summary 124
4.7 SAR Safety Regulations 124
4.8 Shimming in Patterning the B_1^+ field and the Electrical Field 127
4.9 Summaries and Conclusions 129
CHAPTER 5 132
THREE DIMENSIONAL TEMPERATURE STUDY WITHIN THE HEAD/BODY IN MRI 132
5.1 Introduction 132
5.2 Material and Methods 135
5.2.1 Thermal Property Model 135
5.2.2 Bio-Heat Equation and Boundary Condition 138
5.3 Numerical Results and Discussion 141
5.3.1 Temperature Changes in the Head Model 141
5.3.2 Temperature Changes in the Body Model 151
5.4 Summary 158

CHAPTER 6 159
STUDIES IN RF POWER COMMUNICATION, SAR, AND TEMPERATURE ELEVATION IN WIRELESS BRAIN MACHINE INTERFACE APPLICATION 159
6.1 Introduction 159
6.2 Methods 163
6.2.1 The Electromagnetic Model 163
6.2.2 Transmission Line Excitation/Reception and Power Calculations 166
6.2.3 Impedance Matching 171
6.2.4 The Three Dimensional Bio-Heat Model 176
6.3 Validation 179
6.4 Results and Discussions 183
6.4.1 Maximum Receiving Power without SAR Violations 183
6.4.2 Temperature Changes 188
6.5 Summary 193
CHAPTER 7 195
CONCLUSIONS AND FUTURE WORK 195
7.1 Summary and Findings 195
7.1.1 MRI Applications 196
7.1.2 BMI Applications 198
7.2 Future Work 199
7.2.1 Future of MRI 199
7.2.2 Future of BMI 200
BIBLIOGRAPHY 201

LIST OF TABLES

Chapter 2 Tables:

Table 2.2 Properties of some NMR-Active Nuclei. 9

Chapter 4 Tables:

Table 4.1 Electromagnetic properties of the tissues in the head and the body models at 298 MHz. 50
Table 4.2 B_1^+ field distribution homogeneity (calculated by *max/min*) for each slice shown in Figure 4.8 at different B_0 field strengths and under 4-port, 8-port, and 16-port fixed phase/amplitude driving conditions. The 4-port excitations types, "Type A," "Type B," "Type C," and "Type D," and the 8-port excitation types, "Type AC" and "Type BD," are defined in Figure 4.9.....72
Table 4.3 Labels of the optimized regions of interest shown in Figures 4.19-4.23. The columns represent the orientations, thicknesses, and directions of the 3D regions (labeled A through N) over which the homogeneity of B_1^+ field distribution was optimized to achieve minimal coefficient of variation while maintaining total (over the whole head) RF power deposition less than or equal to that obtained with quadrature excitation. 102
Table 4.4 Peak SARs (averaged over any 10 gram of the tissues) in the head model at 7 T and 9.4 T under quadrature excitation and the B_1^+ shimming excitation conditions discussed in section *4.4*. The labels in the first column in the table are the regions of interested (ROIs) defined in Table 4.3. 125
Table 4.5 Peak SARs (averaged over any 10 gram of the tissues) in the body model at 7T under quadrature excitation and the B_1^+ shimming excitation conditions discussed in section *4.5*. Peak SARs are calculated under two cases: considering the whole body and considering the torso only. Note that the arms are always present in the coil during the SAR calculation for both cases. The labels in the first column in the table are the regions of interested (ROIs) as demonstrated in Figure 4.25. 126

Chapter 5 Tables:

Table 5.1 Thermal properties of the tissues in the head and the body models. 136

Chapter 6 Tables:

Table 6.1 Resonant frequencies and input impedances for the loads with different antenna lengths at various positions within the brain.....173

Table 6.2 Thermal properties for white matter tissue and the BMI-chip(s) contained in the human head model.....178
Table 6.3 Maximum receiving power without FCC SAR safety violation for the three dipole antennas at their corresponding resonant frequencies (shown in Table 6.1).184
Table 6.4 Maximum receiving power without FCC peak SAR safety violation at frequency 2.0735GHz (the resonant frequency for 9 mm antenna at 0 mm into the brain).....185
Table 6.5 Comparison of the electromagnetic properties of the human head tissues at 1.27 GHz and 3.39 GHz resonant frequencies of the 5 mm dipole and 15 mm dipole at the surface of the brain, respectively. 186
Table 6.6 The maximum temperature elevations due to SARs from the each case shown in Table 6.3. 189
Table 6.7 The maximum temperature elevations due to SARs for each case shown in Table 6.4. 189
Table 6.8 The maximum temperature elevations due to the external transmitting antenna for the antennas at 0 mm into the brain using different SAR safety regulations. 190
Table 6.9 The maximum temperature elevations for the antennas at 0 mm into the brain using different SAR safety regulations. 193

LIST OF FIGURES

Chapter 2 Figures:

Figure 2.1 Proton spin is regarded as microscopic magnets. 8
Figure 2.2 Nuclear magnetic moment vectors (a) pointing in random directions and (b) aligned in the direction of an external magnetic field. 10
Figure 2.3 In the equilibrium state, the magnetic moment (M_0) of protons along B_0 (z) direction; under RF excitation, M_0 is tipped away from z direction and precesses around the z axis. M_z and M_x (M_y) are longitudinal and transverse magnetizations, respectively. 11
Figure 2.4 (a) The regrowth of the longitudinal component of magnetization from the initial value $M_z(0)$. (b) The decay of the magnitude of the transverse magnetization. 12
Figure 2.5 On-resonance $\pi/2$ spin flip as viewed in primed (a) and unprimed (b) frame. 14
Figure 2.6 A sequence diagram for imaging an entire object in 3D. 18
Figure 2.7 Selection of a slice in $\vec{\mu}_s$ direction 20

Chapter 3 Figures:

Figure 3.1 Yee cell shows the spatial relationship of E and H. 31

Chapter 4 Figures:

Figure 4.1 3D FDTD grid of the single element coil loaded with the small/symmetrical phantom and of the coil element. The coil element is tuned by adjusting the gap between each of the two inner coaxial elements. This figure was presented in [126]. 46
Figure 4.2 Geometry of 16-strut TEM resonator: unloaded resonator picture (a), and loaded with the head model resonator picture (b), simulation unloaded resonator plot (c) and loaded with the head model resonator plot (d). This figure was presented in [128]. 48
Figure 4.3 3D anatomically detailed human VHP body model loaded within the 32-strut TEM resonator. Subfigure (a) is the top-view of the system. There is an open on the coil shield to show the inside body model from a side-view in the subfigure (b). 49
Figure 4.4 FDTD grid of the 16-strut TEM head coil loaded with the human head mesh and the 32-strut TEM body coil loaded with the human body mesh. Subfigure (a) and (c) are the axial cross section of the coil-load system; (b) is the sagittal cross

section of the coil-head system, and (d) is the 2D coronal slice of the coil-body system. 52
Figure 4.5 FDTD calculated frequency spectrum of the 16-strut TEM resonator loaded with the anatomically detailed human head model at 7 tesla. Plot was provided by Mr. R Abraham. 55
Figure 4.6 FDTD calculated frequency response of the B_1^+ field at three different points inside the 32-strut 7 tesla TEM coil operating empty (top subfigure) and loaded with the anatomically detailed body mesh (bottom subfigure). This figure was presented in [135]. 56
Figure 4.7 B_1^+ field distributions across the same axial slice of the head model under different external field strength B_0. All subfigures are normalized to its maximum values, and they share the common normalized color bar. The number on each subfigure is homogeneity measurement *max/min*. 58
Figure 4.8 3D anatomically detailed human head model loaded within the 16-element TEM resonator. The seven individual head cuts show the orientation of seven slices (A1-A4, Sa and Co) used in the power and B_1^+ field calculations. On each slice, 5 points are picked where the B_1^+ field intensity is evaluated by FDTD package. The symbols (X, □, ◊, *, +) show the spatial positioning of these 5 points. The spatial area of each slice is shown under each head cut, respectively.....66
Figure 4.9 Axial slice of the FDTD grid of the 16-element TEM resonator loaded with the 18-tissue anatomically detailed human head model showing a cut of the coil where slice A1 (Figure 4.3) is located. All coil elements ports are used in 16-port excitation; ports labeled A and C are used in 8-port excitation "Type AC;" ports labeled B and D are used in 8-port excitation "Type BD;" 4 ports labeled A are used in 4-port excitation "Type A," and the same naming convention was used for 4-port excitation "Type B," "Type C," and "Type D". 67
Figure 4.10 Plots of required RF power absorbed in the small/symmetrical phantom loaded in the single element coil (Figure 4.1) in order to obtain a fixed average (over the volume of the phantom) B_1^+ or B_1^- field intensity as a function of frequency. "ω^2" plot denotes the square dependence predicted from quasistatic approximations. This figure was presented in [117]. 71
Figure 4.11 Plots of *max/min* (maximum B_1^+ field intensity over minimum B_1^+ field intensity within the same slice) for each slice shown in Figure 4.8 at different B_0 field strengths and under 4-, 8-, and 16- port fixed phase/amplitude driving conditions. The 4-port excitations types, "Type A," "Type B," "Type C," and "Type D," and the 8-port excitation types, "Type AC" and "Type BD," are defined in Figure 4.8. Each subfigure corresponds to a different slice. For a particular driving condition, the *max/min* values are presented with the same symbol at all B_0 field strengths. This figure was presented in [117].....74
Figure 4.12 B_1^+ field distributions for each slice shown in Figure 4.8. The data are presented at 9.4 and 7 tesla using 16-port excitation with 2 conditions, fixed and optimized phase/amplitude (FPA and OPA) driving conditions. In the horizontal direction, every set of 6 sub-figures is orderly positioned to correspond to slices A1-4, slice Sa, and slice Co (Figure 4.8), respectively. In the vertical direction, under

"9.4 tesla, 16-Port Excitation," the top and bottom rows correspond to 16-port FPA and OPA driving conditions, respectively. Under "7 tesla, 16-Port Excitation", the top row corresponds to 16-port FPA driving conditions and the middle and bottom rows correspond to 2 possible solutions for 16-port OPA driving conditions. The two solutions correspond to 2 different B_1^+ field distributions yet have the same homogeneity, i.e., the same "maximum B_1^+ field intensity over minimum B_1^+ field intensity" within the same slice; this value is denoted as *max/min*. The number above each sub-figure corresponds to *max/min* within that slice. All the results are presented for the coil configuration shown in Figure 4.8. Figure 4.12 was presented in [117]. 77
Figure 4.13 Plots of required absorbed (in the human head) power in order to obtain a fixed (1.174 μT) average (over the area of each of the 6 slices shown in Figure 4.8) B_1^+ field intensity as a function of B_0 field strength. The results are presented under 16-, 8-, and 4- port fixed phase/amplitude driving conditions. From left to right, the 3 columns correspond to 16-, 8-, and 4-port excitations, respectively. From top to bottom, the 6 rows correspond to the results for the 6 slices (orderly positioned as slices A1-4, Sa, and Co, respectively). In each sub-plot, the X-axis is the B_0 field (tesla) and the Y-axis is the power absorbed in the head (watts). The excitation types which denote the choice of the excited coil elements in 8- and 4- port excitations are defined in Figure 4.9. All the results are presented for the coil configuration shown in Figure 4.8. Figure 4.13 was presented in [117].....80
Figure 4.14 Top: Comparison of the power absorbed in the human head under 16-, 8-, and 4- port excitations. The results are presented for slice A3 (Figure 4.8). The values on each sub-plot correspond to the power required to achieve average (across slice A3) B_1^+ field intensity = 1.174 μT. The power values at all field strengths and under all the driving conditions are achieved for the same B_1^+ field homogeneity, i.e., *max/min* (defined in Figure 4.9) = 1.70. This value represents the best possible homogeneity achieved using 4-port optimized phase/amplitude driving conditions at 9.4 tesla. Bottom (Color Scale): The corresponding B_1^+ field and total electric field distributions in slice A3 at 4, 7, and 9.4 with *max/min* = 1.70. All the results are presented for the coil configuration shown in Figure 4.8. Figure 4.14 was presented in [117]. 82
Figure 4.15 Plot of the required absorbed power in order to obtain an average (across slice A1 shown in Figure 4.8) B_1^+ field intensity = 1.174 μT under 16-, and 4- port fixed and optimized phase/amplitude driving conditions at different field strengths. The power values for the optimized phase/amplitude driving conditions are presented for the same homogeneity of the B_1^+ field distribution at all field strengths; i.e., *max/min* (defined in Figure 4.11) = 3.03 and 1.74 corresponding to the most optimized homogeneity at 9.4 tesla under 4-port Type C, and 16-port excitations, respectively. This figure was presented in [117].....86
Figure 4.16 Plots of the absorbed power required in order to obtain a fixed (1.174 μT) average (over the area of each of the 6 slices shown in Figure 4.8) B_1^+ field intensity under different B_0 field strengths. The calculations are performed using 16-port optimized phase/amplitude driving conditions. From top to bottom, the 6 rows

correspond to the results for the 6 slices (orderly positioned as slices A1-4, Sa, and Co, respectively.) The number above each sub-figure corresponds to *max/min* (defined in Figure 4.11) for that slice. *max/min* was fixed (most optimized value at 9.4 tesla) at each field strength for each slice. At 4, 7, and 9.4 tesla, 2 solutions of the power calculations (represented by “ “ and “o“) are presented for 2 different B_1^+ field distributions, yet have the same *max/min*. This figure was presented in [117]. 88
Figure 4.17 Plots of the ratios (before and after optimization at 9.4 tesla) of the B_1^+ field intensities at the 5 points positioned in each slice shown in Figure 4.8. All the B_1^+ field intensities were scaled to the same absorbed power. The symbols selection is the same as that used in Figure 4.8. Figure 4.17 was presented in [117]. 90
Figure 4.18 (a) Picture of the highly-coupled 8-element TEM resonator loaded with a spherical phantom filled with brain-like constitutive properties; (b) B_1^+ field distribution and GRE images FDTD-calculated under quadrature and B_1^+ shimming (optimized for minimization of 1) the coefficient of variation of B_1^+ field distribution and 2) total RF power absorption by the phantom) excitation and the corresponding experimental images obtained using 7 tesla whole-body scanner equipped with a multi-transmit array. The images were obtained using 4-port excitation/reception. The phases and amplitudes of the excitation pulses, and parameters for the coil tuning and matching were fully obtained and directly implemented from the rigorous FDTD modeling and without any B_1^+/ B_1^- (transmit/receive) measurements. The picture (a) is provided by Dr. Tamer Ibrahim at the ultra high field lab in University of Pittsburgh; images (b) was presented in [120]. 98
Figure 4.19 Normalized B_1^+ field distributions calculated using the FDTD model at 7 tesla and 9.4 tesla. The 14 subfigures represent the distributions for whole head, brain, 3-cm slabs and 6-cm slabs (all labeled in Table 4.3) under 16-port, quadrature and optimized (B_1+ shimming) excitations. The results are presented for an 18-tissue human head model numerically loaded in a 16-element TEM coil (numerically tuned to approximately 300 MHz and 400MHz) and operating as a transmit array. The homogeneity of B_1^+ field distribution in each region of interest was optimized in order to achieve minimum coefficient of variance while maintaining or reducing the total (over the whole head) RF power deposition (obtained with quadrature excitation.) The letter on each subfigure represents the label of the optimized region of interest as shown in Table 4.3. The numbers above each subfigure represent the values of the Coefficient of Variance/Absorbed Power, where the absorbed power in each case is scaled to achieve a mean B_1^+ field intensity of 1.957 μT in the volume of any ROI. 101
Figure 4.20 Comparisons of the RF power absorption in each ROI shown in Table 4.3 and Figure 4.19 at 7 tesla and 9.4 tesla. The ROIs are shown in *x* axis and “Ax”, and “Co”, “Sa” represent the averaged absorbed power within grouping of the four slabs (three 3-cm thickness slabs and one 6-cm thickness slab) along axial, coronal, sagittal directions, respectively. The numbers on the y axis represent the total RF power absorption in each labeled region which produces a mean B_1^+ field intensity of 1.957μT in that same region. The black bars represent the RF absorbed power

(Watts) under quadrature excitation and the gray bars represent the RF power absorption with B_1^+ shimming.....104
Figure 4.21 Locations of the SAR peaks under quadrature excitation (labeled as "X") and under B_1^+ shimming (labeled as "A" to "N" as shown in Table 4.3); the front view and side view of the 3D head model are shown to visualize each location's relative coordinates.....106
Figure 4.22 SAR peak values (over the whole-head) and the SAR distribution COV values (over the whole-head) under quadrature excitation (labeled as "X") and under optimized excitation (B_1^+ shimming) labeled as "O". The labels for the ROIs on the *x* axis are defined in Table 4.3, and the values on the y axis represent the SAR peaks averaged for every 10 gram tissue (Watts/kilogram per 10gm) or the SAR distribution COV. 107
Figure 4.23 SAR distributions at 7 tesla and 9.4 tesla. The 15 subfigures at each of B_0 field strength represent the SAR distributions under quadrature excitation (labeled as "X") and under optimized excitation (B_1^+ shimming) (labeled as "A" to "N" as shown in Table 4.3). The color bar used in each subfigure is set between zero and the peak SAR value obtained under each excitation condition. 109
Figure 4.24 7 tesla focused and homogeneous 3D shimming without B_1 measurements with successful minimization of 1) local SARs, 2) global SARs, and 3) the variation in the flip angle (B_1^+) distribution inside the ROI. 115
Figure 4.25 The B_1^+ field distributions inside the slices and slabs of interest, the heart, and the pancreas under quadrature condition (Qua) and the B_1^+ shimming excitation conditions in the "with arms" case (Opt/w arms) and "without arms" case (Opt/wo arms). The number under each subfigure is the coefficient of variance (COV) of the B_1^+ field distribution. All the subfigures are normalized from 0 to 1 as shown by the color bar. 117
Figure 4.26 Comparison of the power absorption under quadrature and the B_1^+ shimming excitation conditions, where the ROIs shown on the x axis are same as Figure 4.25. The black bars are the normalized power absorption under initial quadrature condition, and the green bars show the relative decrease of the power absorption after optimizations. The above subfigure is for the "with arms" case and the below one represents the "without arms" case. 119
Figure 4.27 Comparison of the SAR peaks under quadrature condition and the B_1^+ shimming excitation conditions, where the ROIs shown on the x axis are same as Figure 4.25. The black bars are the normalized peak SARs under initial quadrature condition, and the green bars show the relative decrease of the SAR peak values after optimizations. Similar to Figure 4.26, the above subfigure is for the "with arms" case and the below one represents the "without arms" case. 120
Figure 4.28 The SAR peak locations. Subfigure (a) shows the locations before and after optimization of the "with arms" case and subfigure (b) corresponds to optimization of the "without arms" case over 12 regions as same as in Figure 4.25. In both cases, symbol definitions are described in the legend.....121
Figure 4.29 SAR distributions corresponding to average B_1^+=1.957 μT in the specific regions ("without arm" case). The region selections shown in the top row are same as

Figure 4.25. All the subfigures are normalized from 0 to maximum SAR peak (133.32 w/kg) which is the peak SAR to obtain B_1^+=1.957 μT in a pancreas organ under quadrature excitation, as shown in the subfigure located in the second row and first column.....123
Figure 4.30 Axial slice small angle signal ($B_1^+ \times B_1^-$) images with some simple patterns. 128
Figure 4.31 Electric field localizations. E fields were localized in the circles and 0.79 cm in height cylindrical regions at k=60 and k=45 positions. Electric field distributions under quadrature and localization conditions were compared in the two cases.....129

Chapter 5 Figures:

Figure 5.1 Temperature elevation (ΔT) changes with time for 7 tesla MRI. The left subplot is the increased temperature at the position where peak ΔT is located using quadrature excitation condition, and the right subplot is the peak ΔT under B_1^+ shimming exciting condition for the brain. 142
Figure 5.2 Temperature elevation (ΔT) and SAR (averaged over any 10 gram of tissue) distributions at quadrature (Qua) and B_1^+ shimming (Opt) exciting conditions over ROIs at 7 tesla and 9.4 tesla MRI, respectively. The ROI selection is same as section *4.4*.....143
Figure 5.3 The selected slabs. All three slabs are 84mm thick. Slab_A is an axial slab located at the center of the coil; Slab_C and Slab_S are 252mm long in coronal and sagittal directions, respectively.....152
Figure 5.4 Temperature elevation (ΔT) and SAR (averaged over any 10 gram of tissue) distributions within whole body (a) and torso only (arms are removed) (b) under different excitation conditions at 7 tesla MRI. The most left column of the subfigures are ΔT distributions within 3D human body model (a) and torso (b), the right two columns are the comparison between 2D ΔT and SAR distributions at interested planes: the plane where the maximum ΔT is located (the middle column) and the plane where the maximum SAR is located (the most right column).....155

Chapter 6 Figures:

Figure 6.1 Structure of the chip with a 9 mm antenna. 164
Figure 6.2 Positions of the transmitting/external antenna outside of the head and the implanted BMI chips at different depths inside the brain. 165
Figure 6.3 The domain of the head mesh and the antenna system in axial (a), sagittial (b), and coronal (c) directions. The yellow frames in each subfigure are the PML layers, the red dot in (a) and red line in (b) show the position of the external antenna. 166

Figure 6.4 The differentiated Gaussian pulse in time (a) and frequency (b) domains. 167
Figure 6.5 Interface between the coaxial transmission line and the three dimensional FDTD code. 168
Figure 6.6 Frequency responds for antennas with the lengths of 5 mm, 9 mm, and 15 mm at the locations 10 mm into the brain. 173
Figure 6.7 Impedances of the implanted antennas (5 mm, 9 mm, 15 mm) at locations 0 mm, 10 mm, 30 mm and 60 mm from the surface into the brain as shown in Figure 6.2. 176
Figure 6.8 A silicon power plane in the white matter cube. 179
Figure 6.9 Power radiation in (a) lossless (a) and (b) lossy medium. The instantaneous (black line), time averaged (blue line) and analytical result derived from Equation (6.15) (red line) of the power radiation is normalized and shown as a function of radial distance from the source in both (a) and (b). 181
Figure 6. 10 Antenna performances at different frequencies in receiving power without FCC SAR safety violation. Antennas individual operation frequencies are presented in Table 6.1. 187
Figure 6.11 Logarithmic SAR and temperature (T) distributions for the antennas with the lengths of 5 mm, 9 mm and 15 mm located at 0 mm into the brain. 190
Figure 6.12 Temperature distributions within the white-matter cubes containing the 5 mm, 9 mm, and 15 mm antennas. 191
Figure 6.13 Temperature increase with time at the test point. 192

ABSTRACT

The principal advantage of magnetic resonance imaging (MRI) at high field is the increase in signal to noise ratio (SNR), however, high field imaging also leads to an increased *Larmor* (operating) frequency, thus the wavelength in tissue can become comparable to the size of the load and/or the coil. The performance of the radiofrequency (RF) coil, as a result, becomes increasingly dependent on its electromagnetic interactions with the load, human body or head.

Invasive brain machine interface (BMI) technology uses implanted microelectrodes to capture the action potentials of many individual neurons, especially those that code for movement or its intent. Traditionally, stimulating nerves or brain tissue involves cumbersome wiring to power/communicate with the chip. To avoid the limit of the BMI's mobility and freedom, RF powered wireless implementation of a BMI chip has been proposed to widely extend BMI applications. It is essential to perform an analysis of electromagnetic power deposition throughout the human head to determine the amount of power available to BMI devices.

In this dissertation, a complete electromagnetic computational (full wave) analysis, the finite difference time domain (FDTD) method, is applied to calculate the interaction between the radio frequency (RF) magnetic field and the subjects during ultra high field MRI exams and wireless BMI operations. The interactions between the high frequency RF fields with the human head and the body models severely affect the performances of MRI and BMI operations, and they also cause

heating safety concerns to the tissues exposed to the RF radiation. Through precisely numerical calculations, we accomplished in this dissertation 1) an improved optimization scheme using variable phase and variable amplitude excitation to improve the performance of RF transverse electromagnetic (TEM) coils in MRI with safety concerns; and 2) evaluations of the performance and safety for a prototype of the wireless invasive BMI. Temperature changes caused by RF power deposition are calculated in both MRI and BMI applications.

CHAPTER 1

INTRODUCTION

1.1 Magnetic Resonance Imaging and Brain Machine Interface

Magnetic resonance imaging (MRI) is a noninvasive medical imaging technique to produce detailed images of the inside of the human body [1]. As one of the medical procedures associated with acceptable and well controlled risks, MRI has been used for medical diagnoses and has been fast developing in research application for more than 30 years since the first demonstration on small test tube samples by Paul Lauterbur in 1973 [2]. MRI mainly records spatial maps of nuclear magnetic resonance (NMR) properties of water, which composes about 80 percent of human tissue. It provides high spatial resolution and excellent soft tissue contrast to detect subtle tissue differences caused by various pathologies at early stages. There are three types of magnetic field used in MRI systems: static magnetic field (B_0), gradient field, and radio-frequency (RF) field (B_1) [3]. The B_0 field is the strongest among the three, and it provides a stable and intense magnetic environment over the subject (patient body); the gradient field is used to realize the selection of the spatial information; and the RF B_1 field is applied to excite nuclei transmit signals.

Brain-machine interface (BMI) refers to the class of electrical biological sensors to record from and stimulate neurons within the brain in order to develop neuro-prosthetics for individuals with motor and sensory deficits. The classification of BMI includes non-invasive and invasive BMIs. Non-invasive systems primarily exploit

electroencephalograms (EEGS) [4-6], magnetoencephalography (MEG) [7] and functional magnetic resonance imaging (fMRI) [8] to characterize region-specific brain activity in real-time. Invasive BMI technology uses implanted microelectrodes to capture the action potentials of many individual neurons, especially those that code for movement or its intent [9-11].

This dissertation aims to improve the performance of MRI and invasive (yet wireless) BMI by studying the interactions between the radio frequency (RF) magnetic fields with human biological tissues.

1.2 Motivations

1.2.1 Motive for MRI

Since human MRI was first introduced as a clinical diagnostic tool, there has been a constant drive towards more powerful magnets and higher operation frequencies to pursue reduced scan time, increased signal to noise ratio (SNR) [12], chemical shift dispersion [13], susceptibility and related BOLD contrast [14]. High field imaging has also been associated with significant technical and physical difficulties including the inhomogeneous B_1^+ field (circularly polarized component of the time varying transverse magnetic field that excites the spins), the increased RF power requirements and the induced heating problems [15-23] in tissue. Specific absorption rate (SAR) is commonly used to indicate the energy absorbed into a tissue of given density by the radio transmitter. Variable phase and variable amplitude excitation or B_1^+ shimming has demonstrated theoretically [24-31] and

experimentally [32-34] a good potential of achieving a homogeneous B_1^+ field excitation. However, not only is the RF coil's performance an obstacle in high (>1.5 tesla)/ ultra-high (>3 tesla) field MRI applications, but also is the increased power deposition and the worsened local heating. In this work, B_1^+ shimming schemes (to pursue a more homogeneous magnetic excitation field, B_1^+, by varying the phase and amplitude from each excitation element in a transverse electromagnetic resonator RF coil) are explored to improve RF coil performance within safety considerations in numerical simulation and experimental verifications.

1.2.2 Motive for BMI

In invasive BMI applications, a robust and reliable connection to the region of the brain surrounding the implant must be achieved in order for this technology to be realized in a clinical setting. Traditionally, stimulating nerves or brain tissue involves cumbersome wiring to power and communicate with the chip. The wires not only limit the BMI's mobility and freedom, but also increase the likelihood of device failure. They are also major sources of noises. The most promising alternative to eliminate the requirement of wired connections is the implementation of the RF powered wireless BMI, which would widely extend the brain-machine interface applications [35]. In this dissertation, the studies of the available power to the implanted BMI chip as well as the heating effect of placing a wirelessly powered chip in cortical tissue are performed.

The aims of this work are to improve the performances of ultra-high field MRI and wireless BMI within safety limitations through investigating the interaction of

the RF electromagnetic field with human biological tissues. This dissertation applies the finite difference time domain (FDTD) method to study the improvement of the exciting magnetic field with the suppression of the total power depositions and the local absorbing energy rate in MRIs, and the power transmission in BMI applications. The temperature changes due to the ultra high field MRI apparatus and the wireless invasive BMI systems are also covered.

1.3 Organization of the Dissertation

The main body of this dissertation contains seven chapters. Chapter 2 is a background introduction of the mechanisms of MRI and BMI. Basic physics of nuclear magnetic resonance phenomenon and MRI techniques as well as background knowledge of BMI are enclosed in this chapter. Chapter 3 presents a numerical methodology used in this dissertation, the FDTD method [36]. FDTD is applied in the simulation of the electromagnetic wave propagation in MRI and BMI research. Perfectly matched layers (PML) [37] are used as an absorbing boundary condition.

Chapter 4 focuses on the study of the time varying B_1^+ field, power absorption of the load and local SAR in ultra high-field MRI. Uniformity of the excitation field becomes worse with the increase of the static magnetic field strength under quadrature excitation [15, 38-41]. B_1^+ shimming with no constraints is able to greatly improve the homogeneity of B_1^+ field distribution of MRI, but it also results in an increased power deposition and local SAR peaks compared to the quadrature excitation condition. The B_1^+ shimming scheme is optimized in the designs to achieve a more homogeneous B_1^+ field with constrained global and local SAR

distribution. The simulation results show that the improved B_1^+ field homogeneity over the regions of interest (ROI) can be realized with the reduced absorbing power and the lower peak SARs by using appropriate B_1^+ shimming excitations in ultra-high field (7/9.4 tesla) MRIs. The work is accomplished by using transmit electromagnetic (TEM) resonators as RF coils, which are loaded with three-dimensional anatomically detailed human head and body models.

After full-wave model simulations, the optimized phases and amplitudes of the exciting pulses from calculation are directly applied into a 7 tesla scanner without RF/B_1 field measurements (transmit or receive). It is demonstrated in Chapter 4 that the results from the simulation match with the experimental images very well. The agreement of the images from calculation and experiments verifies not only the full-wave computational electromagnetic modeling method but also the B_1^+ shimming optimizing scheme. B_1^+ shimming schemes are applied not only to improve the homogeneity of B_1^+ field, but also to localize the RF magnetic/electric field without increasing the total energy deposition.

Chapter 5 presents three-dimensional temperature studies within the human head model and human body model during MRI exams. Local and global SARs are often used to evaluate the safety of the RF pulse used in MRI. However, they are not easy to measure accurately in experiments. The temperature rise of the tissues, due to the RF energy absorption, depends on parameters such as the electrical, thermal and geometrical tissue properties. In this chapter, three dimensional temperature grids are modeled in the head and body using a finite-difference implementation of the bio-

heat equation with an established convection-based boundary condition. The temperature calculations are performed using the SAR distributions under the quadrature excitation and B_1^+ shimming excitations obtained from Chapter 4. The MRI induced heating problems are analyzed to safety regulatory limits from the Food and Drug Administration (FDA) and the International Electrotechnical Commission (IEC).

Chapter 6 contains RF power and thermal studies of the BMI. RF power and wireless implementation are necessary to extend applications of invasive BMI chips, where RF exposure may result in power deposition and tissue heating inside of the head. In this chapter, we study power deposition due to the radiofrequency electromagnetic and the induced heating effects by placing a wirelessly powered chip in or on cortical tissue. A three dimensional FDTD system, including the human head model with a transmitting antenna and an embedded BMI chip, is developed to calculate SAR distributions caused by the RF electromagnetic field transmitted from the antenna outside of the human head model. Without violating the local SAR peak from different safety regulations, the maximum receiving power by the embedded antenna is calculated. The temperature effect by the power deposition from the BMI chip is studied by the bio-heat simulations.

The last chapter, Chapter 7, concludes the dissertation and gives the future prospects for improving MRI and BMI performance within safety regulations.

CHAPTER 2

BACKGROUND

2.1 Magnetic Resonance Imaging (MRI)

MRI may provide the imaging of soft tissues in the human body and metabolic processes therein, such that it occupies a strong position in biomedical science applications [3]. In 1946, the first successful nuclear magnetic resonance (NMR) experiment was conducted by Felix Bloch and Edward Purcell [42]. Both Bloch and Purcell were awarded the Nobel Prize in 1952 for their work. In 1973, Paul Lauterbur, a chemist and an NMR pioneer, produced the first NMR image [2]. He won the Nobel Prize in 2003. On July 3, 1977, the first human scan was made as the first MRI prototype [43]. Since then, MRI has become a primary technique in the routine diagnosis of many disease processes throughout the body, especially when the disease is located in an organ which is vulnerable or difficult for ionizing-ray related imaging techniques, i.e. in the human head. MRI uses non-ionizing radiation and it also has advantages in high soft-tissue resolution and discrimination in any imaging plane.

An MRI experiment is composed of a two-step process [3]: firstly, the proton "spin" orientation is manipulated by an assortment of applied magnetic fields, and then changes in orientation can be measured through the interaction of the proton's magnetic field with a coil detector. A classical representation of these two processes could be obtained using atomic models.

2.1.1 Nuclear Magnetic Resonance (NMR) phenomenon

2.1.1.1 Spin

Most matter is composed of molecules which have an internal angular momentum, which is analogous to rotation around their own axis at high speeds. This is called spin. A spinning nucleus, such as a proton with electrical charges, creates a magnetic field around it, which is analogous to the magnetic field surrounding a microscopic bar magnet. As shown in Figure 2.1, the spin angular momentum $\vec{J}$ and magnetic moment vector $\vec{\mu}$ is related to each other by

$$\vec{\mu} = \gamma \vec{J} \tag{2.1}$$

where γ is a physical constant known as *gyromagnetic ratio*. The value of γ is nucleus-dependent, i.e. it is constant for a certain nucleus. The γ values of several nuclei are listed in Table 2.1. The contribution of the dominant nucleus to MRI is the proton in hydrogen.

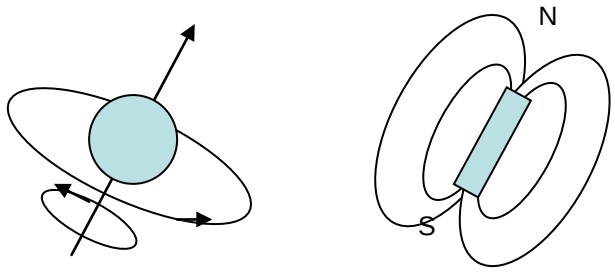


Figure 2.1 Proton spin is regarded as microscopic magnets.

Table 2.1 Properties of some NMR-Active Nuclei.

Nucleus	Spin	Gyromagnetic Ratio $\gamma/(2\pi)$ (MHz/T)
^{1}H	½	42.58
^{13}C	½	10.71
^{19}F	½	40.05
^{31}P	½	11.26

2.1.1.2 Radio Frequency (RF) Excitation

With no external magnetic field, all the protons spinning in random directions (due to thermal random motion) result in a zero net magnetic effect altogether. When the object is placed in a magnetic field of strength B_0 along z direction, the spinning proton will be aligned into parallel (lower energy state) or anti-parallel (higher energy state) directions as shown in Figure 2.2. This particle can undergo a transition between the two energy states by the absorption of energy (photon) [3, 44-46]. A particle in the lower energy state absorbs a photon and ends up in the upper energy state when the energy (photon) exactly matches the energy difference between the two states. The frequency of the photon is in the radio frequency (RF) range, which is also, in classical understanding, the precession frequency of $\vec{\mu}$ experiencing a B_0 field. It is given by

$$\omega_0 = \gamma \times \boldsymbol{B}_0 \tag{2.2}$$

where γ is *gyromagnetic ratio* and ω_0 is *Larmor frequency.*

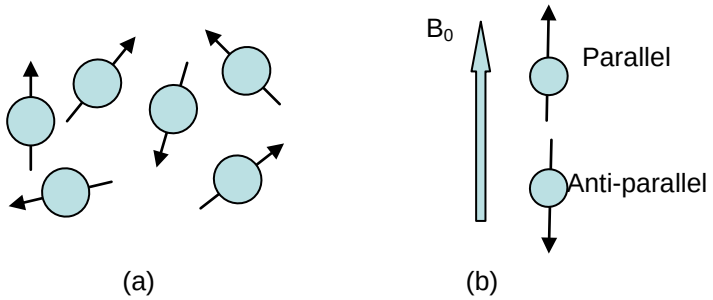


Figure 2.2 Nuclear magnetic moment vectors (a) pointing in random directions and (b) aligned in the direction of an external magnetic field.

At equilibrium conditions under a B_o field in the *Z* direction, the net magnetization vector M_o lies along *Z* direction since the number of protons in the parallel state is little more than in the anti-parallel state. For the Z component of magnetization (longitudinal magnetization), $M_Z = M_o$, and there is no transverse (M_X or M_Y) magnetization here [3, 44-46]. When the nuclear spin system is exposed to energy of a frequency (*Larmor frequency*) equal to the energy difference between the spin states, the magnetic moment of the proton is tipped away from the static field axis and begins to precess around the static field. Figure 2.3 illustrates this process.

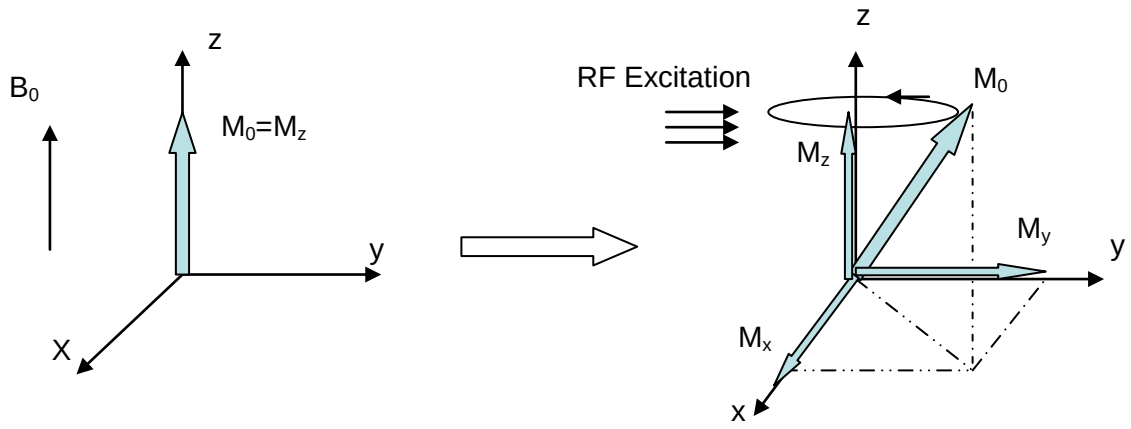


Figure 2.3 In the equilibrium state, the magnetic moment (M_0) of protons along B_0 (z) direction; under RF excitation, M_0 is tipped away from z direction and precesses around the z axis. M_z and M_x (M_y) are longitudinal and transverse magnetizations, respectively.

2.1.1.3 T_1 and T_2 Processes

After RF excitation, the time constant that describes how vector M_0 returns to its equilibrium value is called the spin lattice relaxation time T_1. T_1 is the time to reduce the difference between the M_Z and M_o value by a factor of e. This relaxation procession is governed by the Equation 2.3.

$$M_z(t) = M_o(1 - e^{-t/T_1}) + M_z(0)e^{-t/T_1} \qquad (2.3)$$

In addition to the rotation, the net magnetization $M_o(0)$ also dephases because each of the spin packets experiences a slightly different magnetic field and rotates at its own *Larmor frequency*. Assuming the net magnetization vector $M_o(0)$ is initially along +Y, it is going to spread over the transverse plane. The time describing the

return to equilibrium transverse magnetization is called the spin-spin relaxation time T_2. T_2 is the time to reduce the transverse magnetization by a factor of e. It is always less than or equal to T_1.

$$M_{XY} = M_{XYo}\, e^{-t/T_2} \qquad (2.4)$$

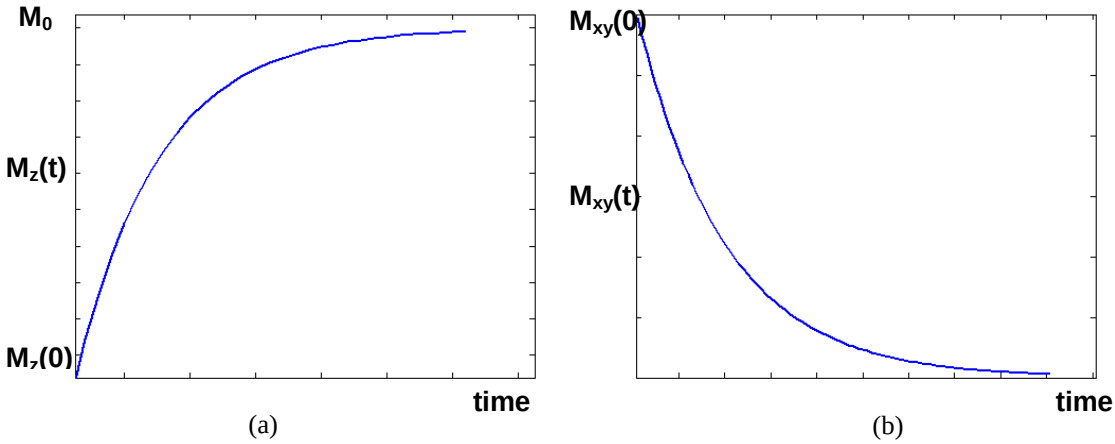


Figure 2.4 (a) The regrowth of the longitudinal component of magnetization from the initial value $M_z(0)$. (b) The decay of the magnitude of the transverse magnetization.

The net magnetization in the XY plane goes to zero and then the longitudinal magnetization grows until $M_Z = M_o$ again. In reality, variations in B_o cause an inhomogeneous T_2 effect. The combination of pure T_2 and inhomogeneous T_2, known as T_2*, results in the actual decay of transverse magnetization. Equation 2.5 shows the relation.

$$1/T_2 * = 1/T_2 + 1/T_{2\text{inhomo}} \qquad (2.5)$$

2.1.1.4 The Rotation Frame for an RF Field

To simplify the description of the RF pulse excitation, a rotation frame is introduced. A new coordinate system, whose transverse plane is rotation clockwise at *Larmor frequency*, was made as equation group 2.6.

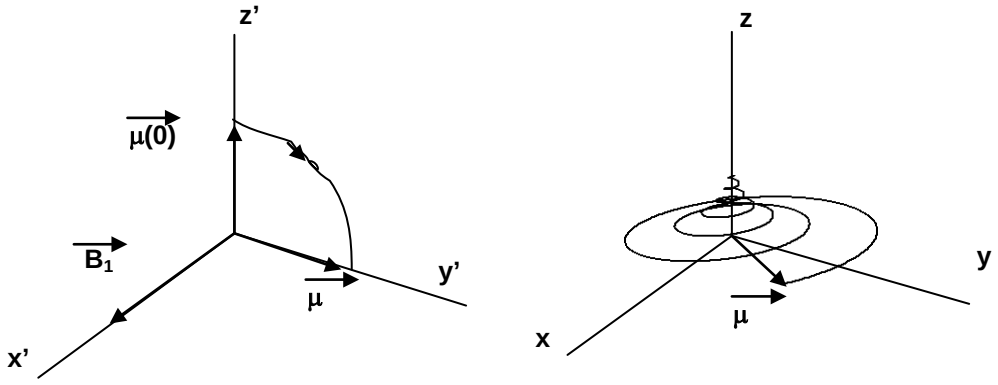
$$\begin{aligned} \vec{i}' &\equiv \cos(\omega_0 t)\vec{i} - \sin(\omega_0 t)\vec{j} \\ \vec{j}' &\equiv \sin(\omega_0 t)\vec{i} + \cos(\omega_0 t)\vec{j} \\ \vec{k}' &\equiv \vec{k} \end{aligned} \tag{2.6}$$

where *i, j,* and *k* are the unit directional vectors in the conventional stationary frame; *i'*, *j'*, and *k'* are the unit vectors in the rotation frame; and ω_0 is the *Larmor frequency.* The magnetization in the conventional stationary frame $\vec{M} \equiv M_x\vec{i} + M_y\vec{j} + M_z\vec{k}$ and in the rotation frame $\vec{M}_{rot} \equiv M_{x'}\vec{i} + M_{y'}\vec{j} + M_{z'}\vec{k}$ are equal to each other, so we have relation

$$\begin{bmatrix} M_{x'} \\ M_{y'} \\ M_{z'} \end{bmatrix} = \begin{bmatrix} \cos(\omega_0 t) & -\sin(\omega_0 t) & 0 \\ \sin(\omega_0 t) & \cos(\omega_0 t) & 0 \\ 0 & 0 & 1 \end{bmatrix} \begin{bmatrix} M_x \\ M_y \\ M_z \end{bmatrix} \tag{2.7}$$

An alternating current, RF excitation, in a transverse plane will produce a magnetic field which alternates in X direction (for example) in a stationary frame. In the rotation frame, the magnetic field along the X' axis will be constant, just as the direct current case in the stationary frame. In magnetic resonance, the magnetic field created by the RF coil at the *Larmor frequency* is called the B_1 magnetic field [3, 44-

46]. The trajectories in the primed (rotational) and unprimed (stationary) frames for on-resonance conditions are shown in Figure 2.5.



(a) (b)

Figure 2.5 On-resonance π/2 spin flip as viewed in primed (a) and unprimed (b) frame.

2.1.1.5 Bloch Equations

From Equation 2.6 and 2.7, the time-dependent behavior of $\vec{M}$ in the presence of an applied magnetic field $\vec{B}_1(t)$ is described as Equation 2.8, which is referred to as the *Bloch equation* [3, 44-46].

$$\frac{d\overrightarrow{M}}{dt} = \gamma \overrightarrow{M} \times \overrightarrow{B_{ext}} + \frac{1}{T_1}(M_0 - M_z)\vec{z} - \frac{1}{T_2}\overrightarrow{M_{xy}} \qquad (2.8)$$

Where $\overrightarrow{B_{ext}} = B_0\vec{z} + B_1\vec{x'}$. The component Bloch equations in the rotational coordinate take form as Equation 2.9.

$$\frac{dM_{x'}}{dt} = (\omega_0 - \omega)M_{y'} - \frac{M_{x'}}{T_2}$$
$$\frac{dM_{y'}}{dt} = -(\omega_0 - \omega)M_{x'} + 2\pi\gamma B_1 M_z - \frac{M_{y'}}{T_2} \quad (2.9)$$
$$\frac{dM_{z'}}{dt} = -2\pi\gamma B_1 M_{y'} - \frac{(M_z - M_{z_0})}{T_1}$$

2.1.1.6 RF Pulse Sequences

The signal received by the RF detector coil is determined not just by the properties of the body but also by a rich set of magnetic field possibilities. After RF excitation, the spin system will be perturbed from its thermal equilibrium state and then return to the equilibrium state. A pulse sequence is a set of RF pulses applied to a sample to produce a specific form of NMR signal [2].

(1) The 90-FID Sequence

Free induction decay (FID) is accompanied with a single RF pulse on a nuclear spin system. The 90-FID sequence turns down the net magnetization M_0 90 degrees to a transverse plane. The transverse magnetization also dephases at the same time. When the sequence is repeated, the amplitude of the signal, after being Fourier transformed, will depend on T_1 and the time between repetitions, or the repetition time TR.

$$signal = k\rho(1 - e^{-\frac{TR}{T_1}}) \quad (2.10)$$

where k is a constant and ρ is the density of spin in the object.

(2) The Spin-Echo Sequence

A 90 degree pulse is first applied to the spin system to turn the magnetization M_0 down into the transverse plane and dephase the transverse magnetization. Then, it is followed by a 180 degree pulse, which rotates M_0 by 180 degrees about the x' axis (the direction which RF pulse was applied from). The 180 degree pulse causes the magnetization to rephase and to produce a signal called an echo. The time between the 90 degree pulse and the maximum amplitude in the echo is defined as echo time (TE).

$$signal = k\rho(1 - e^{-\frac{TR}{T_1}})e^{-\frac{-TE}{T_2}} \tag{2.11}$$

(3) The Inversion Recovery Sequence

A 180 degree pulse is first applied to rotate the net magnetization M_0 down to the $-z$ axis. Before M_0 returns back to $+z$ equilibrium, a 90 degree pulse must be applied which rotates the M_0 into the transverse plane. After that, the transverse magnetization dephases giving an FID. The signal could be presented as function of time of the Inversion Recovery sequence (TI) as follow.

$$signal = k\rho(1 - 2e^{-\frac{TI}{T_1}}) \tag{2.12}$$

With this series of RF excitation pulse, the signal from components with different *Larmor frequencies* is collected to obtain information about the constituents of the sample.

2.1.2 Magnetic Resonance Imaging (MRI)

From the discussion above, nuclear magnetic resonance in a spin system and discussion of the global magnetic resonance signal from a sample were presented. The goal of MR imaging, however, is not only to establish the presence of different nuclei, but also to determine the spatial distribution of a given species within the sample. MRI stems from the application of NMR to radiological imaging. The object of imaging is to determine the spin density ρ(x,y,z) of a sample from the measurement of the signal as a function of time. The spin precession has to be connected to its position, and the signal is a well-known linear integral transform of the spin density [1].

2.1.2.1 Imaging Equation and the Fourier Transform

The *Larmor frequency* of a spin will be linearly proportional to its position if the static field is augmented with a gradient field. The signal from a single RF excitation of the whole sample in the presence of a set of three orthogonal gradients may be written as the 3D Fourier transform [1].

$$S(k_x, k_y, k_z) = \iiint dx dy dz \rho(x, y, z) e^{-i2\pi(k_x x + k_y y + k_z z)}$$
$$= \mathbb{F}[\rho(x, y, z)] \quad (2.13)$$

The three implicitly time-dependent components of $\vec{k}$ are related to the respective gradient-component integrals.

$$k_x(t) = \frac{\gamma}{2\pi}\int G_x(t')dt'$$
$$k_y(t) = \frac{\gamma}{2\pi}\int G_y(t')dt' \qquad (2.14)$$
$$k_z(t) = \frac{\gamma}{2\pi}\int G_z(t')dt'$$

where the integrations run from the onset of the gradient to time *t*. To show the process of an image of an object in 3D k-space, one sequence diagram with a single RF excitation is described in Figure 2.6. This process is repeated every TR until all the necessary k-space data are acquired.

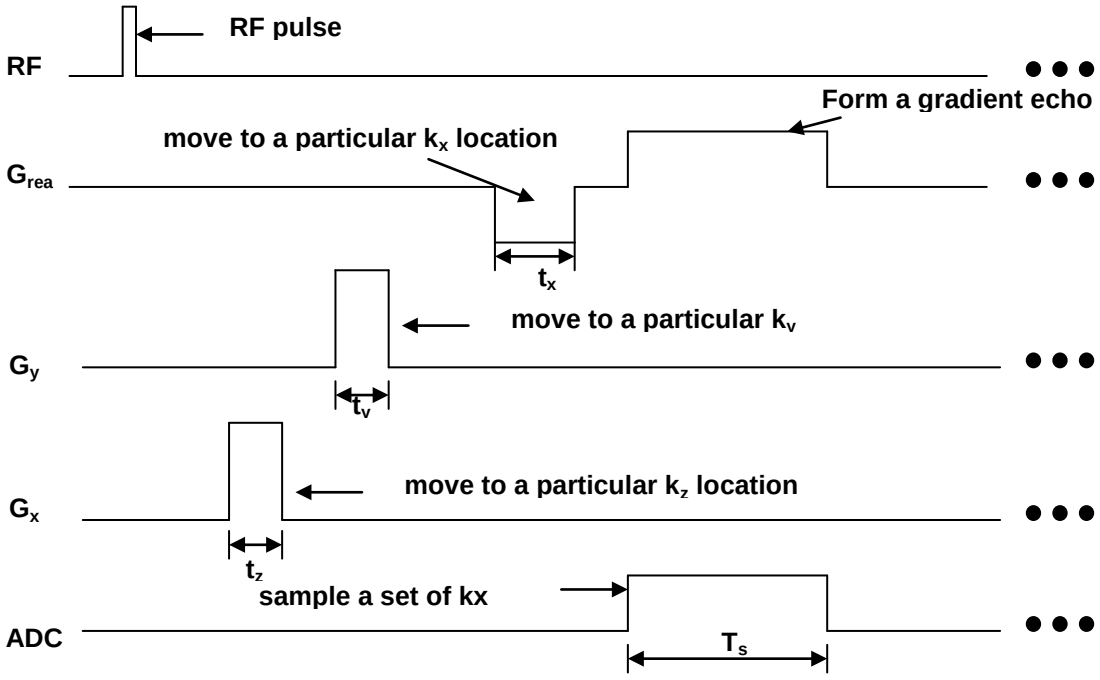


Figure 2.6 A sequence diagram for imaging an entire object in 3D.

2.1.2.2 Signal Localization and Gradient Rephasing

In general, magnetic resonance images are produced by exciting a single thin slice of the body by using a combination of gradient fields and spatially selective RF pulses. The one-to-one correspondence of a given distance along the gradient direction to a particular *Larmor frequency* leads to the possibility of tuning the RF pulse frequency to excite a slice at a desired spatial location. The simplest and most popular form to localize the signal is slice selection. By putting a gradient magnetic field on top of the uniform magnetic field B_0, the total magnetic field has a slight gradient difference. The resonance frequency selects only one slice that is perpendicular to the gradient direction, so we can get two-dimensional images in any arbitrary direction by adjusting the gradient field direction. For example, to select a slice in $\vec{\mu}_s$ direction where

$$\vec{\mu}_S = (\sin\theta\cos\varphi, \sin\theta\sin\varphi, \cos\theta) \tag{2.15}$$

One only needs a slice-selection gradient as $\vec{G}_{ss} = (G_x, G_y, G_z)$ where

$$\begin{aligned} G_x &= G_{ss}\sin\theta\cos\varphi \\ G_y &= G_{ss}\sin\theta\sin\varphi \\ G_z &= G_{ss}\cos\theta \end{aligned} \tag{2.16}$$

as Figure 2.7 shows.

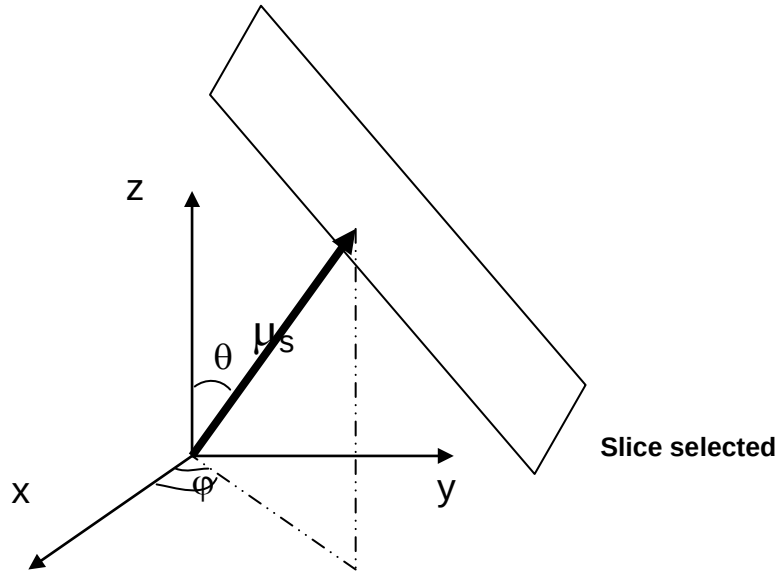


Figure 2.7 Selection of a slice in $\vec{\mu}_s$ direction

The creation of an arbitrary gradient vector requires all three Cartesian gradients to be used simultaneously. The slice select gradient induces dephasing in the slice select direction across the finite slice thickness. The defocusing begins to occur during the excitation, so the rephrasing lobe (gradient echo) has to be applied to return the excited spins in the selected slice back to zero phases.

2.1.2.3 Contrast Mechanisms in MRI

The most basic contrast generating mechanisms are based on spin density ρ, and T_1 and T_2 differences between tissues. There are also other mechanisms such as flow, magnetic susceptibility differences, magnetization transfer contrast, tissue saturation methods, contrast enhancing agents and diffusion [3].

Although each type of contrast is designed to enhance differences in one of the specified parameters (ρ_0, T_1, or T_2), the signal is a function of all three variables, and

each must be kept in mind when determining overall image contrast. As an example, the contrast between tissues A and B for a 90^0 flip angle gradient echo experiment is Equation (2.17).

$$C_{AB} = S_A(T_E) - S_B(T_E) = \rho_{0,A}(1 - e^{-\frac{T_R}{T_{1,A}}})e^{-\frac{T_E}{T^*_{2,A}}} - \rho_{0,B}(1 - e^{-\frac{T_R}{T_{1,B}}})e^{-\frac{T_E}{T^*_{2,B}}} \tag{2.17}$$

To get contrast based primarily on ρ_0, the T_1 and T_2* dependence of the gradient echo tissue signal must be minimized. With appropriate choices of T_E and T_R as below

$$T_E << T^*_{2A,B} \Rightarrow e^{-\frac{T_E}{T^*_2}} \to 1 \tag{2.18}$$

$$T_R >> T^*_{1A,B} \Rightarrow e^{-\frac{T_R}{T^*_1}} \to 0 \tag{2.19}$$

the expression of Equation (2.17) for the contrast between tissues become

$$C_{AB} \approx \rho_{0,A} - \rho_{0,B} \tag{2.20}$$

For T_1 weighting, T_2* effects have to be minimized. Using the same gradient echo example as before, the choice of a very short T_E reduces any T^*_2 contrast, i.e. T_E is chosen as Equation (2.18). Then the expression of Equation (2.17) for the contrast is now

$$\begin{aligned} C_{AB} &\approx \rho_{0,A}(1 - e^{-\frac{T_R}{T_{1,A}}}) - \rho_{0,B}(1 - e^{-\frac{T_R}{T_{1,B}}}) \\ &= (\rho_{0,A} - \rho_{0,B}) - (\rho_{0,A}e^{-\frac{T_R}{T_{1,A}}} - \rho_{0,B}e^{-\frac{T_R}{T_{1,B}}}) \end{aligned} \tag{2.21}$$

where the unique choice of T_R which maximizes the T_1-weighted contrast is

$$T_R = \frac{ln(\frac{\rho_{0,B}}{T_{1,B}}) - ln(\frac{\rho_{0,A}}{T_{1,A}})}{(\frac{1}{T_{1,B}} - \frac{1}{T_{1,A}})} \tag{2.22}$$

T_2* weighting is based on differences in the transverse decay characteristics. To avoid contributions from T_1 confounding the contrast, Equation (2.17) should be met, then Equation (2.17) is given by

$$C_{AB} = \rho_{0,A} e^{-\frac{T_E}{T^*_{2,A}}} - \rho_{0,B} e^{-\frac{T_R}{T^*_{2,B}}} \tag{2.23}$$

where the unique choice of T_E which maximizes the T_2-weighted contrast is

$$T_E = \frac{ln(\frac{\rho_{0,B}}{T^*_{2,B}}) - ln(\frac{\rho_{0,A}}{T^*_{2,A}})}{(\frac{1}{T^*_{2,B}} - \frac{1}{T^*_{2,A}})} \tag{2.24}$$

2.1.2.4 Radiofrequency (RF) Coil

Radiofrequency (RF) coil is the device used to transmit and receive RF signals in MRI. One of the primary considerations in RF coil design is the homogeneity of the magnetization response. Since the first coil used in an NMR experiment [42], many types of surface and volume coils including saddle coil, birdcage coil, and transverse electromagnetic (TEM) resonator etc. have been designed and applied into applications in the past sixty years [15, 41, 47]. Different coil designs have their individual performance characteristics. A saddle coil has a cylindrical body, with one or more turns of wire or foil on each side. It generates a linear and homogenous

magnetic field along the direction of its central axis [48]. Birdcage coil is a popular coil for its quadrature design and excellent radial field homogeneity over the imaging volume [49]. Its limitation is the uniformity of the field decays axially. The surface coil is widely used in MRI too, as it is often a convenient and effective way of obtaining localized signal-to-noise ratio (SNR) higher than the one obtained with volume coils [50, 51]. A phased array generally refers to a set of receive coils which signals are combined to obtain a uniform image over a region larger than any individual coil could cover, while taking advantage of the high SNR available from the smaller individual coils [52]. Transverse electromagnetic (TEM) resonator is another very popular RF coil introduced by Vaughn et al. As a resonant cavity with Roschmann's resonators [47], the TEM resonator has the great advantages in field homogeneity and high quality factor (Q), and it is easy to run. With the drive to increase static magnetic field for better SNR, excellent homogeneity becomes more critical. The TEM coil's superiority in field homogeneity becomes more remarkable. TEM coils used in this dissertation will be described in detail in Chapter 4.

2.2 Brain-Machine Interface (BMI)

A brain-machine interface (BMI), also known as brain-computer interface (BCI), is a direct communication pathway between a brain and an external device. The brain is composed of billions of neurons that integrate multimodal sensory information respond to the environment and control behavior. A BMI is a direct functional interface through which a brain accepts and controls a mechanical device as a part of its body. Research on BMIs began at the University of California in Los Angeles

(UCLA), where the first real-time detection of brain events in EEG was performed [53] in the 1970s. Since then, the field has blossomed spectacularly, mostly toward neuroprosthetics applications that aim at restoring damaged hearing, sight and movement. The design and implementation of BMIs involve the combined efforts of many areas of research, such as computer science, electrical engineering and biomedical engineering including the techniques for micro-stimulating neuronal tissue, microchip design, very large scale integration (VLSI) design and robotics [54]. It is believed that real-time direct interfaces between the brain and electronic and mechanical devices could be used to study brain function and restore sensory and motor functions lost through injury or disease [54].

2.2.1 Components of BMI Neuroprosthetic Devices

In the translation of the thoughts into actions, a BMI motor device experiences four steps: the detection of the brain intent, the exaction of the signal from the available data, the communication with the internal or external actuator devices and the feedback to the task to evaluate the performance of the intent signal. According to this process, the fundamental components of BMI neuroprosthetic devices include signal detection, information extraction, neuroprosthetic actuators, and the feedback and adaptation [55]. In the initial stage, signals produced by the changes in a physiological variable are measured by a sensor. The changes might include neurotransmitter concentration gradients measured with voltammetric electrodes, blood-flow changes detectable with functional MRI, or magnetic fields produced by ionic current flows [55]. Once a signal has been detected, it will be identified,

extracted and interpreted from the collected data, and then the intended action must be implemented through an actuator. For example, the command signals might be used to drive a computer interface [56] or to move a robotic arm [57] in the case of spinal cord injury. The last step is the feedback compensation of the errors since errors may be introduced in the process of measurement, interpretation and execution in any motor control system [55].

2.2.2 Classification of BMI

In BMI classification, BMI is distinguished by non-invasive and invasive (i.e. intra-cranial) methods of electrophysiological recordings [58]. Non-invasive systems primarily exploit electroencephalograms (EEGS) to control computer cursors or other devices [4-6]. However, EEG-based techniques provide communication channels of limited capacity, 20-30 bits min^{-1}. Another two non-invasive technologies used as BMIs are magnetoencephalography (MEG) and functional magnetic resonance imaging (fMRI) [59]. MEG is a measurement of the magnetic fields cause by electrical current dipoles that are generated by neural activity [7]. Real time fMRI measures the haemodynamic response related to neural activity in the brain or spinal cord of humans, and it has been used as another non-invasive BMI due to its ability to characterize region-specific brain activity in real-time [8]. However, both of MEG and fMRI technologies require a high field magnetic environment enclosed in a magnetically shielded room, which greatly increases the cost and limit their applications. Because of the limitations of the non-invasive methods, researchers started to show their interests in more invasive approaches,

implanted microelectrodes, to capture the action potentials of many individual neurons, especially those that code for movement or its intent [9-11].

The idea of implantable BMI neuroprosthetic devices has been prominently featured in science fiction [55]. Invasive BMIs rely on the physiological properties of individual cortical and subcortical neurons that control movements. Recent advances in studies of BMIs have been conducted in behaving rhesus monkeys [60, 61] and in prototype neuroprosthetic BMI devices for human beings [62]. Invasive BMI is able to capture a monkey's complex brain motor center signals to control external devices and reproduce them in a robot arm [57, 61]. And a more exciting news is the initial results about neuromotor prostheses (NMPs) for a tetraplegic human: the early results suggest that NMPs based upon intracortical neuronal ensemble spiking activity could be applied to restore independence for a human with paralysis [62].

The present state of BMI technology requires that human or animal subjects be wired to large equipment racks where the amplified signals are processed to control the robotic interface in real time [63]. The cumbersome wiring is to power as well as to realize the communication with the chip. The wires not only limit the BMI usage mobility and freedom, but also increase the likelihood of device failure. They are also major sources of noise. As the most promising alternatives to eliminate the requirement for wired connections, RF power and wireless implementation of a BMI chip would widely extend brain-machine interface applications [35]. RF exposure may result in power deposition and tissue heating.

In this dissertation, the interaction between the electromagnetic fields and human biological tissues are studied in improving the performance of B_1 shimming with constrained the local and global SARs during high field MRI exams. The calculations of the field interaction are also applied in the research of the power reception and safety evaluations of the wireless invasive BMI applications.

CHAPTER 3

NUMERICAL METHODOLODY – FINITE DIFFERENCE TIME DOMAIN METHOD

3.1 Motivation for Using Finite Difference Time Domain Method

There are a few popular computational electromagnetic methods such as the finite element method (FEM), the method of moments (MOM), and the finite difference time domain method (FDTD). The FEM is a numerical technique for finding approximate solutions of partial differential equations and integral equations. It is usually used in the frequency domain and each solving of the equations gives the solution for one frequency. The MOM method is based on integral equations and Green's functions. MOM is usually used in the frequency domain, and it has the advantage of dealing easily with long thin wires or thin patches. The FDTD method is a numerical technique for solving Maxwell's curl equations directly in the time domain on a space grid. Since it is a time-domain method, solutions can cover a wide frequency range with a single simulation run.

Among these methods, a suitable numerical technique needs to be selected to calculate the interaction of the electromagnetic field with the human model in magnetic resonance imaging (MRI) and brain machine interface (BMI) simulations. In these cases, a large portion of the geometries is non-perfectly conducting, which makes MOM's advantages in modeling surface currents on a perfect conductor indistinct. In high field MRI, higher B_0 field strengths are associated with increases

in the frequency of operation; therefore, the human head and body models are electrically large compared to the shortened wavelengths. In BMI simulations, the operational frequencies of the antennas are in GHz unit, which makes the head model electrically large too. The number of the unknowns needed to solve both problems is huge in the large computation domains. These characteristics require a numerical method with faster computation time and more efficient memory usage. Both FEM and MOM require the solution of a matrix equation, and iterative methods offer the only viable way to solve the matrix equation when the number of unknowns is large; the FDTD method does not require a matrix solution. It is shown that the FDTD method is better in computation time and memory requirement than FEM and MOM methods when the unknown number in our problems is large [64]. Besides the above mentioned benefits, the FDTD technique has more advantages including 1) it is relatively straightforward to implement; 2) it easily accommodates complex geometrical features and non-uniform materials; and 3) solutions can cover a wide frequency range from a single simulation run with transient pulse excitation and Fast Fourier Transform (FFT) [65].

One disadvantage of FDTD method compared to FEM method is that the less flexibility for modeling arbitrary geometries, since FEM is able to be applied to unstructured grid. For the electrically large geometries that are encountered in high field MRI and BMI in this dissertation, the advantages of FDTD method in computation speed and memory usage overwhelm the disadvantage and lead the

applications of the method in the field calculations as it is applied in the previous work in MRI [65-70] and BMI [35, 71, 72].

3.2 FDTD Notations and Equations

FDTD was first developed by Kane S. Yee in 1966 [36]. It has become one of the principal computational approaches for Maxwell's equations. It is essentially based on replacing the spatial and time domain derivatives of Maxwell's equations with finite difference approximations. In other words, all the differential operators of the curl equations are replaced by second-order accurate central difference approximations. The three-dimensional space domain is divided into cells called Yee cells. Figure 3.1 shows one of the Yee cells where the electric and magnetic field are staggered. The electric field values are sampled at the center of every edge on each block and the vector direction of the electric field is along these edges. The magnetic field values are sampled at the centroid of each block face and the vector direction of the magnetic field is perpendicular to each of these block faces. The Yee cell dimension is chosen to be small fractions of the wavelength (λ), which guarantee that the electromagnetic field is properly modeled over one increment of time [36]. For example, this criterion can be guaranteed by defining the spatial resolution in the grid by Equation 3.1.

$$\Delta x = \Delta y = \Delta z = \frac{1}{20f\sqrt{\mu\varepsilon}} = \frac{\lambda_{min}}{20} \tag{3.1}$$

where f (Hz) is the resonate frequency and λ_{min} (m) is the minimum wavelength.

A function *F* of space and time is evaluated at a discrete point in the grid and at a discrete point in time as [73]:

$$F^n(i, j, k) = F(i\Delta x, j\Delta y, k\Delta z, n\Delta t) \tag{3.2}$$

where *x, y, z* and *t* are the steps in the x y and z directions and the time step.

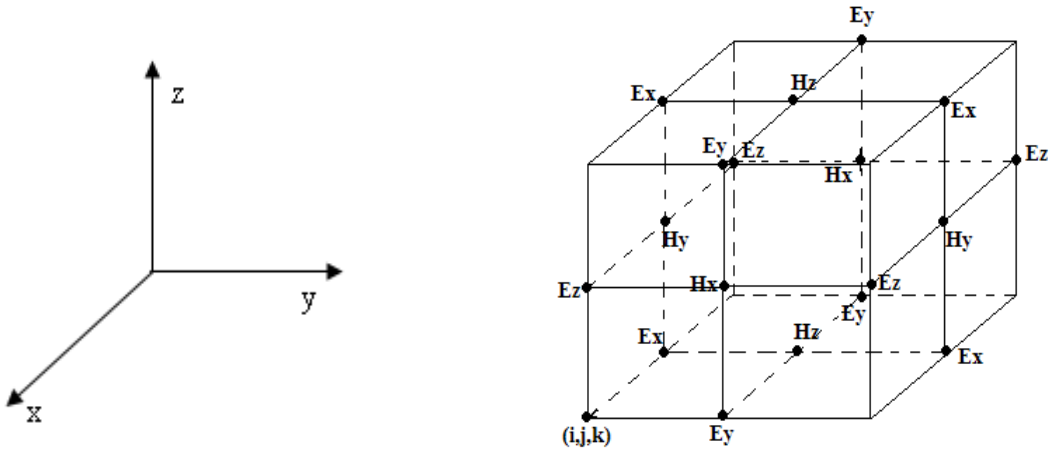


Figure 3.1 Yee cell shows the spatial relationship of E and H.

Using a centered-difference expression for the space and time derivation and ignoring the second-order accuracy in space and time increments, we get the spatial and temporal derivatives of *F* as [73]:

$$\frac{\partial F^n(i,j,k)}{\partial x} = \frac{F^n(i+1/2, j,k) - F^n(i-1/2, j,k)}{\Delta x} \tag{3.3}$$

$$\frac{\partial F^n(i,j,k)}{\partial t} = \frac{F^{n+1/2}(i,j,k) - F^{n-1/2}(i,j,k)}{\Delta t} \tag{3.4}$$

Maxwell's curl equations for an isotropic, source free and homogenous media are [65, 74, 75]

$$\nabla \times \vec{E} = -\mu \frac{\partial \vec{H}}{\partial t} - \sigma_m \vec{H} \tag{3.5}$$

$$\nabla \times \vec{H} = \sigma_e \vec{E} + \varepsilon \frac{\partial \vec{E}}{\partial t} \tag{3.6}$$

$$\nabla \cdot \vec{D} = \rho_e \tag{3.7}$$

$$\nabla \cdot \vec{B} = \rho_m \tag{3.8}$$

The electric and magnetic flux densities are defined as

$$\vec{D} = \varepsilon \vec{E} \tag{3.9}$$

$$\vec{B} = \mu \vec{H} \tag{3.10}$$

where $\vec{\mathrm{E}}$ (V/m) and $\vec{\mathrm{H}}$ (A/m) are the electric and the magnetic fields; σ_m (Ω/m) and σ_e (S/m) are the magnetic and electric conductivities; μ (H/m) and ε (F/m) are the permeability and permittivity respectively; and ρ_e (C/m^3) and ρ_m (Wb/m^3) are the electric and magnetic charge densities. In rectangular coordinates, equations (3.11)-(3.16) are written from equations (3.5)-(3.8).

$$\mu \frac{\partial Hx}{\partial t} = \frac{\partial Ey}{\partial z} - \frac{\partial Ez}{\partial y} - \sigma m Hx \tag{3.11}$$

$$\mu \frac{\partial Hy}{\partial t} = \frac{\partial Ez}{\partial x} - \frac{\partial Ex}{\partial z} - \sigma m Hy \tag{3.12}$$

$$\mu \frac{\partial Hz}{\partial t} = \frac{\partial Ex}{\partial y} - \frac{\partial Ey}{\partial x} - \sigma m Hz \tag{3.13}$$

$$\varepsilon \frac{\partial Ex}{\partial t} = \frac{\partial Hz}{\partial y} - \frac{\partial Hy}{\partial z} - \sigma e Ex \tag{3.14}$$

$$\varepsilon \frac{\partial Ey}{\partial t} = \frac{\partial Hx}{\partial z} - \frac{\partial Hz}{\partial x} - \sigma e Ey \tag{3.15}$$

$$\varepsilon \frac{\partial Ez}{\partial t} = \frac{\partial Hy}{\partial x} - \frac{\partial Hx}{\partial y} - \sigma e Ez \tag{3.16}$$

where E_x , E_y and E_z are the electric field components; H_x , H_y , and H_z are the magnetic field components in the x, y, and z directions, respectively. Substitute equations (3.3)-(3.4) into (3.11)-(3.16) and we could get the basic FDTD updating equations.

$$E_x^{n+1}(i+1/2\,,j,k) = (\frac{2\varepsilon - \sigma e \Delta t}{2\varepsilon + \sigma e \Delta t})E_x^n(i+1/2,j,k) + (\frac{2\Delta t}{2\varepsilon + \sigma e \Delta t}) \{ \frac{1}{\Delta y}[H_z^{n+1/2}(i+1/2,j+1/2,k) - H_z^{n+1/2}(i+1/2,j-1/2,k)] - \frac{1}{\Delta z}[H_y^{n+1/2}(i+1/2,j,k+1/2) - H_y^{n+1/2}(i+1/2,j,k-1/2)]\} \tag{3.17}$$

$$E_y^{n+1}(i,j+1/2,k) = (\frac{2\varepsilon - \sigma e \Delta t}{2\varepsilon + \sigma e \Delta t})E_y^n(i,j+1/2,k) + (\frac{2\Delta t}{2\varepsilon + \sigma e \Delta t}) \{ \frac{1}{\Delta z}[H_x^{n+1/2}(i,j+1/2,k+1/2) - H_x^{n+1/2}(i,j+1/2,k-1/2)] + \frac{1}{\Delta x}[H_z^{n+1/2}(i-1/2,j+1/2,k) - H_z^{n+1/2}(i+1/2,j+1/2,k)]\ \} \tag{3.18}$$

$$E_z^{n+1}(i,j,k+1/2) = (\frac{2\varepsilon - \sigma e \Delta t}{2\varepsilon + \sigma e \Delta t})E_z^n(i,j,k+1/2) + (\frac{2\Delta t}{2\varepsilon + \sigma e \Delta t}) \{ \frac{1}{\Delta x}[H_y^{n+1/2}(i+1/2,j,k+1/2) - H_y^{n+1/2}(i-1/2,j,k+1/2)] + \frac{1}{\Delta y}[H_x^{n+1/2}(i,j-1/2,k+1/2) - H_x^{n+1/2}(i,j+1/2,k+1/2)]\} \tag{3.19}$$

$$H_x^{n+1/2}(i,j+1/2,k+1/2)=\left(\frac{2\mu-\sigma_m\Delta t}{2\mu+\sigma_m\Delta t}\right)H_x^{n-1/2}(i,j+1/2,k+1/2)+\left(\frac{2\Delta t}{2\mu+\sigma_m\Delta t}\right)$$
$$\{\frac{1}{\Delta z}[E_y^n(i,j+1/2,k+1)-E_y^n(i,j+1/2,k)]$$
$$+\frac{1}{\Delta y}[E_z^n(i,j,k+1/2)-E_z^n(i,j+1,k+1/2)]\} \quad (3.20)$$

$$H_y^{n+1/2}(i+1/2,j,k+1/2)=\left(\frac{2\mu-\sigma_m\Delta t}{2\mu+\sigma_m\Delta t}\right)H_y^{n-1/2}(i+1/2,j,k+1/2)+\left(\frac{2\Delta t}{2\mu+\sigma_m\Delta t}\right)$$
$$\{\frac{1}{\Delta x}[E_z^n(i+1,j,k+1/2)-E_z^n(i,j,k+1/2)]$$
$$+\frac{1}{\Delta z}[E_x^n(i+1/2,j,k)-E_x^n(i+1/2,j,k+1)]\} \quad (3.21)$$

$$H_z^{n+1/2}(i+1/2,j+1/2,k)=\left(\frac{2\mu-\sigma_m\Delta t}{2\mu+\sigma_m\Delta t}\right)H_z^{n-1/2}(i+1/2,j+1/2,k)+\left(\frac{2\Delta t}{2\mu+\sigma_m\Delta t}\right)$$
$$\{\frac{1}{\Delta y}[E_x^n(i+1/2,j+1,k)-E_x^n(i+1/2,j,k)]$$
$$+\frac{1}{\Delta x}[E_y^n(i,j+1/2,k)-E_y^n(i+1,j+1/2,k)]\} \quad (3.22)$$

The updated value of the *E* (or *H*) field component is a function of its previous value (one time step before) and the previous value (half time step before) of the surrounding *H* (or *E*) fields at half spatial steps away. In equations (3.17)-(3.22), the time step is calculated using the stability criterion equation

$$v\Delta t \le \frac{1}{\sqrt{\frac{1}{\Delta x^2}+\frac{1}{\Delta y^2}+\frac{1}{\Delta z^2}}} \quad (3.23)$$

where, v (m/s) is the maximum propagation velocity given by

$$v = \frac{1}{\sqrt{\mu\varepsilon}} \tag{3.24}$$

3.3 Boundary Condition

To simulate the electromagnetic field within a domain of interest (DOI) using the FDTD method, the outer boundary conditions are needed to absorb the outward propagating energy. The easiest method is that the geometry of interest can be defined in "open" regions where the spatial domain of the computed field is unbounded in one or more coordinate directions [73]. However, the computational expense and limited computer storage make it impossible to apply the unbounded region into real applications, especially when the computation domain is electrically large. The second method is to introduce an absorbing boundary condition (ABC) at the outer lattice boundary to simulate the extension of the lattice to infinity. A number of analytical techniques have been used to achieve this goal, including Bayliss-Turkel radiation operators [76], Engquist-Majda one-way wave equations [77], and Higdon radiation operators [78]. However, every technique still has limits in its application in FDTD simulations [73]. For example, Baliss-Turdel operators are difficult to adapt to provide ABCs for two and three dimensional Cartesian FDTD grids. In the formulation of Engquist-Majda ABCs, the mismatch between the dispersive $v_p \neq c$ conditions within the interior of the grid and the imposed $v_p = c$ condition at the outer grid boundary generate wave reflections. Higdon ABCs have the fundamental problems of the assumption of a uniform wave velocity in its formulation [73]. An alternate approach to realize an ABC is to terminate the

outer boundary of the space lattice in an absorbing material medium. An early attempt at implementing an absorbing material boundary condition was reported in 1983 by Holland and Williams [79]. They utilized a conventional lossy dispersionless absorbing medium (i.e. EM waves decay in the medium but this property is not frequency dependant) as an absorbing layer. However, this category of lossy-material ABC had only limited application in electromagnetics because it only matches normally incident plane waves [73]. In 1994, a highly effective absorbing-material ABC, the perfectly matched layer (PML), was designed by J. P. Berenger [37]. PML material allows no reflections for a plane wave incident from free space at any angle given that the free space-PML interface is infinite. In Berenger's PML, plane waves of arbitrary incidence, polarization, and frequency are matched at the boundary [73].

In our work, we use PML [37] to absorb outgoing waves at the outer boundary of the computation space.

3.2.1 Perfectly Matched Layer (PML)

Berenger modified Maxwell's equations to propose nonphysical material properties that allow no reflections at a vacuum-PML layer interface with independence of the angle of incidence and frequency of outgoing scattered waves [37]. Chew and Weedon provided a different analysis of the PML by exploiting additional degrees of freedom arising from a set of stretched coordinates [80]. The split-field PML was also posed as a uniaxial anisotropic medium, which was applied within the FDTD method by Gedney [81].

A perfectly matched planar interface is derived by loss parameters consistent with the medium. In Berenger's PML material, each vector field component is split into two orthogonal components. The magnetic and electric conductivity are matched so that there will be no reflection at the vacuum-layer interface or between layers. The wave impedance matching condition is $\frac{\sigma_e}{\varepsilon} = \frac{\sigma_m}{\mu}$. Maxwell's three-dimensional time-domain equations for Berenger's split-field PML in Cartesian coordinate are shown as below [73].

$$(\varepsilon \frac{\partial}{\partial t} + \sigma_y) E_{xy} = \frac{\partial}{\partial y}(H_{zx} + H_{zy}) \tag{3.25}$$

$$(\varepsilon \frac{\partial}{\partial t} + \sigma_z) E_{xz} = -\frac{\partial}{\partial z}(H_{yx} + H_{yz}) \tag{3.26}$$

$$(\varepsilon \frac{\partial}{\partial t} + \sigma_z) E_{yz} = \frac{\partial}{\partial z}(H_{xy} + H_{xz}) \tag{3.27}$$

$$(\varepsilon \frac{\partial}{\partial t} + \sigma_x) E_{yx} = -\frac{\partial}{\partial x}(H_{zx} + H_{zy}) \tag{3.28}$$

$$(\varepsilon \frac{\partial}{\partial t} + \sigma_x) E_{zx} = \frac{\partial}{\partial x}(H_{yx} + H_{yz}) \tag{3.29}$$

$$(\varepsilon \frac{\partial}{\partial t} + \sigma_y) E_{zy} = -\frac{\partial}{\partial y}(H_{xy} + H_{xz}) \tag{3.30}$$

$$(\mu \frac{\partial}{\partial t} + \sigma_y^*) H_{xy} = -\frac{\partial}{\partial y}(E_{zx} + E_{zy}) \tag{3.31}$$

$$(\mu \frac{\partial}{\partial t} + \sigma_z^*) H_{xz} = -\frac{\partial}{\partial z}(E_{yx} + E_{yz}) \tag{3.32}$$

$$(\mu \frac{\partial}{\partial t} + \sigma_z^*) H_{yz} = -\frac{\partial}{\partial z}(E_{xy} + E_{xz}) \tag{3.33}$$

$$(\mu\frac{\partial}{\partial t}+\sigma_x^{*})H_{yx}=\frac{\partial}{\partial x}(E_{zx}+E_{zy}) \tag{3.34}$$

$$(\mu\frac{\partial}{\partial t}+\sigma_x^{*})H_{zx}=-\frac{\partial}{\partial x}(E_{yx}+E_{yz}) \tag{3.35}$$

$$(\mu\frac{\partial}{\partial t}+\sigma_y^{*})H_{zy}=-\frac{\partial}{\partial y}(E_{xy}+E_{xz}) \tag{3.36}$$

Substituting equations (3.2)-(3.3) into (3.25)-(3.36), we could get 12 FDTD updating equations inside the PML.

$$\begin{aligned}E_{xy}^{n+1}(i+1/2,j,k)=&\left(\frac{2\varepsilon-\sigma_{ye}\Delta t}{2\varepsilon+\sigma_{ye}\Delta t}\right)E_{xy}^{n}(i+1/2,j,k)+\left(\frac{2\Delta t}{2\varepsilon+\sigma_{ye}\Delta t}\right)\\&\frac{1}{\Delta y}\{[H_{zx}^{n+1/2}(i+1/2,j+1/2,k)-H_{zx}^{n+1/2}(i+1/2,j-1/2,k)]\\&+[H_{zy}^{n+1/2}(i+1/2,j+1/2,k)-H_{zy}^{n+1/2}(i+1/2,j-1/2,k)]\}\end{aligned} \tag{3.37}$$

$$\begin{aligned}E_{xz}^{n+1}(i+1/2,j,k)=&\left(\frac{2\varepsilon-\sigma_{ze}\Delta t}{2\varepsilon+\sigma_{ze}\Delta t}\right)E_{xz}^{n}(i+1/2,j,k)-\left(\frac{2\Delta t}{2\varepsilon+\sigma_{ze}\Delta t}\right)\\&\frac{1}{\Delta z}\{[H_{yx}^{n+1/2}(i+1/2,j,k+1/2)-H_{yx}^{n+1/2}(i+1/2,j,k-1/2)]\\&+[H_{yz}^{n+1/2}(i+1/2,j,k+1/2)-H_{yz}^{n+1/2}(i+1/2,j,k-1/2)]\}\end{aligned} \tag{3.38}$$

$$\begin{aligned}E_{yx}^{n+1}(i,j+1/2,k)=&\left(\frac{2\varepsilon-\sigma_{xe}\Delta t}{2\varepsilon+\sigma_{xe}\Delta t}\right)E_{yx}^{n}(i,j+1/2,k)-\left(\frac{2\Delta t}{2\varepsilon+\sigma_{xe}\Delta t}\right)\\&\frac{1}{\Delta x}\{[H_{zx}^{n+1/2}(i+1/2,j+1/2,k)-H_{zx}^{n+1/2}(i-1/2,j+1/2,k)]\\&+[H_{zy}^{n+1/2}(i+1/2,j+1/2,k)-H_{zy}^{n+1/2}(i-1/2,j+1/2,k)]\}\end{aligned} \tag{3.39}$$

$$E_{yz}^{n+1}(i,j+1/2,k)=\left(\frac{2\varepsilon-\sigma_{ze}\Delta t}{2\varepsilon+\sigma_{ze}\Delta t}\right)E_{yz}^{n}(i,j+1/2,k)+\left(\frac{2\Delta t}{2\varepsilon+\sigma_{ze}\Delta t}\right)$$
$$\frac{1}{\Delta z}\{[H_{xy}^{n+1/2}(i,j+1/2,k+1/2)-H_{xy}^{n+1/2}(i,j+1/2,k-1/2)]$$
$$+[H_{xz}^{n+1/2}(i,j+1/2,k+1/2)-H_{xz}^{n+1/2}(i,j+1/2,k-1/2)]\}$$

(3.40)

$$E_{zx}^{n+1}(i,j,k+1/2)=\left(\frac{2\varepsilon-\sigma_{xe}\Delta t}{2\varepsilon+\sigma_{xe}\Delta t}\right)E_{zx}^{n}(i,j,k+1/2)+\left(\frac{2\Delta t}{2\varepsilon+\sigma_{xe}\Delta t}\right)$$
$$\frac{1}{\Delta x}\{[H_{yx}^{n+1/2}(i+1/2,j,k+1/2)-H_{yx}^{n+1/2}(i-1/2,j,k+1/2)]$$
$$+[H_{yz}^{n+1/2}(i+1/2,j,k+1/2)-H_{yz}^{n+1/2}(i-1/2,j,k+1/2)]\}$$

(3.41)

$$E_{zy}^{n+1}(i,j,k+1/2)=\left(\frac{2\varepsilon-\sigma_{ye}\Delta t}{2\varepsilon+\sigma_{ye}\Delta t}\right)E_{zy}^{n}(i,j,k+1/2)-\left(\frac{2\Delta t}{2\varepsilon+\sigma_{ye}\Delta t}\right)$$
$$\frac{1}{\Delta y}\{[H_{xy}^{n+1/2}(i,j+1/2,k+1/2)-H_{xy}^{n+1/2}(i,j-1/2,k+1/2)]$$
$$+[H_{xz}^{n+1/2}(i,j+1/2,k+1/2)-H_{xz}^{n+1/2}(i,j-1/2,k+1/2)]\}$$

(3.42)

$$H_{xy}^{n+1/2}(i,j+1/2,k+1/2)=\left(\frac{2\varepsilon-\sigma_{yh}\Delta t}{2\varepsilon+\sigma_{yh}\Delta t}\right)H_{xy}^{n-1/2}(i,j+1/2,k+1/2)-\left(\frac{2\varepsilon\Delta t}{\mu(2\varepsilon+\sigma_{yh}\Delta t)}\right)$$
$$\frac{1}{\Delta y}\{[E_{zx}^{n}(i,j+1,k+1/2)-E_{zx}^{n}(i,j,k+1/2)]$$
$$+[E_{zy}^{n}(i,j+1,k+1/2)-E_{zy}^{n}(i,j,k+1/2)]\}$$

(3.43)

$$H_{xz}^{n+1/2}(i,j+1/2,k+1/2)=\left(\frac{2\varepsilon-\sigma_{zh}\Delta t}{2\varepsilon+\sigma_{zh}\Delta t}\right)H_{xz}^{n-1/2}(i,j+1/2,k+1/2)+\left(\frac{2\varepsilon\Delta t}{\mu(2\varepsilon+\sigma_{zh}\Delta t)}\right)$$
$$\frac{1}{\Delta z}\{[E_{yx}^{n}(i,j+1/2,k+1)-E_{yx}^{n}(i,j+1/2,k)]$$
$$+[E_{yz}^{n}(i,j+1/2,k+1)-E_{yz}^{n}(i,j+1/2,k)]\}$$

(3.44)

$$H_{yx}^{n+1/2}(i+1/2,j,k+1/2)=\left(\frac{2\varepsilon-\sigma_{xh}\Delta t}{2\varepsilon+\sigma_{xh}\Delta t}\right)H_{yx}^{n-1/2}(i+1/2,j,k+1/2)+\left(\frac{2\varepsilon\Delta t}{\mu(2\varepsilon+\sigma_{xh}\Delta t)}\right)$$
$$\frac{1}{\Delta x}\{[E_{zx}^{n}(i+1,j,k+1/2)-E_{zx}^{n}(i,j,k+1/2)]$$
$$+[E_{zy}^{n}(i+1,j,k+1/2)-E_{zy}^{n}(i,j,k+1/2)]\} \quad (3.45)$$

$$H_{yz}^{n+1/2}(i+1/2,j,k+1/2)=\left(\frac{2\varepsilon-\sigma_{zh}\Delta t}{2\varepsilon+\sigma_{zh}\Delta t}\right)H_{yz}^{n-1/2}(i+1/2,j,k+1/2)+\left(\frac{2\varepsilon\Delta t}{\mu(2\varepsilon+\sigma_{zh}\Delta t)}\right)$$
$$\frac{1}{\Delta z}\{[E_{xy}^{n}(i+1/2,j,k+1)-E_{xy}^{n}(i+1/2,j,k)]$$
$$+[E_{xz}^{n}(i+1/2,j,k+1)-E_{xz}^{n}(i+1/2,j,k)]\} \quad (3.46)$$

$$H_{zx}^{n+1/2}(i+1/2,j+1/2,k)=\left(\frac{2\varepsilon-\sigma_{xh}\Delta t}{2\varepsilon+\sigma_{xh}\Delta t}\right)H_{zx}^{n-1/2}(i+1/2,j+1/2,k)-\left(\frac{2\varepsilon\Delta t}{\mu(2\varepsilon+\sigma_{xh}\Delta t)}\right)$$
$$\frac{1}{\Delta x}\{[E_{yx}^{n}(i+1,j+1/2,k)-E_{yx}^{n}(i,j+1/2,k)]$$
$$+[E_{yz}^{n}(i+1,j+1/2,k)-E_{yz}^{n}(i,j+1/2,k)]\} \quad (3.47)$$

$$H_{zy}^{n+1/2}(i+1/2,j+1/2,k)=\left(\frac{2\varepsilon-\sigma_{yh}\Delta t}{2\varepsilon+\sigma_{yh}\Delta t}\right)H_{zy}^{n-1/2}(i+1/2,j+1/2,k)+\left(\frac{2\varepsilon\Delta t}{\mu(2\varepsilon+\sigma_{yh}\Delta t)}\right)$$
$$\frac{1}{\Delta y}\{[E_{xy}^{n}(i+1/2,j+1,k)-E_{xy}^{n}(i+1/2,j,k)]$$
$$+[E_{xz}^{n}(i+1/2,j+1,k)-E_{xz}^{n}(i+1/2,j,k)]\} \quad (3.48)$$

In this dissertation, the FDTD method is applied to analyze the interaction of the electromagnetic field with the model tissues. In the MRI calculations, the human head model (or the human body model) and the transverse electromagnetic (TEM) RF coils are modeled as a system using a full wave analysis; in the BMI simulations, the head model and the antennas are made as a single set of FDTD grid similarly. The PML boundary conditions are applied in both applications.

CHAPTER 4

B1+ SHIMMING TO OPTIMIZE THE RF COIL'S PERFORMANCE IN MRI WITHIN SAFETY REGULATIONS

High field magnetic resonance imaging (MRI) [15, 32, 82-85] provides the potential for increased signal-to-noise ratio (SNR) [86]. This attractive feature combined with advancement in current superconducting wire technology [87, 88] has resulted in significant increases in the field strength of current human scanners to reach 4 [89, 90], 7 [15, 84], 8 [16], 9.4 [82, 91] tesla and even as high as 12 tesla [92]. High field imaging also leads to an increased *Larmor* (operating) frequency, thus the wavelength in tissue can become comparable to the size of the load and/or the coil. The performance of the RF coil, as a result, becomes increasingly dependent on its electromagnetic interactions with the load, human body or head. In other words, variations in the coil load can significantly affect the performance of the coil. As a result, high field imaging has also been associated with significant technical and physical difficulties including inhomogeneous B_1^+ field (circularly polarized component of the time varying transverse magnetic field that excites the spins) distribution, increased radiofrequency (RF) power requirements and thus excessive tissue heating [15-20, 22, 23].

In this chapter, a B_1^+ shimming scheme [24-31] is proposed to optimize the RF coil's performance in MRI within safety regulations. After the background introduction of transmit arrays, the RF coil, the human models and the coil tuning are

described in section *4.2*. Section *4.3* presents calculations of the magnetic field and power. Detailed analyses of the RF power requirements at different field strength B_0 are provided in section *4.4* and an improved B_1^+ shimming scheme is proposed to improve the B_1^+ field homogeneity within the safety considerations using numerical simulations in section *4.5* and section *4.6*. The local SARs are discussed in the concerns of the safety regulations in section *4.7*. In section *4.8*, the B_1^+ shimming schemes are applied to pattern the B_1^+ field and the total electrical field. Finally, a short summary is provided in the last section.

4.1 Background of Transmit Arrays

Transmit arrays (phased arrays) are referred to as radio frequency (RF) excitation on multiple simultaneous channels in MRI. The use of transmit array coil in certain specialized areas of MRI is well established [93]: they can be used in high sensitivity surface coils [94], birdcage RF coils [19, 95] and transverse electromagnetic (TEM) resonators [28, 96]. A variety of phased-array coil designs have been constructed [97-103], where each individual coil in the array needs to be electrically isolated from the others to minimize the correlated noise [93, 104]. The mutual impedance between coils and the relative magnitude of the currents in the coils determine the coil coupling [105].

It is clear that as field strengths continue to increase, the use of transmit array will become more prevalent and dedicated RF coil design is enabling technology for higher field strengths [106, 107]. In high/ultra high field MRI, there are increased interests in multi-element transmit arrays systems that are capable of similarly high

number of independent channels to improve the excitation in combination with parallel transmission [96]. Increasing the B_0 field strength shifts the *Larmor* frequency towards higher frequencies and consequently reduces the wavelength down to the order of the dimensions of the human head and body [28, 108]. The increased field interactions cause an inhomogeneous distribution of the B_1^+ field, increased RF power requirements and thus excessive tissue heating [15-20, 22, 23]. To improve the RF field homogeneity (called B_1, or B_1^+ or RF shimming), transmit arrays are extensively used in RF coil design in recently years [32, 109]. The shimming methods use multiple independent transmit channels with distinctive spatial distribution to compensate RF inhomogeneity. A general solution would provide a parallel array of independent transmit channels allowing to change amplitude, phase, and pulse shape individually. With control of each excitation pulse waveform, it is possible to overcome the B_1 inhomogeneities and susceptibility-induced phase shifts [110]. Parallel transmit arrays could therefore solve the demand for higher RF peak power for whole-body applications with the specific absorption rate (SAR) limit for the human body [110].

Multi-port excitation with variable phase/amplitude approach and the potential to utilize the spatial information in an array during RF transmission offers the possibility to re-distribute the excitation fields in the head [111, 112] and in the body [113] theoretically using full wave electromagnetic methods [19, 20, 27-31, 114, 115] and experimentally [32-34]. In high-frequency operations, with an inhomogeneous human head/body, integer multiple of phased-shifts and uniform

amplitudes are not necessarily the ideal characteristics to impose on the voltages driving the transmit array in order to obtain a homogeneous/localized transmit field [112]. Phased array antenna excitation has been seen as a possible solution for achieving uniform RF transmit field distribution by adjustments of the phase and amplitude of the excitation sources [17, 28, 116]. At the same time, calculations of the power assumption [31, 117] and SAR [16, 18, 23, 118, 119] for transmit coil arrays have to be accurately evaluated for the different possible field distribution from safety concerns. Lower RF power absorption combined with uniform excitation is demonstrated in numerical simulations and experiments at 7T [120]. Van den Berg et al. [114, 121] have demonstrated using electromagnetic simulations a theoretical improvement on the B_1^+ non-uniformity and SAR hotspot for imaging of the pelvis area of body models using 12 idealized TEM elements [122]. Therefore, B_1 shimming (named B_1^+ shimming in this dissertation) of a circular transmit arrays have potentials in improving the RF field homogeneity and lowering the global and local power deposition.

The TEM coils offer sufficient design freedom since the end-rings can be omitted, which allows the rods to function as independent antenna elements [114]. They have been popularly used to improve the B_1^+ field homogeneity [17, 28, 112, 116, 123, 124]. In this chapter, TEM resonators with multi-element transmit arrays are applied in numerical simulations and practical experiments to excite the protons and to receive the signals in ultra high field MRI.

4.2 Materials and Methods

4.2.1 TEM Resonator

As introduced in Chapter 2, TEM resonators are very popular RF coils introduced by Vaughn et al. [47]. Three types of RF coils are used in the simulations in this chapter. The first coil is the shielded single-coaxial element coil which is typically used for extremity imaging at ultra high fields [122, 125]. Figure 4.1 displays 1) the FDTD grid of the loaded coil and 2) a detailed three-dimensional (3D) diagram of the coil's element. The coil length and diameter are 16.4 cm and 10 cm, respectively. The load in this coil is a 9.4 cm long cylindrical phantom with a circular cross section with a diameter of 4.6 cm. The electromagnetic properties of the phantom are assigned to have dielectric constant of 78 and conductivity of 1.154 s/m. A 3D FDTD model ($2mm^3$ resolution) is developed for the loaded coil. A stair-step approximation is used to model the shield of the coil. The coil element is modeled using a modified FDTD algorithm to account for the curvatures of the inner and the outer coaxial elements by making them octagons [112]. To resemble typical experimental settings and to break the symmetry associated with the placement as well as the geometry of the phantom, the coil strut is shifted 2 *mm* from the center axis. Throughout this chapter, we will refer to this coil as "single element coil" and load as "small/symmetrical phantom".

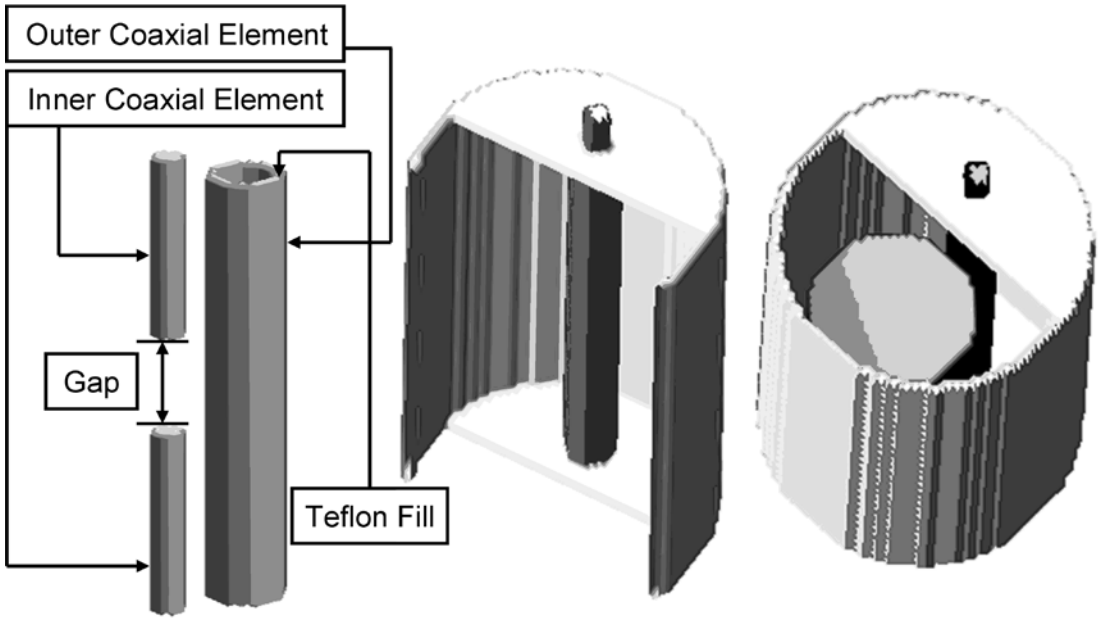


Figure 4.1 3D FDTD grid of the single element coil loaded with the small/symmetrical phantom and of the coil element. The coil element is tuned by adjusting the gap between each of the two inner coaxial elements. This figure was presented in [126].

The other two types of RF coils used in this chapter are 16-strut TEM resonator [31] and 32-strut TEM resonators [123], respectively. The 16-strut TEM resonator is used for the human head simulations, where 16 coaxial lines contained in an open resonant cavity. Each element is identical to that associated with the single element coil (Figure 4.1). The coil shield has a diameter of 34.6 cm and a length of 21.2 cm. The human head mesh (will be introduced in section *4.1.2*) is placed in the coil such that the chin is aligned with the coil's bottom ring. Two circular rings are attached to the top and bottom of the open cavity. Teflon is used as dielectric filler between the two inner rods of each strut. Figure 4.2 shows the geometry of the 16-strut TEM

resonator loaded with the human head. The 32-strut TEM resonator, firstly introduced by Abraham et al. [127], is used to simulate the whole body MRI. It consists of 32 coil elements within a partially enclosed cavity where the cylindrical shield extends along the body load, as shown in Figure 4.3. The coil shield diameter equals 69 cm and the length of the shield is 79.8 cm. The length of the coil element is 19.8 cm. The details of the human models are described in the next section.

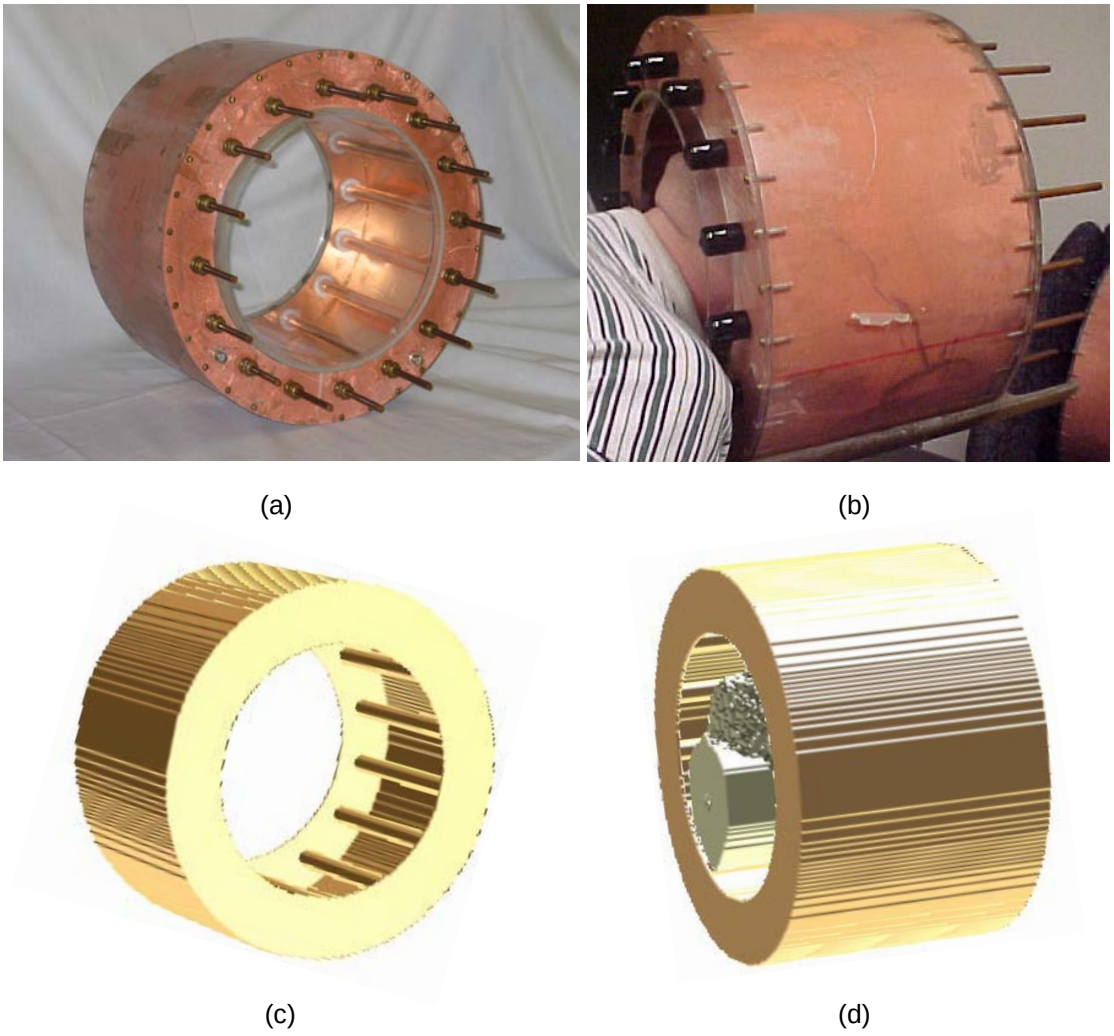
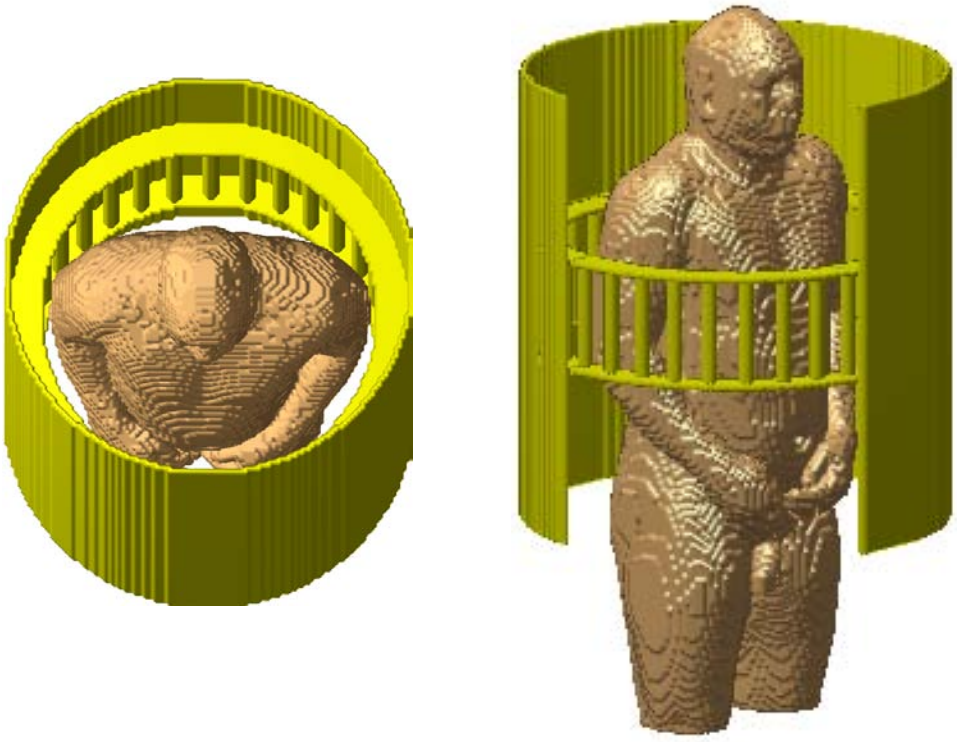


Figure 4.2 Geometry of 16-strut TEM resonator: unloaded resonator picture (a), and loaded with the head model resonator picture (b), simulation unloaded resonator plot (c) and loaded with the head model resonator plot (d). This figure was presented in [128].



(a) (b)

Figure 4.3 3D anatomically detailed human VHP body model loaded within the 32-strut TEM resonator. Subfigure (a) is the top-view of the system. There is an open on the coil shield to show the inside body model from a side-view in the subfigure (b).

4.2.2 Human Model

An 18-tissue anatomically detailed human head model [16] is used in this chapter. The model was developed from 0.5 mm × 0.5 mm × 2mm MRI images obtained at 1.5 tesla. And it is used to generate one FDTD grid of 2 mm × 2 mm × 2 mm for the head model which is used for simulations spanning from 181 to 406 MHz with the 16-strut TEM head coil. Figure 4.4 demonstrates the FDTD grid of the 16-strut TEM head coil loaded with the human head mesh.

An anatomically detailed 40-tissue human body mesh was obtained from visible human project (http://www.brooks.af.mil/AFRL). It is referred to as the VHP body model in this dissertation. FDTD grid of 6 mm × 6 mm × 6 mm for the whole body model (from knees above to top of the head) used in this chapter is generated from original body mesh with 1mm resolution. The body model is used for simulation with the 32-strut TEM body coil at 298MHz. The 32-strut TEM body coil loaded with the human body mesh is shown in Figure 4.4. The conductivity (σ), the dielectric constant (ε_r) and the density (ρ) of these tissue types in the 2-mm/18-tissue head model and the VHP body model are given at 298MHz [129] as a sample shown in Table 4.1.

Table 4.1 Electromagnetic properties of the tissues in the head and the body models at 298 MHz.

	Conductivity σ ($S \cdot m^{-1}$)	Dielectric Constant ε_r	Density ρ ($kg \cdot m^{-3}$)
Air	0	1	1000
Aorta	0.53652	48.357	1000
Aqueoushumor	2.4392	68.24	1000
Bladder	0.31664	20.103	1000
Blood	1.3154	65.689	1060
Blood Vessel	0.53652	48.357	1000
BodyFluid	1.5175	69.017	1000
BoneCancellous	0.21518	23.181	1850
BoneCortical	0.082491	13.446	1850
BoneMarrow	0.027331	5.7608	1900
BrainGreyMatter	0.69143	60.09	1040
BrainWhiteMatter	0.41269	43.821	1040
Breast Fat	0.032679	5.5425	920
Cartilage	0.55183	46.808	1100
Cerebellum	0.97196	59.819	1040
Cerebrospinal Fluid	2.2239	72.784	1060
Cervix	0.79883	52.598	1040
Colon	0.80948	65.074	1000

Cornea	1.1499	61.431	1076
Duodenum	0.97141	68.743	1040
Dura	0.80309	47.991	1000
Eye Sclera	0.97483	58.934	1040
Fat	0.039539	5.6354	920
Gallbladder	1.1165	62.967	1000
Gallbladder Bile	1.669	74.947	1000
Gland	0.85073	62.472	1000
Heart	0.9029	69.391	1900
Kidney	1.0209	70.591	1000
Lens	0.64741	48.972	1000
Liver	0.60892	53.571	1000
Lung Deflated	0.64821	56.231	1100
Lung Inflated	0.35599	24.798	400
Lymph	0.85073	62.472	1000
Mucous Membrane	0.62994	51.957	1020
Muscle	0.77	58.229	1040
Nail	0.082491	13.446	1850
Nerve	0.41777	36.951	1040
Oesophagus	0.97141	68.743	1040
Ovary	0.94467	61.397	1000
Pancreas	0.85073	62.472	1000
Prostate	0.9931	64.875	1000
Retina	0.97483	58.934	1040
Sclera	1.9967	52.698	1000
Skin Dry	0.64038	49.902	1100
Skin Wet	0.62994	51.957	1020
Small Intestine	1.8393	69.863	1000
Spinal Chord	0.41777	36.951	1040
Spleen	0.96784	66.577	1040
Stomach	0.97141	68.743	1040
Tendon	0.53659	48.001	1000
Testis	0.9931	64.875	1000
Thymus	0.85073	62.472	1000
Thyroid	0.85073	62.472	1000
Tongue	0.7443	58.934	1040
Tooth	0.082491	13.446	2160
Trachea	0.61043	45.335	1000
Uterus	1.0378	66.288	1000
Vitreous Humor	1.5175	69.017	1000

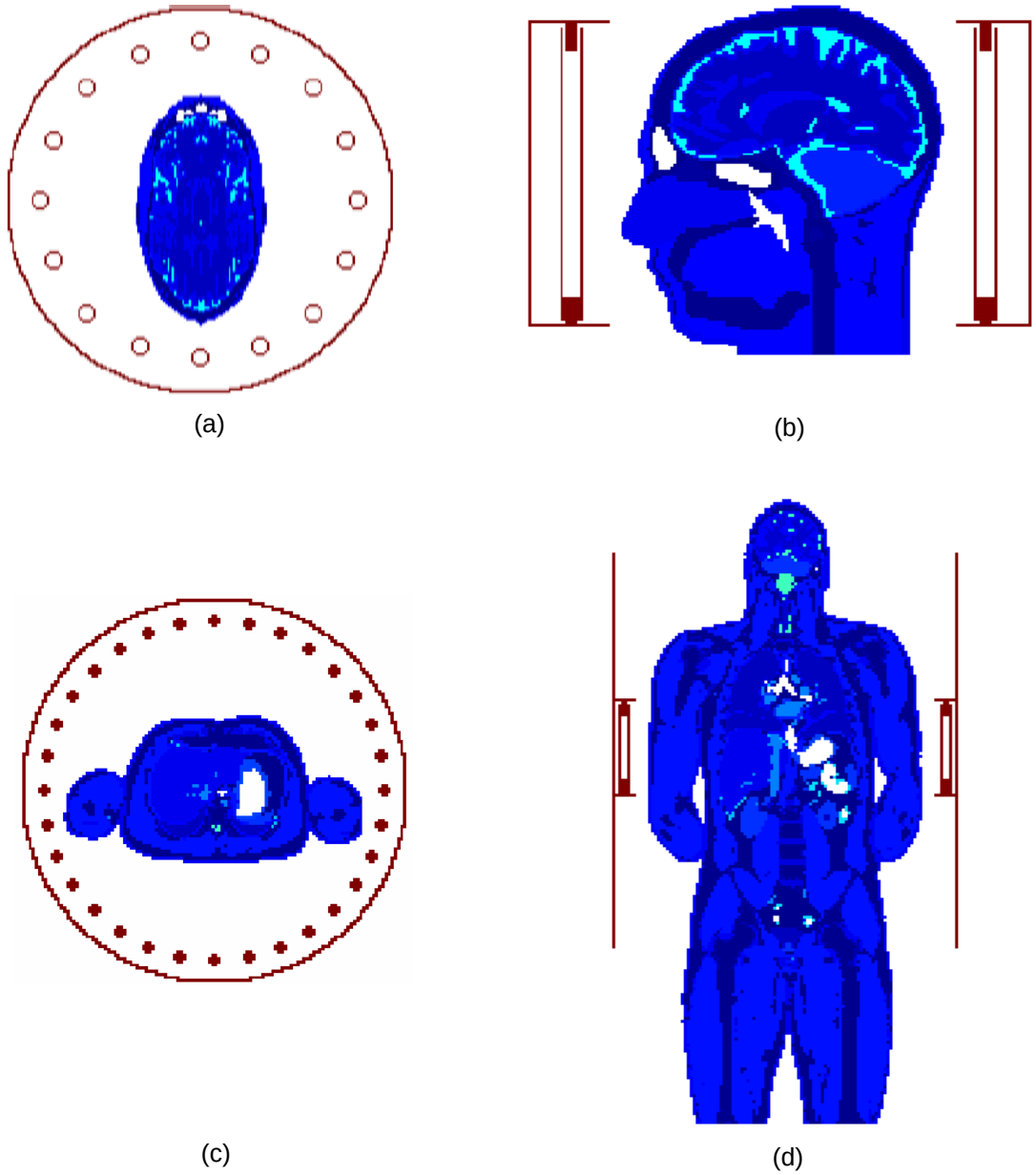


Figure 4.4 FDTD grid of the 16-strut TEM head coil loaded with the human head mesh and the 32-strut TEM body coil loaded with the human body mesh. Subfigure (a) and (c) are the axial cross section of the coil-load system; (b) is the sagittal cross section of the coil-head system, and (d) is the 2D coronal slice of the coil-body system.

4.2.3 Numerical Modeling

The FDTD technique is utilized in the calculations of the electric and magnetic fields and the power requirements. Following the methods suggested by Chen et al. [22] and utilized by Ibrahim et al. [20, 28, 112, 130], both the RF coil and the load are modeled as a single system. The inclusion of the coil as well as the load in a simultaneous modeling approach relies on three main bases. The first is 1) an excitation of the coil with a voltage source with an appropriate bandwidth followed by 2) an examination of the coil's frequency response (comparable to network analyzer S11 plot and Smith Chart) to determine if the coil's mode of interest is tuned to the appropriate frequency. If the coil in question is not tuned to the frequency of choice, numerical tuning of the coil is performed through adjusting the gap size between each pair of the inner coaxial element and steps 1) and 2) are performed again. The second is carrying out of all excitation and tuning steps while the load is numerically present in the coil. The third is an implementation of all aforementioned steps for all of the coil's applicable drive port(s).

The abovementioned technique of modeling the coil and the load as a single system accounts for the electromagnetic effects on the load due to the coil and, reversely, on the coil due to the load, which are interdependent. Note that this technique is different from utilizing "idealized conditions" [19] in calculating RF power requirements. In such a modeling approach [19], the coil is assumed to function as an ideal transmission line [131, 132] and the electromagnetic effects of the load on the coil are neglected. This technique has been shown to provide excellent

agreement with experiments for volume coils in terms of prediction of the magnetic field distribution [39] and the electric field distribution [130].

As shown in Figure 4.4, the FDTD domain of 16-strut resonator and the 2-mm/18-tissue head model system is divided into around 8 million cells, and within each cell the electric and magnetic fields are calculated using an iterative scheme. The perfectly matched layers (PML) are used [36] as the boundary conditions. 16 PML layers are placed on four boundaries in transverse x and y plane and 32 PML layers are on two z boundaries. A stair-step approximation is used to model the coil shield and the top and bottom rings of the coil and modified FDTD algorithm is used by making the coaxial elements octagon shape to minimize the errors [112]. The mathematical model of the coil is tuned while loaded with the human head mesh. From analytical models based on the multi-conductor transmission line theory [131, 133, 134], 9 modes exist for a 16-element TEM resonator. Mode 1, the second mode on the coil's frequency spectrum, is utilized for our power and field calculations as shown in Figure 4.5. The tuning frequencies for the head-coil system were set to be 181 MHz (approximately 4 tesla for ^{1}H imaging), 211MHz (approximately 5 tesla for ^{1}H imaging), 298MHz (approximately 7 tesla for ^{1}H imaging), 338MHz (approximately 8 tesla for ^{1}H imaging), and 406 MHz (approximately 9.4 tesla for ^{1}H imaging).

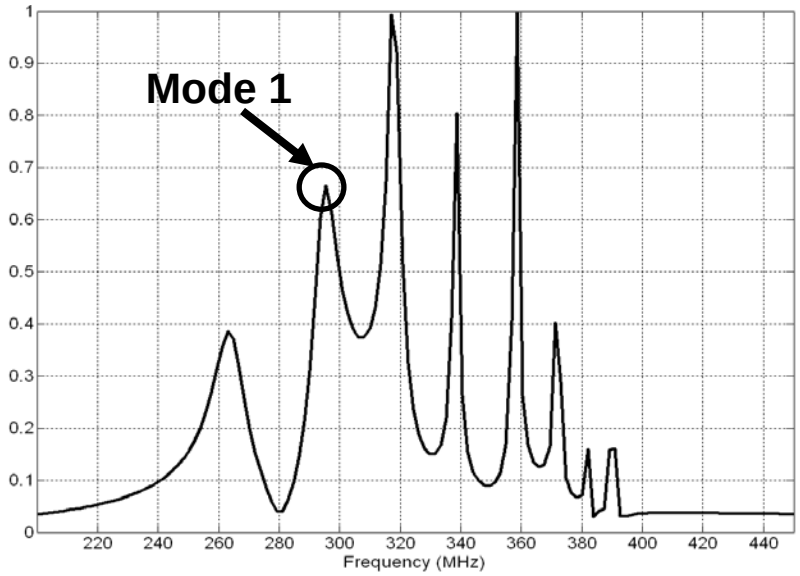


Figure 4.5 FDTD calculated frequency spectrum of the 16-strut TEM resonator loaded with the anatomically detailed human head model at 7 tesla. Plot was provided by Mr. R Abraham.

Similarly, the model of the 32-strut TEM coil is tuned while loaded with the VHP human body mesh (Figure 4.3). According to Abraham et al. [123], the choice of the mode on the frequency spectrum is different from the typical "mode 1" (used in the head model) by studying the operational characteristic of the 7 tesla body-loaded TEM coil. Mode 2, the third mode on the coil's frequency spectrum, is utilized in field calculations in this chapter because this mode delivers a better coverage of electric and magnetic fields on the body tissue and it is the only mode, among the first three modes, that resonates at the same frequency for different excitation ports of the 7 tesla body-loaded TEM coil. Detailed explanation is referred to [123]. Using Teflon material as the filler between each pair of inner and outer coaxial lines [39], tuning frequency is set at 298 MHz (7 tesla for ^{1}H imaging). Slanted perfect conductors are created in

coil's shaping without stair stepping errors. Figure 4.6 shows frequency response of the B_1^+ field at three selected points.

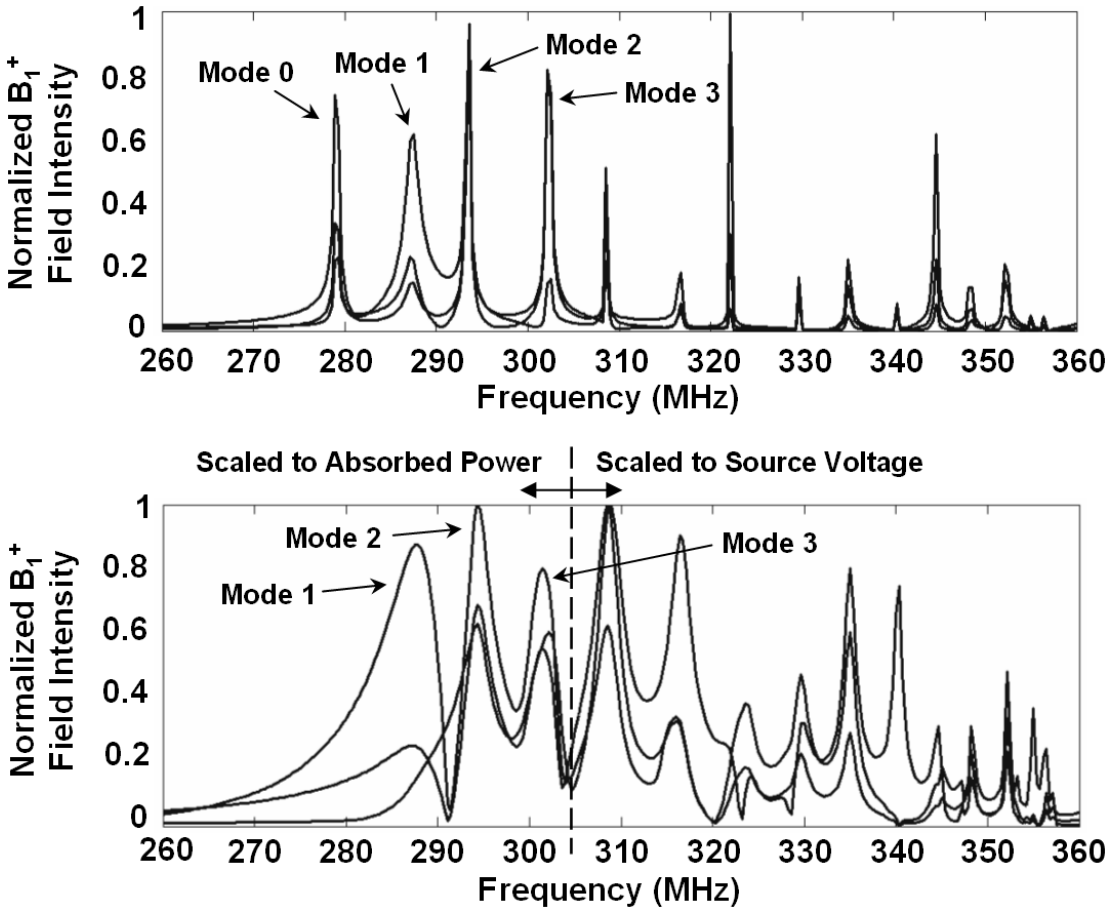


Figure 4.6 FDTD calculated frequency response of the B_1^+ field at three different points inside the 32-strut 7 tesla TEM coil operating empty (top subfigure) and loaded with the anatomically detailed body mesh (bottom subfigure). This figure was presented in [135].

Similar to the TEM resonator, the loaded shielded single coaxial element coil is tuned by adjusting the gap between the inner coaxial elements (Figure 4.1) until the coil's single mode lay at the frequency of interest. Using the FDTD simulations, the lower (gap size = 3 cm) and upper (gap = coil length – 3.6 cm) bounds of the tuning

frequencies are found to be 254 MHz (6 tesla for ^1H imaging) and 485 MHz (11.7 tesla for ^1H imaging), respectively. Note that these values are obtained using a dielectric constant of 2.1 to resemble a Teflon filling between the inner and outer coaxial lines.

4.3 Magnetic Field and Power Calculations

4.3.1 Inhomogeneous B_1^+ field with increase of B_0 field strength

The transverse magnetic (B_1) field contains two circularly-polarized components, defined as counter clockwise (CCW) B_1^+ and clockwise (CW) B_1^- fields. In the calculations used in this dissertation, these components are represented as follows:

$$B_1^+ = \left| \frac{B_{1x} + j * B_{1y}}{\sqrt{2}} \right|; \qquad (4.1) \qquad B_1^- = \left| \frac{B_{1x} - j * B_{1y}}{\sqrt{2}} \right|. \qquad (4.2)$$

Where B_{1x} and B_{1y} are the x and y components of the B_1 field and represented as complex values with amplitudes and phases. Since only the B_1^+ component of the transverse magnetic field is effective in the field excitation (the spin tipping), we only consider the B_1^+ field in the homogeneity optimizations. The two dimensionless factors ***max/min*** and coefficient of variance (COV) are commonly used to read out the homogeneity level of the B_1^+ field. The factor ***max/min*** is defined as the maximum B_1^+ field intensity over the minimum B_1^+ field intensity within the region of interest (ROI). Therefore, the closer ***max/min*** is to unity, the more homogenous (from a B_1^+ field distribution point of view) the slice is considered. COV is calculated

from the standard deviation divided by the mean value over the ROI. Smaller COV value represents a better homogeneity.

Figure 4.7 describes the inhomogeneous B_1^+ field distributions of the same axial slice of the 2-mm/18-tissue head model under different external magnetic field strengths for the RF coil-head system applying the 16-strut TEM resonator. All the subfigures are obtained using the quadrature excitation, i.e. the magnitudes of the ports excitation are set the same and phases are set integer multiples of 2π/(# excitation ports=16). It shows that the uniformity of the B_1^+ field becomes worse with increase of the B_0 field strength (operational frequency).

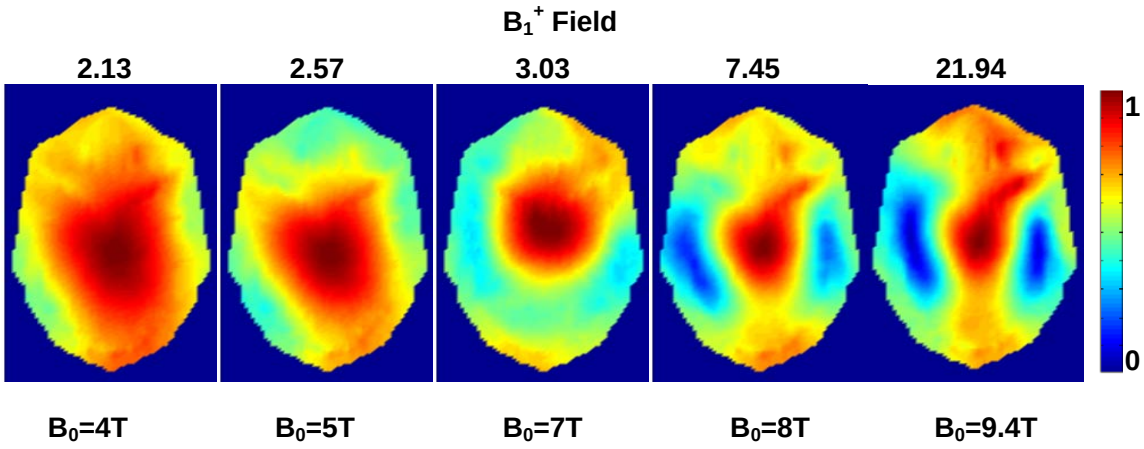


Figure 4.7 B_1^+ field distributions across the same axial slice of the head model under different external field strength B_0. All subfigures are normalized to its maximum values, and they share the common normalized color bar. The number on each subfigure is homogeneity measurement *max/min*.

4.3.2 Power Calculations

The RF power input (after matching circuits) to the coil can be approximated as the sum of the absorbed (in tissue) power and the radiated (exiting from the coil and

not absorbed in the tissue) power. In determining the RF power requirements, we have deliberately only considered the absorbed (in the small/symmetrical phantom or in the human head mesh) power under the aforementioned 5 different frequencies/field strengths. There are two main issues to concern: First, unlike the radiated power, the absorbed power is associated with tissue dissipation and heating concerns. Second, the percentages of the coil's radiated powers vary at different frequencies, making the comparison of power requirements at different field strengths unclear even for the same (in geometry and dimensions) RF coil. As a result, we have utilized the absorbed power rather than the total power entering the coil in determining the requirements for achieving specified flip angle(s) in all or part of the loads, where the coil conductors and dielectric are assumed to be lossless.

Power absorbed in the loads is calculated from Equation (4.3).

$$Power = \Delta x(i,j,k) \times \Delta y(i,j,k) \times \Delta z(i,j,k) \times \sum_i \sum_j \sum_k [\frac{1}{2} \sigma_{(i,j,k)} \times (E^2_{x_{(i,j,k)}} + E^2_{y_{(i,j,k)}} + E^2_{z_{(i,j,k)}})] \quad (4.3)$$

where $\sigma_{(i,j,k)}$ (S/m) is the conductivity of the FDTD cell at the *(i,j,k)* location; E_x, E_y and E_z (V/m) are the magnitudes of the electric field components in the *x*, *y*, and *z* directions, respectively; $\Delta x(i,j,k)$ $\Delta y(i,j,k)$ and $\Delta z(i,j,k)$ are the dimensions of each FDTD cell at location *(i,j,k)* and the summation is performed over the whole volume of the load.

4.3.3 Specific Absorption Rate (SAR) Calculations

The RF energy during MRI experiment induces the thermoregulatory imbalance; therefore the distribution of the RF energy inside the head is very important in assessing safety concerns. The specific absorption rate (SAR) is defined as the energy absorbed into a tissue of a given density by the radio transmitter. In FDTD, it is calculated by the following equation:

$$SAR_{(i,j,k)} = \frac{1}{2}\frac{\sigma_{(i,j,k)}(E^2_{x_{(i,j,k)}} + E^2_{y_{(i,j,k)}} + E^2_{z_{(i,j,k)}})}{\rho_{(i,j,k)}} \tag{4.4}$$

Where $\rho_{(i,j,k)}$ (kg/m^3) and $\sigma_{(i,j,k)}$, (S/m) are the tissue density and conductivity of the FDTD cell at the *(i,j,k)* location, E_x, E_y and E_z (V/m) are the magnitudes of the electric field components in the *x*, *y*, and *z* directions, respectively. SAR is presented in the unit W/kg per 1gm or 10gm for the regulations from the Food and Drug Administration (FDA) and the International Electrotechnical Commission (IEC), respectively.

4.4 Analysis of the RF Power Requirements

Since human MRI was first introduced as a clinical diagnostic tool, many safety concerns have been raised regarding the extent of the associated radiofrequency [136] power deposition in tissue [17, 19, 20, 86, 137-142]. Particularly, characterizing the dependence of the RF power deposition on the frequency of operation, i.e. *Larmor* frequency or MRI system field strength, has been a topic of research interest over the last half century [19, 20, 139]. Since advancements of

human MRI have been linked with higher B_0 field strengths, predicting the necessary RF power absorption in tissue to attain a particular flip angle in all or in part of the human head/body is essential since higher field strengths are typically associated with increases [19, 139] in RF power requirements. The interest in identifying RF power requirements at very high fields however has been more academic than practical, since the technology to build ultra high field ($\geq$ 7 tesla) human systems did not exist. As human MRI is currently performed at field strengths reaching 7 [15, 41], 8 [85, 143], and 9.4 [91] tesla, accurately predicting the RF power absorption associated with such operation has become essential to classify the potential clinical practicality of these systems as well as future ones. It is therefore crucial to determine whether the limitations of RF power absorption in tissue would impede the advancement (at least from a field strength perspective) of human MRI.

Many electromagnetic methods have been used in studying the relationship between RF power absorption in tissue and field strength or frequency of operation. The bases of these methods fall into two main categories, namely quasi-static [138, 139] and full wave [19, 20] models. Originally, quasi-static models have predicted square dependence, i.e. the RF absorbed power required to attain a fixed flip angle in the tissue is dependant on the square of the operating-frequency/field-strength [139]. Full wave models however have predicted otherwise. For example, one model that utilized idealized current sources [19] has shown that the RF power depends initially on the square of frequency, then reduces to linear dependence at higher field strength [19]. For other models that utilized rigorous modeling [20] of the coil source and

treated the coil and the load as a single system, the results illustrated that the power increases with frequency, peaks at a specified value, and then drops as the frequency increases beyond that value[20].

Operation at ultra high field human MRI however has been associated with inhomogeneous RF field distributions [15, 38-41] resulting in significant inhomogeneity in flip angle distribution across the human head/body [15, 38-41]. As a result, predicting or even defining the RF power needed to attain a particular flip angle in all or part of the head/body is difficult and potentially unclear. Consequently, comparative studies between low and high field imaging in regards to RF power requirements become somewhat meaningless due to significant difference in the homogeneity of the field distribution at different field strengths. Recently, however several techniques have been proposed to achieve homogenous excitation of tissue at ultra high field operation, including a variable phase and variable amplitude driving mechanism [27, 28, 32, 112, 116, 144, 145] utilizing transmit array and transmit SENSE [146-149]. Many works have demonstrated numerically [27-30] and experimentally [32] the potential of such methods in achieving highly homogenous slice excitation using variable phase and variable amplitude driving conditions. The power absorption associated with such methods however has not been fully investigated.

In section *4.3*, an in-depth look at the MRI RF power requirements is provided using a full wave model, the finite difference time domain (FDTD) method [36]. The calculations are performed using 2 volume coils: the TEM resonator [133] and a

single element extremity coil [39], and 2 different coil loads: an 18-tissue anatomically detailed human head model [28] and a cylindrical phantom filled with saline like electromagnetic properties. The approach utilized in these calculations employed rigorous modeling of the drive ports, as suggested in previous works [28, 38, 39, 116, 143], and treated the coil and the load as a single system. A roadmap is given for the RF power/MRI field strength dependence as follows. First, numerical studying (up to 11.7 tesla) is presented using the single element coil and the cylindrical phantom that illustrates the regimes of when quasistatic approximation holds or fails. This analysis is then followed with detailed studies of RF power requirements using a TEM resonator loaded with the anatomically detailed 2-mm/18-tissue head model and under field strengths ranging between 4 and 9.4 tesla. These studies focus on the RF power variations as a function of the number of drive ports (4, 8, or 16), the driving mechanism (variable or fixed phase/amplitude excitation), and the orientations and positioning within the human head model. Since it was possible to achieve highly homogenous 2D excitations in several slices across the human head model by varying the amplitudes and phases of the drive ports, relevant studies of the RF power/field strength dependence were achievable under well defined, fixed (at different field strengths), and homogenous excitation fields.

4.4.1 Coil Excitation

The simulations in section *4.3* are performed using numerical models of two coils and loads: 1) a shielded single coaxial-element coil loaded with a cylindrical phantom (Figure 4.1) and 2) a 16-strut TEM resonator loaded with an anatomically

detailed human head mesh (Figure 4.2). The details of the coil-load systems and the coil tuning are described in section *4.1*.

The first coil considered for power calculations is a shielded single coaxial element coil typically used for extremity imaging at ultra high fields [122, 125]. For the single element coil loaded with the small/symmetrical phantom, the excitation can only be performed at a single port as shown in Figure 4.1. As such, one case is considered where we investigate the B_1^+ field intensity within the volume of the small/symmetrical phantom. In terms of the TEM resonator loaded with the human head mesh, several cases are considered at 5 different frequencies/field strengths: 4 tesla (lower bound), 5 tesla, 7 tesla, 8 tesla, and 9.4 tesla (higher bound). Figure 4.9 describes the different excitations utilized in investigating the B_1^+ field intensity/distribution, namely:

1) "16-Port Excitation" where all the coil elements were utilized,
2) "8-Port Excitation", where 8 of the coil elements were utilized. Two different sets of elements were considered as shown in Figure 4.9, "Type AC" (8 elements denoted by A and C) and "Type BD" (8 elements denoted by B and D), and
3) "4-Port Excitation" ("Type A", "Type B", "Type C", and "Type D"), where the coil elements are denoted by A, B, C, and D as shown in Figure 4.9.

When the ports mentioned above are utilized to be the excitation ports, the left unutilized ports simply excited passively. At any of the above mentioned 5 field strengths, the multi-port excitation is done as follows. The TEM resonator is tuned from each of the

coaxial elements while using a uniform gap size between each pair (total of 16) of the inner coaxial elements. As has been observed at 340 MHz [28], the same/uniform gap size is sufficient to such that the coil's mode 1 resonated at the same frequency regardless of which coil element is excited. For "16-Port Excitation", the number of FDTD runs per frequency in this step is 16 + additional runs to obtain the appropriate gap size between each pair of the inner coaxial elements such that "mode 1" lies at the frequency of choice. Once the frequency of "mode 1" is determined with the appropriate gap size, the FDTD code is run again with Fourier transformation across the whole human head. The number of FDTD code runs per frequency in this step is 16 (through driving each element of the transmit array.) By varying the amplitudes and phases of the fields produced by exciting each element of the transmit array, the superposed field from each excitation port contributes homogeneous B_1^+ field distribution over the concerned slices. The optimization routines are gradient-based algorithm functions.

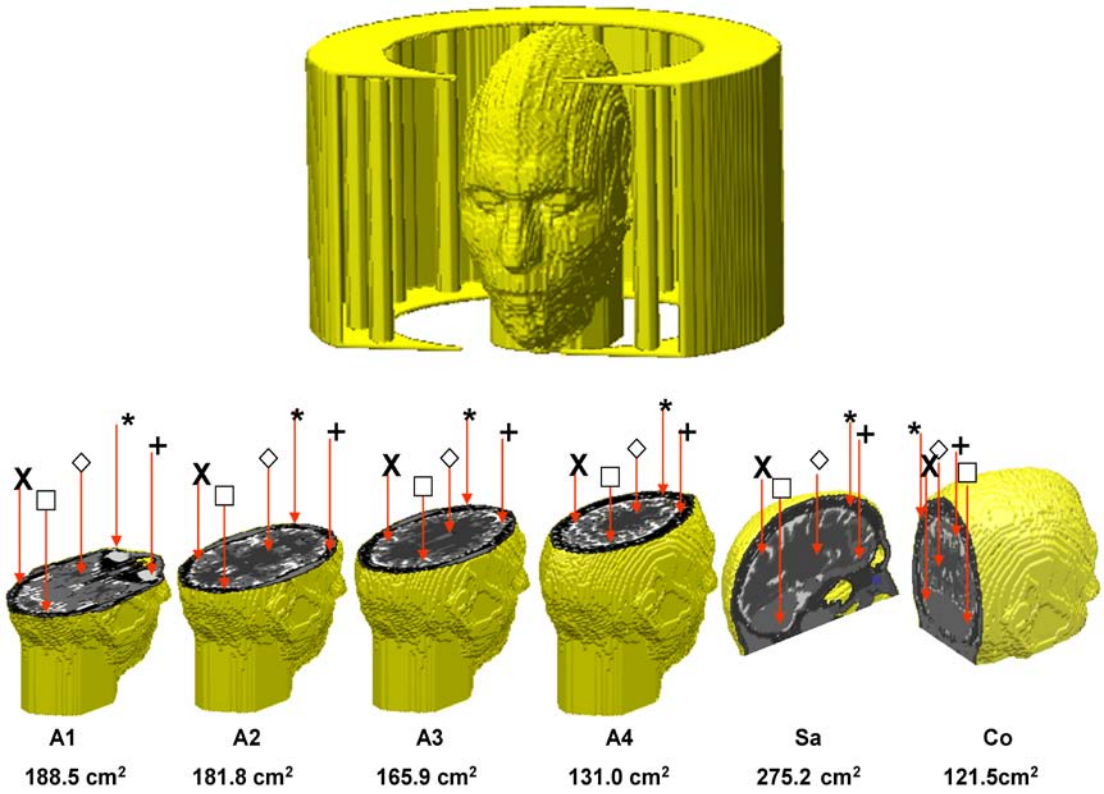


Figure 4.8 3D anatomically detailed human head model loaded within the 16-element TEM resonator. The seven individual head cuts show the orientation of seven slices (A1-A4, Sa and Co) used in the power and B_1^+ field calculations. On each slice, 5 points are picked where the B_1^+ field intensity is evaluated by FDTD package. The symbols (X, □, ◊, *, +) show the spatial positioning of these 5 points. The spatial area of each slice is shown under each head cut, respectively.

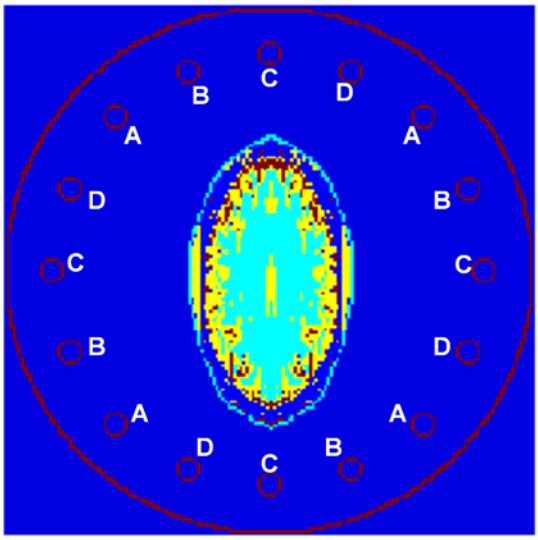


Figure 4.9 Axial slice of the FDTD grid of the 16-element TEM resonator loaded with the 18-tissue anatomically detailed human head model showing a cut of the coil where slice A1 (Figure 4.3) is located. All coil elements ports are used in 16-port excitation; ports labeled A and C are used in 8-port excitation "Type AC;" ports labeled B and D are used in 8-port excitation "Type BD;" 4 ports labeled A are used in 4-port excitation "Type A," and the same naming convention was used for 4-port excitation "Type B," "Type C," and "Type D".

Two different feed strategies that involve the phase and amplitude of the driving voltages are considered at the above mentioned 5 magnetic field strengths: 1) fixed (integer multiples of phase-shifts) phase and fixed (uniform) amplitude (FPA), and 2) optimized phase and optimized amplitude (OPA), which is also referred as B_1^+ shimming. The B_1^+ field calculations and optimizations are all performed upon 4 axial slices (A1-A4), 1 sagittal slice (Sa), and 1 coronal slice (Co), as shown in Figure 4.8. The thickness of each slice is 2mm, 1 cell of FDTD model. In the FPA condition, integer multiples of 2π/(# excitation ports) are utilized; while the OPA (B_1^+ shimming) condition is carried-out to achieve better B_1^+ field distribution homogeneity within the slice of interest after varying the amplitude and phase of each drive port in the

transmitting array. Homogeneity of the B_1^+ field distribution within any of the above mentioned 6 slices is chosen to be evaluated by "***max/min***". This guarantees that the B_1^+ field intensities within any slice of interest lie within a specific range (***max*** and ***min***) and therefore the reported power values would a) facilitate physical interpretation and b) represent more meaningful/definitive findings.

Two dimensional whole-slice uniformity optimizations are performed by varying the amplitudes and phases of the fields produced by exciting each element of the coil. The optimization routines are comprised of a combination of both gradient-based and genetic algorithm functions where a single iteration may go through either of these two methods. These optimization routines are configured to determine the amplitude and phase that should be applied to the voltage driving each coil element in order to achieve better B_1^+ field distribution homogeneity (lower ***max/min***.)

Power absorbed in the load is calculated as the summation of power deposition over the whole volume of the head model by Equation 4.3 as discussed in section *4.2.2*. Except for the single element coil loaded with the small/symmetrical phantom, the excitation amplitudes/phases are adjusted to provide an average B_1^+ field intensity of 1.174 micro tesla (μT), the field strength needed to produce a flip angle o f $\pi/2$ with a 5-msec rectangular RF pulse, in each selected slice, and then the absorbing power is calculated from Equation 4.3. This can be clearly achieved with the linearity of Maxwell's equations since $Driving_Voltage \propto E \propto H$ and therefore, $Power \propto E^2 \propto B_1^{+2}$, where E and H are the electric and magnetic field intensities, and $\propto$ indicates linear dependence.

4.4.2 Results and Discussion

4.4.2.1 Single Element Coil Loaded with Small/Symmetrical Phantom: A Glance into the Quasistatic Predictions

In the quasistatic regime, the power dissipated in a cylinder (assumed for all practical purposes to be the RF power required to obtain a specified flip angle) with radius r and length l is given by [20]:

$$Power = \pi r^4 l \omega^2 \sigma B^2 \tag{4.5}$$

where B is the magnetic flux density, σ is the conductivity, and ω is the frequency. Therefore, until recently [19, 20], it was established that the RF power needed to obtain a specified flip angle in an imaged object varies with ω^2, or with the square of the B_0 field strength (given that the frequency of the applied RF field equals the Larmor frequency). If we examine the quasistatic power relation given by Equation 4.5, it can be easily shown that B was assumed to be the field that excites the spins. This can only be applicable if the transmitted magnetic field that exists in the load is a circularly polarized transverse magnetic field in a specified sense of rotation, i.e. the B_1^+ field. With commonly/clinically used RF excitation methods, this is only valid when the transmit coil is excited in quadrature at low frequency where the dimensions of coil and object to be imaged are small compared to operating wavelength; this is clearly not the case for UHF human MRI [15, 17, 39]. In addition, for the ω^2 dependence to hold, it is also assumed that 1) homogeneity and 2) the strength of the B field do not vary with frequency. If we relate this assumption to the MRI excite (B_1^+) field, this would require that the fraction of the total

transmitted field that contributes/projects to B_1^+ field direction is constant under all B_0 field strengths. Again this is not a valid assumption for a wide frequency range such as 64 MHz (1.5 tesla) and 400 MHz (9.4 tesla).

Previous published results (Figure 3 in [39]) demonstrated that good homogeneity of and similarity between the B_1^+ and B_1^- fields' intensities/distributions are obtained for the small/symmetrical phantom loaded in the single element coil at 6 tesla. As was deduced [39], these two facts indicate that the arrangement of this coil and phantom is effectively producing a close to ideal (quasi-statically predicted) linearly polarized field since it can be evenly split into B_1^+ and B_1^- fields [39]. The polarization of this linearly polarized field can potentially be altered to become circular if quadrature excitation were possible with this coil. The same figure [39] also showed that the similarities between, as well as the good homogeneity of the B_1^+ and B_1^- fields' intensities/distributions were less apparent at 11.7 tesla.

Figure 4.10 displays the RF absorbed power (as a function of frequency) required to obtain a fixed average intensity of either of the circularly polarized fields (B_1^+ and B_1^-), within the volume of the small/symmetrical phantom loaded in the single element coil (shown in Figure 4.1). Figure 4.10 clearly substantiates the frequency/load regimes when the square dependence between RF power and B_0 field strength is applicable and when the quasistatic approximations of RF power requirements begin to fail. It is clearly shown that except near high frequency values, the required RF power for both field components is almost identical despite

the slight asymmetry in the coil model. In addition, the expected power/frequency square dependence is clearly apparent at lower frequencies with deviations as the frequency increases. Therefore, based on 1) the geometries and sizes of the single element coil and of the small/symmetrical phantom load and on 2) the frequency power relation presented in Figure 4.10, the power requirements for loads, such as the human head/body, are expected to deviate greatly from those predicted by quasistatic approximations, most especially with increasing MRI B_0 field strength.

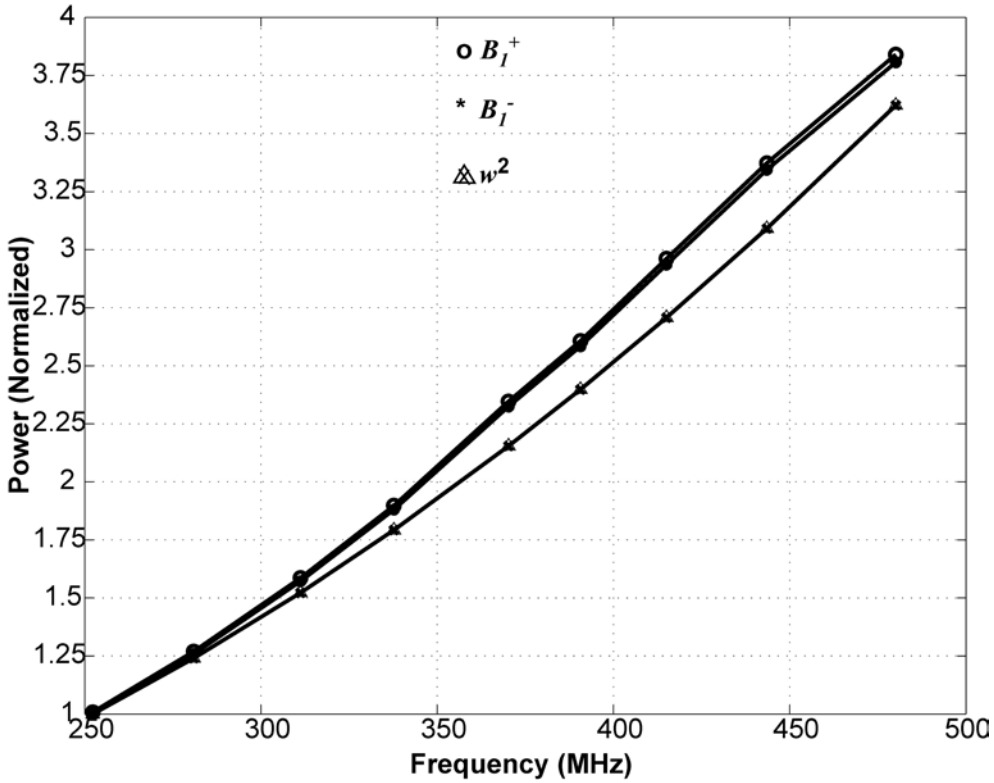


Figure 4.10 Plots of required RF power absorbed in the small/symmetrical phantom loaded in the single element coil (Figure 4.1) in order to obtain a fixed average (over the volume of the phantom) B_1^+ or B_1^- field intensity as a function of frequency. "ω^2" plot denotes the square dependence predicted from quasistatic approximations. This figure was presented in [117].

Excitation	Slice	Type	4 Tesla	5 Tesla	7 Tesla	8 Tesla	9.4 Tesla
4-Port	A1	Type A	2.39	3.62	3.78	11.01	18.62
		Type B	1.97	2.93	3.39	4.91	21.40
		Type C	2.05	2.94	3.16	7.83	24.72
		Type D	2.32	2.94	3.11	11.97	97.73
	A2	Type A	2.05	2.82	2.85	3.94	4.19
		Type B	1.79	2.58	2.68	2.89	3.82
		Type C	1.88	2.63	2.53	4.15	4.16
		Type D	2.09	2.45	2.49	4.75	5.26
	A3	Type A	1.83	2.32	2.12	2.39	2.29
		Type B	1.60	2.21	1.91	1.85	2.00
		Type C	1.65	2.28	1.86	2.41	2.03
		Type D	1.82	2.00	2.06	2.49	2.16
	A4	Type A	1.56	1.89	1.66	1.85	2.12
		Type B	1.36	1.81	1.52	1.71	2.03
		Type C	1.33	1.76	1.70	1.57	1.80
		Type D	1.46	1.54	1.87	1.60	1.94
	A5	Type A	1.50	1.79	1.54	1.81	2.04
		Type B	1.38	1.80	1.45	1.82	2.01
		Type C	1.30	1.74	1.70	1.52	1.93
		Type D	1.39	1.51	1.63	1.56	2.05
	S	Type A	2.02	2.31	2.47	2.94	5.83
		Type B	2.24	2.97	2.28	3.17	4.91
		Type C	2.09	2.94	3.05	2.30	3.47
		Type D	2.08	2.47	2.53	2.38	3.84
	C	Type A	2.45	3.65	1.82	4.54	3.36
		Type B	1.95	2.05	1.51	3.57	3.16
		Type C	1.90	2.13	2.47	2.13	2.65
		Type D	2.14	2.70	1.72	2.33	2.71
8-Port	A1	Type AC	2.16	2.71	3.10	8.20	23.47
		Type BD	2.10	2.44	3.01	6.84	20.22
	A2	Type AC	1.93	2.22	2.38	3.92	4.34
		Type BD	1.90	2.29	2.32	3.65	4.22
	A3	Type AC	1.70	2.00	1.86	2.22	2.01
		Type BD	1.69	1.93	1.89	2.12	1.99
	A4	Type AC	1.40	1.62	1.73	1.60	1.94
		Type BD	1.40	1.60	1.70	1.55	1.97
	A5	Type AC	1.39	1.61	1.60	1.63	1.98
		Type BD	1.39	1.63	1.55	1.66	2.01
	S	Type AC	2.04	2.63	2.75	2.55	4.31
		Type BD	2.12	2.67	2.49	2.74	4.34
	C	Type AC	2.14	2.56	2.10	2.79	2.66
		Type BD	2.03	2.30	1.63	2.84	2.63
16-Port	A1	-----	2.13	2.57	3.03	7.45	21.94
	A2	-----	1.91	2.18	2.35	3.78	4.27
	A3	-----	1.70	1.96	1.87	2.16	1.99
	A4	-----	1.40	1,61	1.72	1.58	1.96
	A5	-----	1.39	1.62	1.57	1.64	2.00
	S	-----	2.07	2.64	2.62	2.64	4.33
	C	-----	2.08	2.43	1.81	2.82	2.60

Table 4.2 B_1^+ field distribution homogeneity (calculated by *max/min*) for each slice shown in Figure 4.8 at different B_0 field strengths and under 4-port, 8-port, and 16-port fixed phase/amplitude driving conditions. The 4-port excitations types,

"Type A," "Type B," "Type C," and "Type D," and the 8-port excitation types, "Type AC" and "Type BD," are defined in Figure 4.9.

4.4.2.2 TEM Resonator Loaded with the Anatomically Detailed Human Head Mesh

(1) B_1^+ Field Distributions under Fixed Phase/Amplitude (FPA) and Optimized Phase/Amplitude (OPA) Conditions

Figure 4.11 provides the ***max/min*** values obtained for 4-, 8-, and 16- port FPA conditions at 4, 5, 7, 8, and 9.4 tesla, and the detailed values is provide in Table 4.2. Figure 4.12 shows a sample of the B_1^+ field distributions within the abovementioned 6 slices for 16-port FPA and OPA conditions at 7 and 9.4 tesla. With OPA conditions, the B_1^+ field distribution in each slice was obtained by minimizing ***max/min*** through applying the most aggressive optimizations at 9.4 tesla and then using resulting ***max/min*** as the homogeneity target in the same slice at 7 tesla. As shown in Figure 4.7, under the higher B_0 field strengths, the more non-homogeneous the slices are, therefore the highest ***max/min*** happens at 9.4 tesla. Aggressive optimization under this condition consumes the most time and work to pursuing the global minimum instead of local minimums (by adding vibrations). Then the minimum ***max/min*** value at 9.4 tesla was used as criterion when doing optimization at 7 tesla. Therefore under both B_0 field strengths, the B_1^+ field distribution within a slice is characterized by the same ***max/min***, or according to this chapter's classification, the same homogeneity.

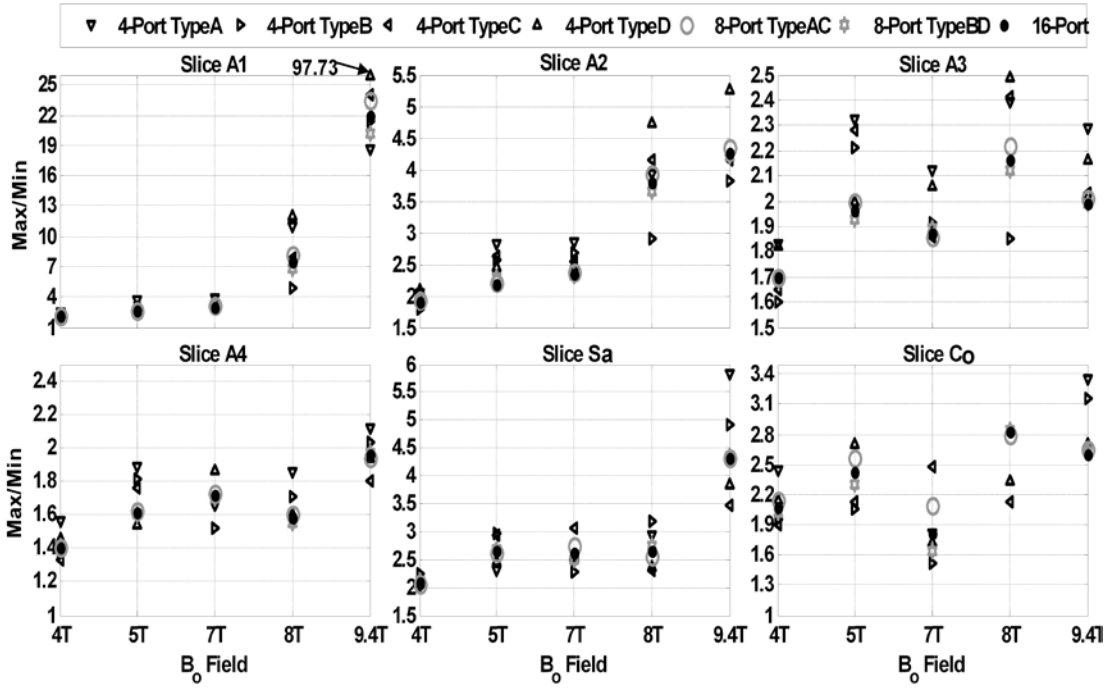


Figure 4.11 Plots of *max/min* (maximum B_1^+ field intensity over minimum B_1^+ field intensity within the same slice) for each slice shown in Figure 4.8 at different B_0 field strengths and under 4-, 8-, and 16- port fixed phase/amplitude driving conditions. The 4-port excitations types, "Type A," "Type B," "Type C," and "Type D," and the 8-port excitation types, "Type AC" and "Type BD," are defined in Figure 4.8. Each subfigure corresponds to a different slice. For a particular driving condition, the *max/min* values are presented with the same symbol at all B_0 field strengths. This figure was presented in [117].

As expected, Figure 4.11 and Figure 4.12 show that with FPA conditions, "9.4 tesla, 16-Port Excitation" provides less homogenous B_1^+ field distributions than with the "7 tesla, 16-Port Excitation" case. Subsequently, under B_0 field strengths lower than 9.4 tesla, it is probable that different B_1^+ field distributions can be obtained within a slice while having the same homogeneity, i.e. the same ***max/min*** (obtained at 9.4 tesla). This is demonstrated in Figure 4.12 with the two distinct 7 tesla B_1^+

field distributions, denoted by “Solution 1” and “Solution 2” that have the same sets of ***max/min***. As was demonstrated in earlier numerical work [27, 28, 116], Figure 4.12 confirms that significant improvement in the homogeneity of the B_1^+ field distributions can be achieved in many slices and in all directions with OPA conditions. It is clearly shown that the homogeneity of the B_1^+ field distributions is better achieved within relatively smaller area slices, as shown with slices A4 and Co (see Figure 4.8).

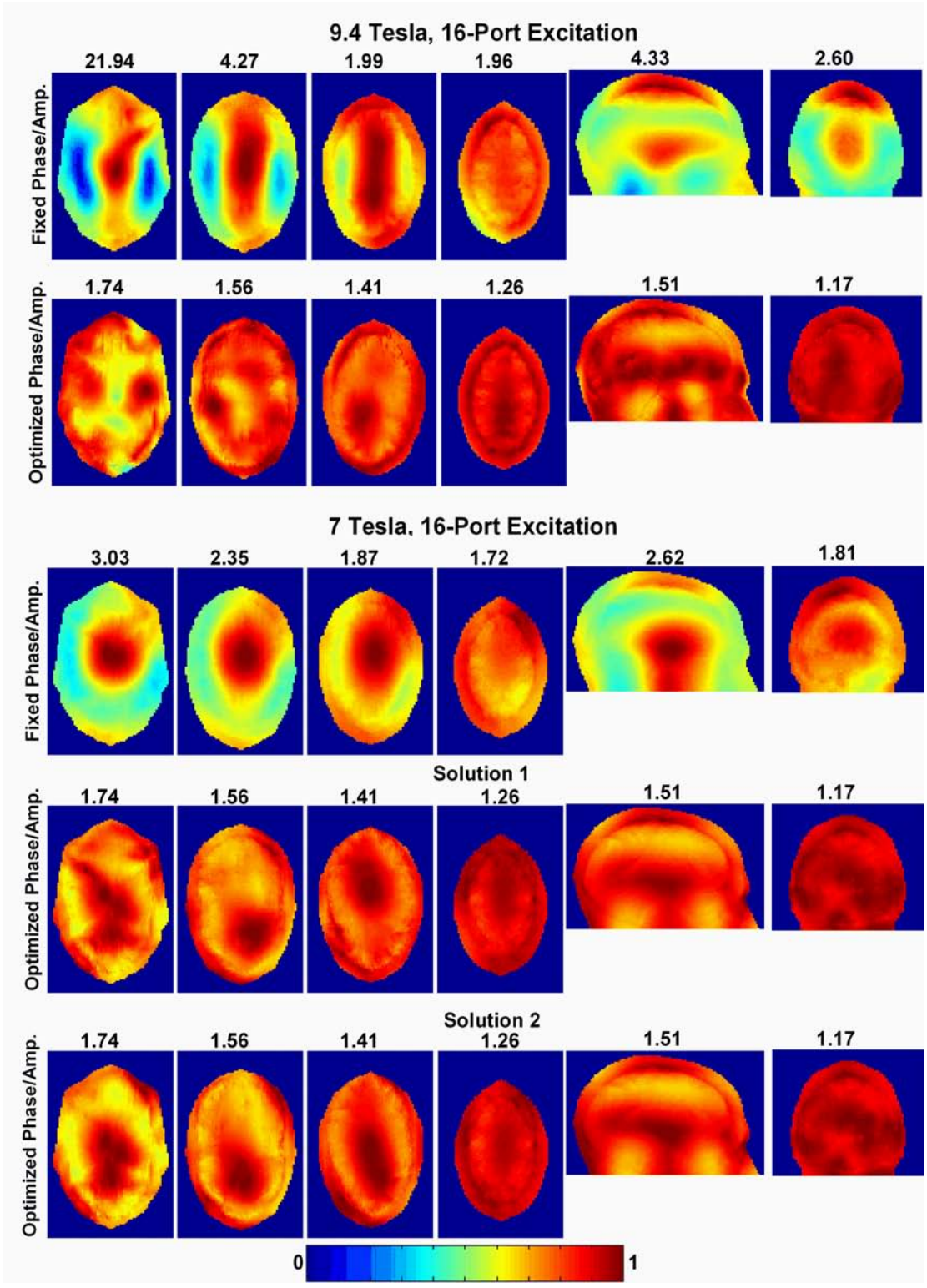

9.4 Tesla, 16-Port Excitation
21.94
4.27
1.99
1.96
4.33
2.60
Fixed Phase/Amp.
1.74
1.56
1.41
1.26
1.51
1.17
Optimized Phase/Amp.
7 Tesla, 16-Port Excitation
3.03
2.35
1.87
1.72
2.62
1.81
Fixed Phase/Amp.
Solution 1
1.74
1.56
1.41
1.26
1.51
1.17
Optimized Phase/Amp.
Solution 2
1.74
1.56
1.41
1.26
1.51
1.17
Optimized Phase/Amp.
0
1

Figure 4.12 B_1^+ field distributions for each slice shown in Figure 4.8. The data are presented at 9.4 and 7 tesla using 16-port excitation with 2 conditions, fixed and optimized phase/amplitude (FPA and OPA) driving conditions. In the horizontal direction, every set of 6 sub-figures is orderly positioned to correspond to slices A1-4, slice Sa, and slice Co (Figure 4.8), respectively. In the vertical direction, under "9.4 tesla, 16-Port Excitation," the top and bottom rows correspond to 16-port FPA and OPA driving conditions, respectively. Under "7 tesla, 16-Port Excitation", the top row corresponds to 16-port FPA driving conditions and the middle and bottom rows correspond to 2 possible solutions for 16-port OPA driving conditions. The two solutions correspond to 2 different B_1^+ field distributions yet have the same homogeneity, i.e., the same "maximum B_1^+ field intensity over minimum B_1^+ field intensity" within the same slice; this value is denoted as *max/min*. The number above each sub-figure corresponds to *max/min* within that slice. All the results are presented for the coil configuration shown in Figure 4.8. Figure 4.12 was presented in [117].

(2) Power Comparisons under 16-, 8-, and 4- Port Excitations and Fixed Phase/Amplitude Driving Conditions

Figure 4.13 displays the required RF power (watts) to achieve a value of 1.174 μT for the average B_1^+ field intensity in each slice shown in Figure 4.8 as a function of B_0 field strength under 16-, 8-, and 4- port FPA excitations. For each slice and number of excited ports, the corresponding ***max/min*** value of B_1^+ field intensity is shown in Figure 4.11. Figures 4.11 and 4.13 provide two main observations in regards to the RF power requirements under FPA driving conditions, namely

a) The fewer number of excitation ports utilized, the more power absorbed in the human head (in order to obtain the same average B_1^+ field intensity in each slice). The difference in power requirements, however, is minimal between the 8-port ("Type AC" or "Type BD") and 16-port excitations and is almost indistinguishable at 4 and 5 tesla. The noticeable, yet still marginal, difference is obtained between 8-port and 4-port excitations at 7-9.4 tesla.

b) The difference between using 8-port “Type AC” and “Type BD” is indistinguishable. Compared to the other 3 types of 4-port excitations, “Type C” (Figure 4.9) requires more absorbed power in the head (in order to obtain the same average B_1^+ field intensity in each slice), most especially at 7-9.4 tesla.

It can also be observed that the dependence of RF power on the B_0 field strength varies in a very similar manner regardless of the number of drive ports utilized. In agreement with previously published data obtained while assuming idealized coil conditions [19], Figure 4.13 shows that the RF power continuously increases as a function of B_0 field strength in the larger axial slices, i.e. the lower ones (A1-A3). In the upper axial slice A4, however, the results differ from those obtained while assuming idealized coil conditions. In accordance with the RF power/frequency relation observed with rigorous modeling of the coil and of the excitation port [20], the required RF power peaks at 8 tesla for slice A4 and then decreases at higher B_0 field strengths. Additionally, the peak-then-decrease behavior was also observed for several slices (not shown) above the axial slice A4. The peaks for these slices however occurred at 7 tesla rather than 8 tesla (A4.)

In the sagittal (Sa) and coronal (Co) slices, the RF power peaks at 7 tesla, drops noticeably for slice Co and negligibly for slice Sa at 8 tesla, then rises again noticeably for slice Co and negligibly for slice Sa at 9.4 tesla. It is noted however that while prior RF power/frequency relation [20] obtained using rigorous modeling conditions showed peak-then-decrease behavior at all the displayed axial slices, the

decrease in the lower axial slice was minimal [20]. This possibly shows that the RF power required in order to obtain a fixed value of the average B_1^+ field intensity at even lower axial slices may continue to increase with frequency. Additionally, the RF power/frequency relation shown in [20] was obtained with a model of an 8-element linearly (one port) excited TEM resonator loaded with the visible human project head model (http://www.brooks.af.mil/AFRL), which is 1) tilted and 2) a volumetrically much larger model than the one utilized in this chapter. These underlined conditions are different than the ones utilized to present the power calculations shown in Figure 4.13.

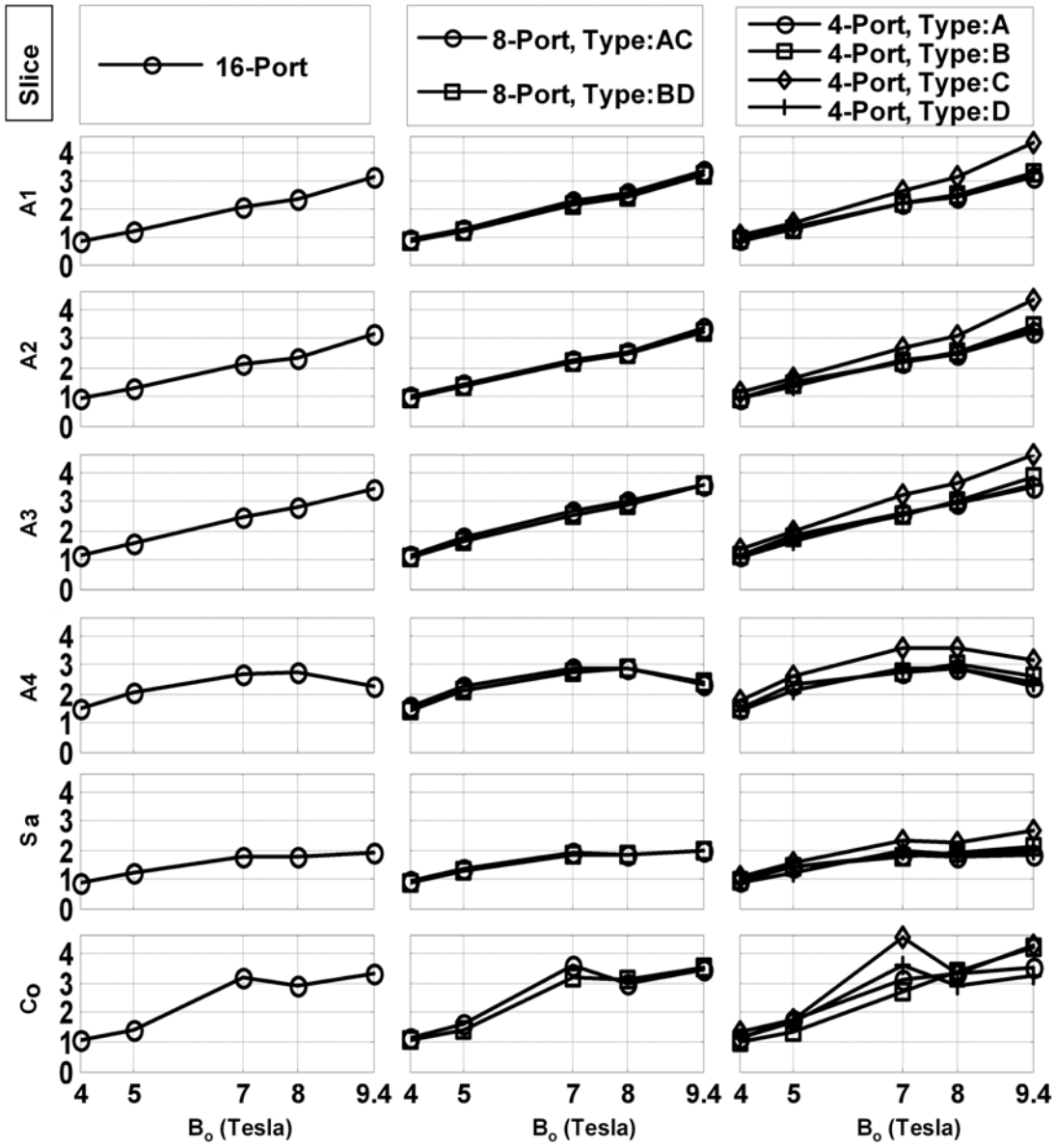


Figure 4.13 Plots of required absorbed (in the human head) power in order to obtain a fixed (1.174 μT) average (over the area of each of the 6 slices shown in Figure 4.8) B_1^+ field intensity as a function of B_0 field strength. The results are presented under 16-, 8-, and 4- port fixed phase/amplitude driving conditions. From left to right, the 3 columns correspond to 16-, 8-, and 4-port excitations, respectively. From top to bottom, the 6 rows correspond to the results for the 6 slices (orderly positioned as slices A1-4, Sa, and Co, respectively). In each sub-plot, the X-axis is the B_0 field (tesla) and the Y-axis is the power absorbed in the head (watts). The excitation types which denote the choice of the excited coil elements in 8- and 4-

port excitations are defined in Figure 4.9. All the results are presented for the coil configuration shown in Figure 4.8. Figure 4.13 was presented in [117].

While the above analysis provides insight into RF power/field strength dependence, it is somewhat vague since the homogeneity of the B_1^+ field distributions is 1) significantly different at different B_0 field strengths and 2) poor at higher B_0 field strengths. In the following sections, we will attempt to address these two specific issues by homogenizing the B_1^+ field distributions using VPA driving conditions to achieve the same homogeneity (***max/min***) in any targeted slice at all the B_0 field strengths of interest.

(3) Absorbed Power Comparisons for the Same Homogeneity of the B_1^+ Field Distribution under Different 1) Number of Drive Ports and 2) Driving Conditions

Starting from FPA 4-port excitation, slice A3 (as described in Figure 4.8) was most aggressively optimized to achieve the lowest possible ***max/min*** using OPA driving conditions at 9.4 tesla. Note that the OPA driving conditions were tested with the four possible excitation types (Figure 4.9) associated with 4-port excitation. The resulting lowest ***max/min*** of 1.70 (achieved for 4-port "Type A") was then utilized as the homogeneity target at all B_0 field strengths under 8-, and 16- port excitations. Except for 4 tesla where FPA driving conditions were utilized for 8-, and 16- port excitations, OPA driving conditions were required to achieve ***max/min*** of 1.70 under all other B_0 field strengths with 4-, 8-, and 16-port excitations. Figure 4.14 displays samples of the resulting B_1^+ field and total electric field distributions in slice A3 at 4, 7, and 9.4 tesla and using 4-, 8-, 16- port excitations where ***max/min*** =

1.70. A very interesting point to note here is the fact that under any of the three B_0 field strengths shown in Figure 4.14, a remarkably similar (not only in terms of ***max/min*** but also in terms of the overall characteristics) B_1^+ field distribution was obtained with 4-, 8-, or 16-port excitations.

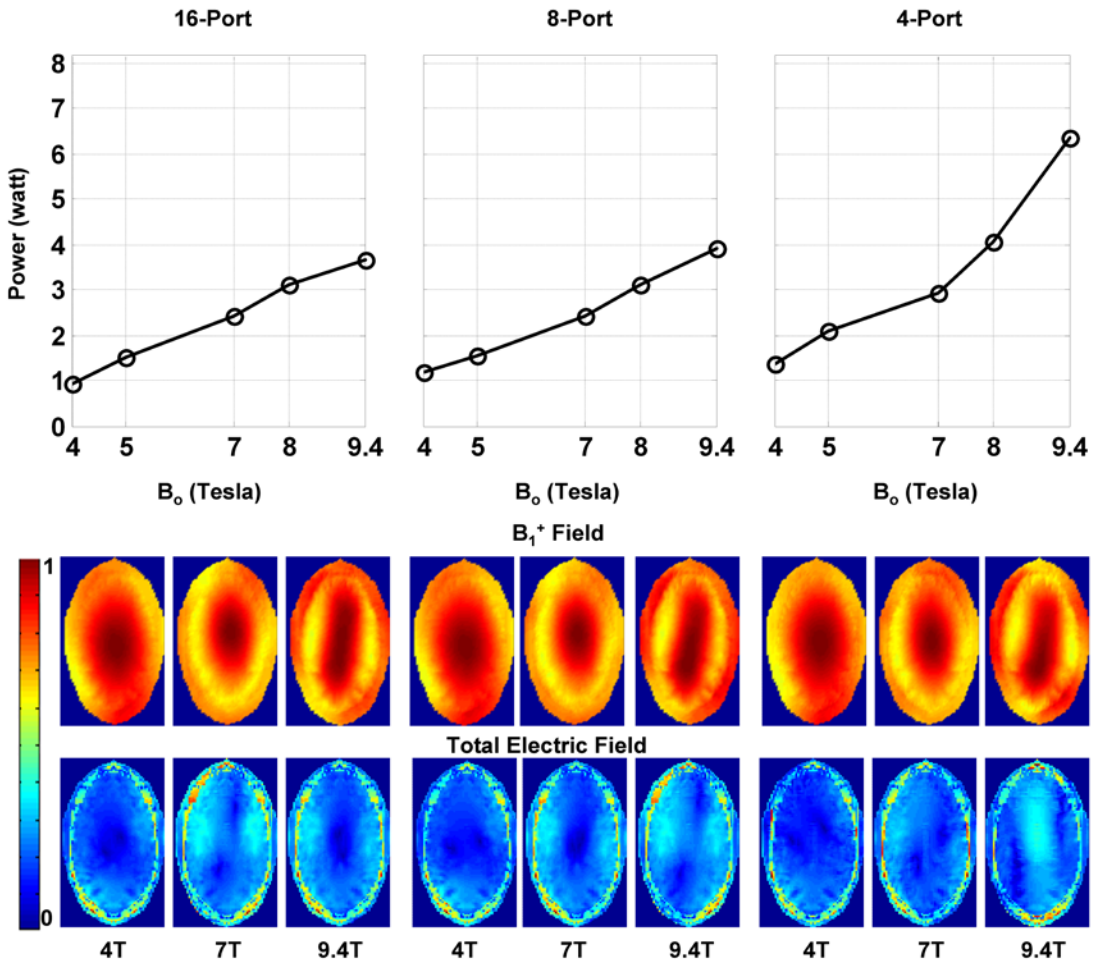


Figure 4.14 Top: Comparison of the power absorbed in the human head under 16-, 8-, and 4- port excitations. The results are presented for slice A3 (Figure 4.8). The values on each sub-plot correspond to the power required to achieve average (across slice A3) B_1^+ field intensity = 1.174 μT. The power values at all field strengths and under all the driving conditions are achieved for the same B_1^+ field homogeneity, i.e., *max/min* (defined in Figure 4.9) = 1.70. This value represents the

best possible homogeneity achieved using 4-port optimized phase/amplitude driving conditions at 9.4 tesla. Bottom (Color Scale): The corresponding B_1^+ field and total electric field distributions in slice A3 at 4, 7, and 9.4 with *max/min* = 1.70. All the results are presented for the coil configuration shown in Figure 4.8. Figure 4.14 was presented in [117].

Figure 4.14 also provides required RF power (watts) to achieve a value of 1.174 μT for the average B_1^+ field intensity in slice A3 as a function of B_0 field strength. It is clearly shown that the use of a fewer number of drive ports results in more power absorbed in the human head while maintaining

1) the same average B_1^+ field intensity,
2) the same homogeneity of the B_1^+ field distribution, and
3) interestingly for the shown slice, almost indistinguishable B_1^+ field distribution as well.

Similar to Figure 4.13 which displays the RF power requirements for FPA driving conditions, Figure 4.14 shows that the significant difference in power absorption comes under high B_0 field strengths and between 4-port and 8-port excitations; for the ***max/min*** of 1.70 and an average B_1^+ field intensity of 1.174 μT, a significant (2.3 watts CW) absorbed power difference is observed between 4-port and 8-port excitations at 9.4 tesla. The electric field distributions shown in Figure 4.14 clearly distinguish brightness in the center of the coil/load at 9.4 tesla and under 4-port excitation. This possibly explains the significant power increase under this condition

compared to the other 8 cases which experience relatively lower electric field intensities in the center of the coil/load[1].

By comparing the power requirements to achieve a ***max/min*** of 1.70 (Figure 4.14) to the corresponding results (Figure 4.13) under FPA driving conditions, it is clear that improvement in the homogeneity (as denoted by this particular criteria) of the B_1^+ field distribution with OPA driving conditions comes at the cost of more power absorption. For example, the 4-port OPA 9.4 tesla results show an approximately 50% increase in the power absorption compared to that obtained with 4-port FPA excitation. However, this power increase diminishes at lower B_0 field strengths. This can be attributed to the lower improvement in homogeneity of B_1^+ field distribution as demonstrated in the change of the ***max/min*** (Figure 4.11) obtained with FPA driving conditions to the ***max/min*** of 1.70 (most optimal only at 9.4 tesla).

While the results of this section were presented exclusively for slice A3, we observed similar patterns for the other axial slices shown in Figure 4.8. For example, Figure 4.15 describes the absorbed power values resulting from optimization on slice A1. With 16-port OPA excitation, Figure 4.9 results show that in order to attain an average B_1^+ field intensity of 1.174 μT, the absorbed power increases from 0.87 to 1.43 (watts) with ***max/min*** decreasing from 2.13 to 1.74 at 4 tesla, while the power increases from 3.13 to 7.81 with ***max/min*** decreasing from 21.94 to 1.74 at 9.4 tesla. Comparison between 4-port excitation under OPA and FPA driving conditions

[1] As the B_1^+ field represents only a component of the total magnetic flux density, similar B_1^+ field distributions will not necessarily produce similar electric field distributions.

reveals the same conclusions (Figure 4.15) As such, 1) reducing the number of drive ports and/or 2) improving the homogeneity (as denoted by this particular criteria) of the B_1^+ field distribution with OPA driving conditions results in increased power absorption. On the other hand, Figure 4.15 indicates that, at particular B_0 field strength, the absorbed power under 16-port OPA excitation is higher than that under 4-port OPA excitation. Clearly, the homogeneity of B_1^+ field distribution is much superior under 16-port (***max/min*** = 1.74) than under 4-port (***max/min*** = 3.03) OPA excitations. In this case, the resulting increase in power absorption due to improved homogeneity overcomes the decrease expected from increasing the number of drive ports from 4 to 16.

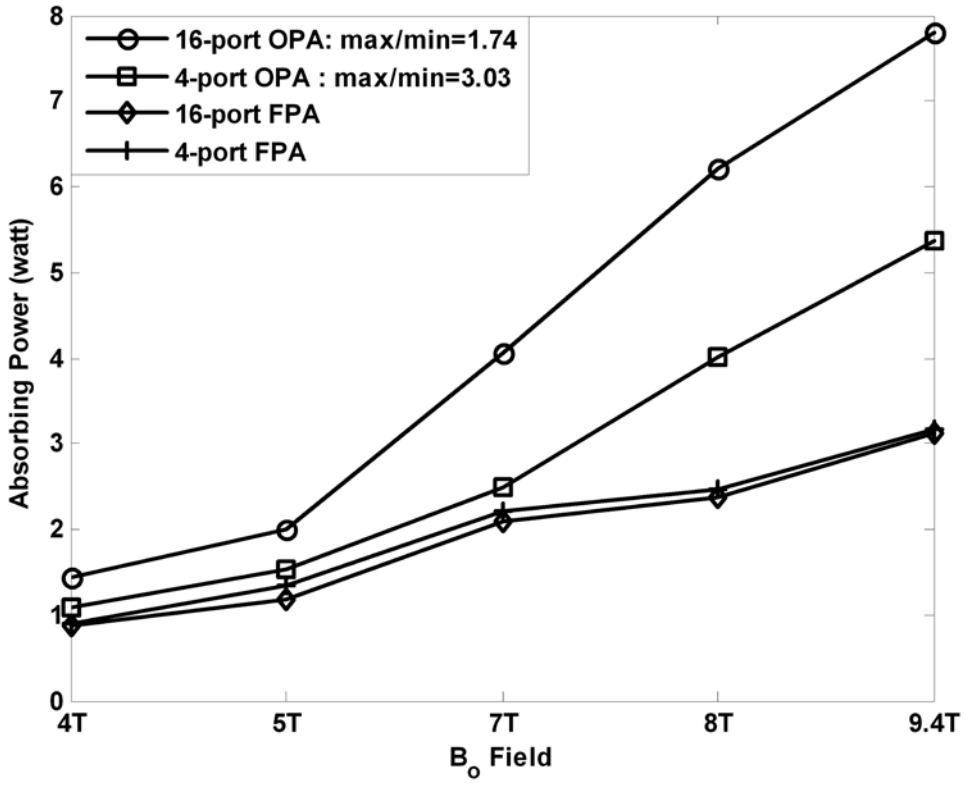


Figure 4.15 Plot of the required absorbed power in order to obtain an average (across slice A1 shown in Figure 4.8) B_1^+ field intensity = 1.174 μT under 16-, and 4-port fixed and optimized phase/amplitude driving conditions at different field strengths. The power values for the optimized phase/amplitude driving conditions are presented for the same homogeneity of the B_1^+ field distribution at all field strengths; i.e., *max/min* (defined in Figure 4.11) = 3.03 and 1.74 corresponding to the most optimized homogeneity at 9.4 tesla under 4-port Type C, and 16-port excitations, respectively. This figure was presented in [117].

(4) Dependence of Absorbed Power on B_0 Field Strength under Variable Phase/Amplitude Driving Conditions

Figure 4.16 provides plots describing the absorbed power required to achieve a fixed 1) average B_1^+ field intensity of 1.174 μT and 2) ***max/min*** (most optimized solution at 9.4 tesla) within each slice shown in Figure 4.8 as a function of B_0 field strength. The results are presented utilizing 16-port OPA excitation. Other possible

solutions (representing different B_1^+ field distributions yet possessing the same ***max/min***) are also provided in some of the plots. When comparing these power results to those obtained with FPA driving conditions (left column Figure 4.13), a noticeable difference can be observed in the characteristics of the relationship between absorbed RF power and B_0 field strength. In slice A1, similarly to FPA excitation, the absorbed power continuously increases as a function of B_0 field strength with 16-port OPA excitation. In the upper axial slices A2-A4 however, the absorbed power peaks at 8 tesla for slices A2 and A4 at 7 tesla for slice A3 and then decreases at greater than 8 (or 7) tesla field strength; it slightly rises again, however, at 9.4 tesla for slice A3. In this way, the nature of absorbed power dependence on B_0 field strength is similar for slice A4 under both 16-port FPA and OPA excitations. The power dependence observed for slices A2 and A3, however, is different from that obtained with 16-port FPA excitation. Therefore, by optimizing the homogeneity of the B_1^+ field distributions while attaining a fixed average B_1^+ field intensity within axial slices, the relationship describing the dependence of the absorbed power on B_0 field strength is somewhat constant: the power typically peaks at some B_0 field strength then decreases at higher values. It is fair to assume that under 16-port OPA excitation, the absorbed power required to obtain a fixed average B_1^+ field intensity in slice A1 will also peak at a B_0 field strength higher than 9.4 tesla and then decrease thereafter. Such assumption cannot be verified with this coil model as 9.4 tesla Larmor frequency represents its upper frequency limit.

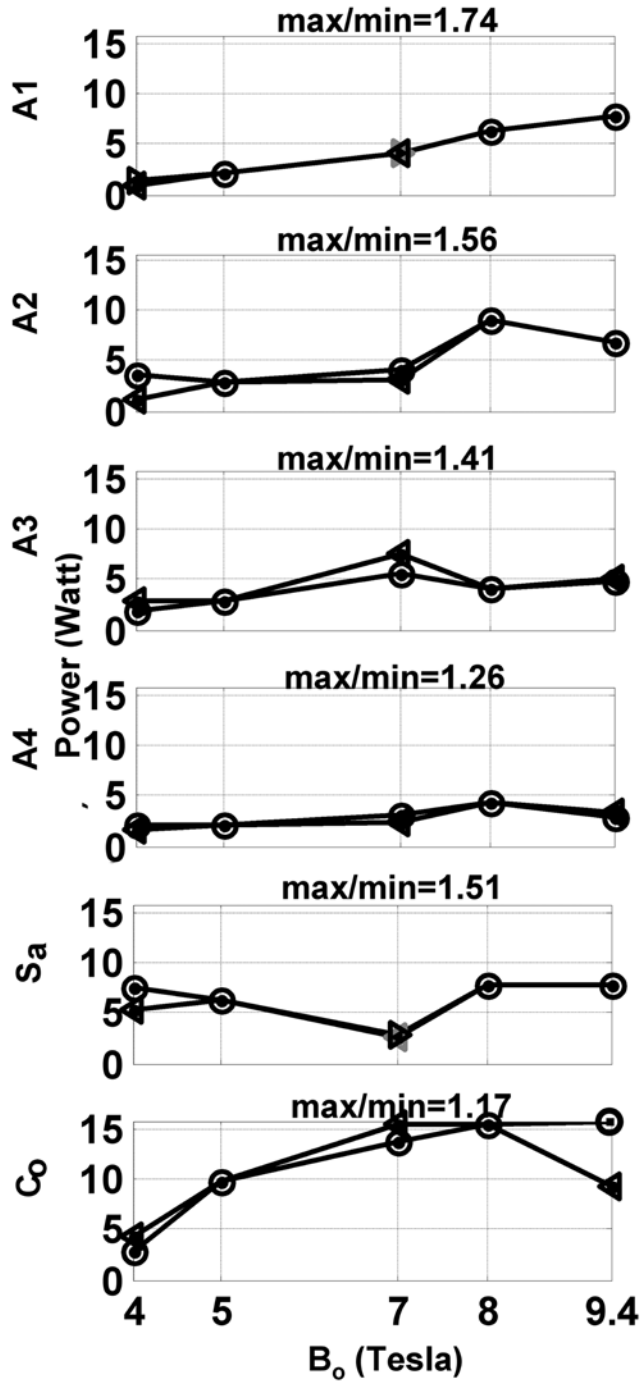


Figure 4.16 Plots of the absorbed power required in order to obtain a fixed (1.174 μT) average (over the area of each of the 6 slices shown in Figure 4.8) B_1^+ field intensity under different B_0 field strengths. The calculations are performed using 16-port optimized phase/amplitude driving conditions. From top to bottom, the 6 rows

correspond to the results for the 6 slices (orderly positioned as slices A1-4, Sa, and Co, respectively.) The number above each sub-figure corresponds to *max/min* (defined in Figure 4.11) for that slice. *max/min* was fixed (most optimized value at 9.4 tesla) at each field strength for each slice. At 4, 7, and 9.4 tesla, 2 solutions of the power calculations (represented by " ▷ " and "o") are presented for 2 different B_1^+ field distributions, yet have the same *max/min*. This figure was presented in [117].

As slices Sa and Co orient differently from axial slices, so does the relationship between the absorbed power and the B_0 field strength. Under 16-port OPA excitation, slice Sa shows that the dependence of the absorbed power on B_0 field strength functions somewhat in an oscillatory fashion. In slice Co for one of the solutions, the power peaks at 8 tesla then decreases at > 8 tesla field strength.

Figure 4.17 displays the ratios of the B_1^+ field intensities at the 5 points positioned in each of the 6 slices shown in Figure 4.8 at 9.4 tesla before (FPA) and after (OPA) optimization (B_1^+ shimming) using 16 ports. For the same absorbed power, as expected, the B_1^+ field intensities for the majority of displayed points (28 out of 30) decrease with OPA driving conditions. Furthermore, it is observed that the most significant decrease in the B_1^+ field intensity typically occurs at the center point of each slice (◊), which typically possesses the highest B_1^+ field intensity with FPA conditions (Figure 4.12). After optimization (shimming), however, within each slice the center point (◊) is typically characterized by a lower B_1^+ field intensity compared to the other four surrounding points. Therefore, OPA driving conditions usually result in significant defocusing of the B_1^+ field intensities within the central portion of the human head. This is clearly opposite to the typically observed [15, 28,

38, 150] field focusing effect that occurs in the central portion of the head with quadrature excitation or FPA driving conditions.

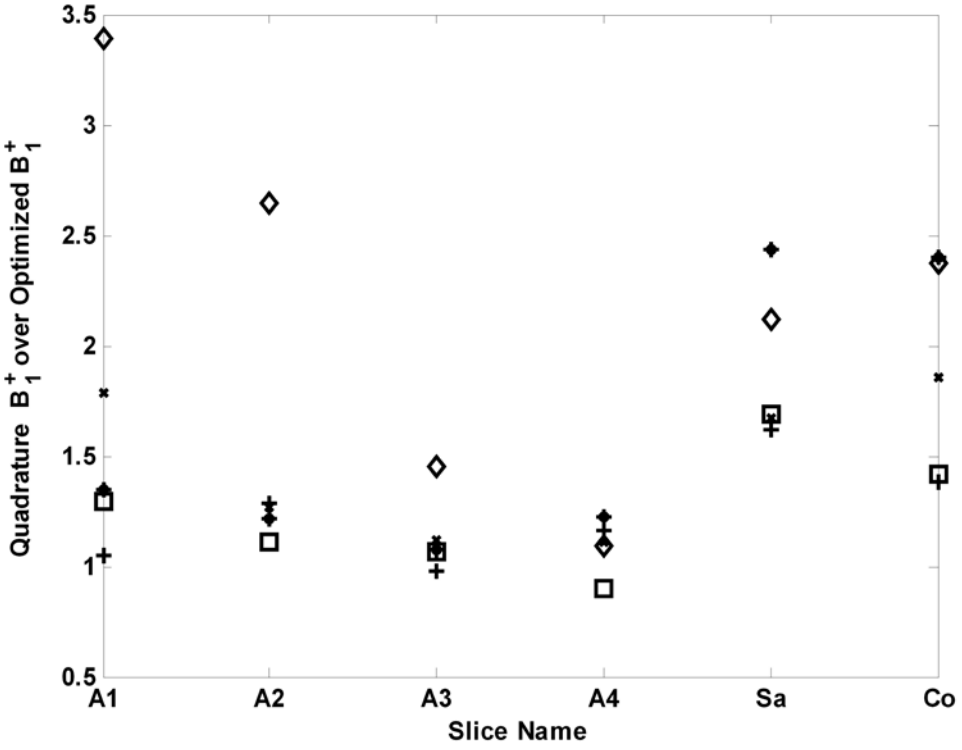


Figure 4.17 Plots of the ratios (before and after optimization at 9.4 tesla) of the B_1^+ field intensities at the 5 points positioned in each slice shown in Figure 4.8. All the B_1^+ field intensities were scaled to the same absorbed power. The symbols selection is the same as that used in Figure 4.8. Figure 4.17 was presented in [117].

4.4.3 Summary

The main difficulty in accurately describing a correlation between power requirements and operating frequency is due to the inhomogeneity of RF fields at high field strengths. As a result, there is an extreme ambiguity in obtaining well

defined relations in regards to this issue. In this section, using a rigorously applied FDTD scheme, we closely studied the RF power/frequency dependence up to 11.7 tesla on models of two coils and two loads: 1) a shielded single coaxial-element coil loaded with a cylindrical phantom and 2) a 16-strut TEM resonator loaded with an anatomically detailed human head mesh. Power relations for potential head imaging were presented by means of varying the amplitudes and phases of the exciting voltages in order to achieve highly homogenous B_1^+ field distributions with fixed/defined uniformity criteria at different B_0 field strengths up to 9.4 tesla.

As expected for small electrical loads, the results show that the RF power required in order to achieve a fixed average B_1^+ field intensity within the load is proportional to the square of the operating frequency, with deviations as frequency increases. This verifies predictions obtained using quasistatic approximations for electrically small loads (dimensions << the operating wavelength). When examining the results in the human head, however, the power dependence is considerably different. Using quadrature excitation (i.e., fixed amplitude and progressive integer multiples of phase shifts), it was clearly shown that the square dependence of the power on frequency vanishes to become 1) linear in axial slices towards the bottom of the brain or 2) peak-then-decrease in axial slices towards the top of the brain. The results also show that the use of more drive ports with this excitation mechanism results in reduction of the power requirements, most especially between 4 and 8 ports.

When utilizing optimized excitation, the nature of the power dependence is different than that with quadrature excitation. First, optimization of the homogeneity of the B_1^+ field distributions results in increased power requirements. On the other hand, the peak-then-decrease relation observed with the upper axial brain slices with quadrature excitation becomes more evident in the lower brain slices as well. The results clearly show that in order to achieve a highly homogenous B_1^+ field distribution with a specified criteria of homogeneity, the use of more drive ports, and therefore more phase-locked transmit channels, will significantly reduce the RF power required to achieve a fixed average B_1^+ field intensity. Several numerical studies were conducted and verified these findings.

While RF penetration plays a major role in the physics of the MRI RF power behavior at different field strengths, the coil-specific induced electromagnetic waves play a major role as well. For example, different results are to be expected between the TEM coils [133, 151] with their axially propagating [131, 152] electromagnetic waves and birdcage coils with their azimuthally propagating [153, 154] electromagnetic waves. In addition, it is essential to note that the presented conclusions are valid only for the ***max/min*** criterion for assessing the homogeneity of the B_1^+ field distributions. Different results are probable if using coefficient of variation (standard deviation) approaches [28, 112], which do not necessarily aim at minimizing ***max/min*** over the region of interest as was done in this section.

4.5 UHF MRI Homogenous B_1 Fields with Minimization of RF Power Deposition

From the previous discussions, optimization of the homogeneity of the B_1^+ field distributions results in increased power requirements. The B_1^+ shimming applied in power analysis needs to be improved to pursue a better homogeneity of the B_1 field and yet keep the RF power requirements within the Food and Drug Administration (FDA) and the International Electro-technical Commission (IEC) limits [155, 156]. To improve the homogeneity of the B_1^+ field, several theoretical and experimental techniques have been proposed. Variable phase and variable amplitude excitation or B_1^+ shimming has demonstrated theoretically using full wave electromagnetic methods [19, 20, 27-31] and experimentally [32-34] a good potential of achieving homogeneous B_1^+ field excitation. In recent work, Van den Berg et al. [114, 121] have demonstrated using electromagnetic simulations a theoretical improvement on the B_1^+ non-uniformity and SAR hotspot for imaging of the pelvis area of the human body model at 3 and 7 tesla using 12 idealized (unaffected by the load as will be considered in this chapter) TEM elements [122].

In this section, full wave electromagnetic technique, FDTD method, is used to provide an elaborate simulation of the coil-head system using a rigorous model of a highly-coupled TEM coil that operates as a transmit array. The analysis is presented for a wide variety of regions that vary in dimension, orientation, and geometry in the human head.

4.5.1 FDTD Modeling of the Transmit Array

The 16-strut TEM resonator (Figure 4.2) and the anatomically detailed human head used in section *4.3* were applied to improve B_1^+ shimming, where both the RF coil and the load were modeled as a single system [22, 39] in the calculations of the electric and magnetic fields and therefore also of the power requirements and SAR. In such a modeling approach, the electromagnetic effects on the load due to the coil and on the coil due to the load are interdependent. Same as section *4.3*, the coil-head system has the resolution of 2 mm × 2 mm × 2 mm.

Following the work in section *4.3*, the mathematical model of the coil was tuned while loaded with the human head mesh for each individual element. To capture the coil's response, the coil-head mesh system was excited with a voltage source with a bandwidth spanning from 200 MHz to 500 MHz which includes both frequencies of interest: 300 MHz and 400 MHz. To tune the coil, the gap between each pair of TEM inner rods was adjusted until the TEM resonator was resonant at the desired frequencies of operation. The FDTD simulations, after tuning, result in 16 sets of individual electric and magnetic field distributions (both phase and amplitude) at the abovementioned frequencies.

4.5.2 Power Calculation and B_1^+ Shimming

Power absorbed in the load is calculated as the summation of the power deposition on the whole volume of the head model by Equation (4.3), and SAR calculation is shown in Equation (4.4). In this section, the power absorbed in

different cases is scaled to obtain a mean[2], in ROI, B_1^+ field intensity of 1.957 μT which is the B_1^+ field strength required to produce a flip angle of π/2 with a 3-msec rectangular RF pulse.

With the superposition of the fields produced by the 16 phased array TEM elements, the B_1^+ field in the ROI is optimized to be homogenous by varying the amplitude and phase of every drive port/coil element (B_1^+ shimming) [29, 34, 114, 116, 121, 123, 157, 158]. Under the typical quadrature excitation [159], the characteristics of the excitation pulses possessed the same amplitudes and integer multiples of 2π/ (# of excitation ports = 16) phase shifts. According to previous work [31], B_1^+ uniformity improvement at many instances results in decreased mean and/or peak B_1^+ field strength in ROI. In this section, the total RF power absorption by the whole head model was constrained and included as a part of the B_1^+ shimming mechanism not to exceed the value obtained under quadrature excitation while still providing maximum B_1^+ uniformity.

The optimization algorithm also called B_1^+ shimming scheme is based on a combination of gradient-based and genetic algorithm functions. Starting from quadrature excitation condition, the COV of the B_1^+ field distribution within the ROI and the total absorbed power are calculated. The optimization function aims to decrease COV to its minimum value while constraining the RF power below the initial value (quadrature excitation condition) through adjusting the 31 variables (16 amplitudes and 15 phase shifts of the B_1^+ fields and of the electric fields induced by the transmit array elements). The

[2]The results demonstrate that the homogeneity of the B_1^+ field is excellent in all of the selected ROIs after performing B_1^+shimming.

total RF power absorption (over the whole head) and the homogeneity of the B_1^+ field distributions of the ROIs (nine 3cm-thick slabs and three 6cm-thick slabs oriented in axial, sagittal, and coronal directions, the whole-brain, and the whole-head as described in Table 4.3) have to be calculated in each iteration.

4.5.3 Experimental Verification

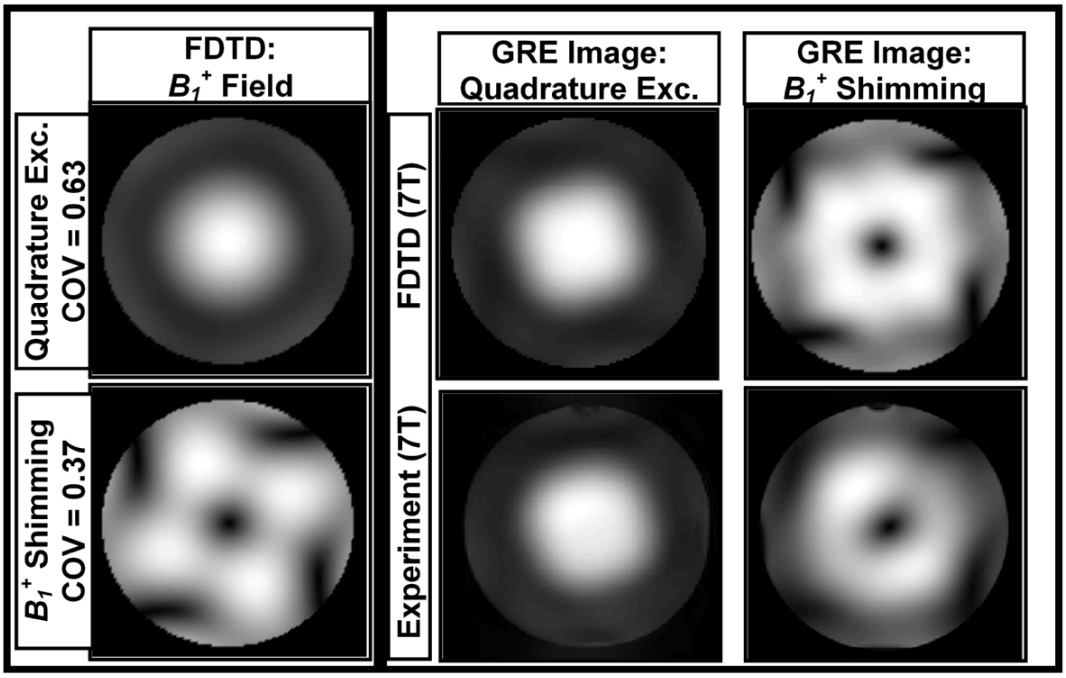
To demonstrate the validity and the future-implementation potential of our RF modeling technique which is capable of RF power minimization simultaneously with B_1^+ field homogenization using highly-coupled transmit arrays, B_1^+ shimming without B_1^+ measurements must be performed. In such scenario, the tuning/excitation/reception of the transmit array is fully based on our RF modeling scheme without implementing B_1^+ measurements or decoupling/matching circuits. A comparable 8-element highly-coupled (minimum of -10dB coupling between the transmit ports) TEM coil design was modeled, built, and tested in a transmit array mode. In the 8-strut TEM coil (outer and inner diameter is 13.5in/10in, length is 7in, half-wavelength semi-rigid coaxial transmission line connected to each excitation/reception port), 4 elements (alternate ones) were used as transmitting and receiving channels. The transmit array was tested with a head-sized spherical phantom (17.5-cm in diameter) filled with brain-like constitutive properties on a 7 tesla human MRI scanner. The electromagnetic properties of the phantom are: conductivity = 0.46s/m and dielectric constant = 80. In essence, the choice of the phantom/load does not affect the accuracy of our RF modeling, i.e. for full-wave computational electromagnetic software that utilize FDTD or FEM (finite element

method), the effectiveness of MRI RF modeling scheme is not measured by how accurately the load is modeled. The true test of the effectiveness of MRI RF modeling is accounting for the RF coupling between the transmit array elements while the head coil is loaded with a head-sized dielectric/conductive load.

B_1^+ shimming was performed with a 7 tesla system equipped with a multi-transmit array system (*Siemens Medical Solutions*, Erlangen, Germany). Using the shimming scheme described in the previous section, the B_1^+ field distribution was optimized to achieve the lowest COV across a 5-mm axial slice while maintaining or lowering the total power absorption by the phantom. Prior to the 7 tesla experiment, FDTD calculations were performed in order to attain the intended amplitudes and phases of the excitation voltages. The calculated values of amplitudes and phases were applied directly to excite the coil elements in the 7 tesla experiment. Figure 4.18 shows a picture of the loaded coil and a very good agreement between the FDTD calculations and the experimental images. The experimental images shown in Figure 4.18 were obtained without B_1^+ measurements and were fully based on the FDTD simulations. Comparing to quadrature excitation, the presented results show that the B_1^+ shimming scheme can lower COV by approximately 59% while consuming only 94% of the total RF power absorbed during quadrature excitation.



(a)



(b)

Figure 4.18 (a) Picture of the highly-coupled 8-element TEM resonator loaded with a spherical phantom filled with brain-like constitutive properties; (b) B_1^+ field distribution and GRE images FDTD-calculated under quadrature and B_1^+ shimming (optimized for minimization of 1) the coefficient of variation of B_1^+ field distribution and 2) total RF power absorption by the phantom) excitation and the corresponding

experimental images obtained using 7 tesla whole-body scanner equipped with a multi-transmit array. The images were obtained using 4-port excitation/reception. The phases and amplitudes of the excitation pulses, and parameters for the coil tuning and matching were fully obtained and directly implemented from the rigorous FDTD modeling and without any B_1^+/ B_1^- (transmit/receive) measurements. The picture (a) is provided by Dr. Tamer Ibrahim at the ultra high field lab in University of Pittsburgh; images (b) was presented in [120].

4.5.4 Results and Discussion

4.5.4.1 Analysis of the B_1^+ Field Distribution

For the human head model, the B_1^+ field distribution was analyzed under quadrature excitation and using B_1^+ shimming. Optimization of the B_1^+ field distribution homogeneity was performed at 7 tesla and 9.4 tesla in 3D regions over the whole head, brain, and twelve slab regions labeled from "***A***" to "***N***" as shown in Table 4.3 and Figure 4.19. Figure 4.19 shows the normalized B_1^+ field distribution through these fourteen regions using quadrature excitation and B_1^+ shimming. The values presented in the corner of each subfigure represent the COV of the B_1^+ field distribution and the total RF power absorbed (by the whole head) scaled to obtain 1.957 μT. Figure 4.19 demonstrates that homogeneity of the B_1^+ field distribution can be significantly improved while minimally reducing the RF power absorbed by the head, compared to quadrature excitation. The results demonstrate that the maximum improvement of B_1^+ field distribution occurred over

1) posterior 3-cm coronal slab "***F***" where the COV of the B_1^+ field distribution improved by 4.26 folds while consuming only 89.1% of the total RF power absorbed during quadrature excitation at 7 tesla and

2) left 3-cm sagittal slab "***I***" where the COV of the B_1^+ field distribution improved by 5.71 folds while consuming 98.9% RF power absorbed under quadrature excitation at 9.4 tesla.

When B_1^+ shimming was applied to large 3D regions such as the whole head compared to quadrature excitation, the COV of the B_1^+ field distribution was improved by 43.7% with 98.9% power consumption at 7 tesla and 34.6% with 99.5% power absorption at 9.4 tesla, respectively.

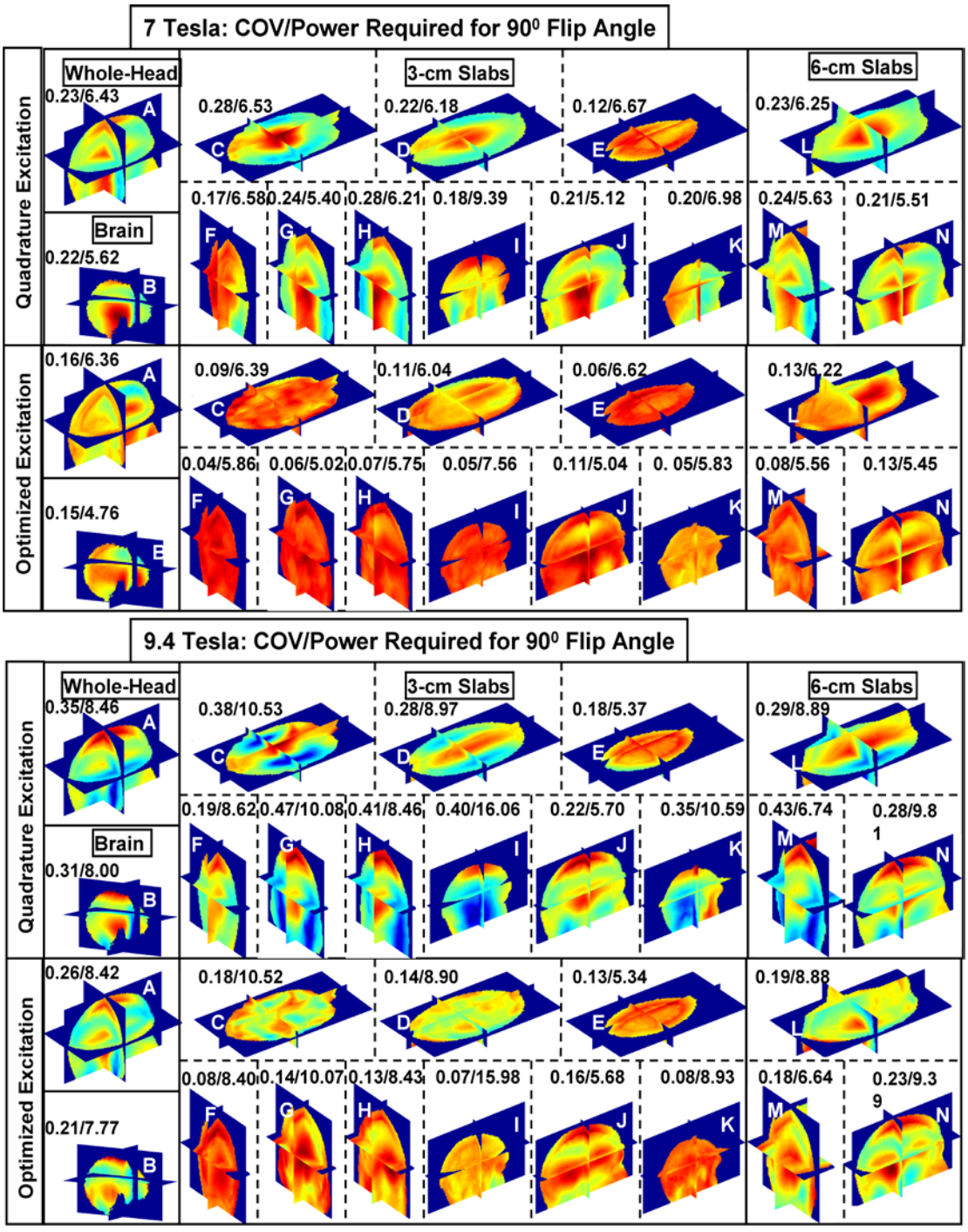


Figure 4.19 Normalized B_1^+ field distributions calculated using the FDTD model at 7 tesla and 9.4 tesla. The 14 subfigures represent the distributions for whole head, brain, 3-cm slabs and 6-cm slabs (all labeled in Table 4.3) under 16-port, quadrature and optimized (B_1+ shimming) excitations. The results are presented for an 18-

tissue human head model numerically loaded in a 16-element TEM coil (numerically tuned to approximately 300 MHz and 400MHz) and operating as a transmit array. The homogeneity of B_1^+ field distribution in each region of interest was optimized in order to achieve minimum coefficient of variance while maintaining or reducing the total (over the whole head) RF power deposition (obtained with quadrature excitation.) The letter on each subfigure represents the label of the optimized region of interest as shown in Table 4.3. The numbers above each subfigure represent the values of the Coefficient of Variance/Absorbed Power, where the absorbed power in each case is scaled to achieve a mean B_1^+ field intensity of 1.957 μT in the volume of any ROI.

Label	Orientation	Thickness	Region
A	N/A	N/A	Whole Head
B	N/A	N/A	Brain
C	Inferior	3cm	Axial Slab
D	Middle	3cm	Axial Slab
E	Superior	3cm	Axial Slab
F	Posterior	3cm	Coronal Slab
G	Middle	3cm	Coronal Slab
H	Anterior	3cm	Coronal Slab
I	Left (seen from the back)	3cm	Sagittal Slab
J	Middle	3cm	Sagittal Slab
K	Right (seen from the back)	3cm	Sagittal Slab
L	Middle	6cm	Axial Slab
M	Middle	6cm	Coronal Slab
N	Middle	6cm	Sagittal Slab

Table 4.3 Labels of the optimized regions of interest shown in Figures 4.19-4.23. The columns represent the orientations, thicknesses, and directions of the 3D regions

(labeled A through N) over which the homogeneity of B_1^+ field distribution was optimized to achieve minimal coefficient of variation while maintaining total (over the whole head) RF power deposition less than or equal to that obtained with quadrature excitation.

4.5.4.2 Power Distribution Analysis

Manipulating the B_1^+ field distribution affects electric field inside the human head and the total power absorption as a result. From Figure 4.19, homogenizing the B_1^+ field distribution (as measured by COV) in a wide variety of ROIs can always be achieved with lower total RF power absorption than it is under quadrature excitation. Figure 4.20 shows the changes of RF power absorption within the 13 specified ROIs (excluding the whole human head shown in Table 4.3) and within 3 other regions that represent the average power absorption over the volume of the combined 4 axial ("***Ax***"), 4 coronal ("***Co***"), or 4 sagittal ("***Sa***") slabs presented in Table 4.3. The black bars show the absorbed power (watts) under quadrature excitation condition by each ROI; the gray bars represent the power absorption after B_1^+ shimming. At 7 tesla, the RF power absorbed by ROIs "***B, H, I, J, N***", and "***Sa***" decrease with B_1^+ shimming when compared to quadrature excitation, while the RF absorbed power in other ROIs increases although the total RF power absorption by the whole head is still lower than that achieved with quadrature excitation. At 9.4 tesla, the power absorption decreases in ROIs "***E, H, I, J, K***" and "***Sa***" while increasing in the remaining ROIs; still the total RF power absorption by the whole head is lower than that achieved with quadrature excitation for all the ROIs.

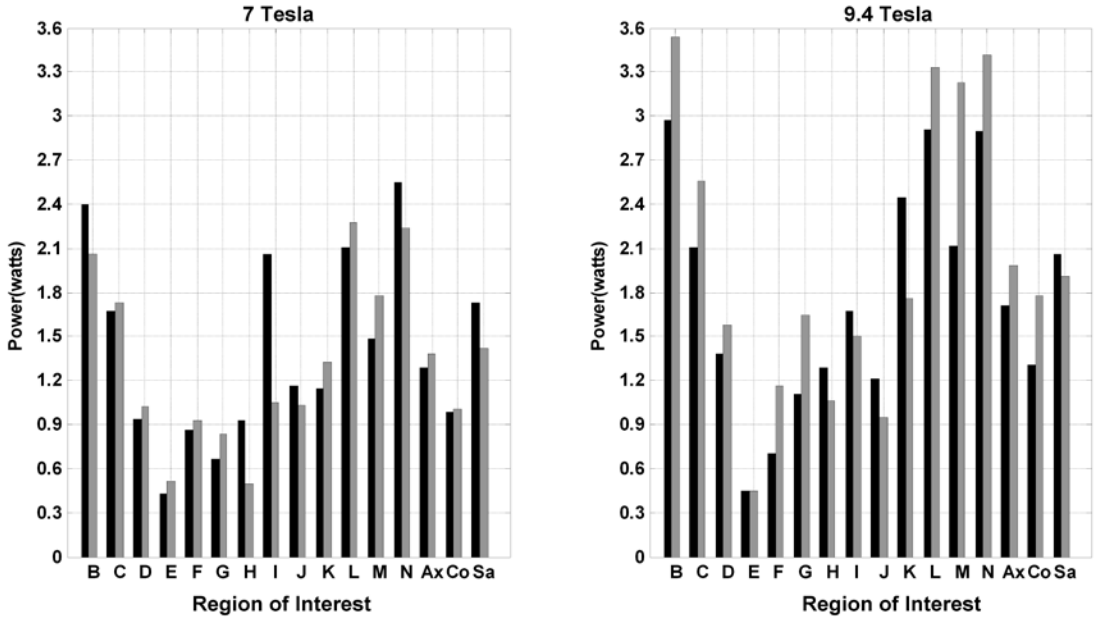


Figure 4.20 Comparisons of the RF power absorption in each ROI shown in Table 4.3 and Figure 4.19 at 7 tesla and 9.4 tesla. The ROIs are shown in *x* axis and "Ax", and "Co", "Sa" represent the averaged absorbed power within grouping of the four slabs (three 3-cm thickness slabs and one 6-cm thickness slab) along axial, coronal, sagittal directions, respectively. The numbers on the y axis represent the total RF power absorption in each labeled region which produces a mean B_1^+ field intensity of 1.957μT in that same region. The black bars represent the RF absorbed power (Watts) under quadrature excitation and the gray bars represent the RF power absorption with B_1^+ shimming.

The results demonstrate that homogeneity of the B_1^+ field distribution can be improved in an ROI with reduction of the RF power absorption in the same ROI. This clearly indicates that the B_1^+ shimming scheme is capable of re-polarizing the transverse magnetic field in the ROI to the MRI necessary polarization (circular). In other words, B_1^+ shimming reverses the relative electric field constructive- and B_1^+ field destructive- interferences caused by multi-port quadrature excitation to relative electric field destructive- and B_1^+ field constructive- interferences [160, 161]. The

opposite also holds true if the total RF absorption in an ROI increases as a result of performing B_1^+ shimming. In addition, the changes of the regional power absorption with B_1^+ shimming do not follow the same patterns at 7 and 9.4 tesla. At ultra high field imaging, both the electric and B_1^+ fields are highly inhomogeneous. Using our shimming routine, it is possible for two sets of the amplitudes and phases to render the same level of homogeneity, i.e. different magnetic field distributions might result in the same COV values across the ROI even at the same frequency [31]. As the electric field distribution also varies with the amplitudes and phases of the voltages exciting the transmit array, the RF power absorption in an ROI can significantly vary even for a homogenous B_1^+ field in an ROI.

4.5.4.3 SAR Analysis

Using Equation (4.4), SAR is calculated under both quadrature excitation and B_1^+ shimming excitations. The influence on SAR by B_1^+ field optimization simultaneously with total RF power minimization is investigated by evaluating the SAR peak values, the SAR COV values, and SAR distribution within the whole head model. FDA regulates SAR in any 1gm of tissue and IEC does the same in any 10gm of tissue. The data in this section are presented for the IEC regulation.

The SAR peak values and distributions throughout the whole head volume are compared under the quadrature excitation and B_1^+ shimming excitations. Figure 4.21 shows the locations of SAR peaks and Figure 4.22 shows 1) the SAR peak values (over the whole head) that occur when a mean B_1^+ field intensity equals to 1.957 μT is in achieved in ROI and 2) the COV of SAR distributions (over the whole head)

obtained at 7 and 9.4 tesla. Figure 4.23 shows SAR distributions over the head model under quadrature excitation (labeled as "X") and under optimized excitation (B_1^+ shimming) (labeled as "A" to "N" as shown in Table 4.3). Several observations are depicted from these results.

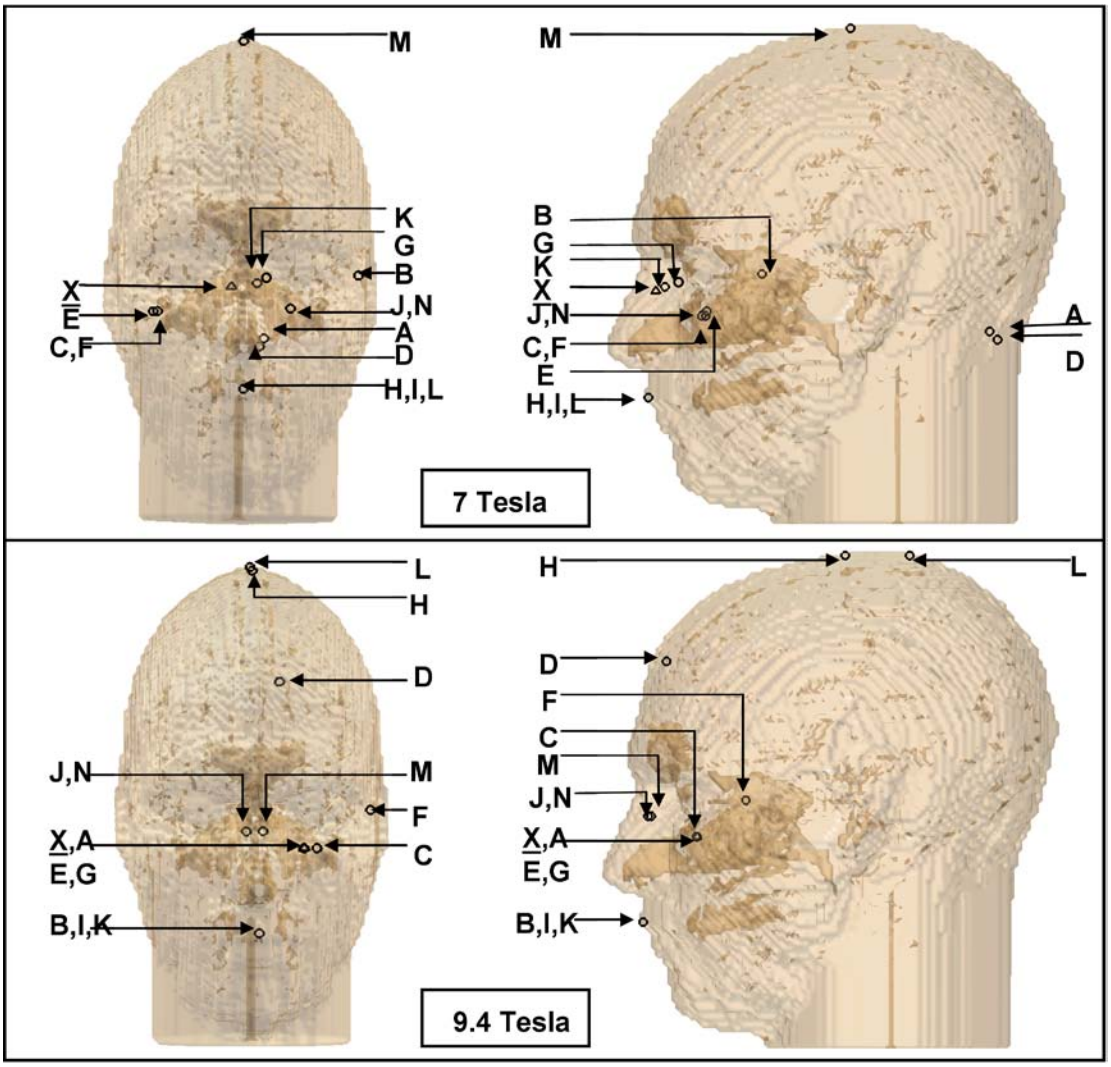


Figure 4.21 Locations of the SAR peaks under quadrature excitation (labeled as "X") and under B_1^+ shimming (labeled as "A" to "N" as shown in Table 4.3); the front view and side view of the 3D head model are shown to visualize each location's relative coordinates.

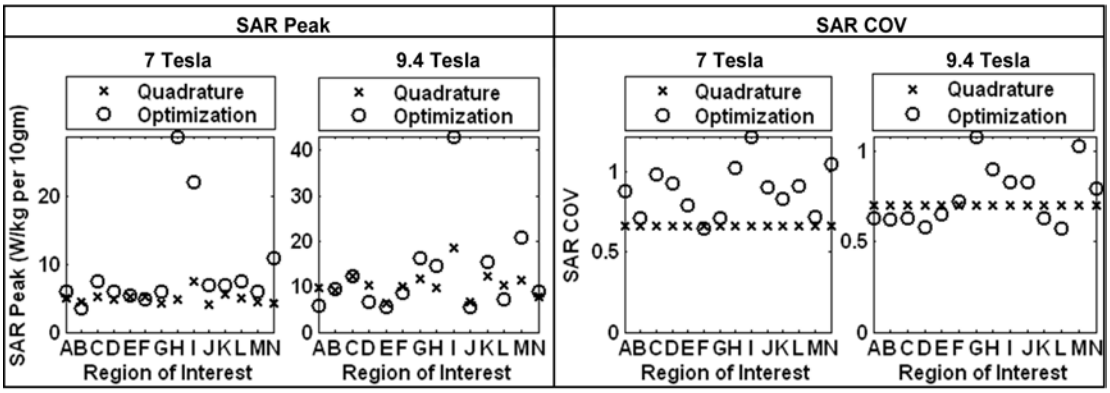


Figure 4.22 SAR peak values (over the whole-head) and the SAR distribution COV values (over the whole-head) under quadrature excitation (labeled as "X") and under optimized excitation (B_1^+ shimming) labeled as "O". The labels for the ROIs on the *x* axis are defined in Table 4.3, and the values on the y axis represent the SAR peaks averaged for every 10 gram tissue (Watts/kilogram per 10gm) or the SAR distribution COV.

1) Figure 4.21 shows that all the SAR peak values occur in tissue near outside air and/or air cavities (nasal, mouth, etc..) namely front, top, and back of the head at both 7 tesla and 9.4 tesla under both quadrature excitation and B_1^+ shimming. The results also show redundancy of the locations of the SAR peak values under B_1^+ shimming with different ROIs. At 7 tesla, B_1^+ shimming targeted for groups ("***C***" and "***F***"), ("***J***" and "***N***"), and ("***H***", "***I***", and "***L***") exhibited identical locations for the SAR peak values. The same is also observed for groups ("***J***" and "***N***"), ("***X***" and "***A***"), ("***E***" and "***G***"), and ("***B***", "***J***", and "***K***") at 9.4 tesla. The interpretation of these observations is cumbersome. On one hand, these results can demonstrate that the SAR peak values (and not overall distributions) are frequently dominated by properties related to the tissue such as location (proximity to air) and geometry more

than the characteristics of the excitation itself. On the other hand, SAR calculations using FDTD possess inherent localized inaccuracies near tissue interfaces in general and near air-tissue interfaces in particular, as the 2nd order accuracy no longer exists [36]. Nonetheless, compared to that obtained in the periphery of the human head model and away from the localized regions near the peak SAR values, the SAR distribution as shown in Figure 4.23 generally (majority of the B_1^+ shimming cases) demonstrates higher intensities in the center of coupled coil/head model.

2) Compared to quadrature excitation, the most increase in the SAR peak values occur in peripheral sagittal/axial slices (region "**H**" for 7 tesla and region "**I**" for 9.4 tesla).

3) Homogenizing the distribution of B_1^+ field in specific regions can lead significant inhomogeneity in the SAR distribution across the human head.

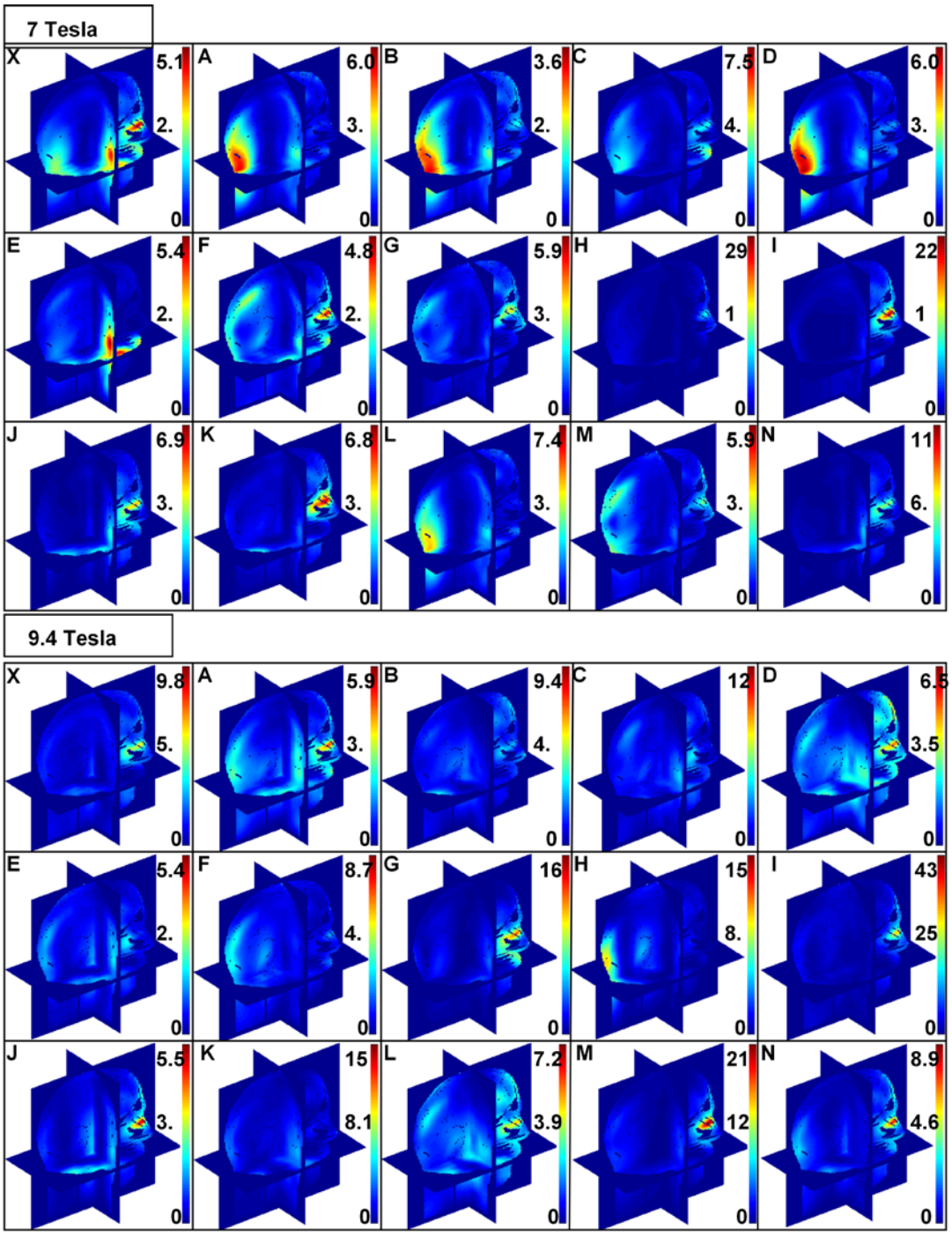


Figure 4.23 SAR distributions at 7 tesla and 9.4 tesla. The 15 subfigures at each of B_0 field strength represent the SAR distributions under quadrature excitation (labeled as "X") and under optimized excitation (B_1^+ shimming) (labeled as "A" to "N" as shown in Table 4.3). The color bar used in each subfigure is set between zero and the peak SAR value obtained under each excitation condition.

4.5.5 Summary

In this section, an in-house finite difference time domain MRI RF modeling package combined with B_1^+ shimming scheme is demonstrated numerically at 7 and 9.4 tesla. The presented numerical results show that the homogeneity of the B_1^+ field distribution can be improved in 14 regions across the volume of the human head model while constraining the total RF power absorbed by the human head. The selection of the 14 regions covers various volumes in different orientations throughout the volume of the whole head model. While maintaining the same or lower RF power absorption, the results demonstrate that the B_1^+ field distribution could be significantly improved when compared to the standard quadrature excitation. The results also show that in many regions across the volume of the human head, the proposed B_1^+ shimming scheme is capable of re-polarizing the transverse magnetic field to the MRI necessary polarization (circular).

4.6 B_1^+ Shimming with Constrained RF Power Deposition and Local SAR Peaks

The work in section *4.4* shows that homogeneity of the B_1^+ field distribution in the ROI can be improved with constrained RF power absorbed by the human head. However, the local SARs are not considered during the B_1^+ shimming, i.e. local SAR peaks might be elevated after B_1^+ shimming although the average global SAR is suppressed, as shown in Figure 4.23. The electrical fields in ultra high field MRI are highly inhomogeneous, and the increased SAR peaks produce local “heating spots”

even with a moderate averaged SAR. The B_1^+ shimming scheme introduced in section *4.4* must be improved with the constraints not only for the total power absorption but also for the local peak SARs in safety considerations. In this section, we apply a 7 tesla MRI whole-body RF excitation scheme [162] on a 40-tissue anatomically detailed VHP body model to study an improved B_1^+ shimming technique with both constrained RF power deposition and local SAR peaks.

4.6.1 Improved B_1^+ Shimming Scheme

The 32-strut TEM coil loaded with the VHP body model (from knees to the head) [112, 162] is shown in Figure 4.3. Detailed geometry of the coil-body system and the coil tuning are described in section *4.1*; RF power and SAR calculations of the VHP body model are introduced in section *4.2*, where SARs in this section are averaged for every 10 grams of human tissues [163]. Due to the of SAR safety regulatory between the extremities and non-extremities, the improved B_1^+ shimming calculations (including homogeneity optimization of the excitation field, the power absorption and the SAR peak) are performed in "with the arms" (whole body) and "without the arms" (torso only) two cases. Note that the arms are always present in the coil during the field calculations. In both cases, the absorbed power (watts) is scaled to obtain a mean B_1^+ field intensity of 1.957 μT, which is the field strength needed to produce a flip angle of $\pi/2$ with a 3-msec rectangular RF pulse.

Compared to the human head model, the VHP body model is electrically larger in ultra high field MRI, therefore, the quadrature excitation used in the head model calculations does not present the circularly polarized feature in the body-coil system.

Instead of a uniform amplitude and a constant phase shift in the excitation elements used in the head model (section *4.3* and *4.4*), the quadrature excitation applied in the body model here (section *4.5*) is defined such that each excitation element provides an equal contribution to the total power absorption in the whole body model from the 32-strut TEM RF coil. The improved B_1^+ shimming scheme is based on a genetic and gradient optimization algorithm [29, 34, 114, 116, 121, 123, 157, 158] as introduced in previous sections. The first generation (input) is composed of total 64 variables including the amplitudes and phases from the 32 excitation elements under quadrature condition. Optimization is performed to pursue a homogeneous field distribution of the superposition of the B_1^+ field from all the TEM elements with the constrained total power absorption and local peak SARs. The new generation (output) with 64 members composes the amplitudes and phases under the B_1^+ shimming excitation condition, where the COV of the B_1^+ field distribution is decreased to the lowest possible value, and the total power depositions in the whole body model and the maximum SAR in the model are limited to be less than or equal to the corresponding values of the first generation (quadrature excitation). By adding the total power and local SAR constrains to the B_1^+ shimming scheme, consumption of the computation time increases because the superposition of the B_1^+ field in ROIs, the total power absorption and the three dimensional SAR distributions over the whole body model have to be calculated within each iteration of the algorithm.

The ROIs in this section include five 6mm-thickness (unit-cell thick) slices and five 84mm-thickness (16-cell thick) slabs of the VHP human body model, as well as the heart and the pancreas organs (Figure 4.25).

4.6.2 Validation of the Optimization Method

To show the validity of the improved B_1^+ shimming scheme, experiments are performed on the comparable 8-element highly-coupled TEM coil described in section *4.4.3*. As with the previous experiments, four elements are used as transmitting and receiving channels in the 8-strut TEM coil. Using the same spherical phantom, the improved B_1^+ shimming optimization was applied to increase the B_1^+ field strength in the ROI with minimization of the local SARs and global power absorption on the phantom. The ROI is a cylindrical volume with 2.22 cm in radius and 2.54 cm in height. Prior to 7 tesla experiment, the TEM coil and the phantom were modeled to calculate the electromagnetic field in the system using the full-wave FDTD method. The improved shimming algorithm was applied to attain the optimized excitation condition. The calculated amplitudes and phases of the excitation voltages were used directly to excite the four coil elements of the multi-transmit array system in 7 tesla experiment.

Figure 4.24 shows the comparison of the outputs from the simulations and the images from the experiments: with a very good match with the experiments, the increased B_1^+ field intensity in the three dimensional ROI can be obtained with successful minimization of 1) local SARs, 2) global SARs, and 3) the variation in the flip angle (B_1^+)

distribution inside the ROI using the proposed shimming scheme. The result demonstrates an excellent control over the magnetic field and SARs without B_1 measurement. In Figure 4.24, 4.5 μT represents the maximum B_1^+ intensity inside the selected cylindrical regions. The MRI images in the right column are the B_1^+ field distribution of the two dimensional slices through the regions of interest. Applying the improved B_1^+ shimming, it is shown that the mean B_1^+ intensity in ROI is improved by more than 5 folds over 4-port quadrature excitation. The local SAR is instantaneously below the FDA local SAR limit for the human head (8watts/kg per 1gm) and the averaged SAR (associated with 8 watts/kg per 1gm local SAR) is 2 watts/kg in the experiments. The agreement between the experimental image and simulation output shown in the Figure 4.24 validates both the FDTD modeling method and B_1^+ shimming algorithm.

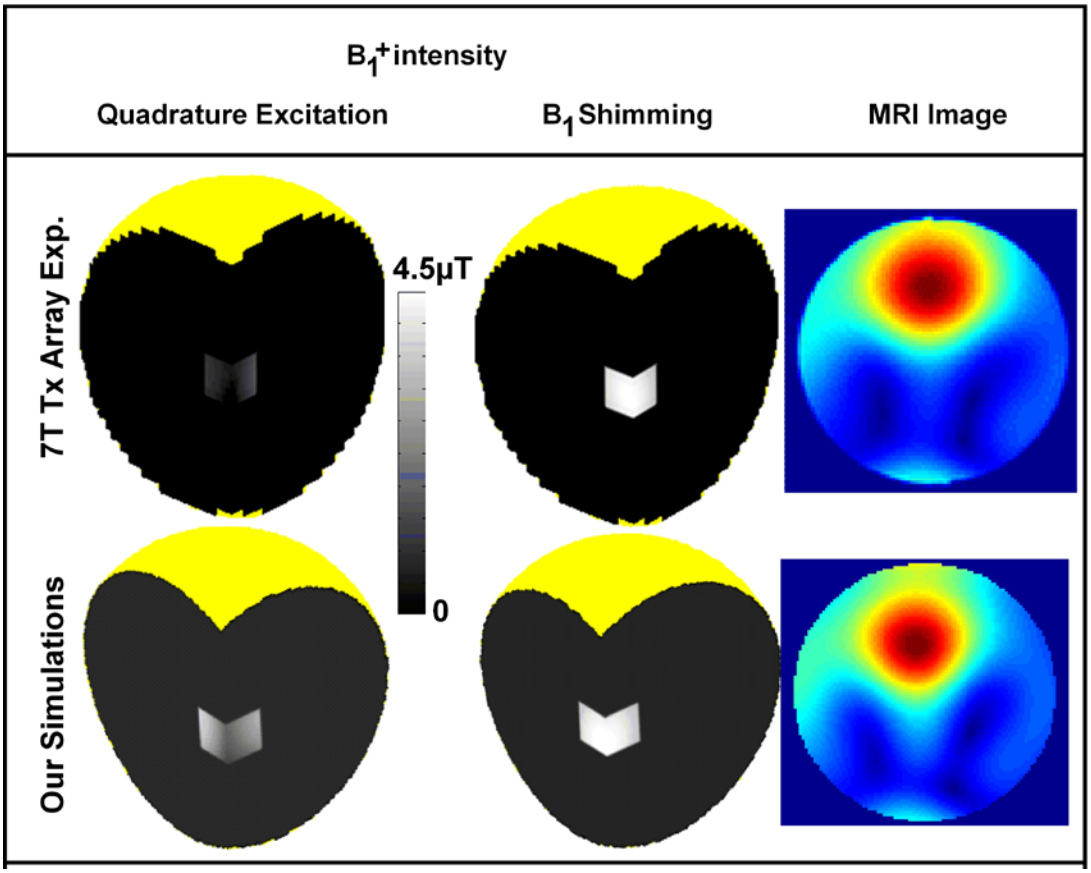


Figure 4.24 7 tesla focused and homogeneous 3D shimming without B_1 measurements with successful minimization of 1) local SARs, 2) global SARs, and 3) the variation in the flip angle (B_1^+) distribution inside the ROI.

4.6.3 Results and Discussion

4.6.3.1 Analysis of the B_1^+ Field Distribution

The B_1^+ field is calculated under the quadrature and B_1^+ shimming excitation conditions in two cases: "with arms" and "without arms". Figure 4.25 shows the homogeneity improvement inside the five slices and five slabs of interest, as well as the heart and pancreas organs. In each subfigure, the B_1^+ field is normalized to its maximum value and the number underneath is COV of the B_1^+ field distribution

across each region under corresponding excitation condition. The improved shimming is designed to homogenize the B_1^+ field distributions while the total power absorption and peak SARs are constrained to be less than the corresponding values under quadrature excitation. Figure 4.25 demonstrates that the homogeneity of the B_1^+ field in the two dimensional slices and the three dimensional slabs/organs could be greatly improved with constrained power absorption and local peak SARs using the improved B_1^+ shimming scheme. For example, COV of the B_1^+ field distribution in the heart organ reduces from 0.31 under quadrature condition down to 0.06 with the shimming excitation in the “with arms” case.

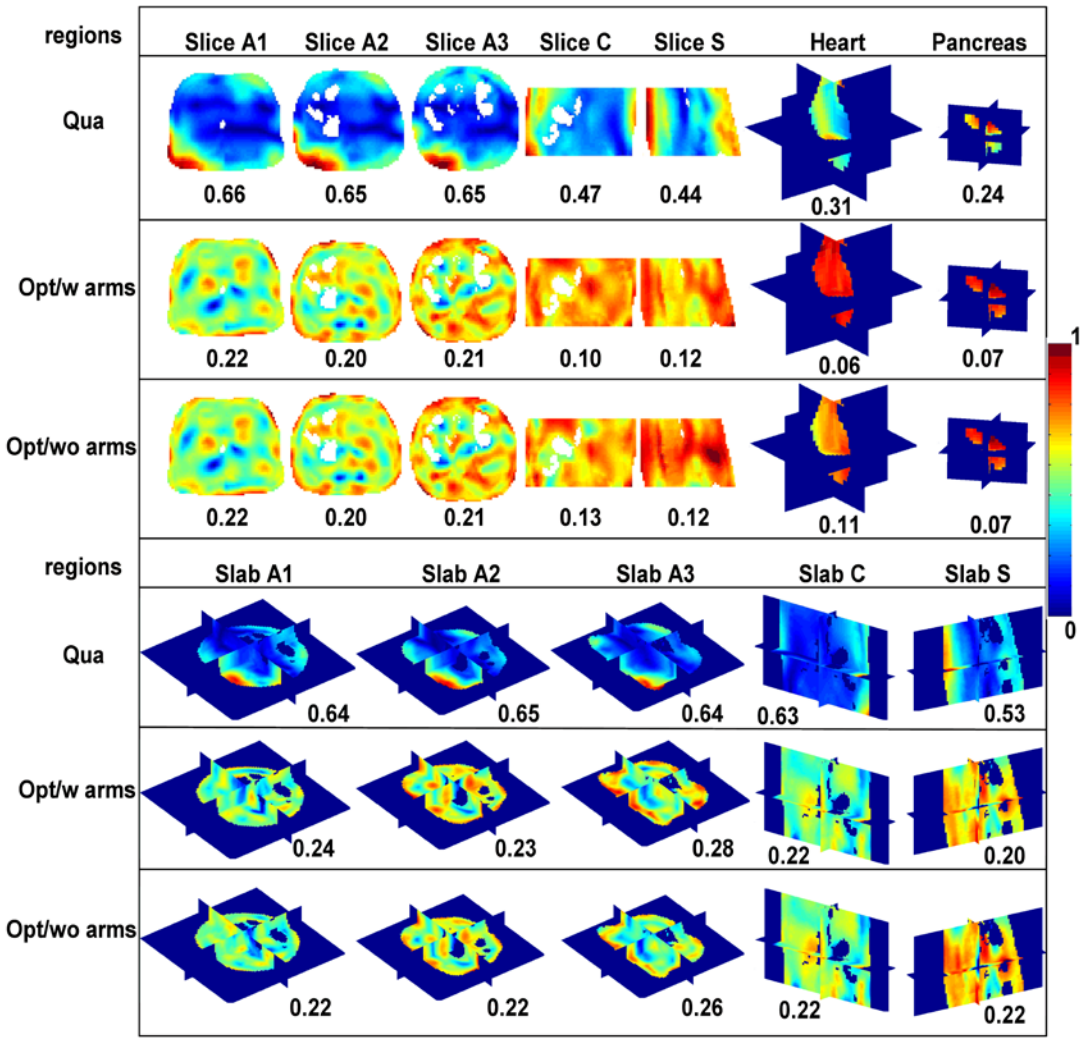


Figure 4.25 The B_1^+ field distributions inside the slices and slabs of interest, the heart, and the pancreas under quadrature condition (Qua) and the B_1^+ shimming excitation conditions in the "with arms" case (Opt/w arms) and "without arms" case (Opt/wo arms). The number under each subfigure is the coefficient of variance (COV) of the B_1^+ field distribution. All the subfigures are normalized from 0 to 1 as shown by the color bar.

4.6.3.2 Reduced Power Absorption and Local Peak SAR

The improved B_1^+ shimming scheme realizes optimization of the B_1^+ field homogeneity with constrained RF power deposition and local SAR simultaneously.

Figure 4.26 represents the decreased absorbing power using the shimming excitations in both the “with arms” and “without arms” cases, where the twelve ROIs on the x axis are the same as Figure 4.25 (5 slices, 2 organs and 5 slabs). In Figure 4.26, the black bars are the normalized power absorption under quadrature excitation condition and the green bars represent the absorbed power after B_1^+ , where the power absorbed in different cases is scaled to obtain a mean B_1^+ field intensity of 1.957 μT in the ROIs. According to Figure 4.26, the scaled power absorption is different with the ROIs under the same quadrature excitation condition because the inhomogeneous B_1^+ field distribution delivers various mean B_1^+ field intensities in different ROIs. It is clearly shown that the absorbing power decreases with the improvement of the homogeneity of the excitation field in the ROIs (shown in Figure 4.25).

The second constraint in the improved B_1^+ shimming scheme is the suppression of the SAR peaks. In this section, the peak SARs under the B_1^+ shimming excitation conditions are constrained to be less than or equal to the values under quadrature condition, as shown in Figure 4.27. From Figure 4.26 and 4.27, the suppressions of the total absorbed power and local peak SARs have closed correlations by using this shimming scheme, for example, the B_1^+ shimming excitation pursuing a uniform B_1^+ field distribution in the pancreas organ results in the most distinct reduction of both the total power absorption and local maximum SAR.

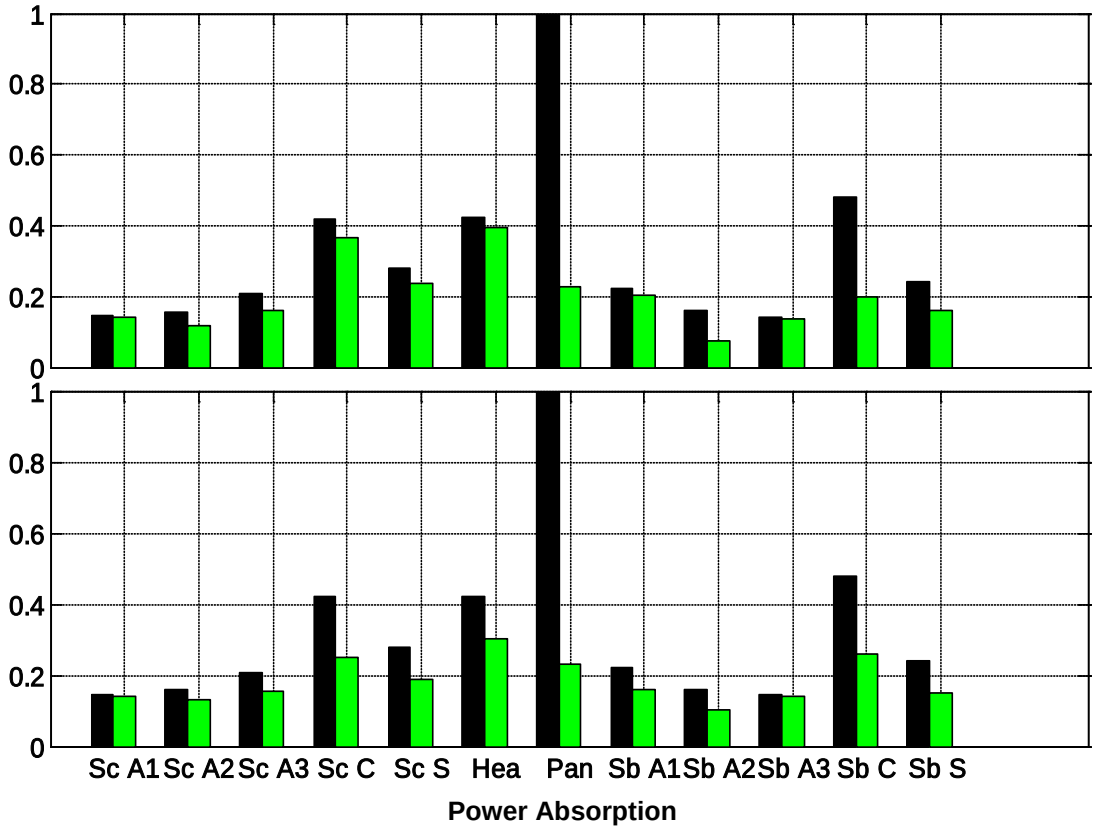


Figure 4.26 Comparison of the power absorption under quadrature and the B_1^+ shimming excitation conditions, where the ROIs shown on the x axis are same as Figure 4.25. The black bars are the normalized power absorption under initial quadrature condition, and the green bars show the relative decrease of the power absorption after optimizations. The above subfigure is for the "with arms" case and the below one represents the "without arms" case.

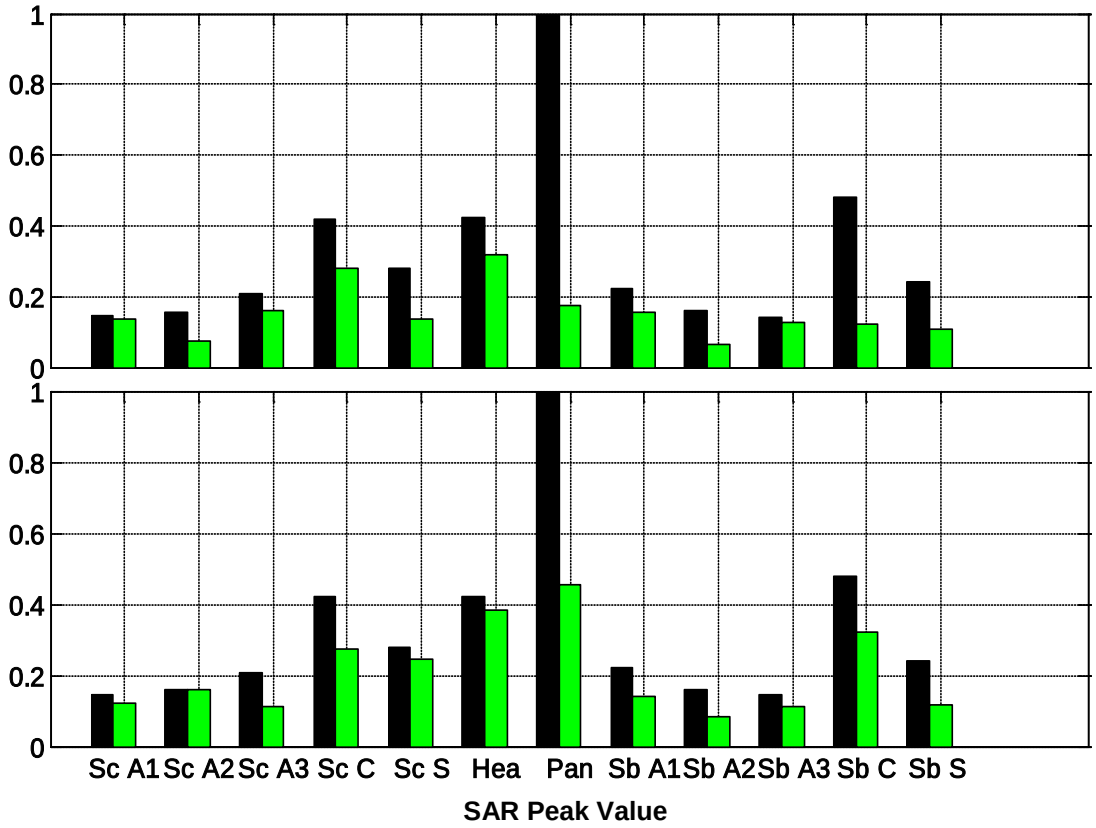


Figure 4.27 Comparison of the SAR peaks under quadrature condition and the B_1^+ shimming excitation conditions, where the ROIs shown on the x axis are same as Figure 4.25. The black bars are the normalized peak SARs under initial quadrature condition, and the green bars show the relative decrease of the SAR peak values after optimizations. Similar to Figure 4.26, the above subfigure is for the "with arms" case and the below one represents the "without arms" case.

The improved B_1^+ shimming scheme causes shifts of the peak SAR locations. Figure 4.28 shows the positions of the peak SAR in the body model under quadrature condition and the B_1^+ shimming excitations in the "with arms" (left subfigure) and "without arms" (right subfigure) cases. In both subfigures, the peak SARs are located at the red "Δ" positions with quadrature excitation and "O" positions with the B_1^+ shimming excitations for the optimizations of the B_1^+ field in the twelve ROIs (ROI

selections are the same as Figure 4.25). The SAR peaks are located at extremities, i.e. the arms, before and after shimming in the "with arm" case; the SAR peaks scatter over the trunk after shimming in the "without arm" case.

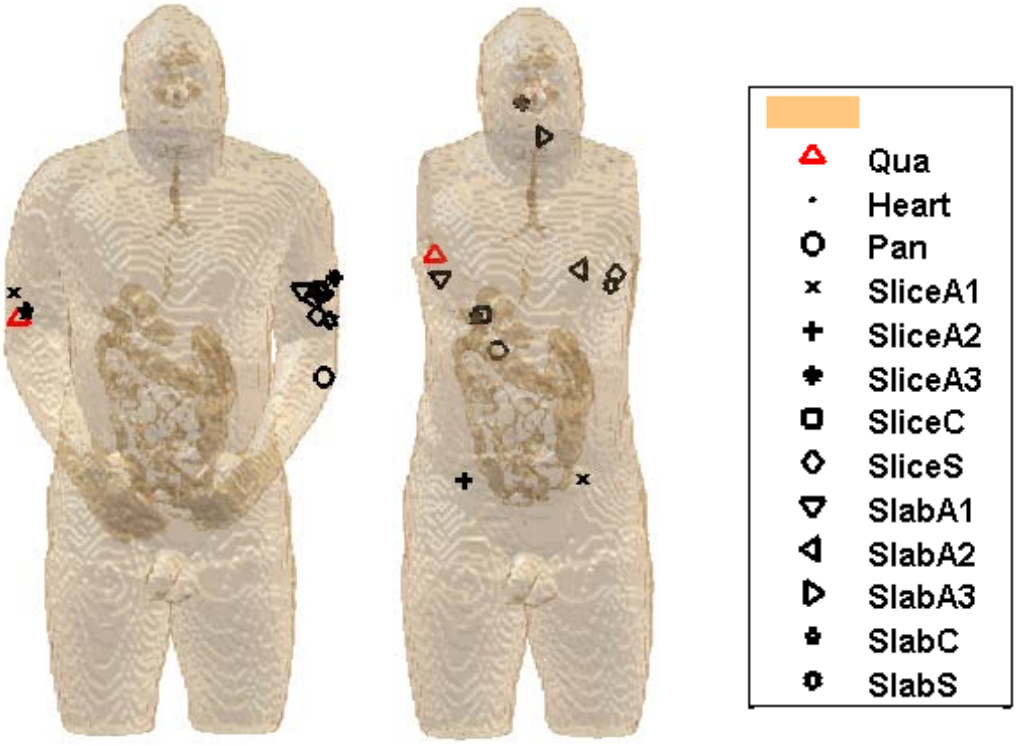


Figure 4.28 The SAR peak locations. Subfigure (a) shows the locations before and after optimization of the "with arms" case and subfigure (b) corresponds to optimization of the "without arms" case over 12 regions as same as in Figure 4.25. In both cases, symbol definitions are described in the legend.

The process of the improved B_1^+ shimming not only changes the distribution of the exciting magnetic field, but also redistributes the inhomogeneous electrical field. The two dimensional SAR distributions ("without arm" case) corresponding to an

averaged B_1^+=1.957 μT in the ROIs are shown in Figure 4.29. The top row provides the contours of the eight ROIs (including the pancreas, the heart, 3 slices and 3 slabs of interest). Under the same quadrature excitation condition, the maximum SARs are different in values and locations with the same mean intensity of B_1^+ field in various ROIs, due to the highly inhomogeneous B_1^+ field distribution over the body model at 7 tesla MRI. The maximum SAR (133.32 w/kg) among all the subfigures to obtain B_1^+=1.957 μT in the pancreas organ (the image at the second row and the first column) is caused by the least B_1^+ field intensity in the pancreas organ compared to the other ROIs under quadrature excitation. It is shown that the peak SARs decreased from the quadrature excitation after the improved B_1^+ shimming in every case. SAR distribution in the plane at which peak SAR occurs due to quadrature excitation are compared to the same plane due to the shimming excitations. It is shown that SAR distributions change patterns concurrently with the greatly decreased peak values after shimming. The SAR distributions in the planes at which peak SAR occurs due to the shimming excitations at the specified regions are also demonstrated in Figure 4.29, where the reduced SAR peak values are located at different positions from the quadrature excitation. In the B_1^+ shimming algorithm, homogeneity of the B_1^+ field distribution is improved with constrained peak SARs while the locations of the maximum SARs and the specifics of the SAR distributions are not considered in the shimming scheme.

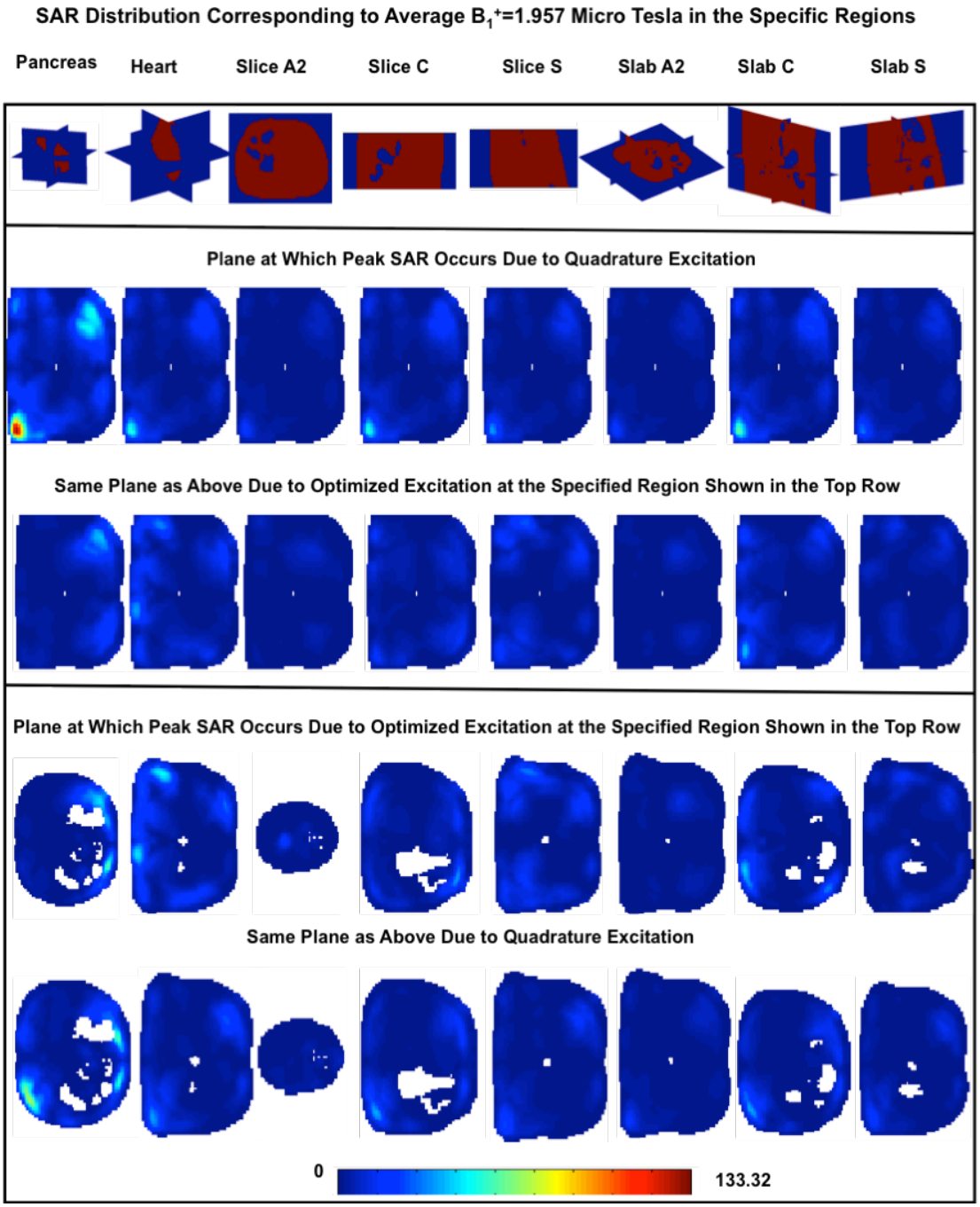


Figure 4.29 SAR distributions corresponding to average B_1^+=1.957 **μT** in the specific regions ("without arm" case). The region selections shown in the top row are same as Figure 4.25. All the subfigures are normalized from 0 to maximum SAR peak (133.32 w/kg) which is the peak SAR to obtain B_1^+=1.957 μT in a pancreas organ under quadrature excitation, as shown in the subfigure located in the second row and first column.

4.6.4 Summary

In this section, the B_1^+ shimming scheme is applied in the body model loaded within the 32-strut TEM resonator. The results from Figure 4.25-4.29 show that the B_1^+ field homogeneity in the twelve ROIs can be greatly improved with constrained total power absorption and peak SARs. The improved B_1^+ shimming scheme is validated by the experiments on an 8-element highly coupled TEM coil. Comparison of the simulation results and the experimental images are shown in Figure 4.24. The results indicate the severe inhomogeneity of MRI signal under the quadrature excitation is a resultant from the lack of B_1^+ field but not necessarily from the lack of electromagnetic energy. By our shimming scheme, both of the interactive fields change to an idea state in which magnetic fields are distributed evenly for better image quality and electric fields generate the least energy deposition on over-all whole body tissues and also least peak SAR.

4.7 SAR Safety Regulations

The safety standards for electromagnetic emissions from MRI devices are different from various safety regulations. The FDA currently recommends that local heating should not exceed 8 W/kg over any gram in the head and trunk, and 12 W/kg over any gram in the extremities, under normal mode operations [164]; the IEC limits for local SAR is restricted to10 W/kg in any 10 grams in the head and trunk, 20 W/kg in the extremities [165].

In section *4.4* and *4.5*, local SARs are calculated for every 10 gram tissues as defined in IEC regulations. Table 4.4 and 4.5 provide the peak SARs under quadrature excitation and the B_1^+ shimming excitation condition, where the calculations of SAR in different cases are scaled to obtain a mean, in ROI, B_1^+ field intensity of 1.957 μT which is the B_1^+ field strength required to produce a flip angle of $\pi/2$ with a 3-msec rectangular RF pulse.

Table 4.4 Peak SARs (averaged over any 10 gram of the tissues) in the head model at 7 T and 9.4 T under quadrature excitation and the B_1^+ shimming excitation conditions discussed in section *4.4*. The labels in the first column in the table are the regions of interested (ROIs) defined in Table 4.3.

	Maximum SAR in the Head Model (Averaged over any 10 gram of tissues) (W/kg)			
Field Strength	7 T		9.4 T	
Excitation	Qua	Opt	Qua	Opt
A	5.08	5.99	9.82	5.86
B	4.44	3.58	9.28	9.42
C	5.16	7.49	12.23	12.38
D	4.88	5.97	10.42	6.54
E	5.27	5.39	6.24	5.46
F	5.20	4.79	10.01	8.72
G	4.27	5.91	11.71	16.21
H	4.90	28.75	9.82	14.61
I	7.41	22.11	18.64	43.11
J	4.04	6.91	6.61	5.47
K	5.51	6.82	12.30	15.48
L	4.93	7.42	10.32	7.16
M	4.44	5.89	11.38	20.95
N	4.35	10.90	7.83	8.92

Table 4.5 Peak SARs (averaged over any 10 gram of the tissues) in the body model at 7T under quadrature excitation and the B_1^+ shimming excitation conditions discussed in section *4.5*. Peak SARs are calculated under two cases: considering the whole body and considering the torso only. Note that the arms are always present in the coil during the SAR calculation for both cases. The labels in the first column in the table are the regions of interested (ROIs) as demonstrated in Figure 4.25.

	Maximum SAR in the Body Model (Averaged over any 10 gram of tissues) (W/kg)			
	Considering the whole body		Considering the torso only	
Excitation	Qua	Opt	Qua	Opt
Heart	307	232	56	51
Pancreas	726	128	133	61
Slice A1	105	100	19	16
Slice A2	150	117	27	15
Slice A3	114	53	21	21
Slice C	305	203	56	37
Slice S	204	100	37	32
Slab A1	161	114	30	19
Slab A2	115	46	21	11
Slab A3	104	91	19	16
Slab C	349	90	64	43
Slab S	174	77	32	15

The data in Table 4.4 show the peak SAR changes after the B_1^+ shimming. Without the constraint of the local peak SARs, most of the maximum SARs increase under the shimming excitation condition, which is consistent with the results from Figure 4.22. At B_0 field strength of 7 tesla, peak SARs are less than 10 W/kg under quadrature excitation condition, while the peak value of the SARs exceed the safety limits from IEC (<=10 W/kg in head) after the B_1^+ shimming on the ROIs of H, I,

and N. At B_0 field strength of 9.4 tesla, peak SARs are lower than 10 W/kg in six of the 14 ROIs (A, B, E, H, J, and N) under quadrature excitation, and in eight ROIs (A, B, D, E, F, J, L, and N) under the B_1^+ shimming excitation condition. Table 4.5 shows the decreased peak SAR after the improved B_1^+ shimming (as described in section *4.5*) compared to quadrature excitation condition. However, all peak SARs shown in Table 4.5 violate the safety regulations about the local heating during MRI exams from IEC.

4.8 Shimming in Patterning the B_1^+ field and the Electrical Field

The B_1^+ shimming is not only able to improve the homogeneity of B_1^+ field, but is also able to rearrange the B_1^+ field distribution to achieve a desired pattern. Figure 4.30 shows interesting results of applying B_1^+ shimming in producing some simple shaped patterns. The electromagnetic field produced by the 8-element TEM resonator loaded with a spherical phantom (the same MR scanner used in the validation experiments in section *4.4* and *4.5*) was recorded firstly and then the B_1^+ shimming algorithm was applied to increase the B_1^+ intensity of the designed shapes with constrained total power deposition and local peak SAR in the phantom. Figure 4.30 demonstrates the two dimensional small angle signal images in axial slice. It is shown that the images can be emphasized or weakened in some designed pattern to make a "U" and a smiley face.

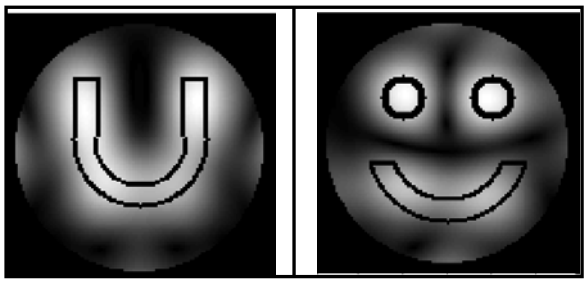


Figure 4.30 Axial slice small angle signal ($B_1^+ \times B_1^-$) images with some simple patterns.

The B_1^+ shimming scheme can also be applied to redistribute the electric field. Applying the same phantom mentioned previously, the total electric field ($E^2=Ex^2+Ey^2+Ez^2$) is focused in the ROIs, the three dimensional cylindrical regions with 1.59 cm in radius and 0.79 cm in height at two locations. Figure 4.31 shows the cross-section views of the *E* field under quadrature excitation condition and the field after shimming (by adjusting the phases and amplitudes of the four excitation elements), where the locations and dimensions of the ROIs are demonstrated with the black circles. From Figure 4.31, the electric field is emphasized inside the ROIs with a suppression of the outside regions. Applying the shimming scheme, the electric field can be focused in patterns that can be quite serious safety concerns.

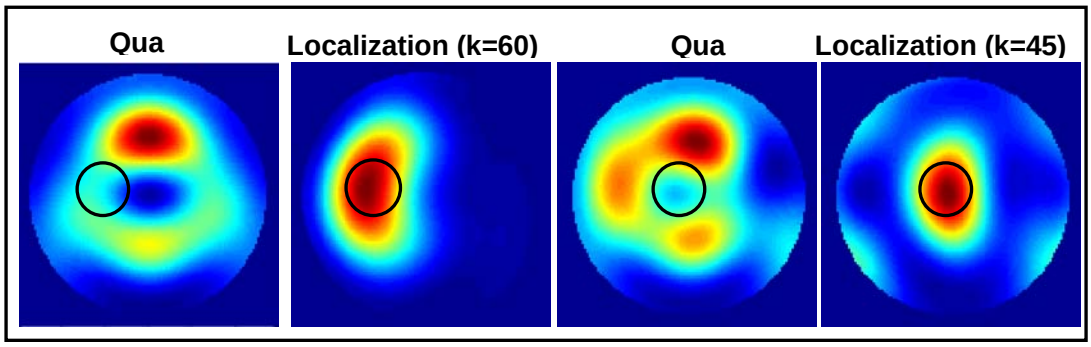


Figure 4.31 Electric field localizations. E fields were localized in the circles and 0.79 cm in height cylindrical regions at k=60 and k=45 positions. Electric field distributions under quadrature and localization conditions were compared in the two cases.

In this section, the shimming algorithm is applied in patterning the B_1^+ field and the electric field. It is shown the potential of the shimming algorithm in changing the distributions of both the excitation magnetic field and the electric field to the designed patterns.

4.9 Summaries and Conclusions

In this chapter, the B_1^+ field, total power deposition and local SARs during high/ultra high field MRI are studied systematically using the FDTD full wave electromagnetic numerical method. After the demonstration of the inhomogeneous B_1^+ fields with the increase of B_0 field strength in section *4.3*, the FDTD is used in studying the relationship between RF power absorption in tissue and the field strength or frequency of operation (section *4.4*). Using the quadrature excitation, it is clearly shown that the square dependence of the power on frequency vanishes to become 1) linear in axial slices towards the bottom of the brain or 2) peak-then-decrease in axial slices towards the top of the brain. When utilizing an optimized

shimming excitation, the nature of the power dependence is different than that with quadrature excitation. First, optimization of the homogeneity of the B_1^+ field distributions results in increased power requirements. On the other hand, the peak-then-decrease relation observed with the upper axial brain slices with quadrature excitation becomes more evident in the lower brain slices as well. The results also show that in order to achieve a highly homogeneous B_1^+ field distribution with a specified criterion of homogeneity, the use of more drive ports, and therefore more phase-locked transmit channels, will significantly reduce the RF power required to achieve a fixed average B_1^+ field intensity.

A set of B_1^+ shimming scheme is designed to improve the homogeneity of the B_1^+ field, while maintaining the constrained power absorption as well as local SAR peak (section *4.6*). The optimization routines are comprised of a combination of both gradient-based and genetic algorithm functions where a single iteration may go through either of these two methods. The total power deposition and the maximum local SAR are constrained to be less than or equal to the values under quadrature excitation condition within each iteration of the algorithm. The numerical results show that the homogeneity of the B_1^+ field distribution can be improved over the large volume of the human head model and human body model while constraining the total RF power absorption and local SAR peak. The proposed B_1^+ shimming scheme is capable of re-polarizing the transverse magnetic field to the MRI necessary polarization (circular) in the ROIs across the volume of the human head and the human body. The validity of the shimming scheme is demonstrated on

comparable coils/transmit arrays, where the calculated values of amplitudes and phases from simulation results are applied directly to excite the transmit array in the 7 tesla experiment. The good matches between the simulation and experimental images prove the validity of both the FDTD modeling method and the B_1^+ shimming scheme. The local SARs are discussed in the concerns of the safety regulations (section *4.7*) The improved shimming schemes also can be applied to localize the magnetic field B_1^+ and the electrical field (section *4.8*).

CHAPTER 5

THREE DIMENSIONAL TEMPERATURE STUDY WITHIN THE HEAD/BODY IN MRI

5.1 Introduction

The majority of the radiofrequency (RF) power transmitted into the patients for MR imaging is transformed into heat within the tissues as a result of resistive losses. The electromagnetic interaction of the RF field with the human body leads to a heterogeneous distribution of electromagnetic power dissipation at the edges between the human tissues with various thermal properties. Specific absorption rate (SAR) is most often used to describe the absorption rate of RF energy. However, to measure the accurate SARs experimentally is not convenient. One direct parameter to read the human thermal responses of the tissue with energy depositions during an MRI exam is the temperature change induced by the RF field. The temperature elevation is a second measurement besides the SAR calculation for the safety considerations. The Food and Drug Administration (FDA) currently recommends that local temperatures (local heating) should not exceed 38°C (8 W/kg over any gram) in the head, 39°C (8 W/kg over any gram) in the trunk, and 40°C (12 W/kg over any gram) in the extremities, under normal mode operations [164]; the International Electrotechnical Commission (IEC) limits for local temperature rise and local SAR as $\Delta T <= 1°C$ and SAR <=10 W/kg in any 10 grams in the head.

The first study of human thermal responses to RF radiation-induced heating during an MR procedure was conducted by Schaefer et al. [166]. Shellock et al. [167] involved volunteer subjects to undergo MR procedures with whole-body averaged SARs ranging from approximately 0.05 W/kg to 6.0W/kg in the later studies. More recent works in vivo 7 tesla MR imaging [168] and 9.4 tesla human MRI [124] experiments showed advantages of a higher signal to noise ratio (SNR) and novel contrast mechanisms, however, significantly increased SAR levels may lead to reduced duty cycles and a consequent increase in acquisition times for some RF-intensive imaging sequences [168]. Generally in a high electromagnetic field, inhomogeneous electric fields result in uneven distributions of the RF power deposition and "hot spots" may develop at locations in association with high electrical field strength and restrictive conductive tissue property [169]. For safety concerns, some research in ultra high field MRI was studied experimentally using a brain like phantom [170], and RF heating was studied in vivo using animals as subjects [171, 172]. A numerical simulation of the induced temperature rise is preferred prior to conducting practical experiments with patients/volunteers involved in MRI.

As two measurements of the RF heating on the human subject during MRI, temperature and SAR calculations are closely related. Numerical calculation of SAR in anatomical models of the human subject for MRI has been exploited in the past years [16, 19, 23, 119, 121, 173-180]: B_1 field and SAR distributions in the human head induced by a Helmholtz coil [180], a birdcage coil [23, 119, 178] and TEM

resonators [16] were studied to reveal the B_1 field homogeneity and SAR level at various frequencies, where SAR analyses were used to describe the distributions of the RF power depositions in the human head models. Since the human thermal responses are more related to the patients' thermoregulatory systems, scientists have shown their interests in the temperature calculations in measuring patients' safety [18, 181-185]. The temperature rise in tissues depends on multiple physiological, physical, and environmental factors, which include the status of the patient's thermoregulatory system, the rate at which energy is deposited, and the ambient conditions within the MR system, and etc. [169]. Nguyen et al. [184] presented temperature calculations for human head models in volume coils at different frequencies; Collin et al. [18] examined the relationships between SAR and temperature distribution in the human head within volume and surface coils at 64 and 300 MHz; Hand et al. [181, 185] reported temperature calculation results for human legs using surface coils; and Wang et al. [182] discussed numerical calculations of SAR and temperature in comparison to regulatory limits. Besides of the temperature calculation in regular MRI applications, finite different computation of the temperature rise in human head was applied to simulate the exposure to the RF energy radiated by cellular telephones [186-191]. In addition, computations of SAR and temperature elevations are also performed in the safety evaluations when the patients with implanted devices (i.e. pacemaker) are exposed to EM field during MR procedures [192, 193].

In this chapter, three dimensional SARs and temperature elevation caused by the RF field during MRIs are studied and analyzed for the human head and whole body models using the full-wave FDTD method. It is the first time to simulate the distribution of the temperature increase within the whole body at 7 tesla MRI. The computations of the temperature elevations in both the 2-mm/18-tissue head model [16] and the VSH body model (introduced in section *4.1*) are performed and compared between different RF excitation conditions: the quadrature excitation and the B_1^+ shimming excitations presented in Chapter 4. In this chapter, section *5.1* and *5.2* describe the thermal properties of the head and body models, and the bio-heat equation and boundary conditions. In section *5.3*, numerical results about the temperature changes within the head model and the body model during ultra high field MRI are presented and discussed. Finally, a short summery is provided in the last section.

5.2 Material and Methods

5.2.1 Thermal Property Model

The 2-mm/18-tissue head model and the VHP body anatomical detailed model are used for the temperature calculations, where the head model has the resolution of 2mm and the body model has the resolution of 6mm as introduced before. The electromagnetic properties of tissues in the head and the body models were described in Table 4.1 in Chapter 4; the thermal properties of the tissues in the models [35, 71, 182, 194, 195] are shown in Table 5.1 below. Three dimensional bio-heat models of

the human head and the VHP body are made to compute temperature changes due to RF power deposition caused by ultra-high field MRI.

Table 5.1 Thermal properties of the tissues in the head and the body models.

	Basal Metabolic Rate A0 [J/(m^3 s)]	Specific Heat C [J/kg °C]	Blood Perfusion Coeff. B [J/ (m^3 s °C)]	Thermal Conductivity K [J/m s °C]
Air	0	1000	0	0.03
Aorta	480	3370	2700	0.476
Aqueoushumor	0	3997	0	0.578
Bladder	1600	3300	9000	0.43
Blood	0	3640	0	0.549
Blood Vessel	1600	3553	9000	0.46
BodyFluid	0	4200	0	0.62
BoneCancellous	590	1300	3300	0.4
BoneCortical	610	1300	3400	0.4
BoneMarrow	5700	2700	32000	0.22
BrainGreyMatter	7100	3700	40000	0.57
BrainWhiteMatter	7100	3600	15925	0.5
BreastFat	300	2500	1700	0.25
Cartilage	1600	3500	9000	0.47
Cerebellum	7100	3700	40000	0.57
CerebroSpinalFluid	0	4200	0	0.62
Cervix[*3]	690	3600	2700	0.5
Colon	9500	3700	53000	0.556
Cornea	0	4200	0	0.58
Duodenum	13000	3700	71000	0.56
Dura	860	2802	4830	0.31
EyeSclera	0	4200	0	0.58
Fat	300	2500	1700	0.25
GallBladder	1600	3500	9000	0.47
GallBladderBile	0	3900	0	0.55
Gland	64000	3600	360000	0.53
Heart	9600	3700	54000	0.54
Kidney	48000	3900	270000	0.54
Lens	0	3000	0	0.40
Liver	12000	3600	68000	0.51
LungDeflated	1700	9500	2700	0.14

LungInflated	1700	9500	2700	0.14
Lymph	5650	3686	31800	0.49
MucousMembrane	1600	3300	9000	0.43
Muscle	690	3600	2700	0.5
Nail	610	1300	3400	0.4
Nerve	7100	3500	40000	0.46
Oesophagus[*4]	1600	3300	9000	0.43
Ovary[*1]	64000	3600	360000	0.53
Pancreas	7300	3500	41000	0.54
Prostate[*1]	64000	3600	360000	0.53
Retina	10000	3680	35000	0.565
Sclera	0	4200	0	0.58
Skin Dry	1620	3500	9100	0.42
Skin Wet	1620	3500	9100	0.42
Small Intestine	13000	3700	71000	0.56
Spinal Chord	7100	3500	40000	0.46
Spleen	15000	3700	82000	0.543
Stomach	5200	3600	29000	0.53
Tendon	1600	3300	9000	0.41
Testis	64000	3800	360000	0.53
Thymus[*1]	64000	3600	360000	0.53
Thyroid[*1]	64000	3600	360000	0.53
Tongue[*3]	690	3600	2700	0.5
Tooth	0	1340	0	0.5
Trachea[*2]	1600	3500	9000	0.47
Uterus[*3]	690	3600	2700	0.5
VitreousHumor	0	4200	0	0.6

*[1] Taken as Glands; *[2] Taken as Cartilage; *[3] Taken as Muscle; *[4] Taken as Mucous Membrane.

The above thermal properties are not constants at any temperature condition. When tissues are heated excessively, regulation mechanisms result in vasodilatation and increasing perspiration, which makes the rates of metabolism, radiation, perfusion, and perspiration are all functions of temperature. According to Wang et al.'s work [183], the presence of thermoregulatory mechanism can decrease the temperature elevation at high RF power absorption condition, however, the case will not occur in normal practice within FDA/IEC temperature regulatory limits (i.e.

obvious changes in thermal properties of the tissues happen only when the temperature increases far beyond the safety regulations). Therefore, physiological response to temperature is ignored in calculations of temperature elevation in this chapter.

5.2.2 Bio-Heat Equation and Boundary Condition

The transport of thermal energy in living tissue is a complex process involving multiple phenomenological mechanisms including conduction, convection, radiation, metabolism, evaporation, and phase change [196]. Based on the suggestion that the rate of heat transfer between blood and tissue is proportional to the product of the volumetric perfusion rate and the difference between the arterial blood temperature and the local tissue temperature, Pennes derived bio-heat equation which is applied in most of the temperature simulations, as shown in Equation (5.1).

$$\rho \boldsymbol{C_p} \frac{\partial \boldsymbol{T}}{\partial \boldsymbol{t}} = \boldsymbol{K} \nabla^2 \boldsymbol{T} + \boldsymbol{A}_0 - \boldsymbol{B}(\boldsymbol{T} - \boldsymbol{T_b}) + \rho \boldsymbol{SAR} \qquad (5.1)$$

where C_p (J/kg ºC) denotes the specific heat (the amount of heat per unit mass required to raise the temperature by one degree Celsius), K (J/m s ºC) denotes the thermal conductivity (the property of a material that indicates its ability to conduct heat), A_o (J/m^3 s) denotes the basal metabolic rate (the minimum calorific requirement needed to sustain life in a resting individual), and B (J/m^3 s ºC) denotes the blood perfusion coefficient [71, 72]. The definition and calculations of SAR are described in Chapter 4. The initial body temperature T_b was set to 37 ºC. The

temperature increase of the tissues due to the RF energy absorption is calculated and analyzed using this bio-heat equation.

The transfer or dispersion of heat can occur by means of three main mechanisms: conduction, convection and radiation. In this chapter, the boundary condition of the thermal modeling contains convection consideration only. Without including sweating and radiation in real cases, the removal of the heat from the body model to the environment in simulation is less than in practical occasions, i.e. the calculated temperature increase within regulatory limit here is more conservative than real applications. The transfer of heat between the domain and the surrounding environment is proportional to temperature difference between the surface and the environment. The following boundary condition is applied:

$$\boldsymbol{K}\frac{\partial \boldsymbol{T}}{\partial \boldsymbol{n}}\boldsymbol{(x,y,z)} = -\boldsymbol{H_a}\boldsymbol{(T_{x,y,z} - T_a)} \tag{5.2}$$

where H_a denotes the convective transfer coefficient (a constant with a value of 20 J/m^2 s ºC) [35]. The ambient temperature, T_a, is set to 24 ºC [71, 72].

The discretization of the bio-heat equation and the boundary condition follows that of the FDTD method introduced in Chapter 3. The spatial steps are set as Equation (5.3).

$$\Delta \boldsymbol{x} = \Delta \boldsymbol{y} = \Delta \boldsymbol{z} = \Delta \tag{5.3}$$

Using the denotation of Equation (3.1)-(3.3) and second-order accurate in space increments, the centered finite-different expressions for the Laplacian of the temperature T is described in Equation (5.4).

$$\nabla^2 T(i,j,k) = \frac{\partial^2 T(i,j,k)}{\partial x^2} + \frac{\partial^2 T(i,j,k)}{\partial y^2} + \frac{\partial^2 T(i,j,k)}{\partial z^2}$$
$$= \frac{1}{\Delta^2}[T(i+1,j,k) + T(i-1,j,k) + T(i,j+1,k) + T(i,j-1,k) + T(i,j,k+1) + T(i,j,k-1) - 6T(i,j,k)] \quad (5.4)$$

Plug Equation (5.4) into Equation (5.1),

$$\rho(i,j,k) \times c(i,j,k) \frac{T^{n+1}(i,j,k) - T^n(i,j,k)}{\Delta t} =$$
$$\frac{K(i,j,k)}{\Delta^2}[T^n(i+1,j,k) + T^n(i-1,j,k) + T^n(i,j+1,k)T^n(i,j-1,k) + T^n(i,j,k+1) + T^n(i,j,k-1) - 6T^n(i,j,k)]$$
$$+ A_0(i,j,k) - B(i,j,k) \times (T^n(i,j,k) - T_b) + \rho(i,j,k) \times SAR(i,j,k) \quad (5.5)$$

From Equation (5.5), the updated temperature is calculated using Equation (5.6).

$$T^{n+1}(i,j,k) = [1 - \frac{6K(i,j,k)\Delta t}{\rho(i,j,k) \times C_p(i,j,k) \times (\Delta)^2} - \frac{B(i,j,k)\Delta t}{\rho(i,j,k) \times C_p(i,j,k)}]T^n(i,j,k)$$
$$+ \frac{\Delta t K(i,j,k)}{\rho(i,j,k) \times C_p(i,j,k)(\Delta)^2}[T^n(i+1,j,k) + T^n(i-1,j,k) + T^n(i,j+1,k) + T^n(i,j-1,k) + T^n(i,j,k+1) + T^n(i,j,k-1)]$$
$$+ \frac{\Delta t}{\rho(i,j,k) \times C_p(i,j,k)}[A_0(i,j,k) + B(i,j,k)T_b + \rho(i,j,k) \times SAR(i,j,k)] \quad (5.6)$$

Similarly, Equation (5.2) could be written as Equation (5.7) at minimum boundary along the x direction.

$$K(i_{min}+1,j,k) \times \frac{T(i_{min},j,k) - T(i_{min}+1,j,k)}{\Delta x} = -H_a T(i_{min},j,k) + T_a H_a \quad (5.7)$$

From Equation (5.7) and Equation (5.3), the $T(i_{min},j,k)$ could be written as

$$T(i_{min,}, j, k) = \frac{K(i_{min}+1, j, k) \times T(i_{min}+1, j, k)}{K(i_{min}+1, j, k) + H_a \Delta} + \frac{T_a H_a \Delta}{K(i_{min}+1, j, k) + H_a \Delta} \quad (5.8)$$

Similar derivation of the boundary condition is performed in other 5 directions as presented in Equation (5.9)-(5.13).

$$T(i_{max,}, j, k) = \frac{K(i_{max}-1, j, k) \times T(i_{max}-1, j, k)}{K(i_{max}-1, j, k) + H_a \Delta} + \frac{T_a H_a \Delta}{K(i_{max}-1, j, k) + H_a \Delta} \quad (5.9)$$

$$T(i_{,} j_{min}, k) = \frac{K(i, j_{min}+1, k) \times T(i, j_{min}+1, k)}{K(i, j_{min}+1, k) + H_a \Delta} + \frac{T_a H_a \Delta}{K(i, j_{min}+1, k) + H_a \Delta} \quad (5.10)$$

$$T(i_{,} j_{max}, k) = \frac{K(i, j_{max}-1, k) \times T(i, j_{max}-1, k)}{K(i, j_{max}-1, k) + H_a \Delta} + \frac{T_a H_a \Delta}{K(i, j_{max}-1, k) + H_a \Delta} \quad (5.11)$$

$$T(i_{,} j, k_{min}) = \frac{K(i, j, k_{min}+1) \times T(i, j, k_{min}+1)}{K(i, j, k_{min}+1) + H_a \Delta} + \frac{T_a H_a \Delta}{K(i, j, k_{min}+1) + H_a \Delta} \quad (5.12)$$

$$T(i_{,} j, k_{max}) = \frac{K(i, j, k_{max}-1) \times T(i, j, k_{max}-1)}{K(i, j, k_{max}-1) + H_a \Delta} + \frac{T_a H_a \Delta}{K(i, j, k_{max}-1) + H_a \Delta} \quad (5.13)$$

In order to ensure the numerical stability, time step Δt is chosen to satisfy Equation (5.14) [189].

$$\Delta t \leq \frac{2\rho C_p \Delta^2}{12K + b\Delta^2} \quad (5.14)$$

5.3 Numerical Results and Discussion

5.3.1 Temperature Changes in the Head Model

In first step, the head model, uniform 37 ºC initially, is put in a 24 ºC environment without power deposition (SAR=0) until equilibrium condition T_0 is

met. A steady-state is defined here when it meets at least dT/dt = 2×10^{-7} °C/s for 30 minutes, where the time step in the calculation of temperature within the head model dt is set as 0.05 second. After equilibrium is achieved, the calculation of temperature continues using Equation (5.6) with SAR inputs. Temperature elevation (ΔT) is calculated by subtracting T_0 from the final T at the equilibrium.

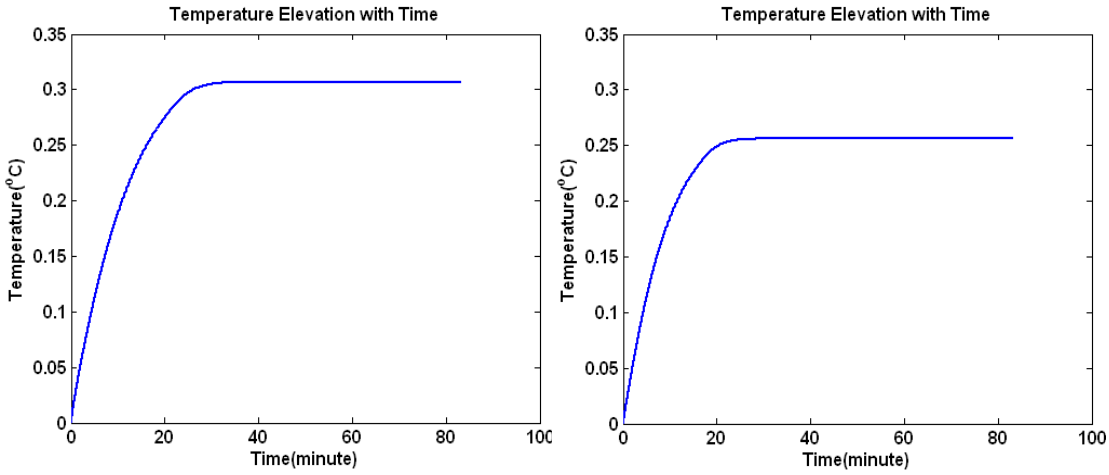


Figure 5.1 Temperature elevation (ΔT) changes with time for 7 tesla MRI. The left subplot is the increased temperature at the position where peak ΔT is located using quadrature excitation condition, and the right subplot is the peak ΔT under B_1^+ shimming exciting condition for the brain.

The SAR is calculated using Equation 4.4, and then scaled to obtain an averaged B_1^+ field intensity of 1.174 μT in the regions of interest (ROI) at 7 tesla and 9.4 tesla B_0 field strengths. 1.174 μT is the B_1^+ field strength required to produce a flip angle of π/2 with a 5-msec rectangular RF pulse. The B_1^+ field strength less than 1.174 μT induces a flip angle smaller than π/2, which only partially converts the z-magnetization into xy-magnetization (imaging plane); with a larger than 1.174 μT B_1^+ field strength, the z-magnetization is flipped more than π/2, which also only

leaves a fraction cosine of the RF pulse along the longitudinal direction. In a word, there is reduction in the value of transverse magnetization with a flip angle smaller or larger than $\pi/2$. SAR is averaged over any 10 gram of tissue. B_1^+ shimming introduced in Chapter 4 is applied to achieve improved homogeneity of the B_1^+ field distribution over the ROIs (defined in Chapter 4) while maintaining controlled total power absorption. Under quadrature and B_1^+ shimming exciting condition, SARs over the whole head are calculated and then applied to bio-heat equation to derive the temperature changes. As shown in Figure 5.1, it takes about 30 minutes for the energy transfer to arrive at the equilibrium state. The results show that the maximum temperature increase are 0.31 °C and 0.26 °C at quadrature and B_1^+ shimming exciting conditions over the brain ROI at 7 tesla, respectively.

Figure 5.2 Temperature elevation (ΔT) and SAR (averaged over any 10 gram of tissue) distributions at quadrature (Qua) and B_1^+ shimming (Opt) exciting conditions over ROIs at 7 tesla and 9.4 tesla MRI, respectively. The ROI selection is same as section *4.4*.

Figure 5.2 continued

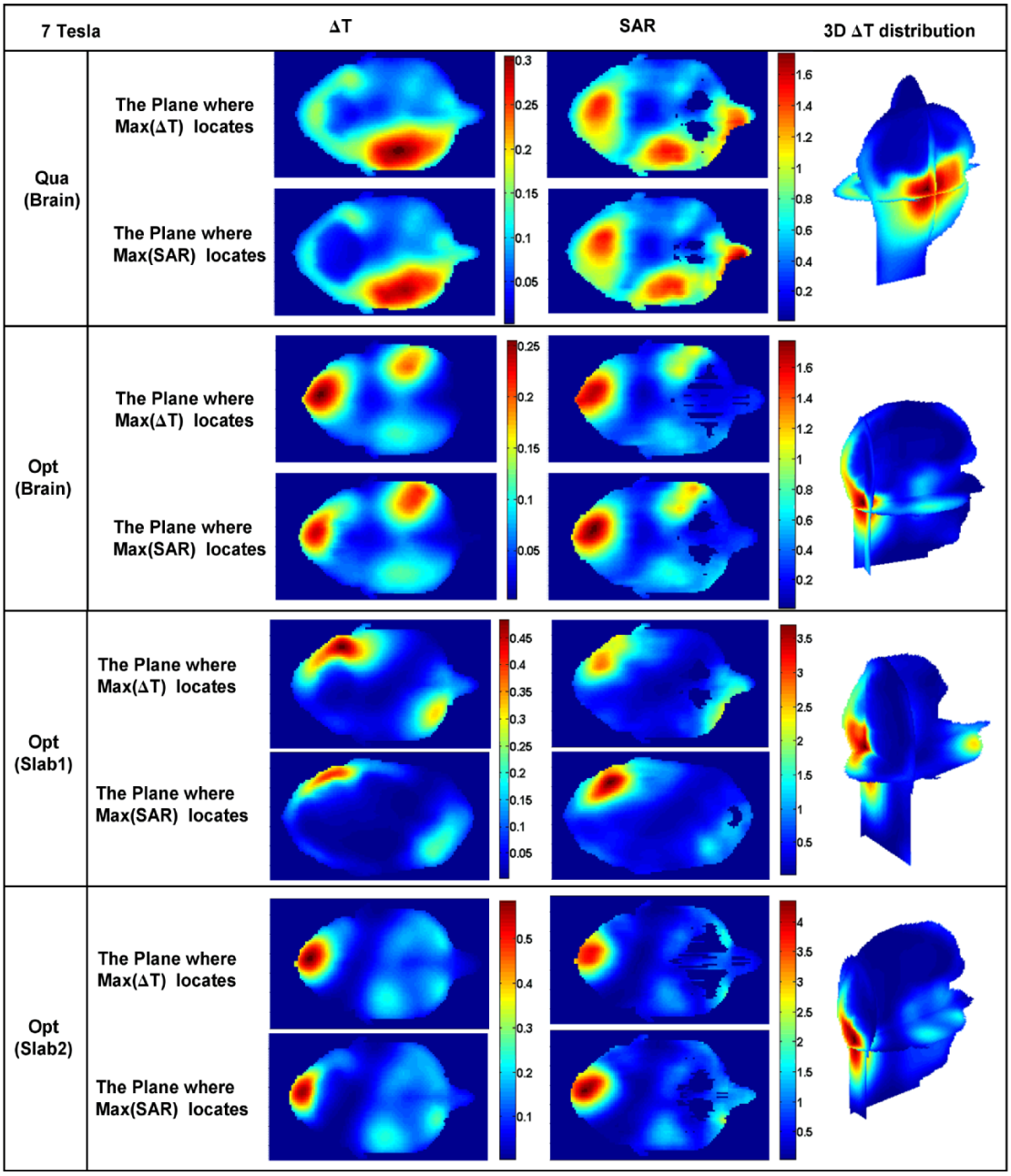


Figure 5.2 continued

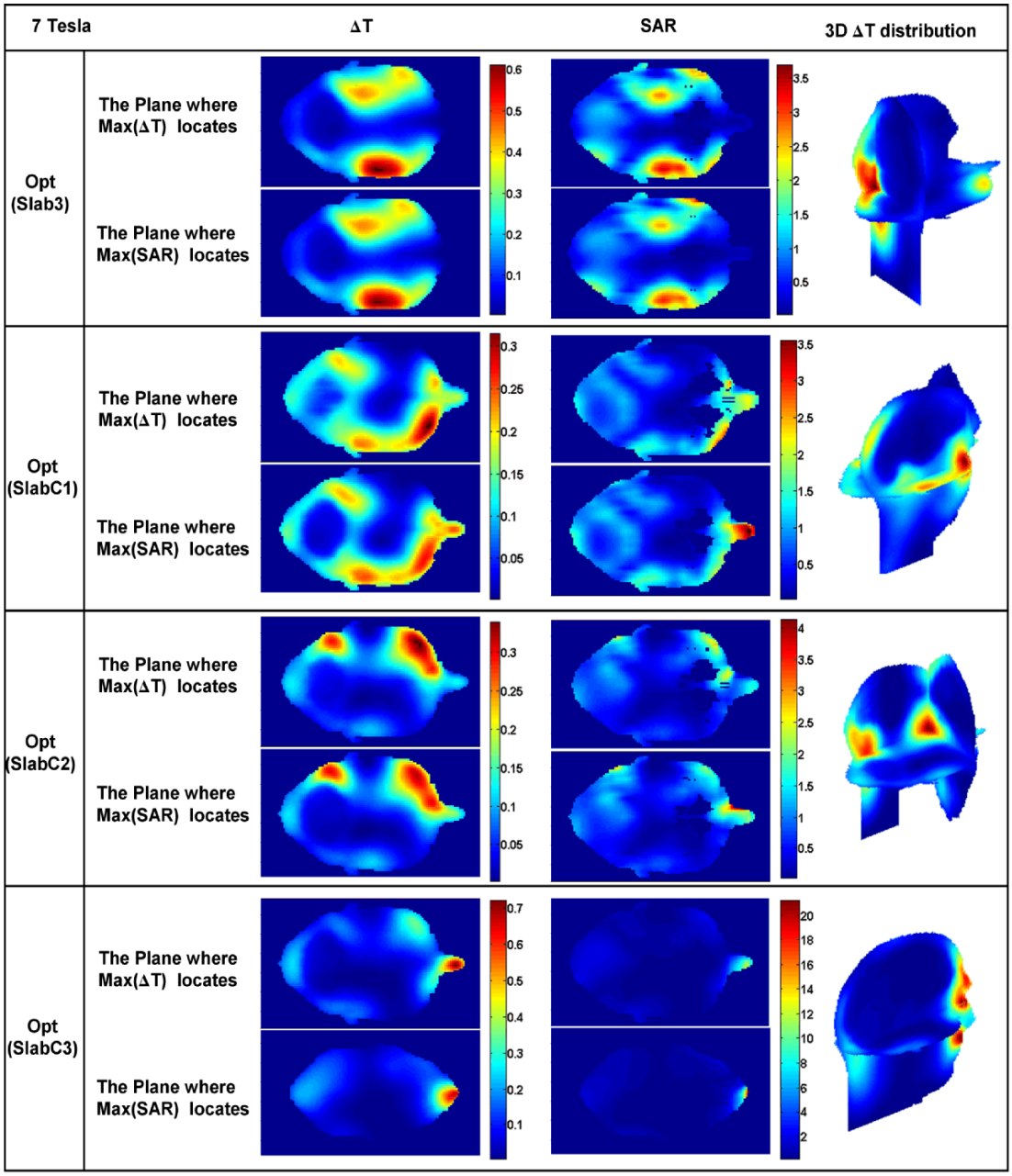


Figure 5.2 continued

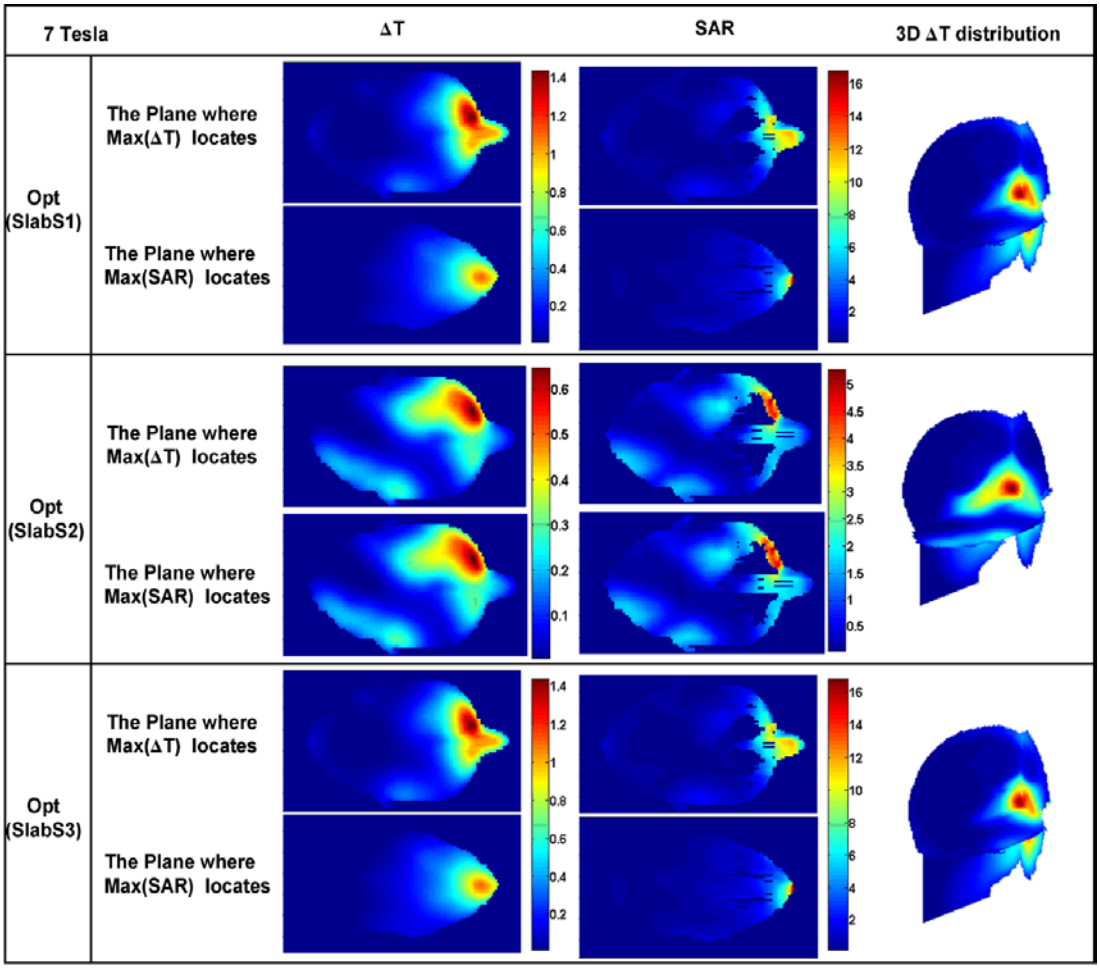


Figure 5.2 continued

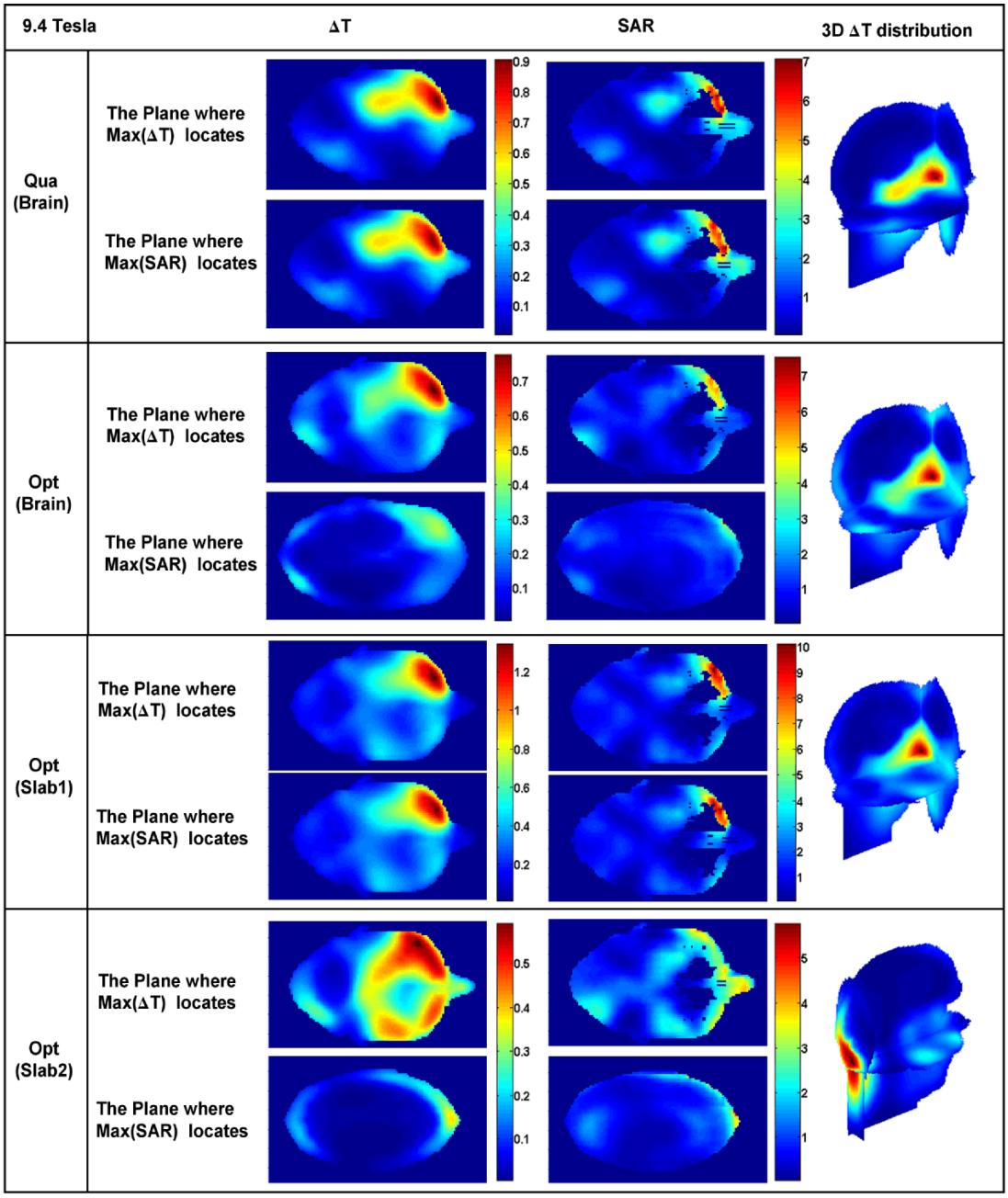


Figure 5.2 continued

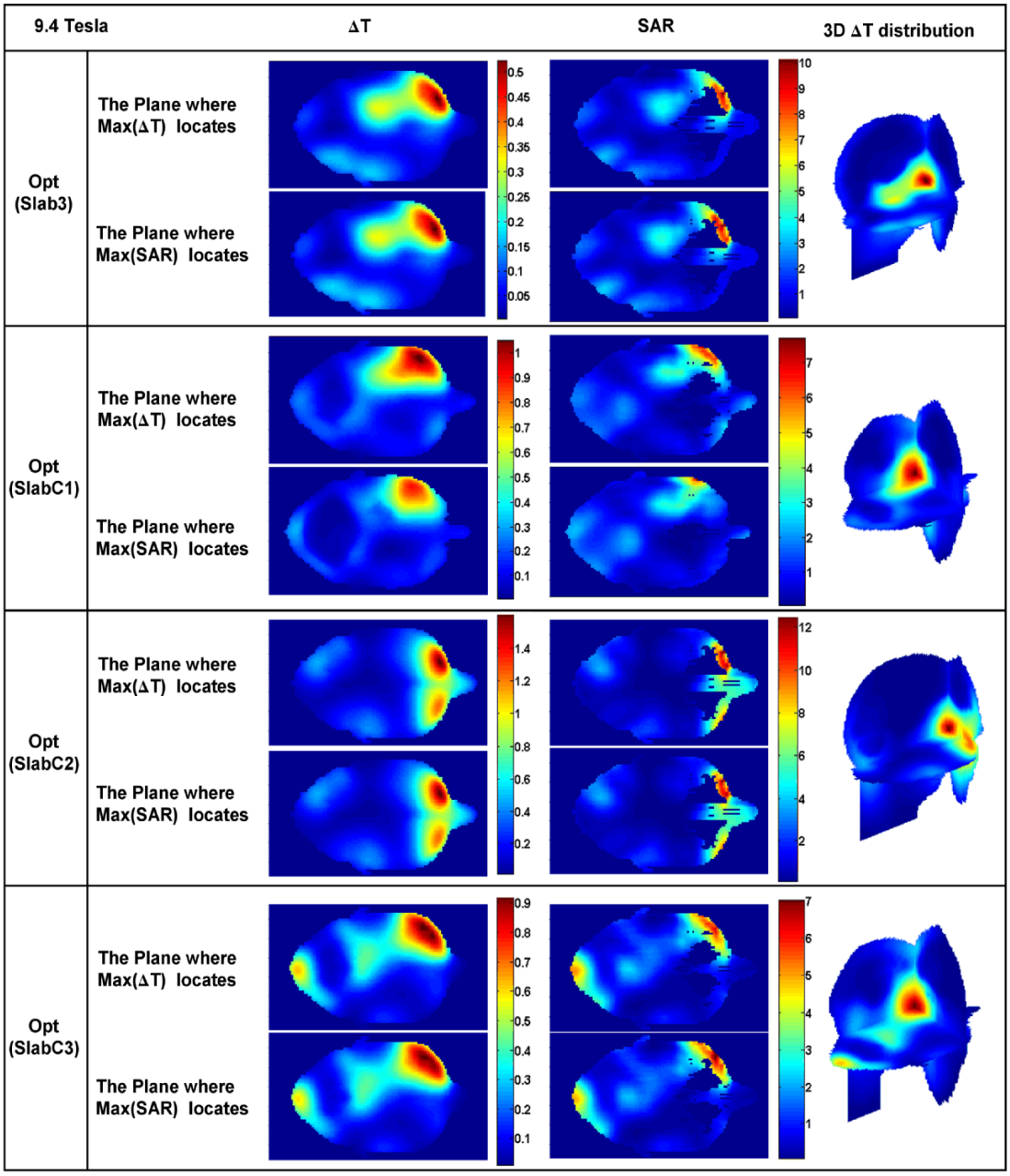


Figure 5.2 continued

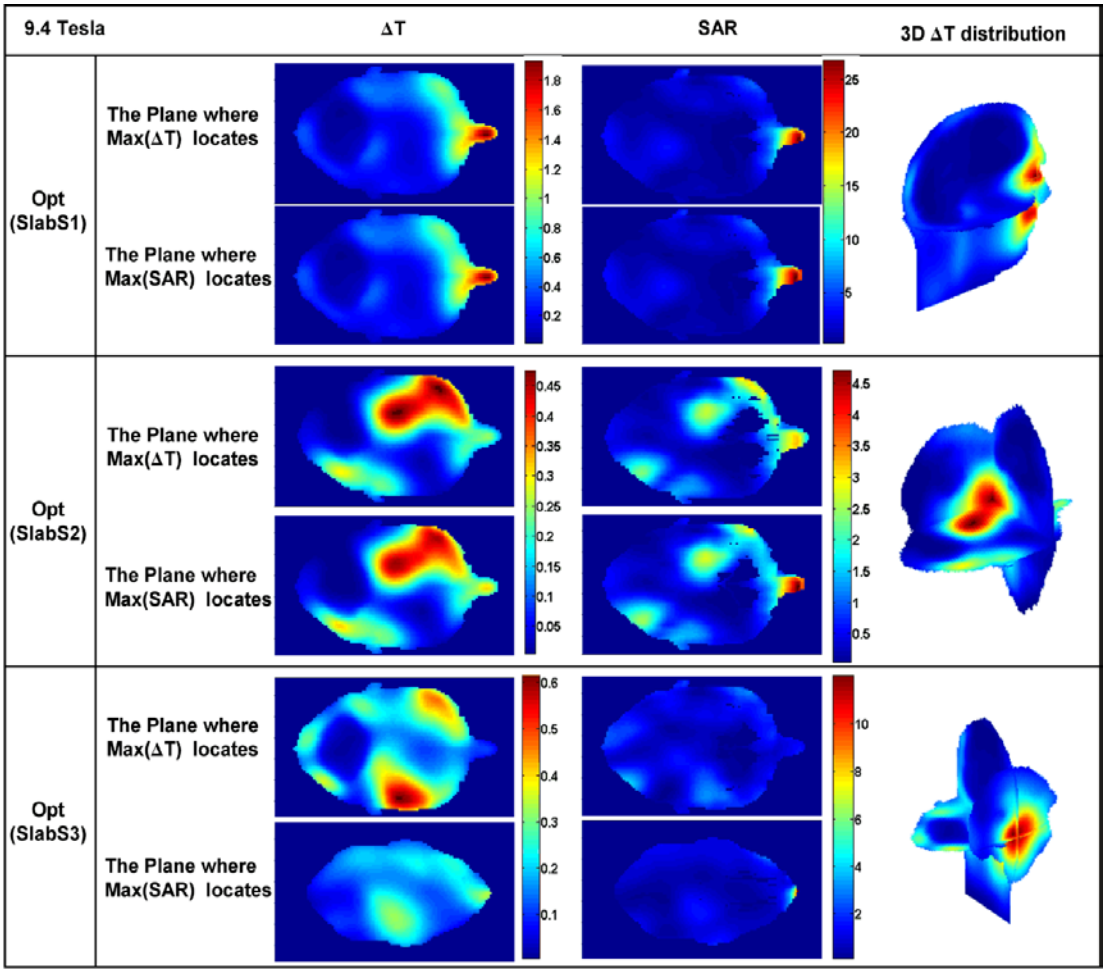


Figure 5.2 demonstrates the simulated results of ΔT and SAR within the human head model at quadrature and the B_1^+ shimming exciting conditions in 7 tesla and 9.4 tesla MRIs. In each excitation case, the ΔT and SAR distributions are shown in the axial planes, where the maximum ΔT and the maximum SAR are located. For example, results of *Qua(Brain)* demonstrates that the maximum local SAR (1.79 W/kg) results in less than 0.31°C temperature elevation using quadrature excitation

to obtain an averaged B_1^+ field intensity of 1.174 μT over the brain. It is shown that the higher SAR results in higher temperature elevation generally, however, the SAR peak and the highest temperature rise do not always occur at the close locations: the planes for *max (Δt)* and *max (SAR)* are apart from each other in the cases *opt(SlabC3), opt(SlabS1),* and *opt(SlabS3)* at 7 tesla, as well as the cases *opt(Brain), opt(Slab2)* and *opt(SlabS3)* at 9.4 tesla. One common feature in these mentioned cases is that SAR peaks are all located at the FDTD cells on the surface skin and these hot spots are much higher than the adjacent cells. The abnormal phenomenon might come from the inaccuracy of the averaged electromagnetic properties at the subject's surfaces in FDTD calculations, or the averaging scheme of SAR (per 10 gram) at the head surface. These SAR peaks at the surface do not induce the highest temperature rise because the thermal energy at the boundary of the head model convects to the cool environment easily.

By studying these computational results, peak SARs in cases *Opt (SlabC3), Opt (SlabS1),* and *Opt(SlabS3)* at 7 tesla, *Opt(Slab1), Opt(Slab3), Opt(SlabC2), Opt(SlabS1)* and *Opt(SlabS3)* at 9.4 tesla, violate the IEC local SAR safety regulations (10 W/kg); temperature elevation (ΔT) in cases *Opt(SlabS1)* and *Opt(SlabS3)* at 7 tesla, *Opt(Slab1), Opt(SlabC1), Opt(SlabC2),* and *Opt(SlabS1)* at 9.4 tesla violate the temperature safety limits (1°C). Case *Opt (SlabC3)* at 7 tesla, and cases *Opt(Slab3)* and *Opt(SlabS3)* at 9.4 tesla do violate SAR but not temperature safety regulatory limits due to the thermal energy transferring to the air at the surface of the head model. On the other hand, case *Opt(SlabC1)* at 9.4 tesla

exceeds the temperature safety limit within the regulations for SARs. The peak of ΔT elevation is 1.06 °C with peak SAR 7.74 W/kg deposition in this case.

Based on above observations, the SAR and temperature regulatory limits for MRI exams on human head from IEC are comparable in most conditions at 7 and 9.4 tesla, except the cases when SAR peaks are located on the surface skin of the head model. (Note that the exceptional case *Opt(SlabC1)* at 9.4 tesla breaks this rule but not very far off it.) In most of the cases, the elevated temperature distributions due to the RF power heating have very close spatial correlations with the SAR distributions when the SAR peaks do not locate on the FDTD cells on the model boundaries to the air. The differences between ΔT and SAR in some cases are due to the variation of the perfusion rate between different tissues.

5.3.2 Temperature Changes in the Body Model

Temperature elevations in the body model caused by the RF field in 7 tesla MRI are computed under different RF coil excitations. To improve the homogeneity of the B_1^+ field in ROIs with controlled total RF power absorption and local SAR peak, the B_1^+ shimming scheme described in Chapter 4 is applied to calculate the SAR distributions and the associated temperature changes. The pancreas organ and three slabs orientated in different directions are selected as the ROIs, shown in Figure 5.3. Under quadrature exciting condition, the SARs averaged in any 10 gram of tissues are scaled to 10 W/kg. After applying the B_1^+ shimming scheme, the SARs with the reduced local peak are also used to calculate the temperature changes caused by the RF power deposition using bio-heat equation (Equation 5.6), where the time step is

0.46 seconds. Similar to the test procedure in section *5.3.1*, the human body model (37 ºC) is put in a cool environment (24 ºC) to compute T_0 before plugging in the SARs under different excitation conditions.

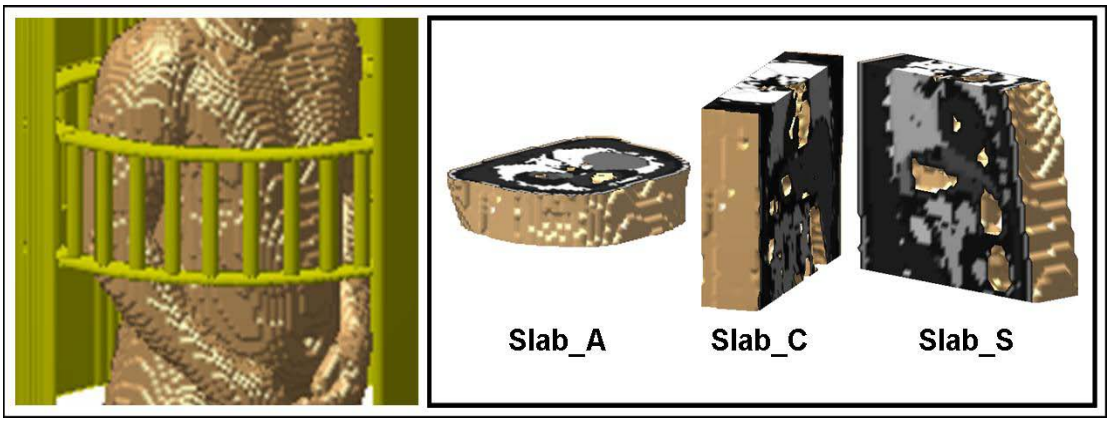


Figure 5.3 The selected slabs. All three slabs are 84mm thick. Slab_A is an axial slab located at the center of the coil; Slab_C and Slab_S are 252mm long in coronal and sagittal directions, respectively.

Figure 5.4 demonstrates the temperature elevation ΔT and SAR distributions within (a) the whole body and (b) the torso portion due to the RF power deposition caused by the MRI apparatus. The 3D subfigures show the three dimensional temperature elevations within (a) the human body model and (b) the trunk under different excitation conditions. The right two columns are the comparison between the 2D ΔT and SAR distributions at the interested planes: the plane where the maximum ΔT locates (the middle column) and the plane where the maximum SAR locates (the most right row). In both (a) with-arms and (b) without-arms cases, ΔT distributions in the two planes are very similar even identical under different excitation conditions, since the physical locations of the two planes are close or the

same: in Figure 5.4 (a), the distance between the two planes are 54mm, 6mm, 18mm, 0mm and 12mm for *Qua*, *Pan_opt*, *SlabA_opt*, *SlabC_opt*, and *SlabS_opt* cases, respectively; in Figure 5.4 (b), the distance between the two planes are 0mm, 78mm, 6mm, 6mm and 6mm correspondingly. The distributions of the 2D ΔT and SAR in the same plane have similar patterns. Compared to the head model (Figure 5.2), more remarkable spatial correlation between the temperature changes and SAR deposition is found in the body model (Figure 5.4). The reason of the closer relation is that the highest SARs or temperature elevations are located at the arms (Figure 5.4(a)) or in the torso regions (Figure 5.4(b)) where the tissue components are relatively simple (i.e. mostly muscles) and the variation of the tissues' thermal properties is minor. In these cases the temperature changes are primarily affected by the amount of the deposited RF power.

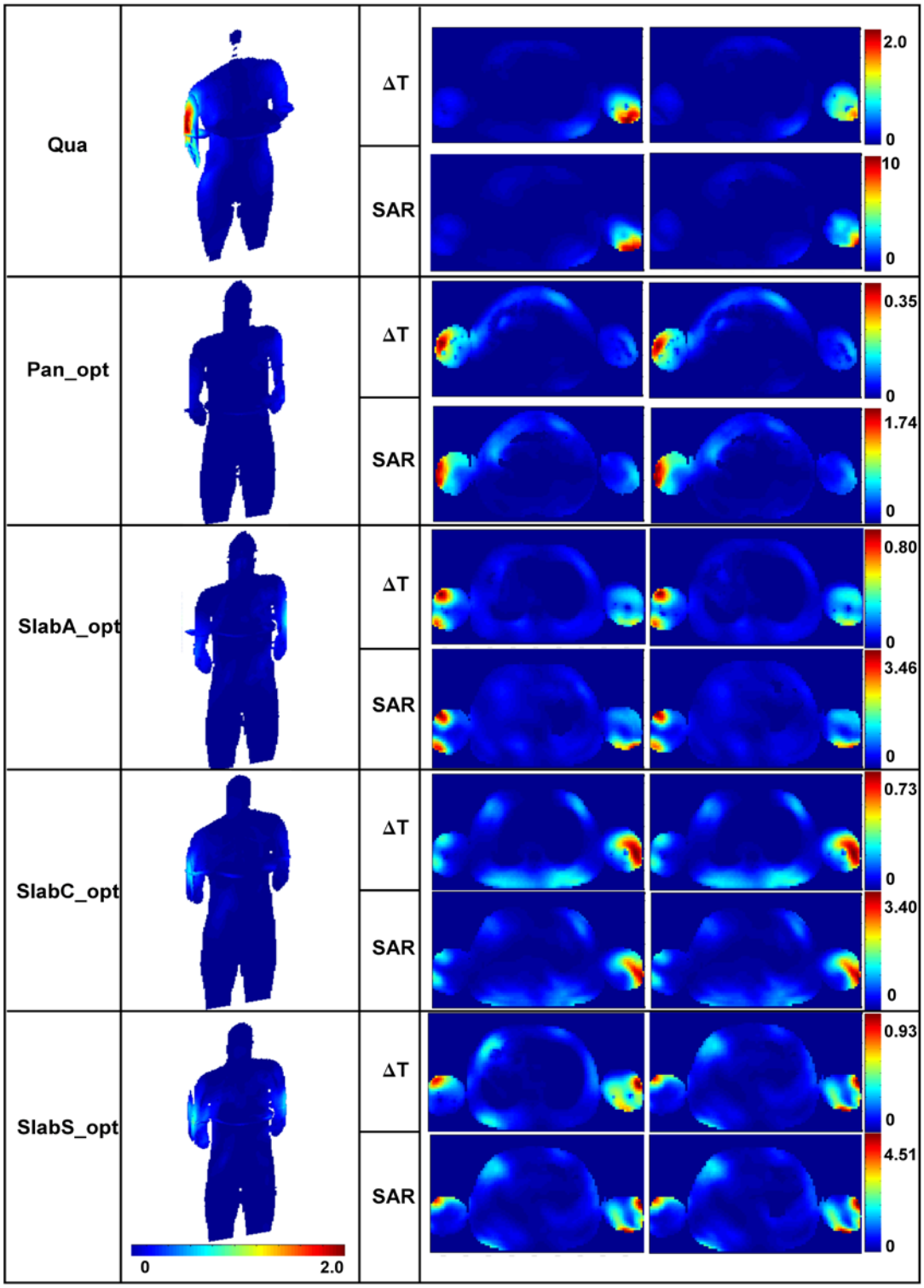
According to the local heating regulations from IEC, the maximum local SAR allowed is the same (10 W/kg) for both torso and extremities, but the maximum ΔT within safety limit is 2 °C for torso and 3 °C for extremities. However, Figure 5.4 demonstrates the higher temperature elevation in torso (2.42 °C) than in extremities (2 °C) under quadrature excitation condition with the same amount of peak SARs (10 W/kg) deposited. The temperature changes within torso (Figure 5.4(b)) are calculated with the arms presented while the peak SAR on torso portion is scale to 10 W/kg (the peak SAR on arms are great than 10W/kg) under quadrature excitation. The 3D temperature distribution over the whole body is masked to remove the arms after equilibrium state is met. Using quadrature excitation, the peak ΔT in torso

locates on the region that physically contacts the arms before removing the arms, therefore, the high temperature elevation in torso might be caused by the energy from the arms that undergo higher SAR deposition. The above analysis about Figure 5.4(b) has to be confirmed using a different human body model with opened arms having no contact with the torso.

Figure 5.4 also shows the reduced temperature elevation by the improved B_1^+ shimming excitation introduced in Chapter 4. Using B_1^+ shimming excitation, B_1^+ field homogeneity in the pancreas organ and the three slabs is greatly improved (Figure 4.25), at the same time, the local SAR peak and heating temperature are dramatically reduced (Figure 5.4). The local peak SAR is lowered from 10 W/kg to less than 4.51 W/kg (Figure 5.4(a)) or 8.09 W/kg (Figure 5.4(b)), and the temperature elevation caused by the RF field during MRI exams is brought from 2 °C down to less than 0.93 °C (Figure 5.4(a)) or from 2.42 °C to less than 1.53 °C (Figure 5.4(b)) compared to the quadrature excitation. The local heating problem in the human body model caused by a whole body MRI exam at 7 tesla can be solved by application B_1^+ shimming excitations.

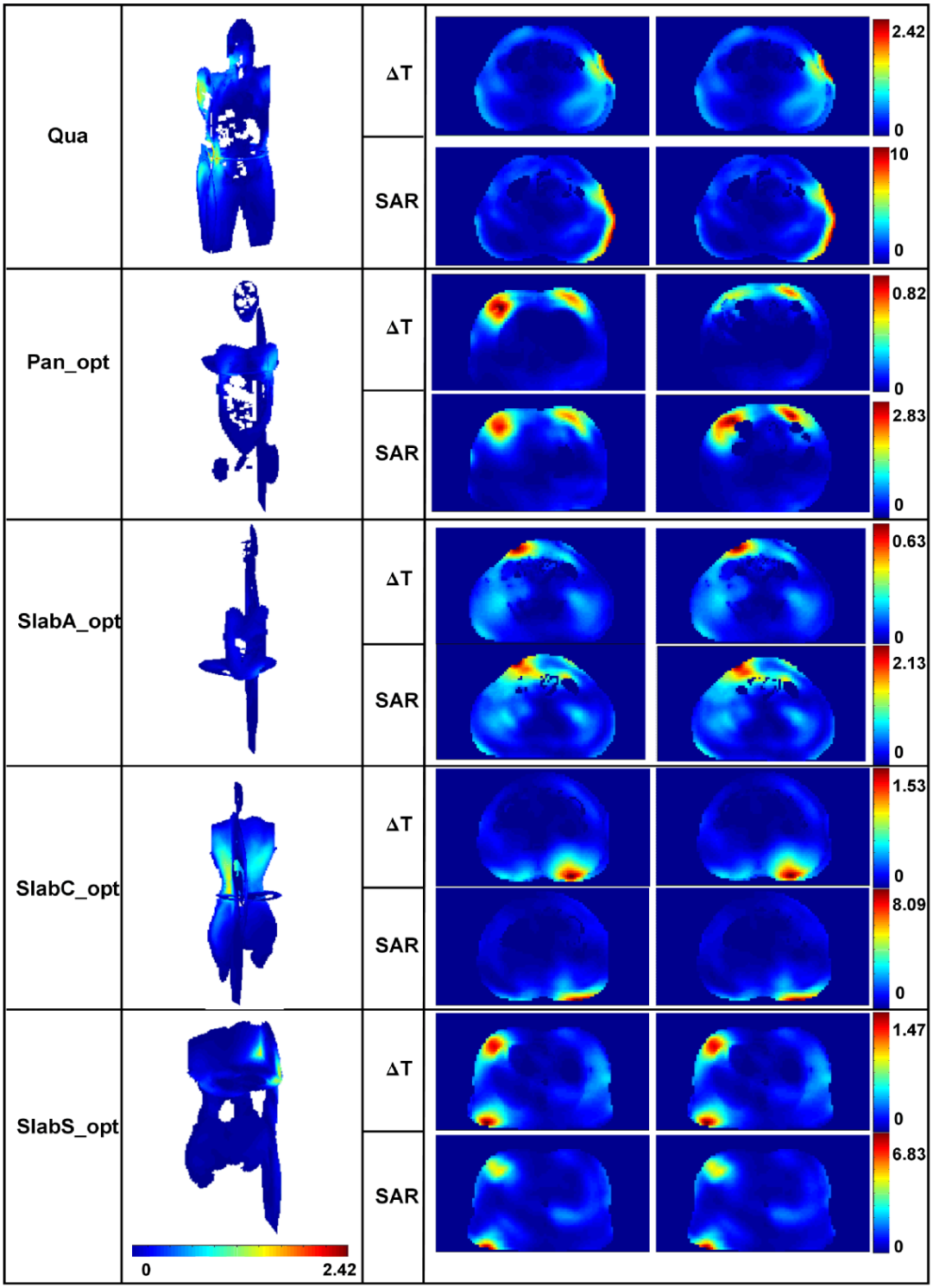
Figure 5.4 Temperature elevation (ΔT) and SAR (averaged over any 10 gram of tissue) distributions within whole body (a) and torso only (arms are removed) (b) under different excitation conditions at 7 tesla MRI. The most left column of the subfigures are ΔT distributions within 3D human body model (a) and torso (b), the right two columns are the comparison between 2D ΔT and SAR distributions at interested planes: the plane where the maximum ΔT is located (the middle column) and the plane where the maximum SAR is located (the most right column).

Figure 5.4 continued



(a)

Figure 5.4 continued



(b)

5.4 Summary

Compared to SAR, human thermal response is a more direct parameter for the heating effect induced by RF radiation during MRI exams. In this chapter, three dimensional bio-heat models of the human head and body (from the knees up to the top of the head) are built to calculate the temperature changes of the tissues when they are exposed to the RF field produced by the 16-strut TEM head coil and 32-strut TEM body coil under the quadrature and the B_1^+ shimming exciting conditions.

Generally, the temperature rise in one type of tissue is proportional to the RF energy deposition: the reduced local SAR peaks cause lower temperature elevation. The results of the temperature calculation in the human head model show that the increased temperature has close spatial correlation with the SARs. The little difference between the ΔT and SAR distributions is due to the variation of the perfusion rate between different tissues. In the temperature computation in the human body model, the patterns of the temperature rise in the body with and without arms provide closer connection to the SAR distributions because of the minor variation of the tissues in the arms or in the torso regions where the maximum local heating is located. As a summary, it is shown that the relation between the SAR and the temperature changes greatly depends on not only the different tissues and geometries, but also meaningful definition and accurate calculation of the averaged local SAR. The safety regulations for SAR and temperature are inter-consistent when the variation of the perfusion rate between the different tissues is small.

CHAPTER 6

STUDIES IN RF POWER COMMUNICATION, SAR, AND TEMPERATURE ELEVATION IN WIRELESS BRAIN MACHINE INTERFACE APPLICATION

6.1 Introduction

The brain is composed of billions of neurons that integrate multimodal sensory information and process it to control behaviors. Brain-machine interfaces (BMI) provide direct functional interfaces with the brain in order to monitor or initiate neural activity. BMIs are typically designed to provide real-time control signals for prosthetic devices, study brain function and/or restore sensory information lost as a result of injury or disease [54]. The design and implementation of BMIs involve the combined efforts of many areas of research, such as computer science, electrical engineering and biomedical engineering including the techniques for micro-stimulating neuronal tissue, microchip design, very large scale integration (VLSI) design and robotics [54]. It is believed that in the near future, real-time direct interfaces between the brain and electronic and mechanical devices could be used to study brain function and restore sensory and motor functions lost through injury or disease [54].

Classes of BMIs can be distinguished by their level of invasiveness (non-invasive and invasive; i.e. intra-cranial) and the type of neural recordings obtained (spikes,

local fields, electroencephalograms)[58]. Non-invasive systems primarily record electroencephalograms (EEGs) to control computer cursors or other devices [4-6] due to its ease of use, portability and relatively low set-up cost. However, EEG-based techniques provide communication channels of limited capacity, 20-30 bits/min. Two other non-invasive technologies that could be considered as BMIs are magnetoencephalography (MEG) and functional magnetic resonance imaging (fMRI) [59]. However, both MEG and fMRI technologies require a high field magnetic environment enclosed in a magnetically shielded room, which greatly increases the cost and severely limit their applications. The invasive approaches use implanted microelectrodes either on the surface of the brain, or inserted through the pia into superficial cortex to capture local field potentials and/or action potentials [9-11].

Invasive BMIs provide the spatial and temporal precision required for implementing real-time prosthetic systems. The utility of BMI's have been demonstrated by several labs using non-human primates to control robotic arm movements [60, 61] and a tetraplegic human to control a cursor on a computer [62]. The initial results suggest that Neuromotor Prosthetics (NMPs) based upon intracortical neuronal ensemble spiking activity could be applied to restore independence for humans with paralysis [62]. Traditional BMIs use wires for power and data transmission. The wires not only limit the utility of BMIs, but also increase the likelihood of device failure and are a major source of noise. Radio frequency (RF) power and wireless communication of a BMI chip would widely extend BMI

applications and potential longevity. However, RF exposure may result in power deposition and tissue heating, which is regulated by the Federal Communications Commission (FCC) and the Food and Drug Administration (FDA) and the International Electrotechnical Commission (IEC). Accurate estimations must be given to the heating effects as a result of wirelessly powering a chip in the brain. In addition, it is essential to perform an analysis of electromagnetic power deposition throughout the human head to determine the amount of available power to BMIs without violating limits on tissue heating and specific absorption rates regulated by federal agencies.

Power deposition analyses have been performed in the design of transcutaneous transmission coils for powering devices (such as cochlear implants), as well as to simulate the effects of external antennas (e.g. cell phones, magnetic resonance imaging probes, and hyperthermia antennas) placed in close proximity to biological tissue [197, 198]. Studies on the consequences of wirelessly powering devices within the skull were performed by Mojarradi et al [199] and Bashirullah et al [200]. In addition, studies have been conducted on the effects of implantable electric devices placed on the retina, cardiac muscle, and other structures within the body [71, 72, 201-206]. A miniaturized neuroprosthesis suitable for implantation into the brain is studied by Mojarradi et al [199], where they measured performance of initial micropower low-noise CMOS preamplifiers for the neuroprosthetic. Bashirullah et al [200] provided a brief over view of developments towards the Florida wireless implantable recording electrode microsystem. Ibrahim et al [35] provided an initial

estimation of the amount of tissue heating with the operation of a wireless BMI device. However, all the calculations were simplified in two dimensions: the chip model was simplified (effect of Tx/Rx antenna was not fully included,) and SARs were calculated using the two dimensional finite different time domain (FDTD) method and the peak temperature changes caused by electromagnetic absorption in the head were predicted using the 2D bio-heat equation. On the base of their work, we designed a three dimensional modeling scheme of the head-BMI system to study the RF power deposition (electromagnetic effects) and the local heating (thermal effects) associated with the operation of a wireless BMI device.

In this chapter, we designed a three dimensional modeling scheme of the head-BMI system to fully study the RF power deposition (electromagnetic effects) and local heating (thermal effects) associated with the operation of a wireless invasive BMI device. The BMI devices numerically were implanted inside of a $(2\text{-mm})^3$/19-tissue head model [16] at different depths to study RF power transmission/reception with miniature/on-chip dipole antennas as well as the associated tissue heating through the use of the bio-heat [71, 72] equation. The study was performed with different antenna lengths and at different frequencies. The three dimensional FDTD method was used to calculate the SARs in conjunction with an accurate excitation/reception algorithm based on virtual transmission line theory [207]. The three-dimensional bio-heat equation was then applied to calculate the temperature changes 1) in the head due to the external antenna and the 2) in cortical tissue surrounding the implanted, wirelessly powered BMI chip(s). In section *6.2*, the three

dimensional electromagnetic model and bio-heat model are introduced. This section includes the methods of antenna excitation, power calculation, and impedance matching. In section *6.3*, the maximum receiving power without violating the SAR safety regulations and the associated temperature elevations are presented and analyzed. A summary is provided in the last section.

6.2 Methods

6.2.1 The Electromagnetic Model

The BMI devices including the antenna and all the electronics (spike detection circuitry, signal condition part, and A/D converters, etc.) are implanted intracranially. These BMI devices extract motor control (or other) signals from the individual cortical and subcortical neurons and use these control signals to reproduce motor behaviors in artificial actuators [54, 208]. In this chapter we focus on the RF power reception by the BMI devices and the associated tissue heating. The BMI chip was modeled as a dipole antenna (receiving RF energy for powering the chip) embedded in a silicon block as shown in Figure 6.1.

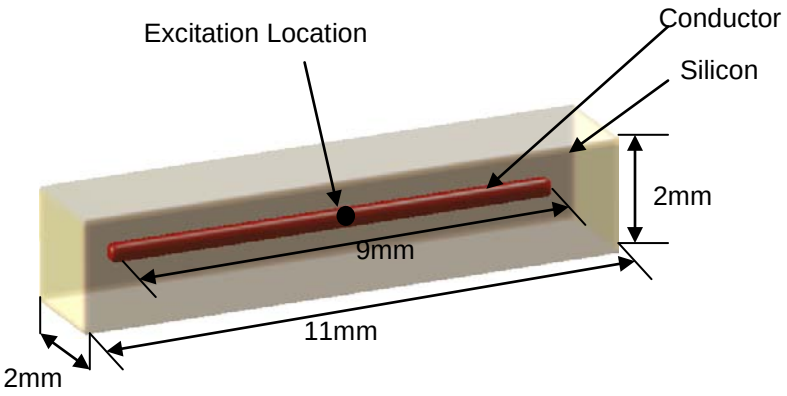


Figure 6.1 Structure of the chip with a 9 mm antenna.

An external transmitting antenna acts as a power source by transmitting RF power to the on-chip receiving antenna. In our analysis, both of the transmitting (outside the head) and receiving antennas (inside the head) were designed as dipole antennas as shown in Figure 6.2. The FDTD grid of the 19-tissue head model developed from 1.5 tesla MR images [16] has a rescaled resolution 1 mm×1 mm×1 mm.

The outside transmitting antenna with a length of 63 mm is located 10 mm away from the back of the head, and it resonates at frequency 2.38GHz in vacuum (achieved numerically). The receiving antenna, as a part of the BMI chip, is implanted in the white matter of the brain to simulate worst case scenario for thermal conductivity. To calculate and analyze the efficiency of the power transmission, the receiving antennas are designed with three different lengths (5 mm, 9 mm, and 15 mm) at tested various depths (0 mm, 10 mm, 30 mm, and 60 mm) from the surface, deep into the brain. The resonant frequency (frequency at which the antenna receives most effectively) of a receiving antenna varies with antenna length and location

within the brain (will be discussed in the next section). The positions of the external antenna and a sample 5 mm long implanted antenna (on the BMI chips) are demonstrated in the 4 specified depths in Figure 6.2.

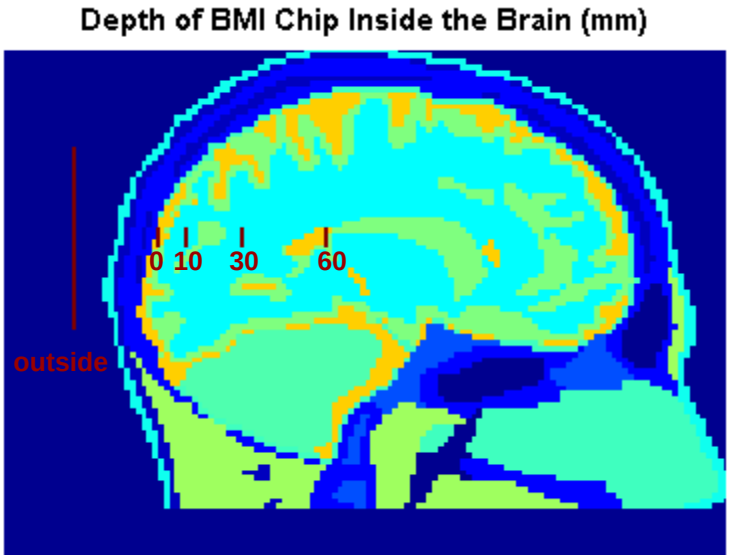
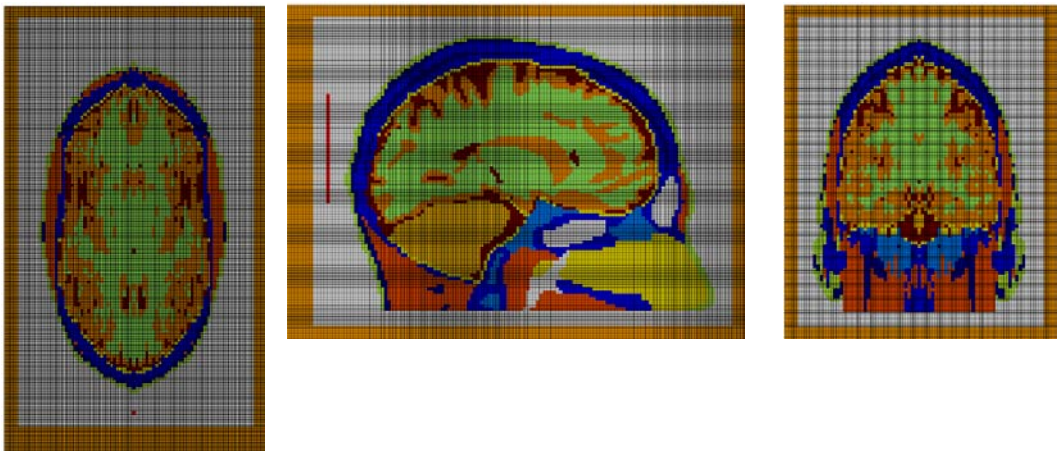


Figure 6.2 Positions of the transmitting/external antenna outside of the head and the implanted BMI chips at different depths inside the brain.

The FDTD grid of the head-BMI system has the dimensions of 162×278×200 cells with a spatial resolution of 0.001m. The time step is 1.8873 picoseconds. Figure 6.3 demonstrates the domain of interests. The rectangular volume is terminated by perfectly matched layers (PML) [37] as the absorbing boundary conditions. There are 8 PML layers at five boundary faces which are the top, bottom, two sides and the front of the head mesh and 16 PML layers at the back of the head where the external antenna is located (as shown in the bottom of Figure 6.3 (a) and the left of Figure 6.3

(b)). Conductivity is set to 1.1 s/m in the x/y direction PML, and 1.5 s/m in z direction PML.



(a) **(b)** **(c)**

Figure 6.3 The domain of the head mesh and the antenna system in axial (a), sagittial (b), and coronal (c) directions. The yellow frames in each subfigure are the PML layers, the red dot in (a) and red line in (b) show the position of the external antenna.

6.2.2 Transmission Line Excitation/Reception and Power Calculations

At the feeding location, the transmitting dipole antenna is excited by a virtual transmission line [209], which is injected with a differentiated Gaussian pulse with sufficient frequency content around the intended operational frequency. The differentiated Gaussian pulse is shown below:

$$G(t) = \frac{1}{T \times 10^{-12}}(t - S \times T \times 10^{-9}) exp(-(\frac{(t - S \times T \times 10^{-9})}{T \times 10^{-9}})^2) \qquad (6.1)$$

A set of suitable parameter S and T have to be chosen for a wide band spectrum that includes resonant frequencies ranging from 1GHz to 4GHz corresponding to the antennas with the lengths of 15 mm, 9 mm and 5 mm (accurate resonate frequency of each antenna will be discussed in the next section). The parameter T affects the time-shift and bandwidth of the differentiated Gaussian pulse, while S affects the time-shift only. We set T = 0.1 and S = 5.8 in this chapter to cover all the interested frequencies. The differentiated Gaussian pulse in the time domain and its frequency respond are shown in Figure 6.4.

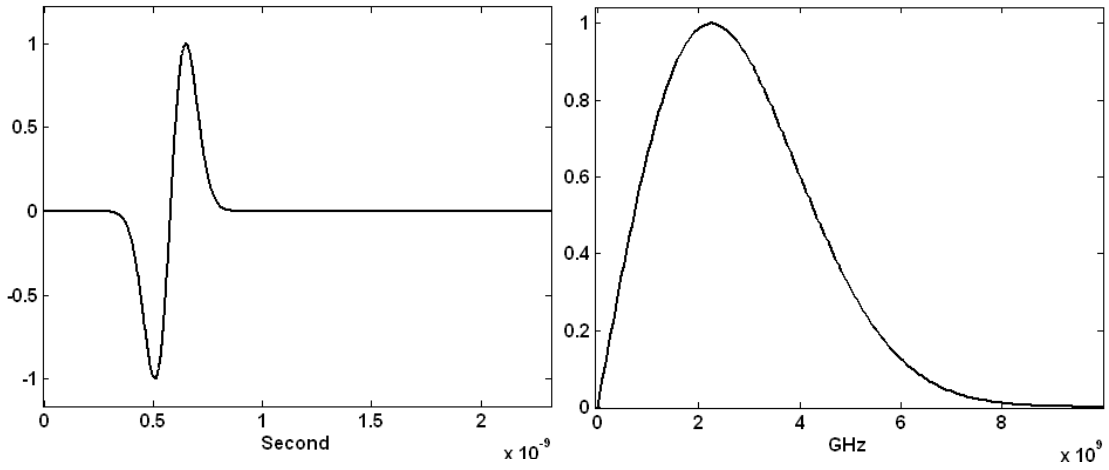


Figure 6.4 The differentiated Gaussian pulse in time (a) and frequency (b) domains.

Custom simulation software using C++, a coaxial probe (one dimensional transmission line) feed model is implemented with the standard three dimensional FDTD algorithms. In the hybrid algorithm, the nature of updated equations at the aperture plane (interface between the coaxial line and the environment) is the key to

make simulation numerically stable (please see the mathematical implementation in Figure 6.5). This hybrid algorithm which is conditionally stable is subject to continuous adjustment according to the geometry, structure and properties of the object in the calculation, therefore it can seldom be found in any commercial FDTD package due to its problem dependant nature.

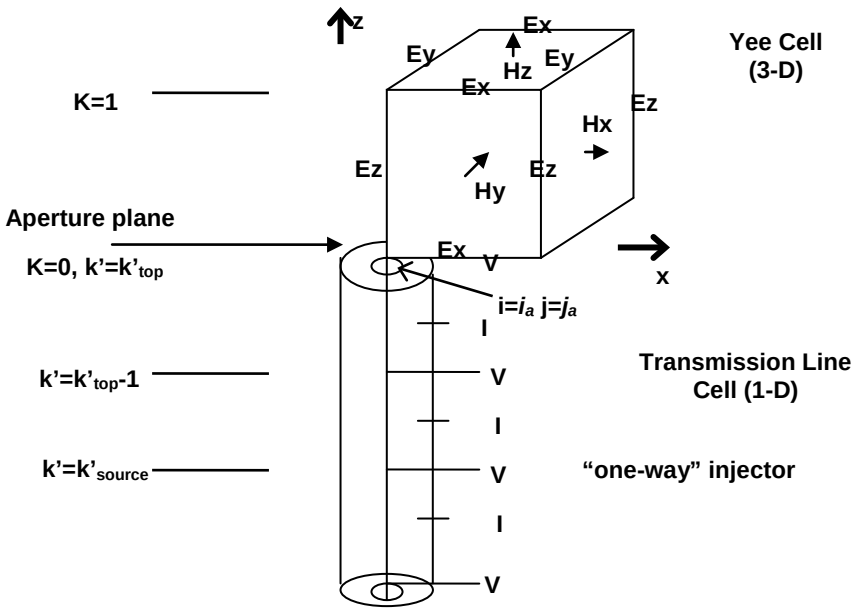


Figure 6.5 Interface between the coaxial transmission line and the three dimensional FDTD code.

A virtual coaxial with a matched impedance (the impedance matching is explained in section *6.2.3*) is modeled as a loss-free one-dimensional transmission line [207] connected to the center-fed dipole antennas. The equations used to calculate the currents and voltages inside the transmission line are given by

$$I_{k'+0.5}^{n+0.5} = I_{k'+0.5}^{n-0.5} - \frac{1}{Z_0}\frac{v\Delta t}{\Delta z}\left[V_{k'+1}^{n} - V_{k'}^{n}\right] \tag{6.2}$$

$$V_{k'}^{n+1} = V_{k'}^{n} - Z_0\frac{v\Delta t}{\Delta z}\left[I_{k'+0.5}^{n+0.5} - I_{k'-0.5}^{n+0.5}\right] \tag{6.3}$$

where v is the speed of propagation of fields within the line and Z_0 is the line impedance. To update the voltage in the aperture, the current above the aperture is needed. This is computed from the adjacent magnetic field values

$$\begin{aligned} I^{n+0.5}(k'_{top}+0.5) &= \Delta y[H_y^{n+0.5}(i_a+0.5, j_a, 0.5) - H_y^{n+0.5}(i_a-0.5, j_a, 0.5)] \\ &- \Delta x[H_x^{n+0.5}(i_a, j_a+0.5, 0.5) - H_x^{n+0.5}(i_a, j_a-0.5, 0.5)] \end{aligned} \tag{6.4}$$

where the indices i_a and j_a locate the axis of the antenna. The unknowns in the 3-D Yee Cells along the transmission line are updated using the standard thin-wire FDTD equations.

$$\begin{aligned} H_y^{n+0.5}(i_a+0.5, j_a, k+0.5) &= H_y^{n-0.5}(i_a+0.5, j_a, k+0.5) \\ &-\left(\frac{\Delta t}{\mu_0 \Delta z}\right)[E_x^n(i_a+0.5, j_a, k+1) - E_x^n(i_a+0.5, j_a, k)] \\ &+\left(\frac{\Delta t}{\mu_0 \Delta x}\right)\left(\frac{2}{(ln(\Delta x/a)}\right)E_z^n(i_a+1, j_a, k+0.5) \end{aligned} \tag{6.5}$$

where a is the radius of the inject coaxial line. The equations for the four H field components that surround the wire at the connection are modified to include the voltage in the aperture.

$$\begin{aligned} H_y^{n+0.5}(i_a+0.5, j_a, 0.5) &= H_y^{n-0.5}(i_a+0.5, j_a, 0.5) \\ &-\left(\frac{\Delta t}{\mu_0 \Delta z}\right)[E_x^n(i_a+0.5, j_a, 1) - \left(\frac{2}{ln(\Delta x/a)}\right)\frac{V^n(k'_{top})}{\Delta x}] \\ &+\left(\frac{\Delta t}{\mu_0 \Delta x}\right)\left(\frac{2}{(ln(\Delta x/a)}\right)E_z^n(i_a+1, j_a, 0.5) \end{aligned}$$

(6.6)

The remainder of the space surrounding the coaxial line is discretized using standard 3D Yee cells. The incident waveform (V_{inc}) is introduced into the coaxial line using a "one-way" injector at position k'=k'$_{source.}$

$$I^{n+0.5}(k'_{source}+0.5)=I^{n-0.5}(k'_{source}+0.5)-(\frac{1}{Z_0})(\frac{v\Delta t}{\Delta z})[V^n(k'_{source}+1)-V^n(k'_{source})] + (\frac{1}{Z_0})(\frac{v\Delta t}{\Delta z})V^n_{inc}(k'_{source}) \quad (6.7)$$

$$V^{n+1}(k'_{source})=V^n(k'_{source})-(Z_0)(\frac{v\Delta t}{\Delta z})[I^{n+0.5}(k'_{source}+0.5)-I^{n+0.5}(k'_{source}-0.5)] + (\frac{v\Delta t}{\Delta z})V^{n+0.5}_{inc}(k'_{source}+0.5) \quad (6.8)$$

The transmission line implementation is also used to make measurements of the power radiated by the transmit antenna outside of the head, as well as the power received by the implanted receiving antennas. The load impedance, Z_L, as seen from the transmission line is calculated using the following equation:

$$\frac{V(z')}{I(z')}=Z_0\frac{Z_L+jZ_0\tan(\beta z')}{Z_0+jZ_L\tan(\beta z')} \quad (6.9)$$

where z' is the distance between a given point located inside the transmission line and the aperture (interface between the dipole and transmission line), $V(z')/I(z')$ is the ratio of the voltage and current (using frequency domain analysis) at this location, and $\beta=\frac{2\pi}{\lambda}$ is the wave number. The power transmitted to the load by the external antenna was calculated through Equation (6.10).

$$\boldsymbol{P_L} = \frac{1}{2}\boldsymbol{Re}\left[\boldsymbol{V_L I_L}^*\right] = \frac{1}{2}\left|\boldsymbol{I_L}\right|^2 \boldsymbol{Re}\left[\boldsymbol{Z_L}\right] \tag{6.10}$$

where the load current, I_L, was obtained using

$$\left|\boldsymbol{I_L}\right|^2 = \left\|\boldsymbol{I_{inc}}\right\|1-\Gamma\right\|^2 \tag{6.11}$$

$|I_{inc}|$ in Equation (6.11) represents the magnitude of the current injected into the transmission line of the external antenna, and Γ represents the reflection coefficient. Γ is calculated using the following equation:

$$\Gamma = \frac{\boldsymbol{Z_L} - \boldsymbol{Z}_0}{\boldsymbol{Z_L} + \boldsymbol{Z}_0} \tag{6.12}$$

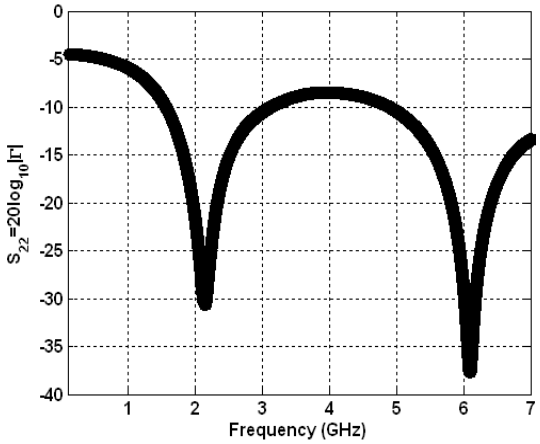
The power received by each of the implanted antennas is calculated using the following equation:

$$\boldsymbol{P_{rec}} = \frac{1}{2}\boldsymbol{Re}\left[\boldsymbol{V_{rec} I_{rec}}^*\right]. \tag{6.13}$$

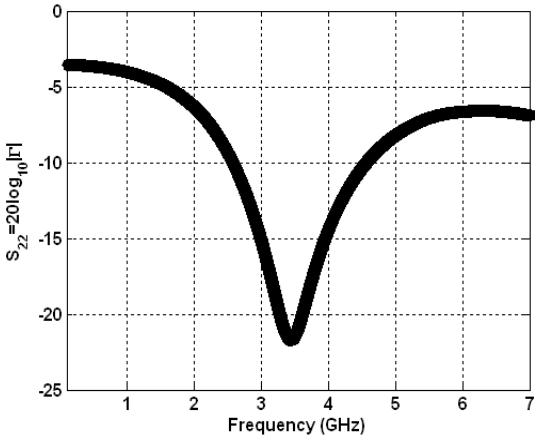
6.2.3 Impedance Matching

From circuit theory, a maximum transfer of power from a given voltage source to a load occurs under “matched conditions” when the load impedance is the complex conjugate of the source impedance. The characteristic impedance of a lossless transmission line is purely real, thus the load impedance is required to be equal to the characteristic impedance of the transmission line when the line is matched [210]. Before calculating the power reception by the implanted antennas, the input matched impedance and the resonant frequency of a load (composed of antenna, BMI chip, human head, and the environment surrounding the head) are computed. A coaxial

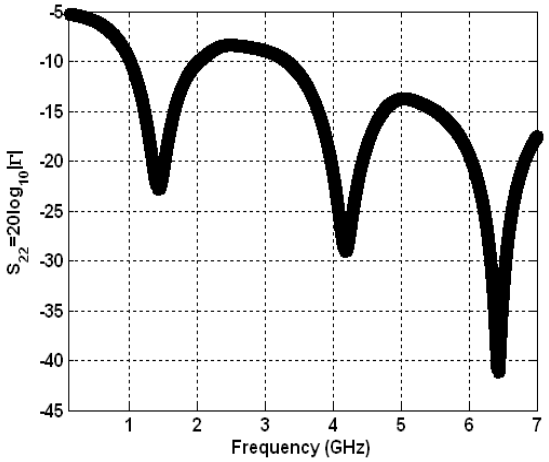
transmission line with an impedance of 50Ω and connected to the implanted antenna is excited with a differentiated Gaussian pulse. The implanted dipole antennas with different lengths at various locations in the human brain radiate electromagnetic waves that resonate at different frequencies. In our arrangement, the input impedance of the loads (as defined above) varies with the antenna length as well as positioning within the human brain. As an example, Figure 6.6 provides the frequency responds of the implanted antennas with the lengths of 5 mm, 9 mm, and 15 mm at the position 10 mm deep into the brain. The impedance responds of the implanted antennas vary with the antenna designs and the geometries of their positions as shown in Figure 6.7. Table 6.1 lists the resonant frequencies (occur when the load input impedance is purely real) and the corresponding input impedance for the 3 specified antennas and at the 4 specified brain depths.



9mm_antenna



5mm_antenna



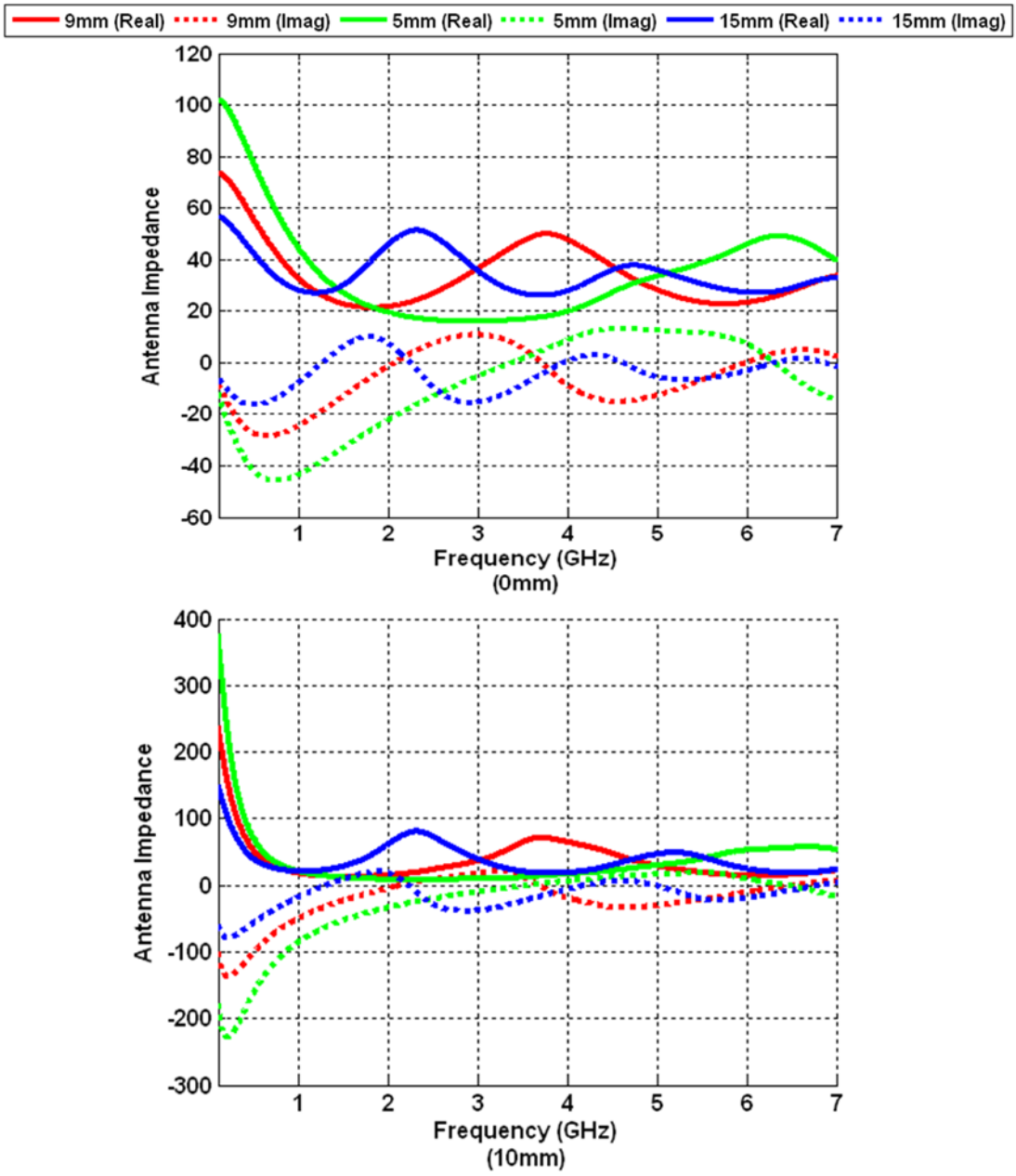
15mm_antenna

Figure 6.6 Frequency responds for antennas with the lengths of 5 mm, 9 mm, and 15 mm at the locations 10 mm into the brain.

Table 6.1 Resonant frequencies and input impedances for the loads with different antenna lengths at various positions within the brain.

Antenna length	0 mm into the brain		10 mm into the brain		30 mm into the brain		60 mm into the brain	
	f (GHz)	Z (Ω)	f (GHz)	Z (Ω)	f (GHz)	Z (Ω)	f (GHz)	Z (Ω)
5 mm	3.39	16.5	3.56	12.0	3.59	12.1	3.01	14.6
9 mm	2.07	22.7	2.16	16.5	2.18	14.6	1.95	16.5
15 mm	1.27	27.1	1.31	23.1	1.37	18.4	1.27	18.3

After calculating the resonant frequencies and impedances of the implanted antennas in conjunction with the human head, we use the external antenna as the transmitting power source and the implanted antennas as the receiving device to study the RF power available to operate the implanted BMI chip. The characteristic impedance of the transmission line connected to the external (transmitting) antenna is 50Ω; while the characteristic impedance of the transmission line connected to the implanted (receiving) antenna is adjusted to the input impedances shown in Table 6.1 for the most efficient power reception. Please kindly note that the relation between the energy deposition in the head-BMI system and the power reception of the implanted antenna is not affected by the efficiency of the external antenna.


9mm (Real)
9mm (Imag)
5mm (Real)
5mm (Imag)
15mm (Real)
15mm (Imag)
Antenna Impedance
Frequency (GHz)
(0mm)
Antenna Impedance
Frequency (GHz)
(10mm)

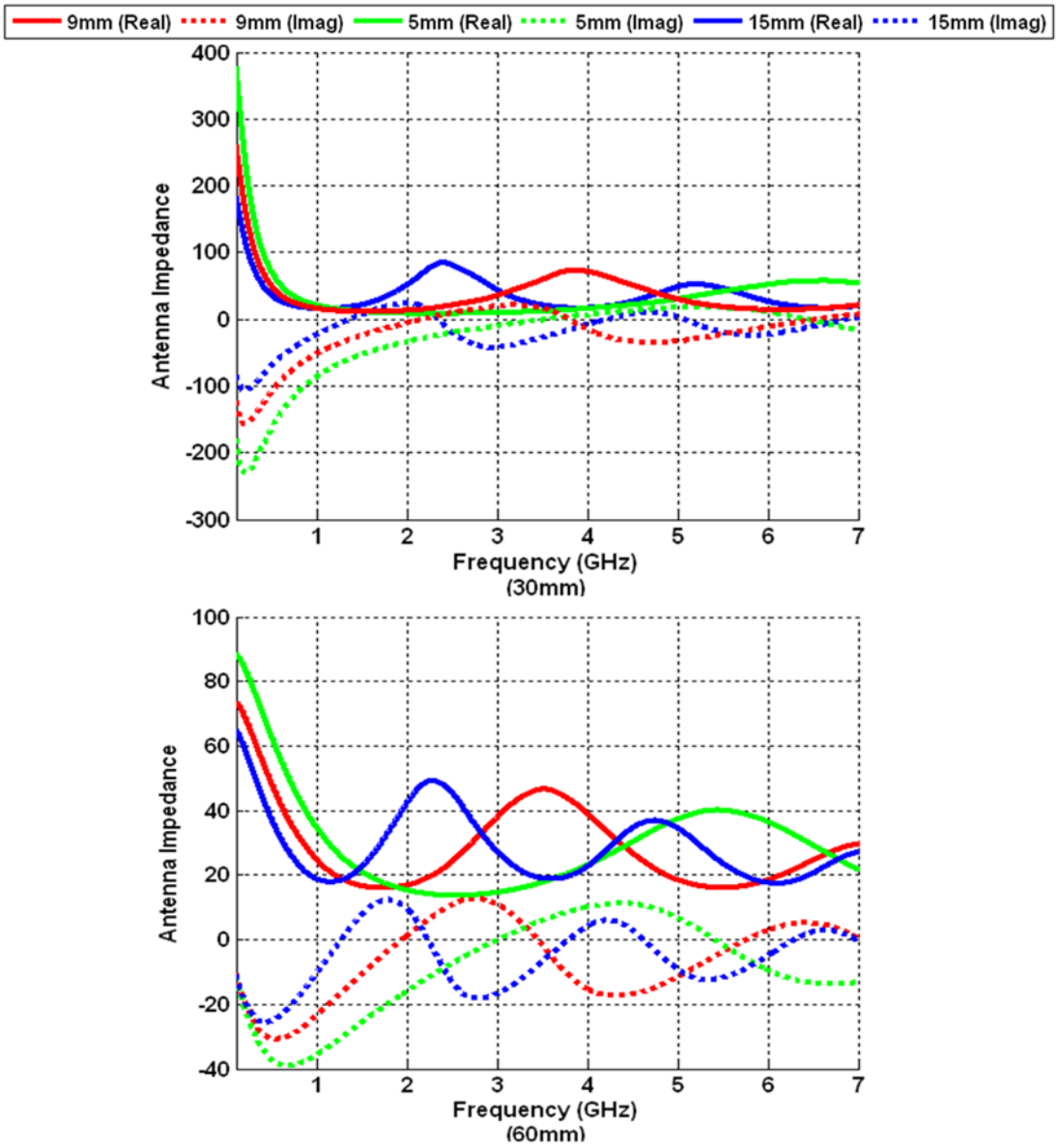


Figure 6.7 Impedances of the implanted antennas (5 mm, 9 mm, 15 mm) at locations 0 mm, 10 mm, 30 mm and 60 mm from the surface into the brain as shown in Figure 6.2.

6.2.4 The Three Dimensional Bio-Heat Model

The temperature changes caused by the RF-powered BMI devices include two components: the energy deposition on the head due to the RF radiation from the

external transmitting antenna and the local heating due to the operation of the implanted BMI device. The total temperature elevation at the worst case scenario is the combination of the two effects.

(a). Temperature Changes due to the RF Radiation by the Transmitting Antenna

After calculating the electromagnetic fields in the human head model due to the communication between the antennas, SAR distribution within the human head model is computed. The temperature T changes due to the RF field from the external transmitting antenna are calculated using Equation (5.6), and Equation (5.7)-(5.13) introduced in Chapter 5 are also used here at the boundary between the tissue and air. The head model, initially at a uniform 37 ºC, is put into 24 ºC environment without RF power deposition (SAR=0) until equilibrium condition T_0 is met. A steady-state is defined as $dT/dt = 2 \times 10^{-7}$ °C/s for at least 20 minutes. Then the SAR due to the RF field is input in order to calculate the temperature elevations caused by the RF power emitted from the external antenna. The spatial and time steps are 1 mm and 0.0125 second, respectively. The thermal properties of the tissues in the head model can be found in Table 5.1.

(b). Temperature Changes due to the Operation of the Implanted BMI-Chip

Temperature changes due to the powered device are calculated using the following equation:

$$\rho C_p \frac{\partial T}{\partial t} = K\nabla^2 + A_0 - B(T - T_b) + P_{chip,density} \qquad (6.14)$$

Equation (6.14) is similar to Equation (5.1) except that the SAR effect is changed to the received power density of the BMI chip. The boundary condition of the T calculation is the same as Equation (5.2). In the three dimensional calculations of the temperature distribution, temperature (T) changes due to the operation of the implanted BMI chip are calculated, where the spatial and time steps are set to 1×10^{-4} meter and 2.2×10^{-5} second, respectively. Initial T condition was set as uniform 37°C. The thermal properties of the white matter (the tissue surrounding the implanted BMI chip) and silicon can be found in Table 6.2.

Table 6.2 Thermal properties for white matter tissue and the BMI-chip(s) contained in the human head model.

	Basal Metabolic Rate	**Specific Heat**	**Blood Perfusion Coeff.**	**Thermal Conductivity**
	A0	**C**	**B**	**K**
	[J/m^3 s]	**[J/kg °C]**	**[J/ m^3 s °C]**	**[J/m s °C]**
Brain – White Matter	7100	3600	40000	0.5
Silicon	0	959	0	150

Figure 6.8 shows the domain for calculating temperature rises due to the operation of the implanted BMI chip. The silicon slab (the blue box) with the power source plane (the red box) is embedded in the center of the white matter block (the yellow box). According to the different sizes of the antennas, the power source regions have dimensions of $0.5mm\times0.1mm\times9mm$, $0.5mm\times0.1mm\times5mm$, and $0.5mm\times0.1mm\times15mm$, respectively. The silicon slabs completely enclose the power planes with one 0.1 mm extension in each direction, and they are embedded in

the center of the white matter block with the dimensions of $4\boldsymbol{mm} \times 4\boldsymbol{mm} \times 13\boldsymbol{mm}$, $4\boldsymbol{mm} \times 4\boldsymbol{mm} \times 9\boldsymbol{mm}$, and $4\boldsymbol{mm} \times 4\boldsymbol{mm} \times 19\boldsymbol{mm}$.

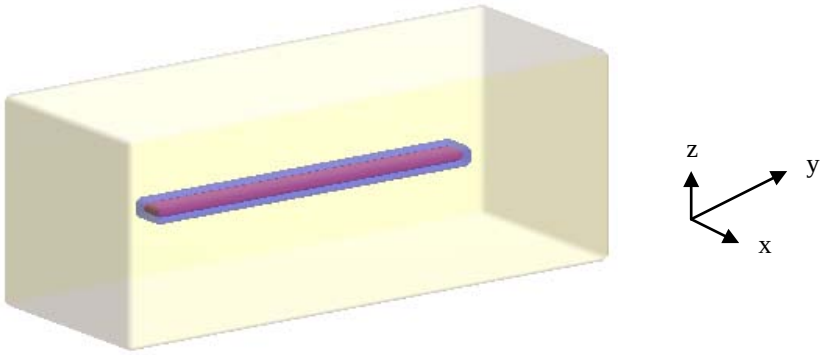


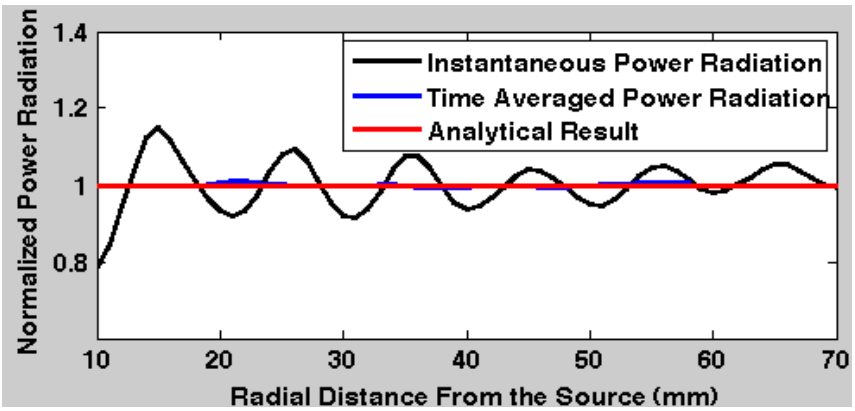
Figure 6.8 A silicon power plane in the white matter cube.

6.3 Validation

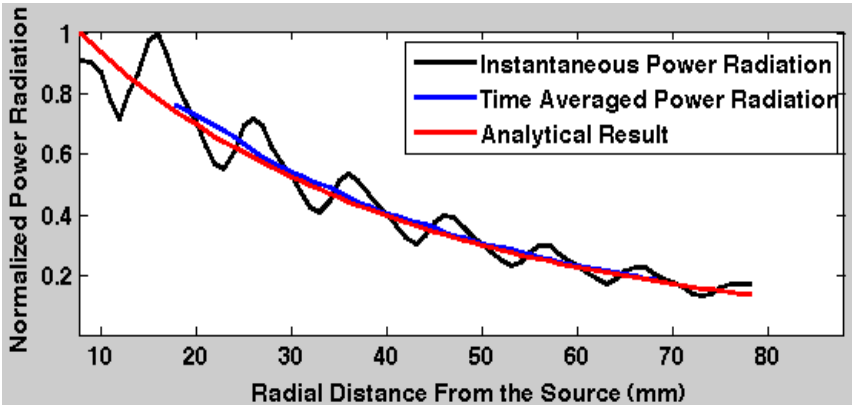
An analytical model of a dipole antenna immersed in a dielectric media is constructed to validate the calculation of the implementation of the power source and the power propagation applied in this chapter.

Two pieces of dielectric (lossless/lossy) blocks with cubic shape are modeled using FDTD electromagnetic numerical method with 32 PMLs [37] on each of the six outer boundaries. Considering the operational frequency of 2.4 GHz and the relative dielectric constant 39.0, the resolution of the domain is set $1\boldsymbol{mm} \times 1\boldsymbol{mm} \times 1\boldsymbol{mm}$ and the time step is 1.8873 Pico seconds. A coaxial probe feed model is implemented at the center of the calculation domain. Bounded with PMLs, the power radiated from the exciting source in the FDTD model propagates similarly as it does in the lossless/lossy medium of infinite extent. After 200000 time steps, the recorded electromagnetic fields in the time domain are calculated at the operational

frequency 2.4 GHz using Fourier transforms. Figure 6.9 demonstrates the results of the power radiation in (a) lossless ($\sigma = 0$) and (b) lossy ($\sigma = 0.46$) medium, respectively. In the simulation of power propagation in a lossless block (Figure 6.9 (a)), the power radiated through a set of cubic-shape surfaces enclosing the excitation source is accurately calculated as a function of the distance from the source. In the case of lossy medium, instead of the rectangular surface, the power radiation is computed through a series of spherical enclosures centered as the excitation source for the comparison with the analytical result from Equation (6.15). The accuracies of the calculations in the spherical surface slightly vary with the radius of the spheres when rectangular cells in the FDTD model are applied into a polar coordinate. Therefore, the power radiation through a sphere enclosure is averaged every three adjacent spherical layers (the resolution of the spherical layers is 1 mm which is the same as the FDTD mode) in Figure 6.9 (b).



(a)



(b)

Figure 6.9 Power radiation in (a) lossless (a) and (b) lossy medium. The instantaneous (black line), time averaged (blue line) and analytical result derived from Equation (6.15) (red line) of the power radiation is normalized and shown as a function of radial distance from the source in both (a) and (b).

The output from the full wave FDTD model in a lossless medium Figure 6.9 (a) shows that the total power radiated outward measured from a cubic surface is conserved: the simulation result of the time average power radiation over one period ($\lambda = \frac{2\pi}{\beta}$ where $\beta = \omega\sqrt{\mu\varepsilon}$ for a lossless medium) does not change with propagation remarkably (less than 1% difference off the analytical result), which is agree with the

energy conservation law [211]. While in a lossy medium, the simulation results show that energy decays with its propagation as shown in Figure 6.9 (b). Similarly, the time average power radiation over one period ($\lambda = \frac{2\pi}{\beta}$ where $\beta \approx \omega\sqrt{\mu\varepsilon'}[1+\frac{1}{8}(\frac{\varepsilon''}{\varepsilon'})^2]$ and $\frac{\varepsilon''}{\varepsilon'} \approx \frac{\sigma}{\omega\varepsilon}$) from the FDTD simulation follows the analytical result very well.

According to the power calculation from Equation (6.15) [212], radiated power of a Hertzian dipole is a function of the operational frequency, the radial distance from the source, and the properties of the excitation source and the medium.

$$P = \mathrm{Re}\, a\left\{ \int_0^{2\pi} \int_0^{\pi} SR^2 \sin\theta d\theta d\varphi \right\}$$

$$= \frac{\omega^3 p^2 \mu}{12\pi(\alpha^2+\beta^2)}[\frac{2\alpha\beta}{R^3} + \frac{4\alpha^2\beta}{R^2} + \frac{2\alpha\beta(\alpha^2+\beta^2)}{R} + \beta(\alpha^2+\beta^2)^2]e^{-2\alpha R} \tag{6.15}$$

Where S is the complex Poynting's vector given as $\boldsymbol{S} = \frac{1}{2}\boldsymbol{E}_\vartheta \boldsymbol{H}_\varphi^*$; R is the radial distance from the source; α and β are the real and imaginary parts of the propagation constant γ given in Equation (6.16).

$$\gamma = \alpha + j\beta = j\omega\sqrt{\mu\varepsilon}(1+\frac{\sigma}{j\omega\varepsilon})^{1/2} \tag{6.16}$$

According to Equation (6.15), analytical calculation is performed and the normalized power radiation is plotted as a function of radial distance from the excitation source shown with the red diamond line in Figure 6.9 (b). The simulation outputs match with the analytical results.

In a summary, the FDTD modeling of the electromagnetic fields, the implementation of the power source and the computation of the power propagation can be accurately applied in the BMI applications.

6.4 Results and Discussions

6.4.1 Maximum Receiving Power without SAR Violations

The SAR safety regulations regarding RF deposition in the head varies for different applications, the FDA limits local SAR <=8 W/kg over any gram and the IEC limits local SAR<=10 W/kg for every 10 grams for the heating due to the RF field from MR machines. According to FCC safety regulations, the local SAR peak for any 1gm of tissue should be limited less than or equal to 1.6 W/kg when a human head is exposed to an external radiofrequency electromagnetic field [213]. For the SAR analysis, the power receptions of the implanted BMI antennas are analyzed within the FCC SAR safety limit, the most stringent among all three agencies (we will consider the safety limits from all agencies when analyzing temperature changes). Table 6.3 shows the maximum receiving RF power before the FCC SAR violation limits for the three dipole antennas with different lengths at their individual resonant frequencies (Table 6.1) and at various depths in the brain. According to Friis transmission formula (Equation 6.17), the receiving power is inversely proportional to the square of the distance between the two antennas and the wavelength in an ideal vacuum environment.

$$\frac{P_r}{P_t} = \frac{A_{er} A_{et}}{r^2 \lambda^2} \tag{6.17}$$

Where *Pr* is the received power, *Pt* is the transmitted power, *Aet* and *Aer* is the effective aperture of the transmitting antenna and the receiving antenna, *r* is the distance between antennas, and λ is the wavelength. In this work, the relation between the power reception and implantation depth of the BMI device does not strictly follow the Friis transmission formula due to the highly inhomogeneous lossy environment inside the head model. Table 6.3 shows that longer antennas receive more power than the ones shorter in length at their individual resonant frequencies. The results clearly show that compared to the longer dipoles, the available (without violation of the FCC SAR limits) RF power decays with greater brain depths at a rapid rate for shorter dipoles.

Table 6.3 Maximum receiving power without FCC SAR safety violation for the three dipole antennas at their corresponding resonant frequencies (shown in Table 6.1).

Antenna Length	0 mm into the Brain	10 mm into the Brain	30 mm into the Brain	60 mm into the Brain
5 mm (μ W)	33.25	9.81	0.74	0.05
9 mm (μ W)	166.03	75.50	16.83	3.42
15 mm (μ W)	737.69	579.53	192.62	51.50

Table 6.4 provides the results of the maximum receiving power without FCC SAR safety violation at the same frequency (2.07GHz, the resonant frequency of 9 mm antenna at 0 mm into the brain) for the antennas with lengths of 5 mm, 9 mm, and 15 mm at different locations. The data show again that longer antennas receive

more RF power without violation of the FCC SAR safety limits. For example, the 15 mm dipole is still the most efficient antenna when compared to the 9 mm and 5 mm antennas even though the operational frequency (2.07 GHz) is 800 MHz away from its resonant frequency (1.27 GHz see Table 6.1). Figure 6.10 demonstrates the performance of the antennas at different operational frequencies.

By studying the results from Table 6.1, 6.3 and 6.4, we conclude that the value of the operating frequency significantly affects the power reception of the implanted antennas: higher frequency results less power availability of RF power without violation of the SAR limits. At higher frequencies, the increased conductivities of the tissues and increased operational frequency reduce the skin depth and thus cause a large portion of the RF energy to be decayed in the head superficially. Table 6.5 provides the examples of the electromagnetic parameters of tissues at two different frequencies 1.27 GHz and 3.39 GHz.

Table 6.4 Maximum receiving power without FCC peak SAR safety violation at frequency 2.0735GHz (the resonant frequency for 9 mm antenna at 0 mm into the brain).

Antenna Length	0 mm into the Brain	10 mm into the Brain	30 mm into the Brain	60 mm into the Brain
5 mm (μ W)	48.47	8.32	2.02	0.66
9 mm (μ W)	166.03	79.96	19.62	2.10
15 mm (μ W)	206.21	119.60	32.75	2.43

Table 6.5 Comparison of the electromagnetic properties of the human head tissues at 1.27 GHz and 3.39 GHz resonant frequencies of the 5 mm dipole and 15 mm dipole at the surface of the brain, respectively.

	ε_r	σ (S/m)	ε_r	σ (S/m)
Frequency	**1.27 GHz**		**3.39 GHz**	
Air	1	0	1	0
Bone (Cancellous)	20.105	0.43393	17.54	1.1559
Bone (Cortical)	12.145	0.19233	10.852	0.59029
Brain – Gray Matter	51.346	1.1105	47.469	2.5409
Brain – White Matter	37.917	0.71226	35.12	1.7418
Cartilage	41.521	0.96776	36.799	2.5464
Cerebellum	47.652	1.4353	43.304	2.7777
Cerebrospinal Fluid	67.98	2.5893	64.759	4.4416
Dura	43.69	1.0906	40.854	2.2856
Fat	5.4108	0.060952	5.1548	0.14975
Mucous Membrane	44.924	0.98968	41.612	2.2258
Muscle	54.314	1.0853	51.58	2.4623
Nerve	31.662	0.67552	29.27	1.5179
Skin (Dry)	39.995	0.99117	37.1	1.9597
Skin (Wet)	44.924	0.98968	41.612	2.2258
Spinal Chord	31.662	0.67552	29.27	1.5179
Tongue	54.446	1.0925	51.313	2.5819
Tooth	12.145	0.19233	10.852	0.59029
Vitreous Humor	68.791	1.7683	67.496	3.3487

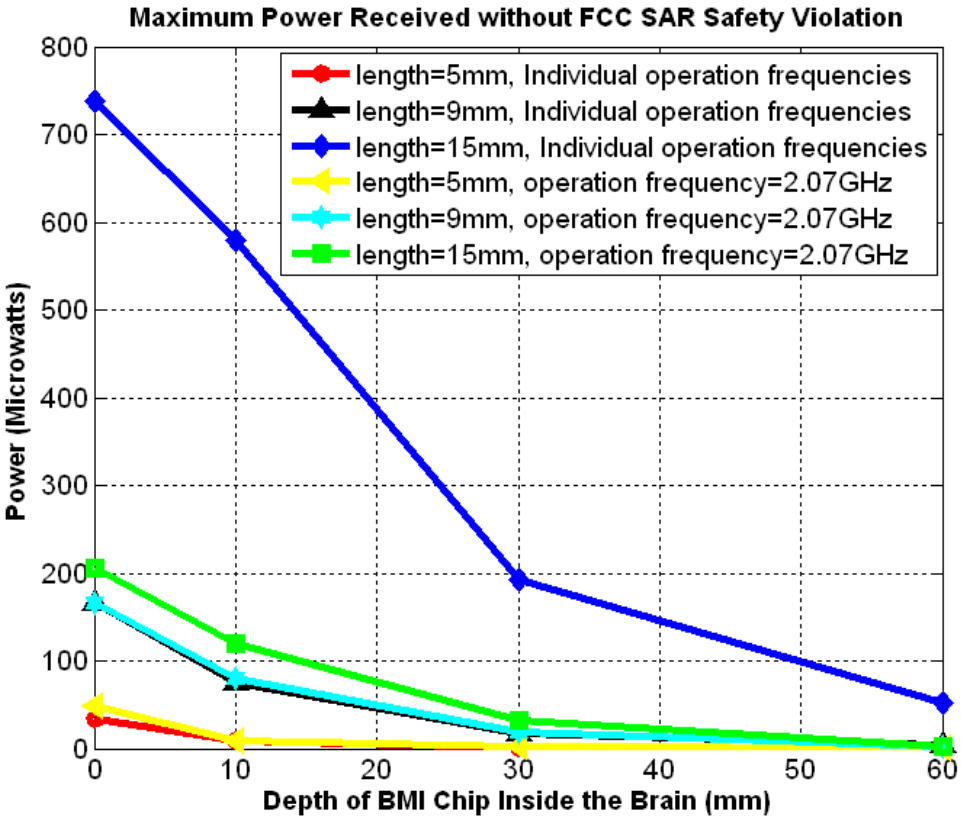


Figure 6. 10 Antenna performances at different frequencies in receiving power without FCC SAR safety violation. Antennas individual operation frequencies are presented in Table 6.1.

Although lower frequencies are desirable, the geometry of the antenna affects its intrinsic impedance. In order to minimize the use of the typically lossy matching circuits (match the antenna intrinsic impedance to the chip circuits), a balanced choice of antenna geometry and operational frequency is crucial. As a result, a crafted combination of shallower implantation depth, lower operational frequencies and longer receiving antennas (when dipole antennas are applied) are preferred purely from the aspects of the RF power reception and the safety concerns.

6.4.2 Temperature Changes

(a). Temperature Changes due to the RF Radiation by the transmitting antenna

SAR distribution within the human head model was computed for each case as shown in Table 6.3 and 6.4, where the maximum SAR was limited as 1.6 W/kg according to the FCC safety regulation. Table 6.6 and 6.7 show the maximum temperature elevations due to the RF radiation by the transmitting antenna for each implanted antenna at various brain depths shown in Tables 6.3 and 6.4. From Tables 6.6 and 6.7, the 1.6 W/kg SAR peak results in the temperature increase less than or equal to 0.02 °C for each case. The results in Table 6.6 show that 1) higher frequencies result in higher temperature elevations while the SAR peaks are constrained to the same value (the details of the resonant frequencies are provided in Table 6.1); 2) the maximum temperature elevation decreases with increase of the implanted depth for each antenna. Using the same operational frequency 2.07GHz, the maximum temperature elevations for different antennas at various brain depths are similar as shown in Table 6.7. Figure 6.11 provides a set of examples of the logarithmic SAR and temperature distributions for three types of antennas at 0 mm into the brain. The top row shows the logarithmic SAR distributions with 5 mm, 9 mm and 15 mm antennas using the same color bar. Comparing the three subfigures in the top row, the deposited energy extends deeper into the brain at the lower frequencies than higher frequencies with the same SAR peak (1.6 W/kg averaged over every gram of the head tissue), for example, the heat deposition on the head model decays faster for the 5 mm antenna than the 15 mm antenna. It is again due to

changes of the electromagnetic properties of the head tissue with the increased frequencies. The bottom row of Figure 6.11 shows the corresponding temperature elevations caused by the input SARs. The highest heated spot is located the region close to the surface of the head, and the 5 mm antenna results in the largest temperature increase.

Table 6.6 The maximum temperature elevations due to SARs from the each case shown in Table 6.3.

Antenna Length	0 mm into the Brain	10 mm into the Brain	30 mm into the Brain	60 mm into the Brain
5 mm (μ W)	48.47	8.32	2.02	0.66
9 mm (μ W)	166.03	79.96	19.62	2.10
15 mm (μ W)	206.21	119.60	32.75	2.43

Table 6.7 The maximum temperature elevations due to SARs for each case shown in Table 6.4.

Antenna Length	0 mm into the Brain	10 mm into the Brain	30 mm into the Brain	60 mm into the Brain
5 mm (°C)	0.010	0.010	0.011	0.011
9 mm (°C)	0.011	0.010	0.011	0.011
15 mm (°C)	0.011	0.010	0.010	0.011

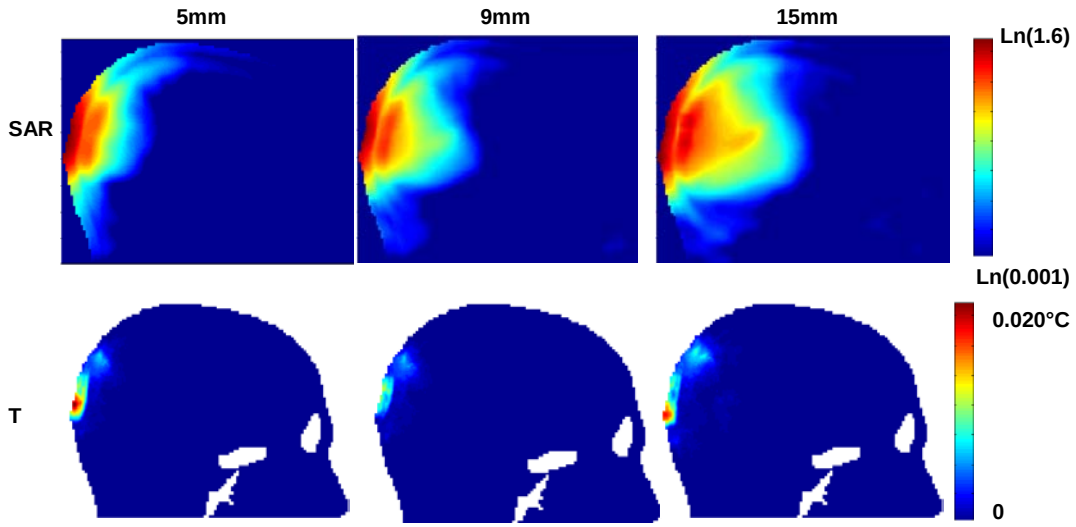


Figure 6.11 Logarithmic SAR and temperature (T) distributions for the antennas with the lengths of 5 mm, 9 mm and 15 mm located at 0 mm into the brain.

The regulations of SAR safety due to the RF radiations are different for various RF devices. The FDA limits local SAR <=8 W/kg over any gram and the IEC limits local SAR <=10 W/kg averaged every 10 gram tissues for the energy deposition on the human head during MRI exams. The maximum temperature elevations under different safety regulations are provided in Table 6.8 for the antennas at 0 mm into the brain. The temperature increases less than 0.84°C for all cases.

Table 6.8 The maximum temperature elevations due to the external transmitting antenna for the antennas at 0 mm into the brain using different SAR safety regulations.

Antenna Length	SAR peak = 8W/kg for any gram	SAR peak = 10W/kg for any 10 grams
5 mm (°C)	0.36	0.70
9 mm (°C)	0.35	0.83
15 mm (°C)	0.37	0.84

(b). Temperature changes due to the power reception by the implanted antenna

According to Table 6.3 and 6.4, the maximum power reception of the implanted antennas without violating FCC SAR safety regulation appears at the position 0 mm into the brain when the antennas perform at their individual resonant frequencies. The temperature changes due to the received power by the three types of antennas are calculated. Figure 6.12 shows the temperature distribution inside the tissue cube with continuous input power of 33.25 μW (5 mm antenna), 166.03 μW (9 mm antenna) and 737.69 μW (15 mm antenna) on the BMI chip. One test point right below the BMI device is used to record the temperature changes with time for these three types of antenna designs (Figure 6.13).

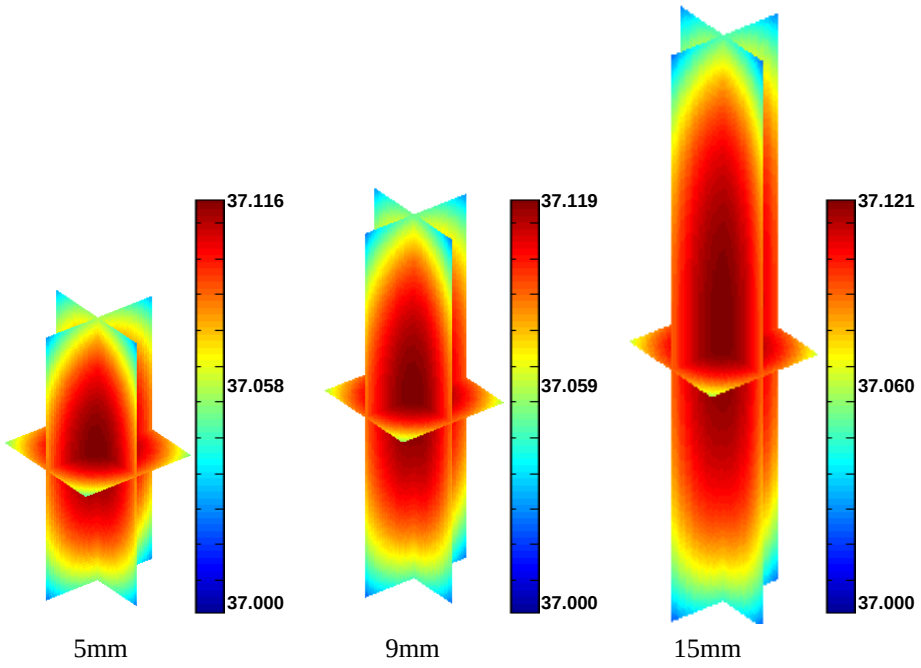


Figure 6.12 Temperature distributions within the white-matter cubes containing the 5 mm, 9 mm, and 15 mm antennas.

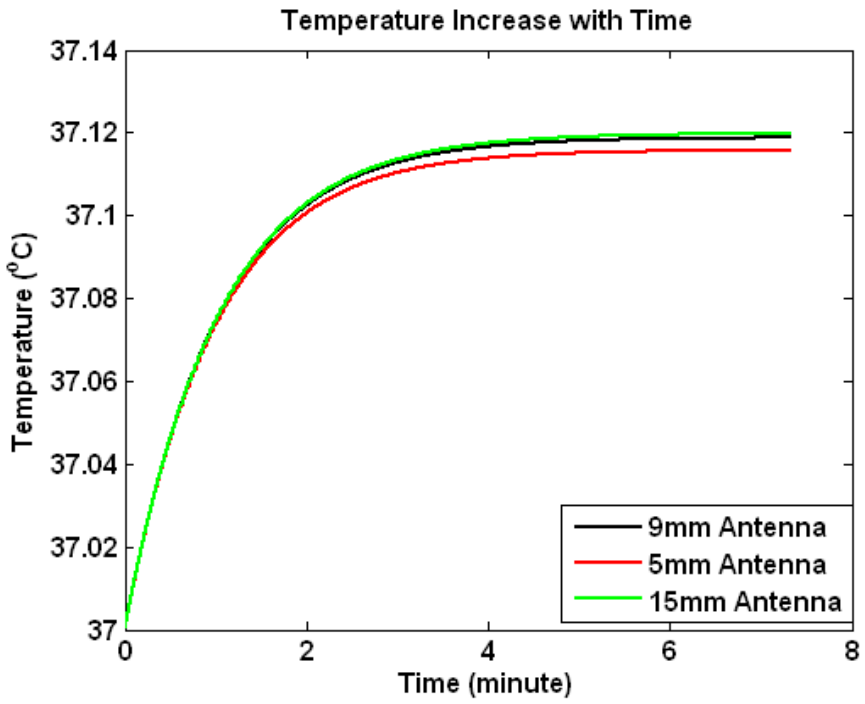


Figure 6.13 Temperature increase with time at the test point.

Table 6.9 provides the maximum power receptions of the three types of implanted antennas at 0 mm into the brain and the induced temperature elevations, without violating the different SAR safety regulations. The data shows that using different SAR safety regulations, the temperature elevations due to the implanted IC chip for each antenna design do not significantly change with the power reception.

Table 6.9 The maximum temperature elevations for the antennas at 0 mm into the brain using different SAR safety regulations.

Safety Regulation	SAR peak = 1.6 W/kg for any gram		SAR peak = 8W/kg for any gram		SAR peak = 10W/kg for any 10 grams	
0 mm into the brain	Power Reception (μW)	T Elevation (°C)	Power Reception (μW)	0 mm into the brain	Power Reception (μW)	T Elevation (°C)
5 mm	33.25	0.116	166.25	5 mm	33.25	0.116
9 mm	166.03	0.119	830.15	9 mm	166.03	0.119
15 mm	737.69	0.121	3688.51	15 mm	737.69	0.121

The total temperature elevation due to a RF powered wireless BMI device is the combination of the changes due to the RF radiation from the external transmitting antenna (Table 6.6 and 6.8) and the changes due to the implanted antenna on the IC chip (Table 6.9). By analyzing the data in Table 6.6, 6.8 and 6.9, the temperature (T) increase is able to be controlled within 1 Celsius-degree that is considered safe.

6.5 Summary

In this chapter, the power reception and temperature elevation associated with wireless powering of a BMI in the brain are studied. A three dimensional FDTD system (including the human head model, transmitting antenna and implanted BMI chips) is developed to calculate SAR distributions within the head model during the communications between the external antenna and the implanted antenna on the BMI chip. Without violating local SAR peak of 1.6 W/kg from FCC regulation, the maximum receiving power by the implanted antennas are calculated for the dipole antenna designs with different lengths at various depths into the human brain. The results demonstrate that a longer receiving antenna (when dipole antennas are

applied) with lower working resonant frequency and shallower implantation depth maximizes RF power reception prior to violating the safety limits.

The local temperature of the human head changes with the RF powered BMI devices. The temperature elevation is due to a summation of the energy deposition on the head from the RF radiation of the external transmitting antenna and the local heating due to the received power by the implanted antenna on the BMI unit. The temperature changes are calculated not only for the FCC SAR safety regulation, but also for the SAR safety limits from the FDA and IEC. The results from the bio-heat simulations show that the highest temperature increase of the head model is less than 1 Celsius-degree. It suggests that wirelessly powered BMIs can be safely implemented in humans by studying well-controlled electromagnetic-field exposure of cell *in vitro*.

CHAPTER 7

CONCLUSIONS AND FUTURE WORK

7.1 Summary and Findings

The interactions between the radio frequency (RF) electromagnetic fields and the human biological tissues during ultra high field MRI exams and RF powered wireless BMI operations severely affect the performances of MRI and BMI operations and also cause the local heating in the tissues arousing safety concerns. In this dissertation, a complete electromagnetic computational (full wave) analysis, the finite difference time domain (FDTD) method [36], is applied to calculate the field interactions to improve and ameliorate the performances of high field MRI and RF powered wireless BMI. Through precisely numerical calculations, we accomplished in this dissertation 1) the design of an improved B_1^+ shimming scheme [24-31] to improve the performance of RF transverse electromagnetic (TEM) coils with safety concerns in MRI applications; and 2) the evaluations of the RF power consumption and safety for a prototype of wireless invasive BMI device.

In this dissertation, the foreword including the motivation for this research is presented in Chapter 1. After the physics background introduction of the MRI and BMI in Chapter 2, the FDTD computational electromagnetic method and the perfectly matched layer (PML) boundary condition [37] are described in Chapter 3. The full wave FDTD method is applied in MRI applications in Chapter 4 and 5, as well as BMI applications in Chapter 6.

7.1.1 MRI Applications

In MRI applications, the designed B_1^+ shimming scheme in this dissertation is improved to be able to greatly improve performance of the TEM RF coil in high/ultra high field, while keeping the patients from excess global and local power deposition.

High/ultra high field MRIs provide the potential for an increased signal-to-noise ratio (SNR) [86]. However, inhomogeneous B_1^+ field distributions, increased radiofrequency (RF) power requirements, and thus excessive tissue heating are the significant technical difficulties in ultra high field MRIs [15-17, 23]. In Chapter 4, the inhomogeneous B_1^+ field with the increase of B_0 field strength [31], and the relationship between the RF power absorption in tissues and the field strength or frequency of operation are studied systematically. It is found that the shimming scheme purely to optimize homogeneity of the B_1^+ field distributions results in increased power requirements. The studies also show that in order to achieve a highly homogenous B_1^+ field distribution with a specified criterion of homogeneity, the use of more drive ports, and therefore more phase-locked transmit channels, will significantly reduce the RF power required to achieve a fixed average B_1^+ field intensity.

To improve homogeneity of the B_1^+ field while maintaining constrained power absorption as well as the local SAR peak, the B_1^+ shimming scheme is improved by adding two constraints of the global power requirement and local SARs: the total power depositions and the maximum SAR in the model have to be less than or equal

to the corresponding values under quadrature excitation within each iteration of the algorithm. The B_1^+ shimming routines are comprised of a combination of both gradient-based and genetic algorithm functions where a single iteration may go through either of these two methods. The numerical results show that the improved homogeneity of the B_1^+ field distribution with constrained total RF power absorption and the local SAR peak could be achieved simultaneously by this improved B_1^+ shimming scheme. It is shown that the shimming scheme is not only able to homogenize and localize the exciting magnetic field in the ROIs, but is also able to rearrange the distribution of the electrical field.

Chapter 4 also provides the experimental validation of the shimming method. The calculated values of amplitudes and phases from simulation results are applied directly to excite an 8-strut TEM coil loaded with a head-sized spherical phantom in 7 tesla experiments. The excellent matches between the simulation and experimental images prove the validity of both the B_1^+ shimming scheme and the FDTD modeling method.

In Chapter 5, the human thermal responses due to the RF field in MRI under quadrature condition and the B_1^+ shimming excitation conditions are studied by finite different computations.. Three dimensional bio-heat models of the human head and body models are built to compute and compare the temperature changes of the tissues under different exciting conditions. The temperature elevations in tissues are spatially correlated with the SARs in high field MRIs, especially when the variation of the perfusion rate between different tissues is minor.

7.1.2 BMI Applications

After studying the RF power transmission without violating the SAR safety regulations and the associated local heating problems in BMI applications, we conclude wirelessly powered invasive BMIs can be safely implemented in humans.

In Chapter 6 of this dissertation, the power reception and the induced temperature changes by RF powered wireless BMI devices are studied. A three dimensional FDTD system (including the human head model, the transmitting antenna and the implanted BMI chips) is developed to calculate the SAR inside of the head model during the communications between the external antenna and the implanted antenna. The maximum receiving power by the implanted antennas without violating different SAR safety regulations are calculated. From the calculation results, while being balanced with the requirements from other designs of the BMI devices, a longer receiving antenna (dipole antenna) with lower operational resonant frequency and shallower implanting depth is preferred to obtain more RF power reception without violating the safety limits.

Chapter 6 also presents the temperature changes associated with the RF powered BMI devices. The results from the bio-heat simulations show that the highest temperature increase inside of the head model is less than 1 Celsius degree without violating the SAR safety regulations. These results suggest that wirelessly powered BMIs can be safely implemented in humans by studying well-controlled electromagnetic-field exposure of cell *in vitro*.

7.2 Future Work

7.2.1 Future of MRI

This dissertation explores the interaction of the high frequency RF field with human tissues. The proposed B_1^+ shimming is able to greatly improve the performance of high field MRIs with assurance of patients' safety. However, the obstacle to apply this algorithm into clinical usages is the computation time. The consuming time of the B_1^+ shimming depends on the size of the ROI, the number of the excitation sources in the TEM RF coil (affects the number of the input variables), the number of constraints in the function, the initial condition of the shimming process, and etc. The typical running time is from 5 to 30 minutes for each two dimensional slice or three dimensional slabs/organs using an Intel Pentium 4 CPU with 3.00 GHz. The B_1^+ shimming scheme improves the performance of high field MRIs, but also elongates the exam time that the patients have to stay in the MR scanners. For the applications of B_1^+ shimming in TEM RF coils as introduced in this dissertation, one possible solution to this problem is that the majority of the shimming calculations are performed prior to MRI exams leaving minor adjustments until the patient is positioned in the MRI system thus to reduce the exam time of the patients on the scanner's table; a more effective solution is to improve the efficiency of the shimming algorithm to reduce the consumption of the calculation time. When we extend the applications of the B_1^+ shimming scheme into different types of RF arrays, one potentially effective solution is to apply the B_1^+ shimming in a subject-insensitive RF

array, Tic-Tac-Toe (TTT) coil, as proposed by Ibrahim et al. [214]. According to Ibrahim et al., the gradient-echo images obtained with a 4-channel Tx/Rx TTT coil loaded with the human head, watermelon and saline spherical phantom have very similar patterns, i.e. the B_1^+ field distribution from the designed TTT array is not sensitive to the electromagnetic properties of the objects. Subject-insensitive TTT array has potential to overcome the subject-dependence issue from the TEM coil [193], therefore, the performance of B_1^+ shimming in TTT array prior to the MRI exams of different patients is more feasible than TEM RF coil in clinical applications.

7.2.2 Future of BMI

Studies of the power transmission and the temperature changes associated with operation of wireless BMI devices are conducted in three dimensional analyses in this dissertation. The BMI unit is simplified as a dipole antenna embedded in a dielectric cube at a single location in each case. In the future work, more complex antenna designs, more complicated structures of the BMI devices and multiple implanting locations need to be added into considerations in the simulations. Within safety limits, combining high data-rate transmission with efficient power reception is one of the important requirements of the antenna design in the implanted BMI chips.

BIBLIOGRAPHY

[1] J. P. Hornak, *The Basics of MRI*, 1996.

[2] P. C. Lauterbur, "Image Formation by Induced Local Interaction: Examples Employing Nuclear Magnetic Resonance," *Nature*, vol. 241, pp. 190-191, 1973.

[3] E. M. Haacke, R. W. Brown, M. R. Thompson, and R. Venkatesan, "Magnetic resonance imaging physical principles and sequence desing." New York, NY: Wiley-Liss, 1999.

[4] E. Niedermeyer and F. Lopes Da Sylva, *Electroencephalography: Basic Principles, Clinical Applications, and Related Fields*, 5th ed, 2004.

[5] H. Sheikh, D. J. McFarland, W. A. Sarnacki, and J. R. Wolpaw, "Electroencephalographic(EEG)-based communication: EEG control versus system performance in humans " *Neuroscience Letters*, vol. 345, 2003.

[6] B. OBERMAIER, G. MÜLLER, and G. PFURTSCHELLER, "'Virtual Keyboard' controlled by spontaneous EEG activity," *IEEE TRANSACTIONS ON NEURAL SYSTEMS AND REHABILITATION ENGINEERING*, vol. 11, pp. 422-426, 2003.

[7] T. Navin Lal, M. Schr¨oder, N. J. Hill, H. Preissl, T. Hinterberger, J. u. Mellinger, M. Bogdan, W. Rosenstiel, T. Hofmann, N. Birbaumer, and B. Sch¨olkopf, "A Brain Computer Interface with Online Feedback based on Magnetoencephalography," presented at Proceedings of the 22nd International Conference on Machine Learning, Bonn, Germany, 2005.

[8] J.-H. Lee, J. Ryub, F. A. Jolesza, Z.-H. Chob, and S.-S. Yoo, "Brain–machine interface via real-time fMRI: Preliminary study on thought-controlled robotic arm " *Neuroscience Letters*, vol. 450, pp. 1-6, 2009.

[9] F. A. Mussa-Ivaldi and L. E. Miller, "Brain–machine interfaces: computational demands and clinical needs meet basic neuroscience " *Trends in Neurosciences*, vol. 26, pp. 329-334, 2003.

[10] J. P. Donoghue, "Connecting cortex to machines: recent advances in brain interfaces," *Nature Neuroscience*, vol. 5, pp. 1085-1088, 2002.

[11] J. K. Chapin, K. A. Moxon, R. S. Markowitz, and M. A. L. Nicolelis, "Real-time control of a robot arm using simultaneously recorded neurons in the motor cortex," *Nature Neuroscience*, vol. 2, pp. 664-670, 1999.

[12] D. I. Hoult and R. E. Richards, "The signal-to-noise ratio of the nuclear magnetic resonance experiment," *Journal of Magnetic Resonance (1969)*, vol. 24, pp. 71-85, 1976.

[13] R. Gruetter, S. A. Weisdorf, V. Rajanayagan, M. Terpstra, H. Merkle, C. L. Truwit, M. Garwood, S. L. Nyberg, and K. Ugurbil, "Resolution Improvements in Vivo 1h nmr Spectra with Increased Magnetic Field Strength," *Journal of Magnetic Resonance*, vol. 135, pp. 260-264, 1998.

[14] J. S. Gati, R. S. Menon, K. Ugurbil, and B. K. Rutt, "Experimental determination of the BOLD field strength dependence in vessels and tissue," *Magnetic Resonance in Medicine*, vol. 38, pp. 296-302, 1997.

[15] J. T. Vaughan, M. Garwood, C. M. Collins, W. Liu, L. DelaBarre, G. Adriany, P. Andersen, H. Merkle, R. Goebel, M. B. Smith, and K. Ugurbil, "7T vs. 4T: RF power, homogeneity, and signal-to-noise comparison in head images," *Magn Reson Med*, vol. 46, pp. 24-30, 2001.

[16] T. S. Ibrahim, A. M. Abduljalil, B. A. Baertlein, R. Lee, and P. M. Robitaill, "Analysis of B1 field profiles and SAR values for multi-strut transverse electromagnetic RF coils in high field MRI applications," *Phys Med Biol*, vol. 46, pp. 2545-55, 2001.

[17] D. I. Hoult, "Sensitivity and power deposition in a high-field imaging experiment," *J Magn Reson Imaging*, vol. 12, pp. 46-67, 2000.

[18] C. M. Collins, W. Liu, J. Wang, R. Gruetter, J. T. Vaughan, K. Ugurbil, and M. B. Smith, "Temperature and SAR calculations for a human head within volume and surface coils at 64 and 300 MHz," *J Magn Reson Imaging*, vol. 19, pp. 650-6, 2004.

[19] C. M. Collins and M. B. Smith, "Signal-to-noise ratio and absorbed power as functions of main magnetic field strength, and definition of "90 degrees " RF pulse for the head in the birdcage coil," *Magn Reson Med*, vol. 45, pp. 684-91, 2001.

[20] T. S. Ibrahim, "A numerical analysis of radio-frequency power requirements in magnetic resonance imaging experiment," *Ieee Transactions on Microwave Theory and Techniques*, vol. 52, pp. 1999-2003, 2004.

[21] A. Kangarlu, F. G. Shellock, and D. W. Chakeres, "8.0-Tesla human MR system: temperature changes associated with radiofrequency-induced heating of a head phantom," *JOURNAL OF MAGNETIC RESONANCE IMAGING*, vol. 17, pp. 220-226, 2003.

[22] J. Chen, Z. M. Feng, and J. M. Jin, "Numerical simulation of SAR and B-1-field inhomogeneity of shielded RF coils loaded with the human head," *Ieee Transactions on Biomedical Engineering*, vol. 45, pp. 650-659, 1998.

[23] C. M. Collins, S. Li, and M. B. Smith, "SAR and B1 field distributions in a heterogeneous human head model within a birdcage coil. Specific energy absorption rate," *Magn Reson Med*, vol. 40, pp. 847-56, 1998.

[24] T. S. Ibrahim, R. Lee, B. A. Baertlein, and P. M. L. Robitaille, "Obtaining a homogeneous B1 field at UHF frequencies: use of multiple drives and variable amplitude/phases," presented at The International Society of Magnetic Resonance in Medicine and European Society of Magnetic Resonance in Medicine and Biology Joint Annual Meeting, Glasgow, Scotland, 2001.

[25] T. S. Ibrahim, R. Lee, B. A. Baertlein, and P. M. L. Robitaille, "Optimized RF coils for clinical MRI applications at ultra high field," presented at International Society of Magnetic Resonance in Medicine Workshop on Hardware, Cleveland, OH, 2001.

[26] T. S. Ibrahim, R. Lee, B. A. Baertlein, and P. M. L. Robitaille, "Optimum field distribution using phased array concepts," presented at European Society of Magnetic Resonance in Medicine and Biology Annual Meeting, Paris, France, 2000.

[27] C. M. Collins, W. Liu, B. J. Swift, and M. B. Smith, "Combination of optimized transmit arrays and some receive array reconstruction methods can yield homogeneous images at very high frequencies," *Magn Reson Med*, vol. 54, pp. 1327-32, 2005.

[28] T. S. Ibrahim, R. Lee, B. A. Baertlein, A. M. Abduljalil, H. Zhu, and P. M. Robitaille, "Effect of RF coil excitation on field inhomogeneity at ultra high fields: a field optimized TEM resonator," *Magn Reson Imaging*, vol. 19, pp. 1339-47, 2001.

[29] T. S. Ibrahim, R. Lee, B. B. Baertlein, and P. M. L. Robitaille, "Optimized radiofrequency resonators for high field NMR clinical imaging," presented at IEEE International Symposium on Antennas and Propagation, Salt Lake City, Utah, 2000.

[30] Z. J. Wang and D. J. Wang, "An RF field pattern with improved B-1 amplitude homogeneity," *Concepts in Magnetic Resonance Part B-Magnetic Resonance Engineering*, vol. 24B, pp. 1-5, 2005.

[31] T. S. Ibrahim and L. Tang, "Insight into RF power requirements and B1 field homogeneity for human MRI via rigorous FDTD approach," *Journal of magnetic resonance imaging*, vol. 25, pp. 1235-47, 2007.

[32] G. Adriany, P. F. Van de Moortele, F. Wiesinger, S. Moeller, J. P. Strupp, P. Andersen, C. Snyder, X. Zhang, W. Chen, K. P. Pruessmann, P. Boesiger, T. Vaughan, and K. Ugurbil, "Transmit and receive transmission line arrays for 7 Tesla parallel imaging," *Magnetic resonance in medicine*, vol. 53, pp. 434-45, 2005.

[33] T. S. Ibrahim, Y.-K. Hue, R. Gilbert, and F. E. Boada, "Tic Tac Toe: Highly-Coupled, Load Insensitive Tx/Rx Array and a Quadrature Coil Without Lumped Capacitors," presented at International Society for Magnetic Resonance in Medicine Annual Meeting, Toronto, Canada, 2008.

[34] K. Setsompop, V. Alagappan, B. Gagoski, T. Witzel, J. Polimeni, A. Potthast, F. Hebrank, U. Fontius, F. Schmitt, L. L. Wald, and E. Adalsteinsson, "Slice-selective RF pulses for in vivo B1+ inhomogeneity mitigation at 7 tesla using parallel RF excitation with a 16-element coil," *Magnetic resonance in medicine*, vol. 60, pp. 1422-32, 2008.

[35] T. S. Ibrahim, D. Abraham, and R. L. Rennaker, "Electromagnetic power absorption and temperature changes due to brain machine interface operation," *Annals of biomedical engineering*, vol. 35, pp. 825-834, 2007.

[36] K. S. Yee, "Numerical solutions of the initial boundary value problems involving Maxwell's equations in isotropic media," *IEEE Trans. Ant Prop*, vol. 14, pp. 302-317, 1966.

[37] J. P. Berenger, "A Perfectly Matched Layer for the Absorption of Electromagnetic-Waves," *Journal of Computational Physics*, vol. 114, pp. 185-200, 1994.

[38] T. S. Ibrahim, R. Lee, A. M. Abduljalil, B. A. Baertlein, and P. M. Robitaille, "Dielectric resonances and B(1) field inhomogeneity in UHFMRI: computational analysis and experimental findings," *Magn Reson Imaging*, vol. 19, pp. 219-26, 2001.

[39] T. S. Ibrahim, C. Mitchell, P. Schmalbrock, R. Lee, and D. W. Chakeres, "Electromagnetic perspective on the operation of RF coils at 1.5-11.7 Tesla," *Magn Reson Med*, vol. 54, pp. 683-90, 2005.

[40] B. L. Beck, K. Jenkins, J. Caserta, K. Padgett, J. Fitzsimmons, and S. J. Blackband, "Observation of significant signal voids in images of large biological samples at 11.1 T," *Magnetic Resonance in Medicine*, vol. 51, pp. 1103-1107, 2004.

[41] L. L. Wald, G. C. Wiggins, A. Potthast, C. J. Wiggins, and C. Triantafyllou, "Design considerations and coil comparisons for 7 T brain imaging," *Applied Magnetic Resonance*, vol. 29, pp. 19-37, 2005.

[42] E. M. Purcell, H. C. Torrey, and R. V. Pound, "Resonance absorbtion by nuclear magnetic moments in a solid," *Physical Review*, vol. 69, pp. 37, 1945.

[43] H. J. Schneider and P. Dullenkopf, "Slotted tube resonator: A new NMR probe head at high observing frequencies," *Review of Scientific Instruments*, vol. 48, pp. 68-73, 1977.

[44] P. C. L. Zhi-Pei Liang, *Principles of magnetic resonance imaging: a signal processing perspective*. New York: Wiley-IEEE Press, 1999.

[45] J. P. Hornak, *The basic of MRI*: http://www.cis.rit.edu/htbooks/mri/, 2005.

[46] E. R. Andrew, *Nuclear Magnetic Resonance*: Cambridge University Press, 1958.

[47] J. T. Vaughan, H. P. Hetherington, J. O. Otu, J. W. Pan, and G. M. Pohost, "High frequency volume coils for clinical NMR imaging and spectroscopy," *Magnetic resonance in medicine*, vol. 32, pp. 206-218, 1994.

[48] D. M. Ginsberg and M. J. Melchner, "Optimum geometry of saddle shaped coils for generating a uniform magnetic field," *Review of Scientific Instruments*, vol. 44, pp. 122-123, 1970.

[49] C. E. Hayes, W. A. Edelstein, J. F. Schenck, O. M. Mueller, and M. Eash, "An efficient, highly homogeneous radiofrequency coil for whole-body NMR imaging at 1.5 T," *Journal of Magnetic Resonance (1969)*, vol. 63, pp. 622-628, 1985.

[50] J. S. Hyde, W. Froncisz, A. Jesmaowicz, J. B. Kneeland, and T. M. Grist, "Parallel imaging acquisition from noninteracting local coils," *Jounal of Magnetic resonance Imaging*, vol. 70, pp. 512-517, 1987.

[51] J. J. Ackerman, "Mapping of metabolites in whole animal by 31P NMR using surface coils," *Nature*, vol. 283, pp. 167-170, 1980.

[52] B. K. Li, F. Liu, and S. Crozier, "Focused, eight-element transceive phased array coil for parallel magnetic resonance imaging of the chest - Theoretical considerations," *Magnetic Resonance in Medicine*, vol. 53, pp. 1251-1257, 2005.

[53] J. J. Vidal, "Real-time detection of brain events in EEG," *IEEE Proceedings*, vol. 65, pp. 633-641, 1977.

[54] M. A. L. Nicolelis, "Actions from thoughts," *Nature*, vol. 409, pp. 403-407, 2001.

[55] P. G. Patil and D. A. Turner, "The Development of Brain-Machine Interface Neuroprosthetic Devices," *Neurotherapeutics*, vol. 5, pp. 137-146, 2008.

[56] N. Birbaumer, T. Hinterberger, A. Kubler, and N. Neumann, "The thoughttranslation device (TTD): neurobehavioral mechanisms and clinical outcome.," *IEEE Trans Neural Syst Rehabil Eng*, vol. 11, pp. 120-123, 2003.

[57] J. Carmena, M. Lebedev, R. Crist, J. O'Doherty, D. Santucci, D. Dimitrov, Patil PG, Henriquez CS, and N. MA., "Learning to control a brain-machine interface for reaching and grasping by primates," *PLoS Biology*, vol. 1, pp. 193-208, 2003.

[58] M. A. Lebedev and M. A. L. Nicolelis, "Brain-machine interfaces: past, present and future," *Trends Neurosci.* , vol. 29, pp. 536-546, 2006.

[59] R. Sitaram, A. Caria, R. Veit, T. Gaber, G. Rota, A. Kuebler, and N. Birbaumer, "FMRI Brain–Computer Interface: A Tool for Neuroscientific Research and Treatment," *Computational Intelligence and Neuroscience*, vol. 2007, 2007.

[60] J. Wessberg, C. R. Stambaugh, J. D. Kralik, P. D. Beck, M. Laubach, J. K. Chapin, J. Kim, S. J. Biggs, M. A. Srinivasan, and M. A. L. Nicolelis, "Real-time prediction of hand trajectory by ensembles of cortical neurons in primates," *Nature*, vol. 408, pp. 361-365, 2000.

[61] J. Carmena, M. Lebedev, R. Crist, J. O'Doherty, D. Santucci, D. Dimitrov, P. Patil, C. Henriquez, and M. Nicolelis, "Learning to control a brain-machine interface for reaching and grasping by primates," *PLoS Biology*, vol. 1, pp. 193-208, 2003.

[62] L. R. Hochberg, M. D. Serruya, G. M. Friehs, J. A. Mukand, M. Saleh, A. H. Caplan, A. Branner, D. Chen, R. D. Penn, and J. P. Donoghue, "Neuronal ensemble control of prosthetic devices by a human with tetraplegia," *Nature*, vol. 442, pp. 164-171, 2006.

[63] J. C. Sanchez and J. C. Principe, *Brain–Machine Interface Engineering*: Morgan & Claypool Publishers, 2007.

[64] T. S. Ibrahim, "Design of Radiofrequency Coils for Magnetic Resonance Imaging Applications: A Computational Electromagnetic Approach," in *Department of Electrical Engineering*, vol. Doctor of Philosophy. Columbus: The Ohio State University, 2003, pp. 268.

[65] *T.S. Ibrahim*, ""Design of Radiofrequency Coils for Magnetic Resonance Imaging Applications: A Computational Electromagnetic Approach"," in *Department of Electrical Engineering*, vol. PhD.: Ohio State University, 2003, pp. 299.

[66] *O.M. Gandhi*, ""FDTD in Bioelectromagnetics: Safety Assesment and Medical Applications"," in *"Advances in Computational Electrodynamics - The Finite Difference Time Domain Method"*, vol. 11, A. Taflove, Ed., 1998, pp. 613-651.

[67] *T.S. Ibrahim, C. Mitchell, P. Schmalbrock, R. Lee, D.W. Chakeres*, ""Electromagnetic Perspective on the Operation of RF Coils at 1.5–11.7 Tesla"," *Magnetic Resonance in Medicine*, vol. 54, pp. 683-690, 2005.

[68] *T.S. Ibrahim, R. Lee, B.A. Baertlein, A.M. Abduljalil, H. Zhu, P.M.L. Robitaille*, ""Effect of RF coil excitation on field inhomogeneity at ultra high fields: A field optimized TEM resonator"," *Magnetic Resonance Imaging*, vol. 19, pp. 1339-1347, 2001.

[69] *T.S. Ibrahim, R. Lee, B.A. Baertlein, A. Kangarlu, P.L. Robitaille*, ""Application of finite difference time domain method for the design of birdcage RF head coils using multi-port excitations"," *Magnetic Resonance Imaging*, vol. 18, pp. 733-742, 2000.

[70] *T.S. Ibrahim*, ""Analytical Approach to the MR Signal"," *Magnetic Resonance in Medicine*, vol. 54, pp. 677-682, 2005.

[71] S. C. DeMarco, G. Lazzi, W. T. Liu, J. D. Weiland, and M. S. Humayun, "Computed SAR and thermal elevation in a 0.25-mm 2-D model of the human eye and head in response to an implanted retinal stimulator - Part I: Models and methods," *Ieee Transactions on Antennas and Propagation*, vol. 51, pp. 2274-2285, 2003.

[72] G. Lazzi, S. C. DeMarco, W. T. Liu, J. D. Weiland, and M. S. Humayun, "Computed SAR and thermal elevation in a 0.25-mm 2-D model of the human eye and head in response to an implanted retinal stimulator - Part II: Results," *Ieee Transactions on Antennas and Propagation*, vol. 51, pp. 2286-2295, 2003.

[73] A. Taflove and S. C. Hagness, "Computational Electrodynamics The Finite Difference Time Domain Method." Boston: Artech House, 2000.

[74] *A. Taflove, "Advances in Computational Electrodynamics - The Finite Difference Time Domain Method"*: Artech House Publishers, 1998.

[75] *K.S. Yee*, "“Numerical solution of initial boundary value problems involving Maxwell’s equations in isotropic media”," *IEEE Trans. Antennas Propagation*, vol. AP-14, pp. 302–307, 1966.

[76] A. Bayliss and E. Turkel, "Radiation boundary conditions for wave-like equations," *Communications On Pure & Applied Mathematics*, vol. 23, pp. 707-725, 1980.

[77] B. Engquist and A. Majda, "Absorbing boundary conditions for the numerical simulations of waves," *Mathematics of Computation*, vol. 31, pp. 629-651, 1977.

[78] R. L. Higdon, "Absorbing boundary conditions for difference approximations to the multidimensional wave equation," *Mathematics of Computation* vol. 47, pp. 437-459, 1986.

[79] R. Holland and J. Williams, "Total-field versus scattered-field finite-difference," *IEEE Trans Nuclear Science*, vol. 30, pp. 4583-4587, 1983.

[80] W. C. Chew and W. H. Weedon, "A 3D perfectly matched medium from modified Maxwell's equation with stretched coordinates," *Microwave and Optical Technology Letters*, vol. 7, pp. 599-604, 1994.

[81] S. D. Gedney, "An anisotropic perfectly matched layer absorbing media for the truncation of FDTD lattices," *IEEE Trans. Antennas and Propagation*, vol. 44, pp. 1630-1639, 1996.

[82] F. Damen, S. Holdsworth, I. Atkinson, E. Boskamp, T. Claiborne, A. Nauerth, B. Li, X. J. Zhou, Z. Liang, and K. R. Thulborn, "Initial Experience with Sodium MRI of Phantoms and Human Brain at 9.4 Tesla," presented at International Society for Magnetic Resonance in Medicine Annual Meeting, Seattle, WA, 2006.

[83] K. Ugurbil, M. Garwood, and A. R. Rath, "Optimization of modulation functions to improve insensitivity of adiabatic pulses to variations in B1 magnitude," *Journal of Magnetic Resonance (1969)*, vol. 80, pp. 448-469, 1988.

[84] R. Lee, R. Xue, R. Brown, C. Stephanescu, Y. Wang, G. Mizsei, T. Ibrahim, and H. Chang, "Implementation of Mode-Scanning Excitation Method with a 16-ch Transmit/Receive Volume Strip Array at 7T," presented at Proceedings 14th Scientific Meeting, International Society for Magnetic Resonance in Medicine, Seattle, 2006.

[85] P. M. L. Robitaille, A. M. Abduljalil, A. Kangarlu, X. Zhang, Y. Yu, R. Burgess, S. Bair, P. Noa, L. Yang, H. Zhu, B. Palmer, Z. Jiang, D. M. Chakeres, and D. Spigos, "Human magnetic resonance imaging at 8 T," *Nmr in Biomedicine*, vol. 11, pp. 263-265, 1998.

[86] C. N. Chen, V. J. Sank, S. M. Cohen, and D. I. Hoult, "The field dependence of NMR imaging. I. Laboratory assessment of signal-to-noise ratio and power deposition," *Magnetic resonance in medicine*, vol. 3, pp. 722-9, 1986.

[87] C. H. Rosner and W. D. Markiewicz, "High-Field Superconducting Tape Magnet Technology," *Ieee Transactions on Magnetics*, vol. 28, pp. 782-786, 1992.

[88] R. W. Heussner, C. B. Nunes, P. J. Lee, D. C. Larbalestier, and P. D. Jablonski, "Properties of niobium-titanium superconducting wires with Nb artificial pinning centers," *Journal of Applied Physics*, vol. 80, pp. 1640-1646, 1996.

[89] H. Bomsdorf, T. Helzel, D. Kunz, P. Roschmann, O. Tschendel, and J. Wieland, "Spectroscopy and imaging with a 4 tesla whole-body MR system," *NMR Biomed*, vol. 1, pp. 151-8, 1988.

[90] J. F. Schenck, C. L. Dumoulin, R. W. Redington, H. Y. Kressel, R. T. Elliott, and I. L. McDougall, "Human Exposure to 4.0-Tesla Magnetic-Fields in a Whole-Body Scanner," *Medical Physics*, vol. 19, pp. 1089-1098, 1992.

[91] J. T. Vaughan, "How to Do RF at High Fields," in *The International Society of Magnetic Resonance in Medicine Annual Meeting: MORNING CATEGORICAL COURSE: Human MRI and MRS at High Static Magnetic Fields*. Miami, Florida: ISMRM, 2005.

[92] OHSU, "OHSU Receives State-of-the-Art MRI Systems," 2006.

[93] P. B. Roemer, W. A. Edelstein, C. E. Hayes, S. P. Souza, and O. M. Mueller, "The NMR phased array," *Magnetic resonance in medicine*, vol. 16, pp. 192-225, 1990.

[94] R. G. Pinkerton, J. P. Near, E. A. Barberi, R. S. Menon, and R. Bartha, "Transceive Surface Coil Array for MRI of the Human Prostate at 4T," *Magnetic Resonance in Medicine*, vol. 57, pp. 455-458, 2007.

[95] E. A. Barberi, J. S. Gati, B. K. Rutt, and R. S. Menon, "A Transmit-Only/Receive-Only (TORO) RF System for High-Field MRI/MRS Applications," *Magnetic Resonance in Medicine*, vol. 43, pp. 284-289, 2000.

[96] P. Vernickel, P. Röschmann, C. Findeklee, K. Luedeke, C. Leussler, J. Overweg, U. Katscher, I. Graesslin, and K. Schuenemann, "Eight-Channel Transmit/Receive Body MRI Coil at 3T," *Mag Reson Med*, vol. 58, pp. 381-389, 2007.

[97] P. A. Bottomley, C. H. L. Olivieri, and R. Giaquinto, "What is the optimum phased array coil design for cardiac and torso magnetic resonance?," *Magn. Reson. Med.*, vol. 37, pp. 591-599, 1997.

[98] J. R. Porter, S. M. Wright, and A. Reykowski, "A 16-element phased-array head coil," *Magn. Reson. Med.*, vol. 40, pp. 272-279, 1998.

[99] J. A. Bankson, M. A. Griswold, S. M. Wright, and D. K. Sodickson, "SMASH imaging with an eight element multiplexed RF coil array," *Magn. Reson. Mater. Phys. Biol. Med.*, vol. 10, pp. 93-104, 2000.

[100] E. A. Barberi, J. S. Gati, B. K. Rutt, and R. S. Menon, "A transmit-only/receive-only (TORO) RF system for high-field MRI/MRS applications," *Magn. Reson. Med.*, vol. 43, pp. 284-289, 2000.

[101] M. Weiger, K. P. Pruessmann, C. Leussler, R. Roschmann, and P. Boesiger, "Specific coil design for SENSE: a six-element cardiac array," *Magn. Reson. Med.*, vol. 45, pp. 495-504, 2001.

[102] J. A. d. Zwart, P. J. Ledden, P. Kellman, P. v. Gelderen, and J. H. Duyn, "Design of a SENSE-optimized high-sensitivity MRI receive coil for brain imaging," *Magn. Reson. Med.* , vol. 47, 2002.

[103] A. Liffers, H. H. Quick, C. U. Herborn, H. Ermert, and M. E. Ladd, "Geometrical optimization of a phased array coil for high-resolution MR imaging of the carotid arteries," *Magn. Reson. Med.*, vol. 50, pp. 439-443, 2003.

[104] C. E. Hayes and P. B. Roemer, "Noise correlations in data simultaneously acquired from multiple surface coil arrays," *Magn. Reson. Med.*, vol. 16, pp. 181-191, 1990.

[105] X. Zhang and A. Webb, "Design of a capacitively decoupled transmit/receive NMR phased array for high field microscopy at 14.1 T," *Journal of magnetic resonance imaging*, vol. 170, pp. 149-155, 2004.

[106] Y. Zhu, "Parallel excitation with an array of transmit coils.," *Magn Reson Med*, vol. 51, pp. 775-784, 2004.

[107] J. T. Vaughan, G. Adriany, C. J. Snyder, J. Tian, T. Thiel, L. Bolinger, H. Liu, L. DelaBarre, and K. Ugurbil, "Efficient high-frequency body coil for high-field MRI," *Magnetic Resonance in Medicine*, vol. 52, pp. 851-859, 2004.

[108] C. M. Collins, W. Liu, W. Schreiber, Q. X. Yang, and M. B. Smith, "Central brightening due to constructive interference with, without, and despite dielectric resonance," *J Magn Reson Imaging*, vol. 21, pp. 192-6, 2005.

[109] E. Boskamp and L. RF., "Whole body LPSA transceive array with optimized transmit homogeneity," *Proc Int Soc Magn Reson Med*, pp. 903, 2002.

[110] P.-M. Robitaille and L. Berliner, *Ultra High Field Magnetic Resonance Imaging*, vol. 26: Springer Science +Business Media, LLC, 2006.

[111] T. S. Ibrahim, "RF Selective Excitation for Localized Imaging at 9.4 Tesla," presented at International Society for Magnetic Resonance in Medicine Annual Meeting, Miami, FL, 2005.

[112] T. S. Ibrahim, "Ultrahigh-field MRI whole-slice and localized RF field excitations using the same RF transmit array," *IEEE transactions on medical imaging*, vol. 25, pp. 1341-7, 2006.

[113] B. K. Li, F. Liu, and S. Crozier, "Focused, eight-element transceive phased array coil for parallel magnetic resonance imaging of the chest-theoretical considerations," *Magnetic Resonance in Medicine*, vol. 53, pp. 1251-1257, 2005.

[114] B. van den Bergen, C. A. T. van den Berg, L. W. Bartels, and J. J. W. Lagendijk, "7 T body MRI: B-1 shimming with simultaneous SAR reduction," *Physics in Medicine and Biology*, vol. 52, pp. 5429-5441, 2007.

[115] C. van den Berg, H. Kroeze, J. Lagendijk, L. Bartels, and B. van den Bergen, "Simultaneous B1+ homogenisation and SAR hotspot suppression by a phased array MR transmit coil," presented at Proceedings 14th Scientific Meeting, International Society for Magnetic Resonance in Medicine, Seattle, 2006.

[116] T. S. Ibrahim, R. Lee, B. A. Baertlein, A. Kangarlu, and P. L. Robitaille, "Application of finite difference time domain method for the design of birdcage RF head coils using multi-port excitations," *Magn Reson Imaging*, vol. 18, pp. 733-42, 2000.

[117] T. S. Ibrahim, L. Tang, and D. Abraham, "A New Look at RF Power Requirements in MRI," presented at International Society for Magnetic Resonance in Medicine Annual Meeting, Seattle, WA, 2006.

[118] W. MAO, Z. WANG, M. B. SMITH, and C. M. COLLINS, "Calculation of SAR for Transmit Coil Arrays," *Concepts in Magnetic Resonance Part B: Magnetic Resonance Engineering*, vol. 31, pp. 127-131, 2007.

[119] T. S. Ibrahim, R. Lee, B. A. Baertlein, and P. M. Robitaille, "B1 field homogeneity and SAR calculations for the birdcage coil," *Phys Med Biol*, vol. 46, pp. 609-19, 2001.

[120] L. Tang, Y. K. Hue, and T. S. Ibrahim, "Lower RF power absorption combined with uniform excitation using multi-port B1 shimming: numerical simulations and experiments at 7T," presented at Proceedings of the 16th International Society of Magnetic Resonance in Medicine Annual Meeting, Toronto, Canada, 2008.

[121] C. A. Van den Berg, B. van den Bergen, J. B. Van de Kamer, B. W. Raaymakers, H. Kroeze, L. W. Bartels, and J. J. Lagendijk, "Simultaneous B1 + homogenization and specific absorption rate hotspot suppression using a magnetic resonance phased array transmit coil," *Magnetic resonance in medicine*, vol. 57, pp. 577-86, 2007.

[122] P. K. Roschmann, "High-frequency coil system for magnetic resonance imaging apparatus," U.S. Patent, 1988.

[123] R. Abraham and T. S. Ibrahim, "Proposed radiofrequency phased-array excitation scheme for homogenous and localized 7-Tesla whole-body imaging based on full-wave numerical simulations," vol. 57, pp. 235-242, 2007.

[124] T. Vaughan, L. DelaBarre, C. Snyder, J. Tian, C. Akgun, D. Shrivastava, W. Liu, C. Olson, G. Adriany, J. Strupp, P. Andersen, A. Gopinath, P. F. van de Moortele, M. Garwood, and K. Ugurbil, "9.4T human MRI: preliminary results," *Magnetic resonance in medicine*, vol. 56, pp. 1274-82, 2006.

[125] P. M. L. Robitaille, A. M. Abjuljalil, T. S. Ibrahim, R. Lee, B. A. Baertlein, and C. Ashman, "A shielded single element TEM Resonator: a simple extremity RF coil for UHFMRI," presented at The International Society of Magnetic Resonance in Medicine and European Society of Magnetic Resonance in Medicine and Biology Joint Annual Meeting, Glasgow, Scotland, 2001.

[126] T. Ibrahim, L. Tang, and D. Abraham, "A New Look at RF Power Requirements in MRI," presented at Proceedings 14th Scientific Meeting, International Society for Magnetic Resonance in Medicine, Seattle, 2006.

[127] R. Abraham and T. S. Ibrahim, "Proposed Radiofrequency Phased-Array Excitation Scheme for Homogenous and Localized 7-Tesla Whole-Body Imaging Based on Full-Wave Numerical Simulations," *Magnetic Resonance in Medicine*, vol. 57, pp. 235-242, 2007.

[128] T. S. Ibrahim, "RF Power Deposition, General Considerations and Implications of Implants/Devices," presented at International Society for Magnetic Resonance in Medicine Annual Meeting MR Safety Study Group, Seattle, WA, 2006.

[129] C. Gabriel, "Compilation of dielectric properties of body tissues at RF and microwave frequencies," 1996.

[130] T. S. Ibrahim and R. Lee, "Evaluation of MRI RF Probes Utilizing Infrared Sensors," *Biomedical Engineering, IEEE Transactions on*, vol. 53, pp. 963-967, 2006.

[131] B. A. Baertlein, O. Ozbay, T. Ibrahim, R. Lee, Y. Yu, A. Kangarlu, and P. M. Robitaille, "Theoretical model for an MRI radio frequency resonator," *IEEE Trans Biomed Eng*, vol. 47, pp. 535-46, 2000.

[132] J. Tropp and S. Sugiura, "A dual-tuned probe and multiband receiver front end for X-nucleus spectroscopy with proton scout imaging in vivo," *Magnetic resonance in medicine*, vol. 11, pp. 405-12, 1989.

[133] J. T. Vaughan, H. P. Hetherington, J. O. Otu, J. W. Pan, and G. M. Pohost, "High-Frequency Volume Coils for Clinical Nmr Imaging and Spectroscopy," *Magnetic Resonance in Medicine*, vol. 32, pp. 206-218, 1994.

[134] G. Bogdanov and R. Ludwig, "Coupled microstrip line transverse electromagnetic resonator model for high-field magnetic resonance imaging," *Magnetic Resonance in Medicine*, vol. 47, pp. 579-593, 2002.

[135] R. Abraham and T. S. Ibrahim, "Human-body coil design for magnetic resonance imaging at 7 tesla," presented at IEEE International Symposium on Antennas and Propagation, Washington, DC, 2005.

[136] M. Nahrendorf, K. H. Hiller, K. Hu, V. Zeijlemaker, M. Griswold, and W. R. Bauer, "Pacing in high field cardiac magnetic resonance imaging," *Pacing Clin Electrophysiol*, vol. 27, pp. 671-4, 2004.

[137] G. H. Glover, C. E. Hayes, N. J. Pelc, W. A. Edelstein, O. M. Mueller, H. R. Hart, C. J. Hardy, M. O'Donnell, and W. D. Barber, "Comparison of linear and circular polarization for magnetic resonance imaging," *Journal of Magnetic Resonance (1969)*, vol. 64, pp. 255-270, 1985.

[138] P. A. Bottomley, R. W. Redington, W. A. Edelstein, and J. F. Schenck, "Estimating radiofrequency power deposition in body NMR imaging," *Magnetic resonance in medicine*, vol. 2, pp. 336-49, 1985.

[139] D. I. Hoult, C. N. Chen, and V. J. Sank, "The field dependence of NMR imaging. II. Arguments concerning an optimal field strength," *Magnetic resonance in medicine*, vol. 3, pp. 730-46, 1986.

[140] P. Roschmann, "Radiofrequency penetration and absorption in the human body: limitations to high-field whole-body nuclear magnetic resonance imaging," *Medical physics*, vol. 14, pp. 922-31, 1987.

[141] P. A. Bottomley and P. B. Roemer, "Homogeneous tissue model estimates of RF power deposition in human NMR studies. Local elevations predicted in surface coil decoupling," *Annals of the New York Academy of Sciences*, vol. 649, pp. 144-59, 1992.

[142] P. M. Robitaille, "On RF power and dielectric resonances in UHF MRI," *Nmr in Biomedicine*, vol. 12, pp. 318-319, 1999.

[143] T. S. Ibrahim, A. Kangarlu, and D. W. Chakeress, "Design and performance issues of RF coils utilized in ultra high field MRI: experimental and numerical evaluations," *IEEE Trans Biomed Eng*, vol. 52, pp. 1278-84, 2005.

[144] P. F. Van de Moortele, C. Akgun, G. Adriany, S. Moeller, J. Ritter, C. M. Collins, M. B. Smith, J. T. Vaughan, and K. Ugurbil, "B(1) destructive interferences and spatial phase patterns at 7 T with a head transceiver array coil," *Magn Reson Med*, vol. 54, pp. 1503-18, 2005.

[145] F. Liu, B. L. Beck, J. R. Fitzsimmons, S. J. Blackband, and S. Crozier, "A theoretical comparison of two optimization methods for radiofrequency drive schemes in high frequency MRI resonators," *Physics in Medicine and Biology*, vol. 50, pp. 5281-5291, 2005.

[146] U. Katscher, P. Bornert, C. Leussler, and J. S. van den Brink, "Transmit SENSE," *Magnetic Resonance in Medicine*, vol. 49, pp. 144-150, 2003.

[147] Y. D. Zhu, "Parallel excitation with an array of transmit coils," *Magnetic Resonance in Medicine*, vol. 51, pp. 775-784, 2004.

[148] P. Ullmann, S. Junge, M. Wick, F. Seifert, W. Ruhm, and J. Hennig, "Experimental analysis of parallel excitation using dedicated coil setups and simultaneous RF transmission on multiple channels," *Magnetic Resonance in Medicine*, vol. 54, pp. 994-1001, 2005.

[149] U. Katscher, J. Rohrs, and P. Bornert, "Basic considerations on the impact of the coil array on the performance of Transmit SENSE," *Magnetic Resonance Materials in Physics Biology and Medicine*, vol. 18, pp. 81-88, 2005.

[150] T. S. Ibrahim, C. Mitchell, R. Abraham, and P. Schmalbrock, "In-depth Study of the Electromagnetics of Ultra High Field MRI " *NMR in Biomedicine*, pp. In Press, 2006.

[151] T. S. Ibrahim, R. Abraham, L. Tang, and J. T. Vaughan, "Comparison of the Coax Element and Stripline Element TEM Head Coils at Ultra-High Field," presented at International Society for Magnetic Resonance in Medicine Annual Meeting, Seattle, WA, 2006.

[152] B. A. Baertlein, O. Ozbay, T. Ibrahim, R. Lee, X. Zhang, Y. Yu, A. Kangarlu, and P. M. L. Robitaille, "Comments on "Theoretical model for an MRI radio frequency resonator [1]" - Reply," *Ieee Transactions on Biomedical Engineering*, vol. 49, pp. 496-496, 2002.

[153] J. Tropp, "The theory of the bird-cage resonator," *Journal of Magnetic Resonance (1969)*, vol. 82, pp. 51-62, 1989.

[154] R. J. Pascone, B. J. Garcia, T. M. Fitzgerald, T. Vullo, R. Zipagan, and P. T. Cahill, "Generalized electrical analysis of low-pass and high-pass birdcage resonators," *Magn Reson Imaging*, vol. 9, pp. 395-408, 1991.

[155] FDA, "FDA Safety Regulations: http://ntp.niehs.nih.gov/index.cfm?objectid=03DB98A9-E505-AA26-833749D41A8F0B67."

[156] IEC, "IEC SAR Regulations: http://www.iec.ch/news_centre/release/nr2005/nr0405.htm."

[157] K. Ugurbil, J. Vaughan, L. DelaBarre, and C. Snyder, "A Parallel Transceiver for Human Imaging at 9.4T," presented at Proceedings 14th Scientific Meeting, International Society for Magnetic Resonance in Medicine, Seattle, 2006.

[158] C. Collins, M. Smith, J. Vaughan, Z. Wang, W. Mao, J. Fang, W. Liu, G. Adriany, and K. Ugurbil, "Multi-coil Composite Pulses for Whole-Brain Homogeneity Improved over RF Shimming Alone," presented at Proceedings 14th Scientific Meeting, International Society for Magnetic Resonance in Medicine, Seattle, 2006.

[159] D. I. Hoult, C. N. Chen, and V. J. Sank, "Quadrature detection in the laboratory frame," *Magn Reson Med*, vol. 1, pp. 339-53, 1984.

[160] T. S. Ibrahim, C. Mitchell, R. Abraham, and P. Schmalbrock, "In-depth study of the electromagnetics of ultrahigh-field MRI," *NMR Biomed*, vol. 20, pp. 58-68, 2007.

[161] T. S. Ibrahim, R. Lee, B. A. Baertlein, A. Kangarlu, and P. M. L. Robitaille, "On the physical feasibility of achieving linear polarization at high-field: a study of the birdcage coil," presented at International Society for Magnetic Resonance in Medicine Annual Meeting, Philadelphia, PA, 1999.

[162] R. Abraham and T. S. Ibrahim, "Proposed Radiofrequency Phased-Array Excitation Scheme Homogenous and Localized 7 Tesla Whole-Body Imaging Based on Full-Wave Numerical Simulations," *Magnetic resonance in Medicine*, vol. 57, pp. 236-243, 2007.

[163] IEC, "International Electrotechnical Commission. International standard, medical equipment — part 2: particular requirements for the safety of magnetic resonance
equipment for medical diagnosis," *second edition*, vol. 60601-2-33, 2002.

[164] FDA, "Guidance for Industry: Guidance for the Submission of Premarket Notifications for Magnetic Resonance Diagnostic Devices," U.S. Food and Drug Administration, Center for Devices and Radiological Health, 1998, pp. 24.

[165] IEC, "62B/706/CDV Medical electrical equipment: Parts2-33. Particular requirements for the safety of mangetic resonance equipment for medical

diagnosis. ," *Draft proposal 2008 for the next edition of standard EN/IEC 60601-2-33*, 2008.

[166] D. Schaefer, B. Barber, C. Gordon, J. Zielonka, and J. Hecker, "Thermal effects of magnetic resonance imaging," presented at In: Book of abstracts, Society for magnetic resonance in medicine, Berkeley, CA, 1985.

[167] F. Shellock, D. Schaefer, and K. E., "Physiologic responses to MR imaging performed at an SAR level of 6.0 W/kg," *Radiology*, vol. 192, pp. 865-868, 1994.

[168] B. P. Thomas, E. B. Welch, B. D. Niederhauser, W. O. Whetsell Jr, A. W. Anderson, J. C. Gore, M. J. Avison, and J. L. Creasy, "High-Resolution 7T MRI of the Human Hippocampus In Vivo," *Journal of Magnetic Resonance Imaging*, vol. 28, pp. 1266-1272, 2008.

[169] F. G. Shellock, "Radiofrequency Energy-Induced Heating During MR Procedures: A Review," *JOURNAL OF MAGNETIC RESONANCE IMAGING*, vol. 12, pp. 30-36, 2000.

[170] Q. X. Yang, J. Wang, C. M. Collins, M. B. Smith, X. Zhang, K. Ugurbil, and W. Chen, "Phantom Design Method for High-Field MRI Human Systems," *Magnetic Resonance in Medicine*, vol. 52, pp. 1016-1020, 2004.

[171] S. Oh, A. G. Webb, T. Neuberger, B. Park, and C. M. Collins, "Experimental and Numerical Assessment of MRI-Induced Temperature Change and SAR Distributions in Phantoms and In Vivo," *Magnetic Resonance in Medicine*, vol. 62, pp. 1-6, 2009.

[172] D. Shrivastava, T. Hanson, R. Schlentz, W. Gallaghar, C. Snyder, L. DelaBarre, S. Prakash, P. Iaizzo, and J. T. Vaughan, "Radiofrequency Heating at 9.4T: In Vivo Temperature Measurement Results in Swine," *Mag Reson Med*, vol. 59, pp. 73-78, 2008.

[173] C. M. Collins and M. B. Smith, "Calculations of B(1) distribution, SNR, and SAR for a surface coil adjacent to an anatomically-accurate human body model," *Magn Reson Med*, vol. 45, pp. 692-9, 2001.

[174] C. M. Collins and M. B. Smith, "Spatial resolution of numerical models of man and calculated specific absorption rate using the FDTD method: a study at 64 MHz in a magnetic resonance imaging coil," *J Magn Reson Imaging*, vol. 18, pp. 383-8, 2003.

[175] Z. Zhai, G. DeMeester, M. Morich, S. Shvartsman, and R. Kleihorst, "Numerical evaluation of B1-field and SAR for heterogeneous and

homogeneous body model," presented at Proceedings of the 12th Annual Meeting of ISMRM, Kyoto, Japan, 2004.

[176] J. Hand, Y. Li, E. Thomas, M. Rutherford, and J. Hajnal, "Prediction of specific absorption rate in mother and fetus associated with MRI examinations during pregnancy," *Magn Reson Med*, vol. 55, pp. 883-893, 2006.

[177] W. Liu, W. Mao, M. Smith, and C. Collins, "Calculated Local and Average SAR in Comparison with Regulatory Limits," presented at Proceedings 14th Scientific Meeting, International Society for Magnetic Resonance in Medicine, Seattle, 2006.

[178] J. M. Jin and J. Chen, "On the SAR and field inhomogeneity of birdcage coils loaded with the human head," *Magnetic Resonance in Medicine*, vol. 38, pp. 953-963, 1997.

[179] A. J. Schwarz, M. Rijpkema, D. J. Collins, G. S. Payne, T. Prock, A. C. Woodward, A. Heerschap, and M. O. Leach, "SAR and tissue heating with a clinical (31)P MRS protocol using surface coils, adiabatic pulses, and proton-decoupling," *Magn Reson Med*, vol. 44, pp. 692-700, 2000.

[180] D. Simunic, P. Wach, W. Renhart, and R. Stollberge, "Spatial distribution of high-frequency electromagnetic energy in human head during MFU: numerical results and measurements," *IEEE Trans Biomedical Engineering*, vol. 43, pp. 88-96, 1996.

[181] J. W. Hand, R. W. Lau, J. J. W. Lagendijk, J. X. Ling, M. Burl, and I. R. Young, "Electromagnetic and thermal modeling of SAR and temperature fields in tissue due to an RF decoupling coil," *Magnetic Resonance in Medicine*, vol. 42, pp. 183-192, 1999.

[182] Z. Wang, J. C. Lin, W. Mao, W. Liu, M. B. Smith, and C. M. Collins, "SAR and Temperature: Simulations and Comparison to Regulatory Limits for MRI," *JOURNAL OF MAGNETIC RESONANCE IMAGING*, vol. 26, pp. 437-441, 2007.

[183] Z. Wang, J. C. Lin, J. T. Vaughan, and C. M. Collins, "Consideration of Physiological Response in Numerical Models of Temperature During MRI of the Human Head," *JOURNAL OF MAGNETIC RESONANCE IMAGING*, vol. 28, pp. 1303-1308, 2008.

[184] U. Nguyen, J. Brown, I. Chang, J. Krycia, and M. Mirotznik, "Numerical evaluation of heating of human head due to magnetic resonance image," *IEEE Trans Biomedical Engineering*, vol. 51, pp. 1301-1309, 2004.

[185] J. W. Hand, J. J. W. Lagendijk, J. V. Hajnal, R. W. Lau, and I. R. Young, "SAR and temperature changes in the leg due to an RF decoupling coil at frequencies between 64 and 213 MHz," *Journal of Magnetic Resonance Imaging*, vol. 12, pp. 68-74, 2000.

[186] W.-X. Li and O. P. Gandhi, "Thermal Implications of the New Relaxed IEEE RF Safety Standard for Head Exposures to Cellular Telephones at 835 and 1900 MHz," *IEEE TRANSACTIONS ON MICROWAVE THEORY AND TECHNIQUES*, vol. 54, pp. 3146-3154, 2006.

[187] G. M. J. V. Leeuwen, J. J. W. Lagendijk, B. J. A. M. V. Leersum, A. P. M. Zwamborn, S. N. Hornsleth, and A. N. T. J. Kotte, "Calculation of change in brain temperatures due to exposure to a mobile phone," *Physics in medicine and biology*, vol. 44, pp. 2267-2379, 1999.

[188] P. Bernardi, M. Cavagnaro, S. Pisa, and E. Piuzzi, "Specific Absorption Rate and Temperature Increases in the Head of a Cellular-Phone User," *IEEE TRANSACTIONS ON MICROWAVE THEORY AND TECHNIQUES*, vol. 48, pp. 1118-1126, 2000.

[189] J. Q. Wang and O. Fujiwara, "FDTD computation of temperature rise in the human head for portable telephones," *Ieee Transactions on Microwave Theory and Techniques*, vol. 47, pp. 1528-1534, 1999.

[190] O. P. Gandhi, Q.-X. Li, and G. Kang, "Temperature Rise for the Human Head for Cellular Telephones and for Peak SARs Prescribed in Safety Guidelines," *IEEE TRANSACTIONS ON MICROWAVE THEORY AND TECHNIQUES*, vol. 49, pp. 1607-1613, 2001.

[191] P. Bernardi, M. Cavagnaro, S. Pisa, and E. Piuzzi, "Power Absorption and Temperature Elevations Induced in the Human Head by a Dual-Band Monopole-Helix Antenna Phone," *IEEE TRANSACTIONS ON MICROWAVE THEORY AND TECHNIQUES*, vol. 49, pp. 2539-2546, 2001.

[192] S. Pisa, G. Calcagnini, M. Cavagnaro, E. Piuzzi, M. Triventi, and P. Bernardi, "SAR Temperature Elevations in Pacemaker Holders Exposed to EM Fields Produced by MRI Apparatus," *Microwave Symposium Digest, 2006. IEEE MTT-S International*, pp. 1754-1757, 2006.

[193] E. Mattei, M. Triventi, G. Calcagnini, F. Censi, W. Kainz, H. I. Bassen, and P. Bartolini, "Temperature and SAR measurement errors in the evaluation of metallic linear structures heating during MRI using fluoroptic probes," *PHYSICS IN MEDICINE AND BIOLOGY*, vol. 52, 2007.

[194] F. A. Duck, *Physical properties of tissue: a comprehensive reference book*: Academic Press, 1990.

[195] P. Bernardi, M. Cavagnaro, S. Pisa, and E. Piuzzi, "Specific Absorption Rate and Temperature Elevation in a Subject Exposed in the Far-Field of Radio-Frequency Sources Operating in the 10–900-MHz Range," *IEEE TRANSACTIONS ON BIOMEDICAL ENGINEERING*, vol. 50, pp. 295-304, 2003.

[196] G. Beckmann and P. V. Gilli, *Thermal Energy Storage: Basics, Design, Applications to Power Generation and Heat Supply*: Springer; 1 edition (October 30, 2002), 2002.

[197] J. Y. Chen and O. P. Gandhi, "Numerical simulation of annular-phased arrays of dipoles for hyperthermia of deep-seated tumors," *IEEE transactions on bio-medical engineering*, vol. 39, pp. 209-16, 1992.

[198] G. Kang and O. P. Gandhi, "SARs for pocket-mounted mobile telephones at 835 and 1900 MHz," *Phys Med Biol*, vol. 47, pp. 4301-4313, 2002.

[199] M. Mojarradi, D. Binkley, B. Blalock, R. Andersen, N. Ulshoefer, T. Johnson, and L. Del Castillo, "A miniaturized neuroprosthesis suitable for implantation into the brain," *IEEE TRANSACTIONS ON NEURAL SYSTEMS AND REHABILITATION ENGINEERING*, vol. 11, pp. 38-42, 2003.

[200] R. Bashirullah, J. G. Harris, J. C. Sanchez, T. Nishida, and J. C. Principe, "Florida Wireless Implantable Recording Electrodes (FWIRE) for Brain Machine Interfaces," *IEEE International Symposium on Circuits and Systems, 2007. ISCAS 2007*, pp. 2084-2087, 2007.

[201] P. Bernardi, M. Cavagnaro, J. C. Lin, S. Pisa, and E. Piuzzi, "Distribution of SAR and temperature elevation induced in a phantom by a microwave cardiac ablation catheter," *Microwave Theory and Techniques, IEEE Transactions on*, vol. 52, pp. 1978-1986, 2004.

[202] C. Rappaport, "Cardiac tissue ablation with catheter-based microwave heating," *Int J Hyperthermia*, vol. 20, pp. 769-80, 2004.

[203] Z. J. Gu, C. M. Rappaport, P. J. Wang, and B. A. VanderBrink, "A 2 1/4-turn spiral antenna for catheter cardiac ablation," *Ieee Transactions on Biomedical Engineering*, vol. 46, pp. 1480-1482, 1999.

[204] S. A. Shock, K. Meredith, T. F. Warner, L. A. Sampson, A. S. Wright, T. C. Winter, D. M. Mahvi, J. P. Fine, and F. T. Lee, "Microwave ablation with loop antenna: in vivo porcine liver model," *Radiology*, vol. 231, pp. 143-9, 2004.

[205] K. Gosalia, G. Lazzi, and M. Humayun, "Investigation of a microwave data telemetry link for a retinal prosthesis," *Microwave Theory and Techniques, IEEE Transactions on*, pp. 1925-1933, 2004.

[206] J. Kim and Y. Rahmat-Samii, "Implanted antennas inside a human body: Simulations, designs, and characterizations," *Ieee Transactions on Microwave Theory and Techniques*, vol. 52, pp. 1934-1943, 2004.

[207] R. Makinen, V. Kangas, J. Lahtinen, and M. Kivikoski, "A coaxial probe feed model for FDTD," *Microwave and Optical Technology Letters*, vol. 34, pp. 193-198, 2002.

[208] M. Nicolelis, "Brain-machine interfaces to restore motor function and probe neural circuits," *Nature Reviews Neuroscience*, vol. 4, pp. 417-422, 2003.

[209] J. G. Maloney, K. L. Shlager, and G. S. Smith, "A Simple FDTD Model for Transient Excitation of Antennas by Transmission Lines," *IEEE TRANSACTIONS ON ANTENNAS AND PROPAGATION*, vol. 42, pp. 289-292, 1994.

[210] D. K. Cheng, *Field and Wave Electromagnetics*, Second Edition ed: Pearson Education Inc., 2001.

[211] C. A. Balanis, *Advanced Engineering Electromagnetics*: Wiley; Solution Manual edition (May 9, 1989), 1989.

[212] C. T. Tai and R. E. Collin, "Radiation of a Hertzian dipole immersed in a dissipative medium," *IEEE Transactions on Antennas and Propagation*, vol. 48, pp. 1501-1506, 2000.

[213] FCC, "FCC Policy on Human Exposure to Radiofrequency Electromagnetic Fields," 1996.

[214] T. Ibrahim, Y.-K. Hue, R. Gilbert, and F. Boada, "Tic Tac Toe: Highly-Coupled Load Insensitive Tx/Rx Array and a Quadrature Coil Without Lumped Capacitors," presented at ISMRM Meeting, Toronto, Canada, 2008.